Investigation on Metallurgical and Mechanical Behavior of Thick-Sectioned Inconel 617 Weldments by Laser-based Welding Processes

A Thesis Submitted

by

MOHD AQEEL

Reg. No. 16ETPM02

In partial fulfillment of the requirements for the award of the degree of

DOCTOR OF PHILOSOPHY

In

MATERIALS ENGINEERING

Under the supervision of

Prof. Jai Prakash Gautam

Professor, School of Engineering Sciences and Technology, University of Hyderabad

Dr. S M Shariff

Scientist – F, International Advanced Research
Centre for Powder Metallurgy and New
Materials (ARCI), Hyderabad



School of Engineering Sciences and Technology,
University of Hyderabad, Hyderabad, India
Feb 2022

DECLARATION

I, MOHD AQEEL hereby declare that this thesis work entitled "Investigation on metallurgical and mechanical behavior of thick-sectioned Inconel 617 weldments by laser-based welding processes" submitted in partial fulfillment of the requirements for the award of Doctor of Philosophy in Materials Engineering at the School of Engineering Sciences and Technology (SEST), University of Hyderabad is completely my own work except for those referred. This work was carried out under the supervision of Prof. Jai Prakash Gautam and Dr. S.M Shariff. This report is a record of bonafide work carried out by me and results incorporated are not been reproduced/copied from any source. This work has not been submitted to any other University or Institute for the award of any other degree or equivalent.

MOHD AQEEL

Reg. No.: 16ETPM02

School of Engineering Sciences

and Technology, University of Hyderabad



CERTIFICATE

This is to certify that the thesis work entitled "Investigation on metallurgical and mechanical behavior of thick-sectioned Inconel 617 weldments by laser-based welding processes", submitted by MOHD AQEEL bearing Reg. No. 16ETPM02 in partial fulfillment of the requirements for the award of the degree of Doctor of Philosophy in Materials Engineering is a bonafide record of the work carried out by him under our supervision. This thesis has not been submitted previously in part or in full to this or any other University or Institution for the award of any degree or diploma.

Prof. Jai Prakash Gautam

Professor, School of Engineering Sciences and Technology, University of Hyderabad

(Supervisor)

Dr. JAI PRAKASH GAUTAM

School of Engineering Sciences & Technology
University of Hyderabad
Hyderabad-Form 46

Approved by:

Dr. S M Shariff

Scientist – F, International Advanced Research
Centre for Powder Metallurgy and New
Materials (ARCI), Hyderabad

(Co-Supervisor)

Dr. S.M.SHARIFF, Ph.D(Engg.)

Scientist-F
INTERNATIONAL ADVANCED RESEARCH CENTRE FOR
POWDER METALLURGY AND NEW MATERIALS (ARCI)
Dept. of Science & Tech., Govt. of India
P.O.Balapur, Hyderabad-500005.TS, INDIA

Prof. Dibakar Das

Prof. Dibakar Das DEAN

School of Engineering Sciences and Technology

Dean, School of Engineering Sciences and Telepharatory Hyderabad 500 046.

University of Hyderabad



CERTIFICATE

This is to certify that the thesis entitled "Investigation on metallurgical and mechanical behavior of thick-sectioned Inconel 617 weldments by laser-based welding processes" submitted by MOHD AQEEL bearing registration number 16ETPM02 in partial fulfillment of the requirements for award of Doctor of Philosophy, in Materials Engineering at the School of Engineering Sciences and Technology (SEST) is a bonafide work carried out by him under my supervision and guidance.

This thesis is free from plagiarism and has not been submitted previously in part or in full to this or any other University or Institution for the award of any degree or diploma.

a. Publications from thesis work:

- Liquation cracking in Inconel 617 alloy by Laser and Laser-Arc Hybrid welding, 2020, Journal of Materials and Manufacturing Processes, DOI:10.1080/10426914.2020.1866200.
- 2. Influence of heat input on bead profile and microstructure characteristics in laser and laser-hybrid welding of Inconel 617 alloy, 2022, *Welding International Journal*, DOI/10.1080/09507116.2022.2063093
- 3. Process optimization and analysis of deep penetration welding of Inconel 617 superalloy using fiber-coupled diode laser, 2022, *Journal of Optics and Laser Technology, (Under Review)*
- 4. Comparative study on autogenous Diode Laser, CO₂ Laser-MIG hybrid and multi-pass TIG welding of 10-mm thick Inconel 617 Superalloy, 2022, Journal of Materials Processing Technology (Under Review)
- 5. Statistical modeling of Autogenous single-pass diode laser welding process of Inconel 617 alloy, (Under Submission)
- 6. A Novel method for single-pass diode laser welding of thick-sectioned Inconel 617 alloy, (Under Submission)

b. Patents from thesis work:

 Autogenous Laser Welding System and Method for Joining Thick Metallic Parts without Filler Wire Feeder, 2022, Indian Patent No. 202211005404 dated 01-02-20222

c. Presentations in conferences:

 Oral Presentation in International Structural Integrity Conference & Exhibition (SICE-2018) entitled "Laser Hybrid welding of Inconel 617 for Advanced ultra-super critical Boiler (A-USC) Applications" (25 – 27 July 2018) Further, the student has passed the following courses towards fulfilment of coursework requirement for Ph.D.

Course Code	Name	Credits	Pass/Fail
MT-801	Research Methodology	4	Pass
MT-802	Characterization of Materials -Microscopy	4	Pass
MT-805	Mechanical Behavior of Materials	4	Pass
MT-807	Materials Processing & Characterization Laboratory	4	Pass
MT-808	Advanced Engineering Mathematics	2	Pass

Dr. JAI PRAKASH GAUTAM
Professor
School of Engineering Sciences & Technology
University of Hyderabad
Hyderabad-500 046.

Prof. Dibakar Das

DEAN
School of Engineering Sciences and Technology
University of Hyderabad, Hyderabad 500 046.

ACKNOWLEDGEMENTS

First and foremost, I express my deep sense of gratitude and respect to my research supervisor *Prof. Jai Prakash Gautam*, Professor, for his keen interest, constant and valuable guidance, strong motivation and constant encouragement during my research work. I would like to express my special respect and thanks to my co-supervisor **Dr. S M Shariff** for giving me an opportunity to work with him and inspiring me to become an independent researcher. I am indebted to him for his continuous guidance, thumping encouragement, regular discussions and constant support which has always been a motivating factor for me to keep going forward and challenging myself.

I am thankful to my doctoral review committee members *Prof. Koteswararao V Rajulapati, and Prof. Ing. V.V.S.S. Srikanth* for their insightful comments and keeping track of my research progress and making this work better. I am also very thankful to the Dean of School of Engineering Sciences and Technology, *Prof. Dibakar Das* and all other faculties in the department for providing me the facilities to carry out my research work.

I express my deep sense of gratitude and respect to Late. Dr. G Padmanabham, ARCI, for his support and providing an opportunity to work with him in his life. Forwarding the vote of thankfulness, I really appreciate the technical assistance and guidance from Dr. Ravi Bathe, Mr. K.V. Phani Prabhakar, Dr. Sudharshan Phani Pardhasaradhi, Dr. Joydeep Jordar, Dr. Ravi Chandra Gundakaran, Dr. N Ravi, Dr. Koppoju Suresh, Mr. E. Anbu Rasu, Mr. J. Shyam Rao, Mr. N. Venkat Rao and all technical staff from different labs at University of Hyderabad and ARCI who helped me with their knowledge, skill and warm-hearted gesture. I also extend my gratitude to all my colleagues and friends for their continuous help, support and friendship. Thanks to S. Janakiram, Akash Chouhan, Mohsin Hasan, L Subashini, E. Anusha, P. Sankar Ganesh, Hitesh Kumar, M. Swarna, Santoshsarang DM, Nazeer Basha, B. Amarendar Rao and all other colleagues for stimulating discussions and all the good times we have had in my Ph.D journey.

I am also thankful to *Dr. Sharma Paswan* for his help and support to carry out high temperature corrosion test at NML. I am also thankful to *Dr. Murugaiyan Amirthalingam* IIT-Madras for welding simulation work. I am very thankful to Mishra Dhatu Nigam Limited (MIDHANI) for providing superalloy material.

In addition, I would also like to acknowledge Department of Science and Technology (DST), New Delhi for funding the project "National Centre for Development of Advanced Materials and Manufacturing Processes for Clean Coal Technologies for Power Applications"

(Program code. SNCD), under which this work was undertaken and special thanks to ARCI for supporting my PhD work and for providing me the scholarship. I would also like to acknowledge DST-FIST and DST-PURSE grant for the FESEM-EDS facility and its maintenance at School of Engineering Science and Technology, University of Hyderabad.

I would like to thank my teachers at my former college, without whose initial support and guidance I would not have chosen research as a career. Last but not least, I express my heartfelt thanks to my parents, brothers and family for their ceaseless blessing, love and support. Without their strong support and encouragement, I could not have translated my dream into reality.

MOHD AQEEL

Dedicated

to

my

Father Late. Mohd Waheed

Mother: Ruqia Begum

Brothers: Mohd Fareed

Mohd Arif

Mohd Altaf

Mohd Ataullah

Mohd Shoeib

Sisters: Yasmeen Fatima

Saba Fatima

Abstract

In the 21st century, the major challenge facing worldwide is to provide abundant and cheap electricity to the growing global demand and at the same time reduce pollution to preserve the environment. Although several technologies such as solar and wind renewable energy resources are in the offing with development and use, effective utilization of existing thermal power plants for prolonging their life as well as enhancing the boiler efficiency is the need of the hour. Thus, future advanced ultra-super critical (AUSC) boilers are aimed at increasing the efficiency of coalbased power generation in the range of 46 - 50% with application of advanced nickel-based superalloy materials to withstand higher temperatures $(710 - 760^{\circ}\text{C})$ and pressures (25 - 35 MPa). Inconel 617 is considered one of the most promising candidate materials for AUSC boiler components owing to its superior high-temperature structural stability coupled with hot corrosion/oxidation and creep resistance. Fusion welding is an essential joining process for fabrication and construction of boiler parts in thermal power plant. Although, several conventional fusion welding processes such as SMAW, SAW, GMAW, TIG and their advanced variants are currently in use for joining thick-sectioned boiler parts, but these multi-pass welding processes characterized by their high heat input entail certain disadvantages such as high component distortion, excessive filler material consumption and induced high residual stresses in the components which deteriorate their life.

Single-pass welding process employing laser heat source such as Autogenous Laser Welding (ALW) and Laser-Arc Hybrid Welding (LHW) are anticipated to provide great promise in these aspects. Laser welding is a fusion joining process wherein a laser beam with sufficiently high-power density interacts with the material resulted in a high depth to width ratio weld joints. Laser-Arc Hybrid Welding (LHW) technique is developed by combining the electric arc and the laser beam as heat sources in a common weld pool. As compared to conventional multi-pass arc welding processes, single-pass laser-based welding process (ALW and LHW) produces welds with reduced heat-input, narrow heat-affected-zone, high welding speed leading to higher production rate, minimal distortion and residual stress and thus provide tremendous technological and economic benefits. However, several research works reported on welding of Inconel 617 alloy employing various types of arc and laser welding processes with often occurrence of liquation cracking being observed in multi-layer weld bead and HAZ regions. Although, some attempts were tried to reduce weld cracking susceptibility by controlling heat-input, employing additional preheating and modification of filler-material, but detailed understanding in terms of identification of low melting eutectic (LME) phases and their mechanical behavior on weld performance is still lacking. Moreover, when welding thick-section which is essential for boiler components, the satisfactory through-thickness penetration in single pass welding of thick-section material was lacking due to formation of surface underfill / undercuts with root hump defects associated with high viscous nature of Inconel 617 alloy. As on date, no report is available on the single pass autogenous laser and laser-hybrid welding of thick-sectioned Inconel 617 alloy with comprehensive metallurgical and mechanical behavior analysis. Therefore, the present thesis work is targeted to investigate, analyze and compare metallurgical, mechanical and corrosion behavior with comprehensive characterization of weldments of 10-mm thick Inconel 617 superalloy produced by single pass laser and laser-hybrid welding techniques with conventional multi-pass TIG welding process.

Firstly, preliminary feasibility study was conducted for optimization of autogenous CO₂ laser welding (ALW) and CO₂ laser + MIG hybrid welding (LHW) processes illustrating influence of heat input on weld bead characteristics of Inconel 617 alloy material. Weld-bead profile formed in LHW was a typical "wine-cup" shape profile with wider top due to MIG effect and narrow at bottom zone due to laser, whereas laser-alone ALW produced a Y-shape bead profile on account of high intensity laser beam during autogenous CO₂ laser welding. Weld bead width, penetration, and fusion area were found to increase with an increase in heat input in both LHW and ALW processes. Radius of curvature (ROC) at neck zone, which is a critical factor determining liquation cracking susceptibility was found to be significantly larger in LHW with influence of low cooling rate than that of ALW counterpart.

Liquation cracking was normally observed in the vicinity of fusion boundary in both ALW and LHW weldments. Thus, understanding mechanism of liquation cracking susceptibility and mitigate its effect with detailed study has become tantamount. Thus, microstructural analysis using FESEM, EDS/Elemental mapping, micro-focused XRD and high-speed Nano Indentation techniques were utilized for co-relating its effect on resulting cracking behavior. Results indicated that the eutectic structure formed in Partially Melted Zone (PMZ) constitutes multiple phases enriched with Cr and Mo and attributed to the account of eutectic reaction during welding. Further, micro-focused XRD analysis in PMZ indicated that the eutectic networks composed of ternary phase comprising γ-Ni+M₆C/M₂₃C₆. These eutectic networks were observed to be doubled with wider PMZ in neck region of LHW than ALW, indicating the direct influence of heat input. LHW provided enhancement in nano-hardness of eutectic network than that of ALW and attributed to dissolution of Mo content in PMZ. With the decreased heat input, the total crack length (TCL) increased steadily in both ALW and LHW processes. LHW showed nearly 50% reduction in TCL than ALW, whereas the quantity of GB re-solidified phase enhanced by 50% in LHW than ALW.

LHW was more beneficial in terms of resistance to liquation cracking susceptibility as compared to ALW process.

Although LHW using CO₂ laser could effectively reduce liquation cracking susceptibility, employing single laser source with enhanced coupling efficiency under controlled heat input effectively improved the weldability of Inconel 617 alloy thick-sections. However, LHW on account of low aspect ratio could not enhance process speeds with deeper penetration in a single pass in thick-section welding. Thus, high-power diode laser welding (DLW) processing was utilized to develop weld joint in 10-mm thick Inconel 617 alloy in single pass autogenously. For the purpose, systemic study with bead-on-plate configuration welding to butt-welding to final novel adaptive diode laser welding has been taken up and assessed their performance. Firstly, bead-onplate (BOP) welding experiments were conducted with varying defocusing distance (DF) from -14 to +10 mm at constant optimal laser power (LP) and welding speed (WS) followed by butt-joint experiments by varying the welding speed in the range of 4 - 18 mm/s. Results indicated that the weld penetration and width is mainly controlled by DF and WS. Full penetration could only be achieved at optimum parameters but with many a times with underfill/undercuts and root hump defects. It was very critical to obtain full penetration without underfill/undercuts and root hump defect in deep penetration autogenous laser welding of thick-sections. However, tensile testing of weldment specimen with a maximum of 9 mm weld penetration instead of complete penetration showed maximum joint efficiency of 98%.

As weld defects such as underfill and root sag could not be eliminated by optimizing parameters of DF and WS in DLW process, thus, influence of all three critical DLW laser processing parameters of LP, DF and WS on weld quality was optimized using statistical model RSM-BBD. Using RSM model, optimal values obtained were 6 kW LP, 6 mm/s WS and -1.489 mm DF. Validation of the model was carried out using desirability approach and the experimental results were found to be in good agreement with the predicted one with less than 5% error. Thus, weldments s obtained employing processing parameters obtained by statistical modeling approach were found to be superior as compared to that conventional approach of optimization, more specifically for DF optimization. However, elimination of underfill/root hump defects remained elusive in deep penetration single-pass laser welding of Inconel 617 superalloy.

As occurrence of underfill/root hump defects in single-pass thick-section DLW weld joints persistent whenever full penetration was achieved, development of an alternative method became the need of the hour. Thus, a novel adaptive diode-laser welding (ADLW) method was developed by employing a special modified groove design and setup with pre-placement of filler wire and employing a two-step welding strategy. As a result of this novel ADLW technique, the method

entailed production of full penetration welds with complete elimination of underfill/undercuts and root hump defects. Furthermore, the weld joints produced by this novel method constituted of uniform weld bead seam throughout the weld length with minimal porosity, minimized distortion as well as small HAZ as compared to previously produced techniques. Cross-sectional macrograph indicated typical Y-type bead shape with high aspect (depth-to-width) ratio. Moreover, developed process showed joint efficiency of 99 - 100 % with 10 - 15 % improvement in yield strength and 20 - 25 % improvement in impact strength as compared to that of unwelded substrate.

As multi-pass arc welding processes are currently being utilized for joining boiler components, thus, single-pass LHW and newly developed ADLW processes compared with conventional multi-pass TIG welding process with assessment of their metallurgical, mechanical and high temperature corrosion behavior. Results indicated that the bead profile obtained in LHW, ADLW and TIG welds were "wine-cup", Y-type shape and bath-tub shape respectively on account of heat source intensity profile distributions, number of heat sources and weld passes with aspect (depth-to-width) ratio increasing in the order of ADLW>LHW>TIG and distortion level was found reduce in the order of TIG>LHW>ADLW. Further, microstructural analysis indicated, nonhomogenous microstructure in both LHW and TIG welds due to multiple number of heat sources and weld passes with XRD analysis indicating presence of large number of strong carbide peaks of M₂₃C₆ and M₆C in multi-pass TIG weldment as compared to that of LHW and ADLW counterparts. These effects found to be convergent with repeated thermal cycles of multiple passes in TIG, lowheat inputs of laser welding processes and their associated cooling rates. Furthermore, tensile test results indicated the joint efficiency of ADLW, LHW are slightly higher than that of TIG weldments with highest elongation being in ADLW weldment as compared to LHW and TIG processes. Hot corrosion studies employing both salt-coated and coal-ash mixed flue gas environment indicated that laser welded specimens provide higher resistance than that of TIG and BM counterparts owing to refined microstructure with reduced micro-segregation. Overall, the joint efficiency produced in single-pass LHW and ADLW was found to be sufficiently enough to apply in various components of thermal power plant. Indeed, ADLW processed developed proved advantageous in terms of producing laser welding in single pass with joint efficiency on par with other laser-hybrid based and multi-pass fusion welding techniques. The hot corrosion resistance DLW and ADLW joints were also found to be superior to other LHW and TIG counterparts owing to improved microstructure with refinement and reduced micro-segregation.

Thesis work is believed to add significant contribution to the existing literature from the point of both industrial importance and academic interest.

TABLE OF CONTENTS

Chapter I:	Introduction Pa	age No.
1.1	Overview of Thermal power plant	01
1.2	Properties Requirements for Boiler Components	03
1.3	Materials for Boiler Components	05
	1.3.1 Ferritic Steels	05
	1.3.2 Austenitic steels	06
1.4	Nickel based superalloys for boiler applications in thermal power plan	t 07
	1.4.1 Inconel 617 superalloy material	09
1.5	Metallurgy of Inconel 617	10
1.6	Weldability of Inconel 617	11
	1.6.1 Liquation cracking susceptibility	11
	1.6.2 Issues in thick sections welding	12
1.7	Fusion welding processes	13
	1.7.1 Tungsten Inert Gas welding process	14
	1.7.2 Metal Inert Gas welding process	14
	1.7.3 Submerged arc welding process	15
	1.7.4 Shielded metal arc welding	15
	1.7.5 Plasma arc welding	15
	1.7.6 Cold metal transfer welding	16
1.8	High-energy beam welding processes	16
	1.8.1 Electron beam welding	17
	1.8.2 Laser beam welding	17
	1.8.2.1 Carbon dioxide laser welding	18
	1.8.2.2 Nd:YAG laser welding	18
	1.8.2.3 Disc Laser welding	19
	1.8.2.4 Fiber laser welding	19
	1.8.2.5 High power diode laser welding	19
1.9	Laser-Arc Hybrid Welding	20
	1.9.1 Hybrid Laser-MIG welding process	22
	1.9.2 Hybrid Laser-TIG welding process	23
	1.9.3 Hybrid Laser-Plasma welding process	23
1.10	Statistical Modelling applied for welding	24
1.11	Motivation and Research Objectives of the Thesis work	25
1.12	Overview of the Thesis	27
1.13	References	28
Chapter II	: Literature Review	32
2.1	Welding of Inconel 617	33
2.2	Thick-Sections welding	42
2.3	Recent developments on welding techniques for Inconel 617	

		superalloy material	44
		2.3.1 Arc welding processes	44
		2.3.2 Laser-based welding processes	49
	2.4	Recently developed narrow-gap multi-pass laser welding methodology	53
	2.5	Hot corrosion behavior of superalloy materials	56
	2.6	Statistical modelling applied for welding process optimization	58
	2.7	References	61
Chaj	oter II	I: Experimental Details	67
	3.1	Methodology of Experiments	67
	3.2	Materials	67
	3.3	Design of Joint configurations	69
	3.4	Welding Systems and Setup Conditions	70
		3.4.1 Slab CO ₂ laser	70
		3.4.2 Metal Inert gas (MIG) welding equipment	71
		3.4.3 CO ₂ laser - MIG arc hybrid welding (LHW)	72
		3.4.4 Conventional TIG welding	73
		3.4.5 Fiber-coupled high-power diode laser welding (DLW)	74
	3.5	Response surface methodology (RSM) based statistical modelling	78
	3.6	Design of novel joint with setting up of diode laser apparatus for	
		development of novel welding process (ADLW)	81
	3.7	Characterization of weldments	84
		3.7.1 Bead profile analysis	85
		3.7.2 Macro and Microstructural analysis	86
	3.8	Phase analysis	87
		3.8.1 Conventional X-ray diffraction (XRD)	87
		3.8.2 Micro-focused X-ray diffraction (XRD)	88
	3.9	Mechanical Properties of Weldments	89
		3.9.1 Hardness analysis	89
		3.9.1.1 Conventional	89
		3.9.1.2 Nano Indentation	89
		3.9.2 Tensile and Impact tests	90
	3.10	Hot corrosion analysis of weldments	92
	3.11	References	93
Chaj	oter IV	V: Comprehensive study on process optimization of CO ₂	
		Laser and CO ₂ Laser-MIG Arc Hybrid welding of	
		Inconel 617 alloy	95
	4.1	Introduction	95
	4.2	Experimental Methodology	95
	4.3	Bead profile analysis	96
	4.4	Microstructure and hardness distribution analysis	101

4.5	HAZ and ROC analysis at neck zone	105
4.6	6 Conclusions	108
4.7	7 References	109
Chapter	·V: Investigations on liquation cracking susceptibility of	
	Inconel 617 alloy during CO ₂ Laser and CO ₂ Laser-MIC	j
	Arc Hybrid welding processes	110
5.1	Introduction	110
5.2	2 Experimental Methodology	110
5.3	Bead profile analysis	111
5.4	X-ray phase analysis	112
5.5	Hardness distribution analysis	114
5.6	Fusion zone microstructural Analysis	115
5.7	7 Analysis of PMZ and HAZ	116
5.8	Mechanism of liquation cracking susceptibility in laser weldments	120
5.9	O Conclusions	124
5.1	0 References	125
Chapter	VI: Optimization of high-power fiber-coupled diode laser	
	process parameters for deep penetration welding of	
	Inconel 617 superalloy	126
6.1	Introduction	126
6.2	2 Experimental Methodology	126
6.3	Weld Bead profile analysis	127
	6.3.1 Influence of defocusing distance on melt-runs in BOP	
	configuration	128
	6.3.2 Influence of welding speed on welds of square-butt joint	
	configuration	132
6.4	•	135
6.5		139
6.6		141
6.7	7 References	142
Chapter	VII: Statistical Analysis and Multi Objective Optimization	
	of Diode Laser Welding Process by means of RSM and	
	Desirability Approach	145
7.1	Introduction	145
7.2	2 Experimental Methodology	146
7.3	Statistical model for upper bead width (UBW)	147
7.4	Statistical model for weld penetration (WP)	149
7.5	Statistical model for fusion zone area (FZA)	153
7.6	Statistical model for radius of curvature (ROC)	156

7.7	Optimization using desirability approach	159
7.8	Validation of the optimum solutions	161
7.9	Analysis of tensile properties of optimized butt joint produced by RSM	162
7.10	Conclusions	163
7.11	References	164
Chapter V	III: Development of novel two-step diode laser welding	
	technique without filler-wire feeding and designing of	
	specific joint configuration for thick-section welding of	
	superalloy	166
8.1	Introduction	166
8.2	Experimental Methodology	167
8.3	Joint design configuration with setup conditions	168
8.4	Process optimization of laser tack welding	169
8.5	Process optimization of laser seam welding	171
8.6	Weld joint characterization	173
8.7	Conclusions	176
8.8	References	176
Chapter I	X: Comprehensive Comparative Study on Metallurgical and	
_	Mechanical behavior of Weldments Produced by employing	ıg
	LHW, ADLW and TIG Processes	178
9.1	Introduction	178
9.2	Experimental Methodology	178
9.3	Weld bead profile and macrostructure analysis	179
9.4	X-ray diffraction phase analysis	183
9.5	Microstructural analysis	184
9.6	Mechanical properties of the weldments	191
	9.6.1 Hardness distribution analysis	191
	9.6.2 Tensile and Impact properties	194
9.7	High temperature corrosion behaviour of superalloy joints and	
	base metal	199
9.8	Conclusions	205
9.9	References	206
Chapter X	: Conclusions and Future work	209
10.1	Conclusions	209
10.2	Future Scope of work	213
List of Public	cations from the Thesis	215
Curriculum V	Vitae	216

LIST OF FIGURES

Figure 1.1	Overview of thermal power plant boiler operating conditions	01
Figure 1.2	Schematic evolution of the proposed materials for the	
	development of AUSC power plant	02
Figure 1.3	(a) Overview of the development of the boiler technology,	
	(b and c) Schematic overview of the various properties and	
	fabrications encountered in boiler system, and (d) Demonstration	
	showing fabrication of AUSC boiler components	05
Figure 1.4	100,000 hours creep rupture test data	07
Figure 1.5	Phase diagram of Inconel 617 alloy obtained by Thermo-Calc	10
Figure 1.6	Schematic representation of Tungsten Inert gas (TIG) welding	
	process	14
Figure 1.7	Schematic representation of Metal Inert gas (MIG) welding	
	process	15
Figure 1.8	Schematic representation of laser keyhole welding	18
Figure 1.9	Schematic representation of laser-arc hybrid welding process	20
Figure 1.10	Schematic representation of joining arc and laser in laser	
	hybrid welding process	21
Figure 1.11	Schematic representation of (a) laser-MIG hybrid and	
	(b) laser-TIG hybrid welding processes	23
Figure 2.1	(a) Thermal cycle utilized in simulated HAZ study and	
	(b) Micrograph showing lamellar type structure in TIG	
	welded joint and micrographs of thermal simulated HAZ at	
	(c) 1250 ^o C and (d) 1300 ^o C	34
Figure 2.2	NG-TIG welded Inconel 617 (a) HAZ and (b) magnified view	35
Figure 2.3	Micrograph showing weld metal liquation cracking	36
Figure 2.4	Variation of total GB resolidified phase and total crack length as a	
	function of heat input and preheating temperature	37
Figure 2.5	(a) Optical micrograph showing cracks in HAZ and (b) variation in	
	total crack length with heat input	37
Figure 2.6	Effect of welding speed and laser power on cracking phenomena	38
Figure 2.7	Relation between HAZ liquation cracks and radius of curvature	
	at neck zone	40

Figure 2.8	Variation of liquation cracks and liquated grain boundary in	
	different regions of laser weld cross-sectional	41
Figure 2.9	Variation in strain rate gradient as a function of welding speed	41
Figure 2.10	Deep-penetration laser weld top and bottom bead along with	
	weld cross-sectional showing huge underfill and root hump	
	defects	43
Figure 2.11	(a) Graph showing manufacturing time for CMT, pulse-mix	
	and pulse arc processes and (b) Optical macrograph of CMT	
	welded joint	45
Figure 2.12	Welded samples (a) Continuous current and (b) Pulsed current	
	GTAW	46
Figure 2.13	Room and high temperature tensile properties of base and welded	
	Inconel 617 alloy	47
Figure 2.14	Small punch creep test specimens extracted from Inconel 617	
	TIG weldments	49
Figure 2.15	Variation in weld bead profile with heat input in (a) Fiber and	
	(b) CO ₂ laser welding of Inconel 617 alloy	50
Figure 2.16	(a) Multi-pass narrow-gap laser weld joint and (b) Defects in	
	Y-shaped weld bead	55
Figure 2.17	(a) Laser multi-pass narrow gap of 140-mm thick Inconel 617	
	alloy pipe, (b) magnified view of weld interface and (c) EBSD	
	analysis	55
Figure 3.1	Flow chart of methodology adopted for welding experimentation	
	and weld quality analysis	67
Figure 3.2	As-received microstructure of Inconel 617 alloy (a) optical and	
	(b) FESEM	68
Figure 3.3	XRD of as-received Inconel 617 alloy BM	69
Figure 3.4	Joint configuration of (a) LHW, (b) TIG, and (c) DLW	70
Figure 3.5	(a) Slab CO ₂ laser system setup and (b) Schematic of Slab CO ₂	
	laser	71
Figure 3.6	(a) KEMPPI MIG welding equipment with zoom in inset image	
	of controller and (b) Standalone workstation with wheel base	71
Figure 3.7	CO ₂ laser – MIG hybrid welding setup	72
Figure 3.8	Manual TIG welding experimental setup	74

Figure 3.9	(a) High power fiber-coupled Diode Laser system setup	
	(b) 10 kW diode laser and (c) Robot and process controller	75
Figure 3.10	(a) Optical setup with inset image of variation in laser spot	
	diameter with defocusing distance and (b) Schematic representation	
	of overview of diode laser welding fixturing and process setup	76
Figure 3.11	High power Diode Laser welding setup and zoom-in image of	
	optics and fixturing setup	78
Figure 3.12	Schematic representation of laser weld bead profile showing	
	various weld bead characteristics	80
Figure 3.13	Schematic overview of the high-power fiber-coupled diode	
	laser welding experimental setup	81
Figure 3.14	Schematic illustration (a) Design of joint configuration and fit up,	
	(b) Filler wire pre-placed in the groove	82
Figure 3.15	Schematic illustration showing Tack welded plate	83
Figure 3.16	Schematic illustration showing Laser seam welded plate	84
Figure 3.17	Schematic representation of laser-based weld bead profile showing	
	various weld bead characteristics	86
Figure 3.18	Field emission scanning electron microscope (FESEM) attached to	
	EDS/EBSD	87
Figure 3.19	Micro-focus X-ray diffraction system (XRD)	88
Figure 3.20	High speed Nano Indentation system	90
Figure 3.21	(a) Universal tensile testing machine, (b) Samples extracted from	
	welded plates and (c) Transverse tensile test specimen as per ASTM	
	E8 (All dimensions in mm)	91
Figure 3.22	(a) Impact testing machine, (b) Impact test specimen as per ASTM	
	E23-18 (All dimensions in mm)	91
Figure 3.23	(a) Horizontal tubular furnace for hot corrosion study (b) inside view,	
	(c) controller and (d) samples placed in the crucible	92
Figure 4.1	Schematic representation of (a) Laser conduction mode (b) Laser	
	keyhole mode, (c) MIG arc mode (d) Laser-MIG Hybrid mode,	
	and (e) Laser-MIG hybrid weld bead geometry	97
Figure 4.2	Macrographs of ALW and LHW welds at different heat input	
	conditions	99

Figure 4.3	Effect of heat input on (a) weld bead geometry, and (b) Area of	
	fusion zone and HAZ	100
Figure 4.4	Optical micrographs in various regions (a) UFZ, (b) NFZ, (c) LFZ	
	of LHW, (d) UFZ (e) NFZ, and (f) LFZ of ALW, UFZ - Upper fusion	
	zone, NFZ - Neck fusion zone, LFZ - Lower fusion zone	101
Figure 4.5	FESEM micrographs (a) UFZ and (b) NFZ of LHW at 480 J/mm and	
	(c) UFZ and (d) NFZ of ALW at 190 J/mm heat input and (e) Cooling	
	rates vs heat input in NFZ of ALW and LHW	103
Figure 4.6	SDAS and Hardness distribution as a function of heat input in Neck	
	fusion zone (NFZ) of ALW and LHW	104
Figure 4.7	Width of HAZmax (microns) at neck zone of both ALW and LHW	
	with inset microstructure of LHW interface	106
Figure 4.8	Effect of heat input on radius of curvature of both ALW and LHW	107
Figure 5.1	Macrographs of (a) Laser-MIG hybrid weld (LHW) processed at	
	480 J/mm and (b) Autogenous Laser weld (ALW) processed at	
	190 J/mm with vickers hardness values and (c) Micrograph of LHW	
	Inconel 617 alloy interface processed at 480 J/mm	111
Figure 5.2	Micro XRD patterns of ALW and LHW in FZ, PMZ, HAZ and	
	base metal	113
Figure 5.3	FESEM micrographs of fusion zone in different regions (a) LHW	
	and (b) ALW	115
Figure 5.4	FESEM images of PMZ of (a) LHW specimen (b) magnified view	
	of eutectic phase marked as a dotted box in (a) and (c) ALW specimen	
	(d) magnified view of eutectic phase marked as a dotted box in (c)	116
Figure 5.5	Element map analysis of the eutectic phase	116
Figure 5.6	(a), (d) and (g): FESEM images of Base material (BM) carbides,	
	LHW_LME (Low melting eutectic), and ALW_LME respectively.	
	(b), (e) and (h): Hardness contour map of BM, LHW and ALW	
	respectively (c), (f) and (i): Modulus map of BM, LHW and ALW	
	respectively obtained by Nano Indentation technique	118
Figure 5.7	FESEM images of HAZ of (a) LHW specimen (b) magnified view	
	of carbides marked as a dotted box in (a) and (c) ALW specimen	
	(d) magnified view of carbides marked as a dotted box in (c)	119
Figure 5.8	Schematic illustration of Liquation cracking phenomena	121

Figure 5.9	(a) PMZ liquation crack in neck zone region (b) Elemental mapping	
	analysis (c) EDS results of GB resolidified phase and matrix of LHW	122
Figure 5.10	Variation of total crack length (TCL) and quantity of grain boundary	
	(GB) resolidified phase (%) of LHW and ALW under different	
	heat input	123
Figure 6.1	Cross-sectional optical macrographs of BOP welds at different	
	defocusing distances	129
Figure 6.2	Variation in WP, UBW and FZA as a function of defocusing	
	distance	130
Figure 6.3	Cross-sectional optical macrographs of butt welds at various welding	
	speeds (a) 18 mm/s, (b) 14 mm/s (c) 10 mm/s, (d) 6 mm/s and	
	(e) 4 mm/s	133
Figure 6.4	Variation in (a) WP and UBW and (b) Aspect ratio (depth to width)	
	and FZA as a function of welding speed	134
Figure 6.5	XRD of substrate BM and weld fusion zone of Inconel 617 alloy	136
Figure 6.6	FESEM micrographs of (a) weld fusion zone and (b) weld interface	
	with an inset image showing Micro-Vickers hardness values and	
	EDS results (D – Dendritic core, IR – Interdendritic)	137
Figure 6.7	Stress-strain graphs of substrate and welded Inconel 617 alloy,	
	with inset of fractured tensile test specimens with cross-section	
	macrographs (yellow dash line indicates fusion boundary)	139
Figure 6.8	Fracture surfaces of the tensile test specimens (a) substrate and	
	(b) welded	140
Figure 7.1	Perturbation plot of UBW	148
Figure 7.2	Contour plots showing influence of all three input parameters	
	(LP, WS and DF) on UBW	149
Figure 7.3	Perturbation plot of WP	151
Figure 7.4	Contour plots showing influence of all three input parameters	
	(LP, WS and DF) on WP	152
Figure 7.5	Perturbation plot of FZA	155
Figure 7.6	Contour plots showing influence of all three input parameters	
	(LP, WS and DF) on FZA	156
Figure 7.7	Perturbation plot of ROC	158

Figure 7.8	Contour plots showing influence of input parameters (LP, and WS)	
	on ROC	158
Figure 7.9	Contour plots for overall desirability for laser welding process	160
Figure 7.10	Macrograph obtained from the optimized parameters	161
Figure 7.11	Stress-strain graphs of welded Inconel 617 alloy produced by RSM	
	optimized parameters	162
Figure 8.1	Schematic illustrations of (a) Design of joint configuration and	
	fit-up and (b) Filler wire pre-placed in the groove	169
Figure 8.2	Laser tack welds with variation in laser power	170
Figure 8.3	(a) Cross-sectional macrograph of tack-welded spot (b) Pre-placed	
	filler wire on the top groove of base plate after tack welding	171
Figure 8.4	(a) Schematic representation of different methodologies adopted	
	for laser welding and (b) Macrographs of the representative	
	methodologies	172
Figure 8.5	Weld obtained by novel method (a) Seam welded plate and	
	(b) Macrograph	174
Figure 8.6	Novel DLW macrograph with high magnification FESEM images	
	at top, neck and bottom regions	175
Figure 9.1	Schematic illustration of distortion measured in but joint after	
	welding	180
Figure 9.2	Cross-sectional weld-bead macrographs of (a) LHW, (b) ADLW	
	and (c) TIG welded joints	181
Figure 9.3	XRD patterns of BM, fusion zones of LHW, ADLW and TIG welds	183
Figure 9.4	Optical micrographs of fusion zones produced in weld joints of	
	(a) LHW, (c) ADLW, and (e) TIG with zoomed sections of respective	
	NFZs in (b), (d) and (f)	184
Figure 9.5	High magnification FESEM fusion zone microstrucrures of	
	(a) UFZ of LHW, (b) NFZ of LHW, (c) UFZ of ADLW and	
	(d) NFZ of ADLW	185
Figure 9.6	High-magnification FESEM fusion zone microstrucures with various	
	regions of TIG welded joint	186
Figure 9.7	EBSD analysis of fusion zone microstructure of (a) LHW, (b) ADLW,	
	(c) TIG welds and (d) BM	187
Figure 9.8	Weld interface micrographs of (a) LHW/ADLW and (b) TIG	190

Figure 9.9	Micro-hardness contour plots of welded joints of (a) LHW, (b) ADLW	
	and (c) TIG	191
Figure 9.10	Load-displacement curves in FZ matrix of LHW, ADLW, TIG and	
	BM (inset image illustrating typical representative hardness mapping	
	and FESEM image for BM)	192
Figure 9.11	Tensile stress-strain curves of LHW, ADLW, TIG and BM	194
Figure 9.12	Impact energy (J) of LHW, ADLW, TIG and BM	195
Figure 9.13	Cross-sectional tensile-test fractured micrographs of LHW, ADLW,	
	and TIG welds	197
Figure 9.14	Fractographs of fractured tensile-tested coupons of (a)BM, (b)LHW,	
	(C) ADLW, and (d) TIG	198
Figure 9.15	Variation of thickness of the corroded area in fusion zones of ADLW	
	(laser), TIG welded and BM in coal-ash and salt-coated conditions	200
Figure 9.16	XRD patterns of hot corroded specimens after exposed to 1000 hours	
	at 600°C (a) Coal-ash coated and (b) Salt-coated conditions	201
Figure 9.17	FESEM micrographs of hot corroded specimens in Coal-ash condition	
	(a) ADLW, (b) TIG and (c) BM	202
Figure 9.18	FESEM micrographs of hot corroded specimens in Salt-coated condition	
	(a) ADLW, (b) TIG and (c) BM	202
Figure 9.19	Elemental mapping of the BM cross-sectional after exposed to 1000	
	hours in salt-coated condition	203

LIST OF TABLES

Table 1.1	Nominal compositions (wt %) of various Ni-based superalloys	07
Table 1.2	Comparing various advantages of LHW process over individual	
	laser and arc welding processes	21
Table 3.1	Chemical composition (wt %) of Inconel 617 base and filler metal	68
Table 3.2	EDS analysis (wt %) of the carbides and surrounding matrix in BM	68
Table 3.3	Slab CO ₂ laser system variables	71
Table 3.4	Process variables for LHW	72
Table 3.5	Diode Laser welding process variables	76
Table 3.6	Input process parameters with 3-factors and 3-levels used for BBD	
	experiments	78
Table 3.7	Experiments obtained from BBD method based on 3-factors and	
	3-levels and their results	79
Table 3.8	Optimized variables for joint configuration and filler wire	82
Table 3.9	Optimized process parameters for laser tack and seam welding	
	experiments	84
Table 3.10	Details of various characterization tools used in the present study	85
Table 4.1	Process parameters of LHW and CLW BOP welding experiments	96
Table 4.2	Chemical composition of the Interdendritic region (IR) and the	
	Dendrites (D) as determined by EDS analysis (wt %)	103
Table 5.1	Cross-sectional bead profile analysis of Autogenous Laser (ALW)	
	and Laser-MIG hybrid (LHW) weldments	112
Table 5.2	EDS analysis in wt % of the eutectic phase and surrounding matrix	
	in PMZ of LHW and ALW	117
Table 5.3	Nano hardness range (GPa) of the eutectic phases, carbide in base	
	material, HAZ, FZ and surrounding matrix of LHW and ALW	
	specimens	118
Table 5.4	EDS analysis in wt % of the grain boundary (GB) carbide and	
	surrounding matrix in HAZ of LHW and ALW	119
Table 6.1	Laser welding process parameters	127
Table 7.1	ANOVA analysis for UBW	147
Table 7.2	ANOVA analysis for WP	149
Table 7.3	ANOVA analysis for FZA	153

Table 7.4	ANOVA analysis for ROC	156				
Table 7.5	Optimization criteria using desirability approach	159				
Table 7.6	Optimized solutions obtained from the model	160				
Table 7.7	Validation of experimental results with predicted one	161				
Table 8.1	Optimized variables for joint configuration and filler wire	169				
Table 8.2	Optimized process parameters for laser tack welding experiments	171				
Table 8.3	Optimized process parameters for laser seam welding experiments	172				
Table 8.4	Bead geometry measurements of welds obtained by various					
	methodologies	173				
Table 9.1	Bead geometry measurements	182				
Table 9.2	EDS analysis of fusion zones in LHW, ADLW and TIG welds					
	(D – Dendritic core, IR – Interdendritic region, SR – Segregation ratio)	188				
Table 9.3.	Nano hardness range (GPa) of dendrites/interdendritic region carbides					
	in welds and grains/grain boundary carbides in substrate, LHW.					
	ADLW, and TIG specimens	193				

ABBREVIATIONS

Abbreviations Description

AUSC Advanced ultra-super critical boiler

USC Ultra-super critical boiler

SH Superheater tubes
RH Reheater tubes

ALW Autogenous CO₂ laser welding

DLW Diode laser welding

ADLW Adaptive diode laser welding

MIG Metal Inert gas welding

TIG Tungsten Inert gas welding

NG-TIG Narrow gap Tungsten Inert gas welding

LHW Laser-MIG hybrid welding

LP Laser power
WS Welding speed

DF Defocusing distance

BM Base metal FZ Fusion zone

PMZ Partially melted zone
HAZ Heat affected zone
UFZ Upper fusion zone
NFZ Neck fusion zone
LFZ Lower fusion zone

UBW Upper bead width
LBW Lower bead width
RSW Root sag width

WP Weld penetration FZA Fusion zone area

AR Aspect (depth-to-width) ratio

D Dendritic core

IR Interdendritic region

SR Segregation Ratio

LME Low melting eutectics

TCL Total crack length
GB Grain boundary

ROC Radius of curvature

RSM Response surface methodology

BBD Box-Behnken Design
ANOVA Analysis of variance
HV Vickers Hardness

FESEM Field Emission Scanning Electron Microscope

EDS Energy Dispersive Spectrometer
EBSD Electron Backscatter Diffraction

XRD X-Ray Diffraction

1.1 Overview of Thermal power plant

Today, the major challenge facing worldwide is to provide abundant and cheap electricity for the necessity of a growing global population and at the same time significant reduction in the CO₂ emissions from the fossil fuel to preserve the environmental issues. Coal, being the most inexpensive, readily available, reliable, and affordable, energy source for most current power generation industries across the world, it is expected to be a primary source even for the next few decades. However, it is also a fact that coal is the largest source of CO2 emissions, which is the primary cause of global warming through power generation. Therefore, increasing the efficiency of the thermal power plant by enhancing the steam parameters such as temperature and pressure, which in turn minimize the CO₂ emissions to preserve the environment is the primary need [1,2]. Coal-based thermal power plants are classified based on the operating steam temperatures and pressures. Figure 1.1 shows the different types of boilers and their operating steam parameters. The Subcritical boiler typically operates with main steam temperature of 540°C and a pressure of 167 bar, resulting in a thermal efficiency of 38%. Meanwhile, in supercritical (SC) boiler, the operating steam temperature and pressure increased to 600°C and 270 bar respectively, to achieve an efficiency of 42%. The ultrasupercritical (USC) boilers have an efficiency of 42-46% by enhancing the temperature and pressure of the steam to around 620°C and 280 bar respectively. Further, future advanced ultrasupercritical (AUSC) boiler is targeted to operate in a temperature range of 700 – 720°C and at a pressure of 365 bar to obtain an efficiency nearly 50% [3-5].

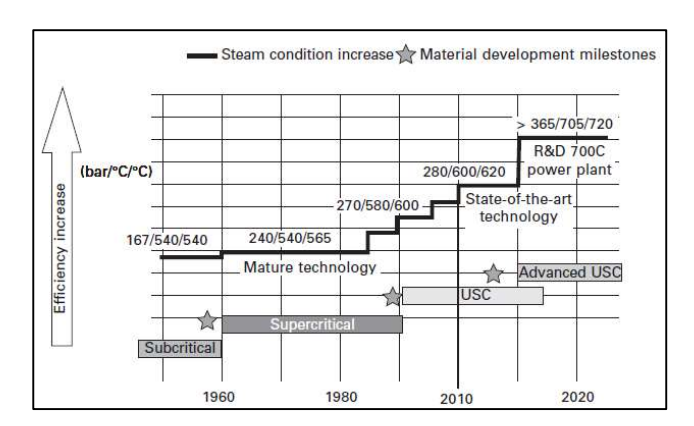


Figure 1.1. Overview of thermal power plant boiler operating conditions [3]

Since the overall efficiency of a coal-based thermal power plant is directly influenced by steam parameters such as steam temperature and pressure, incorporation of advanced ultrasupercritical (AUSC) boiler technology promises not only to improve plant efficiency, but also significantly reduce greenhouse gas emissions. However, the resultant steam temperature of the intended AUSC boilers is just 100°C higher to that of existing supercritical/ultrasupercritical boilers. Although, it is pertinent to note that basic configurations remain unchanged without any drastic changes in the peripheral components of the existing power station except for the few high temperature zones. Figure 1.2 describes the schematic layout of the proposed material selected for AUSC boilers. In which, green color represents gas turbine (GT) materials which are basically Ni-based superalloys, sky blue color represents conventional materials including ferritic and austenitic steels and pink color represents Nibased alloys which is under development. Ni-based superalloys, which were not used in ultrasupercritical (USC) boiler, were selected for the highest temperature sections of the AUSC boiler such as superheater (SH) and reheater (RH) tubes, large steam pipings and the valves connecting boiler to the turbines, headers, and some parts of the turbines [6]. Therefore, an AUSC boiler can be retrofitted to the existing power stations facility. This technology is expected to realize the effective use of coal and enable to contribute CO₂ reduction worldwide.

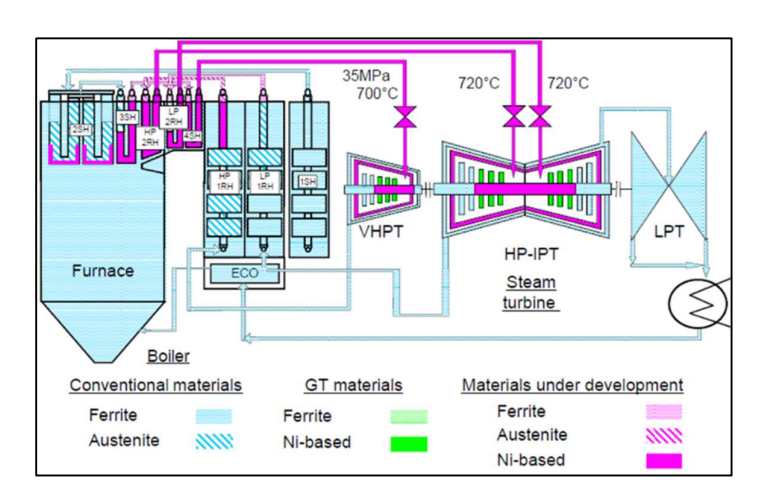


Figure 1.2. Schematic evolution of the proposed materials for the development of AUSC power plant [6]

Accordingly, in recent years, for further raising the plant efficiency and reduction of CO₂ emissions, development of AUSC thermal power plant has been initiated in several countries such as Europe, United States, Japan, China, and India. Dedicated R & D efforts worldwide focused on enabling the development of AUSC thermal power stations operating

with steam temperature higher than 700°C and steam pressures over 35 MPa, such conditions can potentially increase plant efficiencies to greater than 47% and reduce CO₂ emissions by almost 25% [2].

In line with the global efforts, to achieve the goal of increasing the power plant efficiency and reduction of CO₂ emissions, a National Mission Programme was initiated in India as well for the development of AUSC boiler technology and detailed R & D efforts are in progress to develop indigenous technology on-par with the worldwide systems. AUSC boiler steam conditions for Indian AUSC thermal power plant are expected to serve in the temperature of 710/720°C and steam pressure up to 350 bar. With such proposed steam conditions, the efficiency of the Indian AUSC boiler is expected to 45-47%, with a 20-25% reduction in CO₂ potential as compared to conventional sub-critical boilers [7,8]. In India, due to the greater dependency on coal for power generation and limited access to the supercritical technology, the leapfrogging into the AUSC involves greater efforts in developing materials, their fabrication processes including welding technologies and their testing, etc. One of the core exercises vital for the accomplishment of these future necessities is that of materials technology. Although the materials for the components experiencing lower temperatures in AUSC will be similar to that of mature sub-critical technology, high-performance materials are required for top-end of superheater/reheater tubes, main steam pipes and reheat pipes, high pressure and intermediate pressure control valves and turbines integral piping etc. to withstand at higher steam parameters of AUSC boilers. Further the characteristics need to be optimized for steam temperature and pressure values and also need to comply with ASME or equivalent international code [7,8].

1.2 Properties Requirements for Boiler Components

In order to develop and successfully use a new material in AUSC boiler, it is preliminary to thoroughly investigate the technologies including fabrication, welding, weld performance, creep, fatigue and tensile properties both at fire-side corrosion and steam side oxidation, designing and maintenance of the components as shown in Figure 1.3 [1,5,6]. The important properties needed for the new materials to be used in the boiler industry are: Sufficient mechanical properties for successful fabrication of the components including welding, bending, forging and machining, Adequate weldability (for thin or thick sections pipes or tubes), and formability (bendability), Excellent high temperature long-term reliability for prolong service, Low thermal expansion coefficients and high thermal conductivity similar to

that of other boiler materials in order to avoid thermal stresses specially at dissimilar weld joints transition during startups and shutdowns. High temperature corrosion and oxidation resistance in steam and flue gas (coal-ash) environment, Satisfactory creep-rupture strength to withstand deformation induced by high mechanical and thermal stresses due to operating at high temperature high pressure steam, Sufficient low-cycle fatigue strength to avoid cracking and premature failure due to experiencing thermal cycle by steam temperature which varies with load commercial availability and indigenous technology, and materials must be cost effectiveness, due to large number of tubes and pipes required for boiler fabrication which affect the overall cost of the power station.

The key components of AUSC boilers whose performance is critical including highpressure steam pipes and headers, superheater, reheater tubing and waterwall tubes. All these components mandatory to meet sufficient creep strength requirements. Additionally, heavy sections such as heavy pipes and headers experience fatigue due to thermal stresses. Materials used in the AUSC components are also required to have high oxidation and corrosion resistance as these components experience fire-side corrosion outside the walls and steam flows inside the tubes/pipes as depicted in Figure 1.3. Heavy oxidation and corrosion cause premature failure of the components due to accelerated material losses. All of these properties requirement for the boiler components is represented schematically in Figure 1.3b and 1.3c [5]. Superheater and reheater (SH/RH) tubes must possess high creep and thermal fatigue strength, high resistance to fireside corrosion/erosion and resistance to steam-side oxidation and spallation, as well as good formability and weldability. Welding is an essential joining technique along with bending, and NDT to fabricate boiler components. Figure 1.3d shows the demonstration of successful various fabrication techniques which mainly include dissimilar welding between CCA617 and Super 304H, bending and machining applied to AUSC boiler components [1]. Additionally, tensile test, bend test, impact test, fracture toughness, creep-fatigue interactions also needed for the qualification of the weldments for AUSC boiler components.

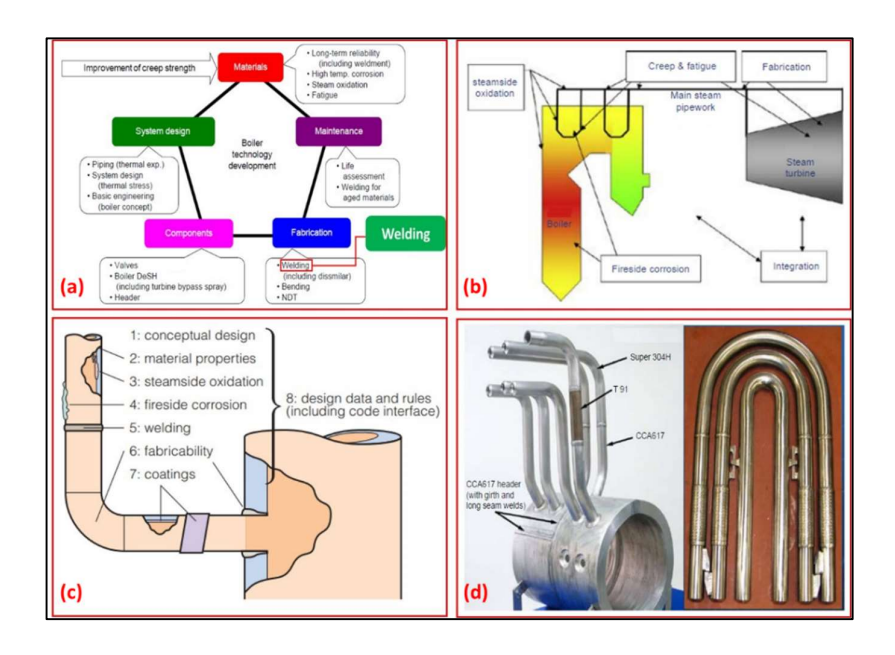


Figure 1.3. (a) Overview of the development of the boiler technology, (b and c) Schematic overview of the various properties and fabrications encountered in boiler system, and (d) Demonstration showing fabrication of AUSC boiler components [1,5,6]

1.3 Materials for Boiler Components

1.3.1 Ferritic Steels

Conventional supercritical (SC) boilers utilize standard low alloy ferritic and austenitic stainless steels, whereas ultra-super critical (USC) boilers utilize both creep-strength enhanced ferritic steels and advanced austenitic stainless steels. Low alloy ferritic steels are generally referred as Cr-Mo steels in which Grade-11 and Grade-22 are widely used for water wall components in supercritical boiler. Alloy Grade-22 has better high temperature strength and steam side oxidation resistance. This alloy can be easily welded by any conventional welding techniques. However, HAZ has reduced creep strength and at nearly 480°C steam temperature, this alloy suffers high steam side oxidation, thus, alternative alloy material with higher chromium content must be used for high temperature steam [9-11].

Creep-Strength enhanced ferritic steels include Grade-23, Grade-91, Grade-92 and Grade-122. Grade 23 is widely used for water wall components in USC boilers, whereas Grade-91 & 92 can be used for superheater and reheater tubes as well as heavy pipes and headers sections. The presence of higher Cr content in these alloys provide higher steam-side oxidation and fire-side corrosion resistance and the creep strength is upto twice as compared to that of

Grade-22 steels. Grade-91 is allowed to use upto 600°C steam temperature, whereas Grade-92 is suitable for steam temperature upto 620°C. However, preheating at a temperature of 200°C and PWHT at a temperature of 760°C is mandatory for these alloys to be used for boiler components. Additionally, filler materials must be properly selected to weld these alloys and temperatures limited during the welding process. However, weldments of these alloys remain weak as compared to base metal and premature creep failure were observed in the HAZ during high stress conditions [11,12].

1.3.2 Austenitic steels:

Alloy in this category includes 304H and 347H austenitic stainless steels (ASS) and Super304H, HR3C, 347HFG, and NF709 advanced austenitic stainless steels. These alloys have higher chromium content (min. 16%) and high nickel content (8%) for better corrosion and oxidation resistance and to stabilize austenitic phase. These alloys have superior steamside oxidation, fire-side corrosion resistance and creep strength as compared to previously explained low alloy steels and CSEF steels. Although, these alloys have good weldability but are prone to sensitization problem. These conventional ASS are well suited for steam temperature upto 630°C and advanced ASS are applicable upto steam temperature of 680°C. These alloys can be used for superheater and reheater tubing. However, it is limited to be used in thick-walled sections including heavy pipes and headers due to high thermal expansion. They are also not suitable for water wall components due to susceptible for stress corrosion cracking in wet sections. However, operating temperature of these alloys is limited to around 620-680°C and beyond this temperature these alloys experience heavy fire-side corrosion and steam-side oxidation and loss of creep strength hence not suitable for AUSC boilers steam conditions. Therefore, Ni-based superalloys including Inconel 740/740H, Haynes 282, Alloy 617, and Haynes 230 are preferred to meet the required AUSC steam conditions [12].

Some of the proposed materials intended to be used for Indian AUSC power plants are: Grade-23 steel (2.25Cr-1.6W-V-Nb-B) for WW, Grade-91 steel (9Cr-1Mo-V-Nb-N) for initial stages of SH and RH tubes at low temperature zones, 304HCu austenitic stainless steel (18Cr-9Ni-3Cu-Nb-N) for the final stage of SH tube, Nickel-base Alloy 617 (52Ni-22Cr-13Co-9Mo), for the final stage of SH and RH tubes at the hottest zone of AUSC boilers. Water walls: WW, Superheater: SH, Reheater: RH.

1.4 Nickel based superalloys for boiler applications in thermal power plant:

Figure 1.4 shows the minimum criteria of 100,000 h creep rupture strength at 100 MPa for various steel alloys and Ni-based superalloys with their temperature limits. Any material to be used in thermal power plant boiler must have the capability to withstand at 100 MPa for 100,000 h at the required temperature. Therefore, the requirement for 700°C AUSC boiler conditions rules out the use of steel alloys and only Ni-based superalloys such as Alloys 740, 282, 617, 230 and similar alloys are the choice to operate at 700°C AUSC conditions due to sufficient creep rupture strength [13-16]. However, Ni-based superalloys are expensive as compared to alloy steels, so their usage is limited to the only hottest portion of the boiler and steam turbine as shown in Figure 1.2. Age-hardened Ni-based superalloys Inconel 740 and Haynes 282 possess higher creep-rupture strength as compared to that of other solid-solution hardened Ni-based superalloys Alloy 617 and Haynes 230 as shown in Figure 1.4. The higher creep rupture strength of these age-hardened alloys is due to the presence of large amount of fine $\gamma^{\rm I}$ -Ni₃(Al,Ti) precipitates as a result of high Al and Ti contents as compared to Alloy 617 and Haynes 230. The nominal composition of some Ni-based superalloys provided in Table 1.1 [1]. However, hot working of age-hardened alloys becomes difficult due to the presence of high amount of γ^{I} precipitates [17]. Therefore, for higher steam temperature above 760°C, Inconel 740 and Haynes 282 must be used, whereas for temperature above 700°C but below 760°C, Alloy 617 and Haynes 230 are acceptable for construction of boiler components [18].

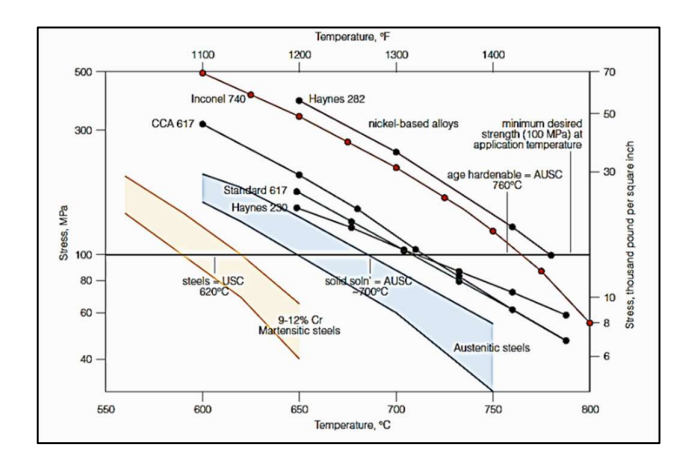


Figure 1.4. 100,000 hours creep rupture test data [16]

Table 1.1. Nominal compositions (wt %) of various Ni-based superalloys [1,5]

Alloy	С	Cr	Со		Al	Ti	Nb	Fe	В	Mn	Si
Inconel 740H	0.005- 0.08	23.5 - 25.5	15 - 22	<2	0.2	0.5 - 2.5	0.5 - 2.5	<3	0.006	<1	<1
Haynes 282	0.06	20	10	8.5	1.5	2.1	-	<1.5	0.005	< 0.3	< 0.15
Haynes 230	0.10	22	0.3	2	0.3	-	-	1.5	0.004	0.5	0.4
Inconel 617	0.05 - 0.15	20 – 24	10 - 15	8 - 10	0.8 - 1.5	≤0.6	-	≤3	≤0.006	≤1	≤1

Among various Ni-based superalloys, Inconel 740 a precipitation-hardened Ni-based superalloy was initially developed in year 2000 for AD700 AUSC European project to operate at a steam temperature of 700° C and pressure of 35 MPa [19]. Inconel 740 alloy is characterized by the highest creep-rupture strength after Haynes 282 alloy (shown in Figure 1.4), coupled with high corrosion and oxidation resistance among other Ni-based superalloys. However, Inconel 740 alloy is found to be susceptible to HAZ micro-fissures in thick-section weldments [18]. Moreover, unstable microstructure was also observed at 760° C during long term aging, due to high coarsening rate of γ^{I} -Ni₃(Al,Ti) precipitates, formation of acicular η -(Ni₃Ti) phase and high brittle G-phase form at grain boundaries [20]. Therefore, a modification of Inconel 740 for improvement of high temperature microstructure stability by specific adjustments of Al/Ti ratio, with reduced silicon and niobium contents was developed and named as Inconel 740H [21]. Inconel 740H is now a suitable candidate material to be used in highest temperature portion above 760° C such as main steam pipes, SH and RH tubes, whereas Haynes 282 is a promising material for turbine rotor and discs in US DOE/OCDO [1], Japan [8], and in China AUSC project [22].

Haynes 282 alloy possess higher creep rupture strength as compared to Inconel 740 alloy (see Figure 1.4), coupled with high-temperature microstructural stability, corrosion and oxidation resistance. Haynes 282 alloy is also a suitable candidate material for high-temperature AUSC power plant applications. However, Haynes 282 alloy is not included in the ASME code and it is still under development for SH and RH tube products [23]. Haynes 230 is a solid-solution strengthened Ni-based superalloy with high Cr and W contents and it is characterized by the high temperature strength, excellent oxidation resistance, and long-term thermal stability. However, Haynes 230 alloy didn't meet the creep-rupture requirements

higher than 100 MPa at 750°C for 100,000 h, plausibly due to the low fraction of strengthening phase formation [23].

1.4.1 Inconel 617 superalloy material

Alloy 617 also designated as Inconel 617 (IN 617), UNS N06617 is mainly a solid solution strengthened nickel-based superalloy was initially developed by INCO Alloy International in the early 1970's. It is specifically designed for high-temperature applications due to its exceptional combination of high-temperature structural stability, high creep strength, excellent corrosion and oxidation resistance characteristics. Inconel 617 has been found in a wide range of applications since its development and properties have made it an attractive material for use in aircraft, land-based gas turbines, industrial furnaces, manufacturing components, fossil, and nuclear power generation components [24,25].

In the late 1970's and early 1980's, Inconel 617 became a strong primary candidate structural material for the construction of Gen IV Nuclear Reactor components serving in temperature range of 760 to 950°C and pressure up to 7 MPa for an expected life about 60 years. This alloy was approved by ASME and VdTUV. Extensive research works on Inconel 617 alloy including creep and corrosion testing were investigated within the framework of German high-temperature reactor project [26-29]. Further in 1998, high temperature material Inconel 617 has gained importance in the development of first boiler power stations in Europe with steam temperatures in excess of 700°C under AD700 project due to its excellent oxidation and creep resistance. The purpose of this project was to enhance the efficiency of the pulverized coal-based power stations to above 50% by replacement of existing Fe-based alloys with nickel-based superalloys for the highest temperature components [30]. For further increase in the creep rupture strength of standard 617 alloy at 100 MPa for the period of 10⁵ hours, a modified version of Alloy 617 was designed with addition of boron and narrowly scatter of alloying elements such as Cr, Co, Al, Ti, Fe and may also contain Nb and V which were approved by VdTUV in 2003 but not included in ASME [31]. Most recently 617 alloy is treated as the prime candidate material for the construction of the Indian AUSC boiler parts with temperature of 710/720°C and pressures up to 35 MPa [32]. Alloy 617 has been a choice in all countries pursuing 700°C AUSC for SH and RH tubes, main steam piping, and valves, as well as for the highest temperature portion of the turbine rotor. The selection of these materials for AUSC boilers is based on the commercial availability of the alloy, experience of use in various applications, and detailed material design data available in ASME codes [5,7].

1.5 Metallurgy of Inconel 617

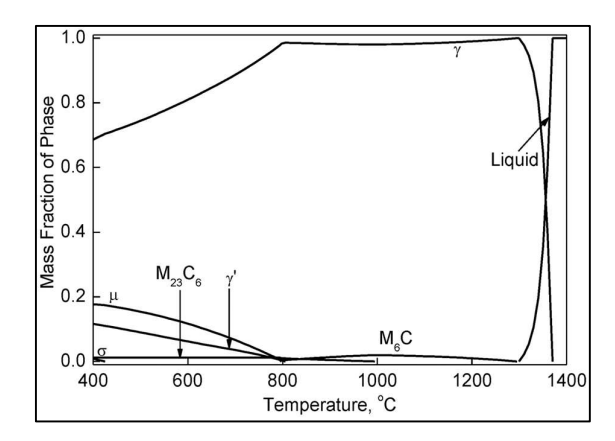


Figure 1.5. Phase diagram of Inconel 617 alloy obtained by Thermo-Calc [23].

Inconel 617 is a Ni-Cr-Co-Mo solid-solution strengthened Ni-based superalloy having an FCC crystal structure and additionally strengthened by Ti and Al precipitation-hardening elements. The chemical composition of Alloy 617 specified by ASTM standards is given in Table 1.1. Alloying elements plays a vital role in determining the materials properties. Presence of high amounts of Ni and Cr contents in Inconel 617 alloy provide better resistance to various oxidizing and reducing environments. Cr and Al offer oxidation resistance to the alloy at high temperature by forming their protective oxide layers. Mo and Co provide solid solution strengthening to the alloy. At intermediate temperature additional strength is provided by Al and Ti by precipitating γ^{1} - Ni₃(Al,Ti) phase. Strengthening is also derived by the presence of secondary carbides phases such as MC, M23C6 and M6C carbides [24,25,33]. Gariboldi et al. [34] reported that the primary carbides in solution-annealed 617 alloy were found to be Ti(C, N), M₂₃C₆ and M₆C types. M₂₃C₆ and M₆C types precipitated both at grain boundaries and within the grains. Further, Quanyan et al. [35] identified that the major secondary phase particles such as Ti(C, N), γ^I , M₂₃C₆ and M₆C formed in Inconel 617 alloy after long term exposure at a temperature range of 482 to 871°C. Inconel 617 alloy is nominally a wrought alloy generally used in solution-annealed condition (typically water quenched or rapid cooled by other means from a temperature range of 1175°C and a soaking time based on the section size). In this condition, the coarse grain size microstructure could be obtained for better creeprupture properties [25,33]. Figure 1.5 shows the equilibrium phase diagram of Inconel 617 alloy obtained by Thermo-Calc software at temperature range from 400°C to 1400°C. M₂₃C₆ carbides, where M belongs Cr, Mo and Fe is the most abundant phase in this alloy and it could form when the temperature reduces below 1000^{0} C as shown in Figure 1.5 [23]. M_{23} C₆ carbides was found to be in vast majority in this alloy as compared to other strengthening carbides such as MC, and M₆C carbides and it is predominantly present along the grain boundaries as well as inside the grains [34]. M₆C carbides, where M belongs Cr, Mo and Fe is the second most abundant phase in this alloy which generally observed at higher temperatures. Phase diagram shown in Figure 1.5, indicated that the M₆C phase could form at a temperature greater than 800° C. As mentioned, γ^{\parallel} - Ni₃(Al,Ti) phase formation provided additional strength at an intermediate temperature, this phase could form at a temperature below 800° C. As can be seen in Figure 1.5, the equilibrium phase content of γ^{\parallel} increased with decreased in the temperature down to 800° C.

1.6 Weldability of Inconel 617

1.6.1 Liquation cracking susceptibility:

Liquation cracking is one of the significant weldability issues during fusion welding of Inconel 617 superalloy, and is generally attributed to the formation of the liquid film by preferential localized melting along the grain boundaries in the vicinity to the fusion line and thereby leading to tearing of the liquated grain boundaries under high thermal stresses during weld cooling cycle [36,37]. The susceptibility of constitutional liquation cracking in superalloy welds is governed by the critical partially melted zone (PMZ) regions formed due to the welding method adopted. Inconel 617 superalloy in solution-annealed condition constitutes of several (Cr, Mo)-rich M₂₃C₆ carbides with distinguishably different morphologies and size dispersed along grain boundaries and within austenitic grains. On heating above solvus temperature of the carbides present in the vicinity to the fusion line during welding, these carbides become unstable and undergo partial dissolution and release solute elements such as Cr and Mo. Due to variation in diffusion coefficient of Cr and Mo, Mo segregates at the boundary of $\gamma/M_{23}C_6$ whereas Cr atoms diffuse into the surrounding γ matrix causing the compositional gradient at the network between the decomposed (Cr, Mo)-rich M₂₃C₆ carbides and matrix. As the temperature increases and reached to eutectic temperature, then a proportion of liquid film form by a eutectic reaction between γ matrix and (Cr, Mo)-rich M₂₃C₆ carbides. During solidification of the process, this liquid film gets strained and degrade the ability to accommodate thermal stress developed at boundary and thereby result in cracking with decohesion along the solid-liquid interface. These cracks are generally referred to as liquation cracks. It is well reported that evolution of carbides in PMZ/HAZ close to fusion boundary

during fusion welding of this superalloy plays a vital role in formation of the liquid film and thereby cracking, and as a result, many researchers focused on the control of carbides evolution by employing different fusion welding processes and heat-input control [38,39].

1.6.2 Issues in thick sections welding:

Furthermore, when thick-section welding of highly viscous nature Ni-based superalloy Inconel 617 is involved for boiler components, several weld imperfections are generally encountered. It is a daunting task to obtain satisfactory appearance on surface as well as bottom of the weld as several studies reported occurrence of imperfections such as underfills, undercuts, spatters, root humps, porosity, lack of fusion etc. in various alloys during singlepass autogenous laser welding of thick sections. These defects are attributed to intense evaporation of the weld metal caused by the extreme turbulence of molten metal in the weld pool. These defects of underfill and root sagging in weldments are found to affect both the surface integrity, joint efficiency and thereby mechanical properties. Usually undercuts and/or root sagging are caused by the welding process parameters, setup conditions, process instability and poor controllability which results in incompletely filled groove or excessively filled molten material with poor melt pool stability. However, due to highly viscous nature of Inconel 617 superalloy, in addition to the above discussed weldability issues, this alloy is also more susceptible to lack of side-wall fusion and weld metal liquation cracking during multi-pass arc welding, laser-induced porosity formation during laser welding, these all together deteriorates the performance of the weldments such as creep and fatigue resistance specially at high temperatures which needs to be resolved [40.41].

As mentioned, underfill and root sag hump defects are the major challenges encountered during thick section welding. Therefore, in recent times, multi-pass welding with process variants such as both side autogenous welding, multi-layer/multi-groove welding with filler addition, hybrid welding with combination of two or more heat sources, single-pass welding with additional setups of magnetic stirring, welding with pre-heating of filler-wire and/or work piece were observed to resolve the issues of undercut/underfill and root sagging defects in thick section welding. Moreover, the recently developed multi-pass narrow-gap laser welding technique effectively produced joints in thick plates. In this method, joint was made by continuous feeding of filler wire during laser seam welding with laser being focused on filler wire to fill the gap. Several patents and publications available in literature since beginning of the twentieth century on development of laser beam welding process on diverse materials

constituting steel, superalloy, non-ferrous and composites with thicknesses varying from few millimeters to centimeters. However, very few works successfully presented laser welding methodology on thick-section metallic materials as the process entails effective controlling of melt pool stability with continuous defect-free seam production with the available laser systems [42-46].

Although the welding of large thick components could be made by above method with multi-pass and multi-layer deposition, the high heat-input welding strategy due to multiple weld passes will reduce the joint efficiency in terms of impact strength, elongation and creep resistance on account of producing large heat affected zone and distortion/deformation. Additionally, the economy of the process will be higher due to the additional wire-feeding apparatus required for the purpose. Many a times, post-weld treatments and post-process machining requirements become mandatory to overcome these issues in thick-section welding for use in actual application. Thus, a novel laser welding technique with appropriate design of groove/edge preparation with simple single-pass welding of thick metallic materials as need of the hour that resolve all those issues connected with single-pass thick-section welding such as underfill, root sagging, undercuts, porosity, weld structure non-uniformity, lack of penetration, lack of fusion and various other metallurgical defects generally encountered during narrow gap laser/arc welding processes. Additionally, avoiding filler-feeding subsystems will greatly reduce engineering maneuverability and cost economics in moderate to thick metallic material welding.

1.7 Fusion welding processes

As mentioned, fusion welding is essential joining technology for fabrication of various components of thermal power plants. Fusion welding is a joining process in which localized coalescence between the metals/non-metals produced either by heating or by application of pressure followed by subsequent solidification to form a weld joint. The welding processes sometime requires use of a filler material depending type of joint, configuration, thickness of the joint and welding process employed. Inconel 617 superalloy can be welded by various conventional joining methods including tungsten inert gas (TIG), hot-wire narrow gap (NG-TIG), metal inert gas (MIG), submerged arc welding (SAW), plasma arc welding (PAW) and high-energy beam processes including Laser beam welding (LBW) and Electron beam welding (EBW) [5,13].

1.7.1 Tungsten Inert Gas welding process:

In Tungsten inert gas (TIG) welding process, the heat is generated between the non-consumable W electrode and the workpiece to form a weld joint. The fused area and the electrode are protected by the inert shielding gas such as Argon and Helium from atmospheric contamination as shown in Figure 1.6. TIG welding processes offers several advantages such as high-quality joint, very controllable process, highly versatile in nature and applicable to wide variety of materials including high reflective materials like Al and Mg. However, there are certain limitations that encountered during this process such as low deposition rate due to low welding speed and manual operation. Highly dependent on the manual skills for welding procedures. Applicable for thin sheets, as thick sections require multiple weld passes which impose high component distortion and residual stresses [47-49].

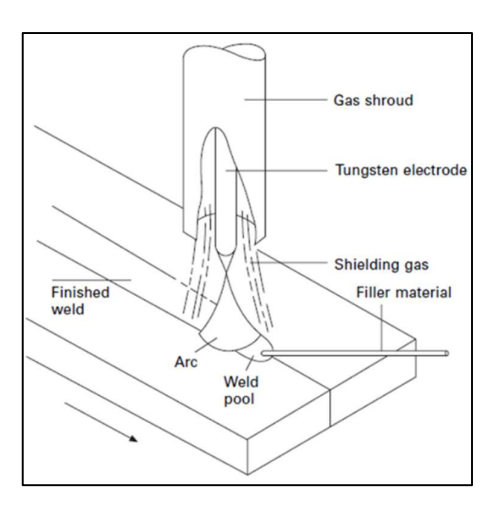


Figure 1.6. Schematic representation of Tungsten Inert gas (TIG) welding process [49]

1.7.2 Metal Inert Gas welding process:

In Metal inert gas (MIG) welding process, the heat is generated between the continuously fed consumable electrode and the workpiece to form a weld joint. Consumable filler wire can be similar or dissimilar composition to that of workpiece based on the application and weld joint properties requirements. The molten pool is protected from atmospheric contamination by the inert shielding gas such as Argon and Helium or non-inert gas as well in case of MAG welding. Schematic representation of the MIG welding process is shown in Figure 1.7. However, the skill requirements for welding procedure are not high as required in TIG welding process, still MIG process limits due to high amount of spatter formations.

Moreover, these arc welding processes are generally characterized by the low power density processes, but still these processes can be successfully used semi-automatically with inexpensive equipment specially for thin section welding [47,50].

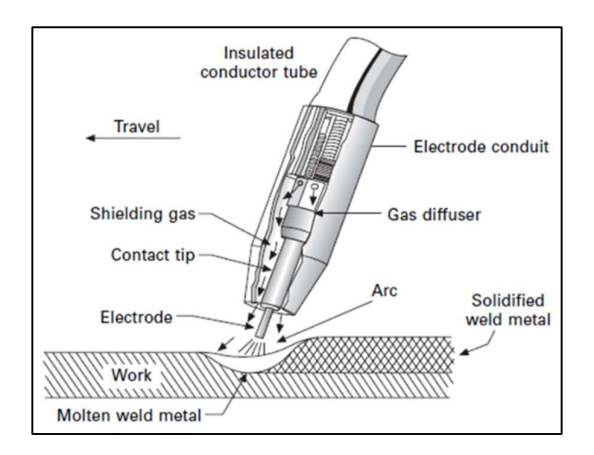


Figure 1.7. Schematic representation of Metal Inert gas (MIG) welding process [50]

1.7.3 Submerged arc welding process:

Submerged arc welding (SAW) process is a similar welding technique to that of other conventional arc welding processes like MIG/MAG wherein melting and subsequent joining occurs by establishment of an arc between a continuously feed consumable electrode and the workpiece. However, arc is submerged by the flux in SAW and thus invisible. In this regard, spatters reduced during this process due to submerging of the arc, and this process is limited to welding of flat or circumferential objects [47-49].

1.7.4 Shielded metal arc welding:

Shielded metal arc welding (SMAW) is a manual arc welding technique in which heat is generated between the consumable flux-coated electrode and the workpiece to form a weld joint. The fused area and the electrode are protected by the layer of slag that act as shielding gas as the flux coating of the electrode disintegrates. SMAW welding processes offers several advantages as compared to other conventional welding methods such as lower equipment cost, light in weight and portable, highly versatile, and no additional shielding required as the flux-coated electrode produces its own shielding gas [47-49].

1.7.5 Plasma arc welding:

Plasma arc welding (PAW) is a similar arc welding technique to that of GTAW process, wherein heat is generated with a constricted arc established between the non-consumable W electrode and the workpiece that melts and form a weld joint. The fused area and the electrode are protected by the shielding gas as well as additional orifice gas. However, the arc in PAW is constricted or collimated in this process due to converging nature of the orifice gas nozzle and thus allow arc to expands slightly with increase in arc length. It has certain advantages over GTAW; keyhole mode welding is possible with PAW, which produces a full penetration weld with high welding speed. PAW process is less sensitive to unintended arc length differences and therefore less skill needed than during GTAW manual welding [47-49].

1.7.6 Cold metal transfer welding:

Cold metal transfer (CMT) is a modified version of GMAW (Gas metal arc welding) which typically operates at low heat input. In this process, the moment short circuit established between filler wire and workpiece, then the filler wire is retracted by a CMT controller causing welding current drops to zero and then the droplets occur at zero current. Thus, the name of the process is cold metal transfer. These types of metal transfer welding process produce shallow weld bead with spatter free and high-quality welds and widely applicable for joining dissimilar sections, but limited to only thin parts [47-50].

1.8 High-energy beam welding processes

Joining thick sections by conventional arc welding processes requires multiple number of weld passes which results in heavy metal deposition owing to high heat input and high filler metal consumption as a results high component distortion and residual stresses in the components. As a solution, modern high energy beam welding processes are sought-after. Expected advantages are the reduction of welding passes, increase welding speed that in turn reduce overall heat input, which results in low distortion and thus less rework for straightening of the components. Therefore, these processes have gained widespread importance for joining thick-sections for various high temperature and high-pressure applications in comparison to multi-pass arc welding techniques due to its capability to produce welds with deeper penetration, low thermal distortion and minimal residual stress due to high welding speed, low heat input, narrow weld bead and HAZ [51]. High energy density welding processes such as Laser and Electron beam are most recent and improved welding techniques with sufficiently high-power densities as compared to that of conventional arc welding processes.

1.8.1 Electron beam welding:

Electron beam welding (EBW) is a fusion welding process whereby electrons produced from the electron beam and these high-speed electrons bombard the workpiece, causing melting and joining together upon solidification. The high intensity of the electron beam results in a weld with high depth to width aspect ratio. EBW are usually performed in high vacuum usually around 10⁻⁶ mbar, thus, increases the cost of the process and restricts to high value components only. However, high cooling rates are achieved in EBW process as similar to that of laser welding process resulted in high hardness of the components, but has greater tendency for porosity formation as vacuum encourage trapped gas to escape during EBW. Moreover, EBW provides low heat input, narrow hear-affected zone (HAZ) and low thermal distortion and residual stresses as similar to laser beam welding [47].

1.8.2 Laser beam welding:

Laser beam welding (LBW) is a fusion joining process wherein coalescence is produced between workpieces by the use of laser. LBW produces a weld with high aspect (depth-towidth) ratio and with relatively low heat-input, narrow HAZ and low distortion and residual stresses owing to its high-power density and focusability as compared to that of conventional arc welding processes [47,52]. Generally, two different welding modes are distinguished in LBW processes; conduction and keyhole mode. In conduction mode welding, the surface of the workpiece is heated by the low energy density laser beam i.e., the threshold energy needed to initiate a keyhole is not attained, therefore only surface melting occurs and the weld obtained by conduction mode welding which is typically a shallow bead with a bowl-shaped profile. In contrast, in keyhole mode welding, the energy density increase to a level beyond threshold level wherein strong evaporation occurs on the melt surface, therefore the recoil pressure developed will be sufficient to induce a deep narrow depression through the thickness of material, generating a keyhole (vapor column). The schematic illustration of keyhole LBW process is shown in Figure 1.8. A keyhole in LBW is a unique phenomenon that induce various factors such as multiple reflections, Fresnel absorption, recoil pressure and pressure due to surface tension. Welds obtained by keyhole mode of welding entail high aspect ratio (depthto-width) [53-55].

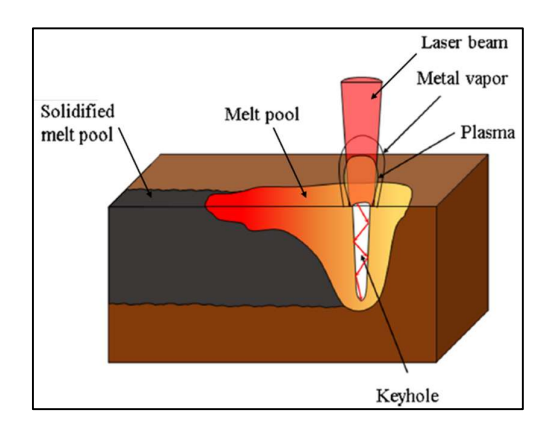


Figure 1.8. Schematic representation of laser keyhole welding [55]

1.8.2.1 Carbon dioxide laser welding:

CO₂ lasers typically consists of mixture of gases such as N₂, He and CO₂ with varying in proportion as lasing medium. The stimulation of the laser active medium carried out by the electric discharge. Characteristically, conversion efficiencies of these lasers typically in the range of 10 – 13 % and it emits laser with a highest wavelength of 10.6 µm [56]. The use of metallic optical mirrors in focusing system of CO₂ lasers prevent beam attenuation due to high reflective characteristics of mirrors [52]. Moreover, CO₂ lasers can be operated in both continuous and pulsed wave modes. CO₂ lasers offer certain advantages like high focusability, are mechanically robust, and are the most cost-effective beam sources in terms of investment and operating costs per kilowatt of laser power. However, due to longer wavelength, CO₂ laser beam is likely to absorbed heavily by the plasma generated by keyhole and heavily reflected while welding Al and Cu [56,57]. Further detailed explanation provided in experimental sections as CO₂ laser has been used in our present work.

1.8.2.2 Nd:YAG laser welding:

Neodymium-doped yttrium-aluminum-garnet (Nd:YAG) lasers are the class of solid state laser types which constitutes of a single crystal rod typically made of YAG doped with small quantity of Nd rare earth element. This YAG crystal rod is surrounded by lamps made by either Xe or Kr to excite the dopant by giving high intensity lights. Thus, laser produces with a wavelength of 1.06 µm when the excited electrons come back to the normal state. The emitting wavelength of Nd:YAG is quite low as compared to that of CO₂ laser as a result reduced reflectivity by the metal surface being welded. These types of lasers can be used for

both continuous and pulse wave mode of materials processing. In recent times, high power and use of fiber optics in Nd:YAG is now utilized for welding applications [51,58].

1.8.2.3 Disc Laser welding:

Disc lasers are the class of solid-state laser types which constitutes of a thin disc or slice of Yb-doped Yettrium-Aluminium garnet crystal as lasing medium. This typically emits a laser with a wavelength of 1030 nm. However, disc lasers produces very close wavelength to that of Nd;YAG lasers, but the shape of the crystals in both the lasers are different. In Nd;YAG lasers, the lasing crystal is in the form of rod of several mm in diameters and hundreds of mm in lengths and the this type of lasers is excited by flash lamp or diodes. However, Nd;YAG lasers has typical thermal lensing issues which causes divergence of the laser beam. Altogether it effects the overall beam quality. Thus, this issue was solved by disc laser by utilizing a thin crystal disc (few hundreds of microns in thickness but several mm in diameter) as lasing medium with low surface to volume ratio [51,58].

1.8.2.4 Fiber laser welding:

Fiber laser welding (FLW) are recently developed welding technique in which diodepumped solid state fiber laser is utilized which emits wavelength of around 1 μm. The laser active medium for this type of laser is made up of active fiber which is doped by rare earth elements and pumped by multimode diodes. The laser beam can be transport through optical fiber which eliminates the need of an optical system as needed in CO₂ lasers. Due to shorter wavelength, high beam quality, focusability and high-power density, the FLW produced weld with low heat input and high depth to width ratio [58,59].

1.8.2.5 High power diode laser welding:

Diode laser is a semiconductor device which converts electrical energy to the laser light directly. High-power diode lasers (HPDL) typically emit light in the near IR region with wavelength range of 800 – 1000 nm. Each individual emitter in the diode laser bars emits a few Watts of output power. So, the total output power from a single monolithic semiconductor device will be as high as 150 W. These devices combined together in horizontal and vertical stacks to generate a HPDL system with maximum output laser power in tens of hundreds of kilowatts range. Nearly 60% of conversion efficiency (electrical energy to laser light) can be achieved in HPDL, which is typically high as compared to other lasers systems. High

conversion efficiency of HPDL results in low operating cost of the system. In recent years, significant improvement in the beam quality of diode lasers with maximum output power in tens of hundreds of kilowatts encourages to adopt these lasers for joining applications previously used by employing high power CO₂, Nd:YAG and Fiber lasers. Thus, it is now necessitates encashing potential of high power diode lasers for joining counterbalancing economic advantages of low capital investment, low foot print and low operating costs in comparison with other laser types. Apparently, high power diode laser has got advantages of high energy efficiency, high absorptivity, high reliability, longer serviceability and portability as diode laser leverages focusing to large beam size due to high beam divergence and poor beam quality [60,61]. Further detailed explanation provided in experimental sections as HPDL has been used in our present work.

1.9 Laser-Arc Hybrid welding:

As mentioned, joining thick sections by conventional arc welding processes requires multiple number of weld passes which results in heavy metal deposition due to high heat input and high filler metal consumption as a results high component distortion and residual stresses in the components. Therefore, employing laser beam welding processes are expected to solve the above issues. However, in certain typical applications of shipbuilding or pipe laying or tube-tube joints and tube to fin joints in heavy industries such as thermal power plants cannot maintain zero gap between the components as it is the basic requirement for laser welding. Thus, as a solution, modern laser hybrid welding processes are sought-after. Expected advantages are to improve gap bridgeability of the components, increase welding speed and welding thick sections in single pass.

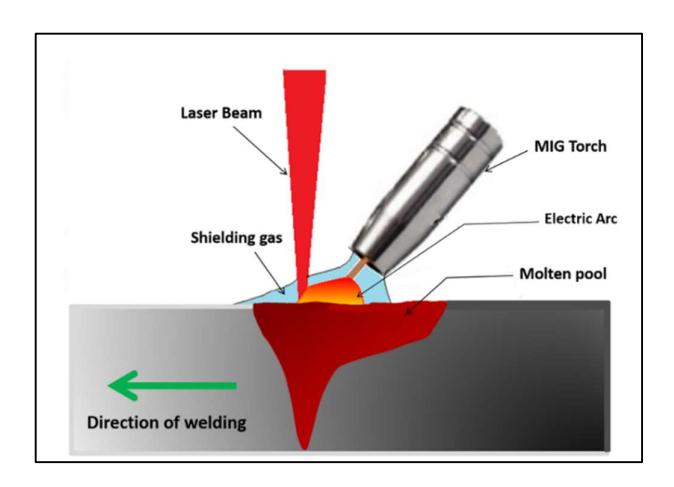


Figure 1.9. Schematic representation of laser-arc hybrid welding process [63]

Laser hybrid welding (LHW) technique is a unique metal joining process developed by combining the electric arc and laser heat sources in a common weld pool. The concept of LHW was first introduced in the 1970's as "arc augmented laser welding" by W. M. Steen and coresearchers [62] by combining a CO₂ laser with TIG arc. Since then, a wide range of LHW systems are commercially available now based on type of arc use including GTAW, GMAW, and plasma arc welding (PAW) and the type of laser such as CO₂, Nd:YAG, and fibre laser. A schematic representation of a LHW process set up is shown in Figure 1.9 [63]. In LHW processes, the focused laser beam with sufficiently high energy density as a primary heat source resulting in deep penetration mode of welding while the electric arc considered to be the secondary heat source, carry out additional functions in this process in order to improve process stability and gap bridgeability. Therefore, their synergic effect between these two heat sources is employed to produce a deep and narrow weld with improved welding speed which in turn enhanced productivity [63]. Some of the notable principal advantages of LHW process is the good gap bridging ability between two workpieces which is the limitation of laser welding process and high depth of penetration which is the limitation of arc welding process [63,64]. Figure 1.10 showing schematic representation of joining arc and laser in laser hybrid welding process. It indicates that the LHW bead is a combination of both laser and arc welds beads. Therefore, the synergic effect between two heat sources is gainfully utilized to produce a deep and narrow weld bead with good gap tolerance. Table 1.2 compares the LHW bead with those of arc and laser weld beads [65-67].

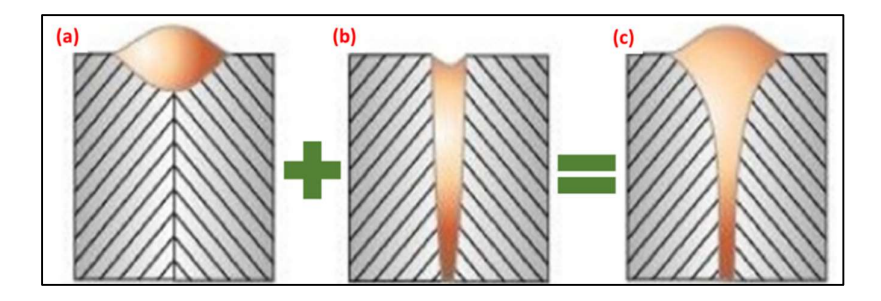


Figure 1.10. Schematic representation of joining arc and laser in laser hybrid welding process [63]

Table 1.2. Comparing various advantages of LHW process over individual laser and arc welding processes [65-69]

	Arc welding	Laser beam welding	Laser Hybrid welding
Gap bridgeability	Good Due to use of filler results in wide fusion	Poor	Good Due to use of filler results in wide fusion
Depth of penetration	Shallow	High	High
Process stability	Relatively poor at high welding speed	Instability of keyhole	Interaction of laser and arc stabilizes the process
Heat Input	High	Low	Low
Distortion level	High	Low	Low
Cooling rates	Low	High	Relatively low
Reflective materials	Weldable	Difficult to weld	Weldable
Formation of Pores	Less porosity	Porosity in deep welds	Less porosity
Undercuts	Low	High	Low
Productivity	Low	High	High

As mentioned, a wide number of LHW systems has been developed based on various groupings of laser and arc. Among which, Fiber, CO₂ and Nd:YAG lasers are found to be the most common laser heat sources whereas MIG, TIG and PAW are widely used arc heat sources in LHW system [68].

1.9.1 Hybrid Laser-MIG welding process:

In this type of system, a Fiber, CO₂ or a Nd:YAG laser is used as a primary heat source, while MIG arc is used as a secondary heat source. Arc is established between consumable MIG electrode and the base metal. This consumable electrode is continuously fed with a predefined wire feed rate. While the high energy density laser beam (Fiber, CO₂ or a Nd:YAG) produces a keyhole in the weld pool and ensure a deep weld penetration. Thus, laser produces a deeper penetration whereas the molten filler metal produces a shallow weld bead and ensure to fill the gaps between the components and permits welding with high bridgeability of the parts. Laser-MIG hybrid welding process schematically shown in Figure 1.11a [69]. It is reported that, this type of welding process improves MIG arc stability due to addition of laser heat source. Also, the use of consumable filler metal with varying alloying elements to that of workpiece can improve the chemistry in terms of composition of the welds and thus in turn improve the weld joint mechanical properties. Moreover, higher amount of melt volume is produces in this

process due to addition of consumable filler metal makes this process superior for gap bridging capability than compared to other hybrid welding systems such as hybrid-TIG and hybrid-plasma. Because of utilization of two heat sources in common weld pool, increase the welding speed without occurrence of undercuts. However, the weld bead form in hybrid-MIG process has greater variation of filler material composition in the top and in the bottom weld bead, since the filler metal concentrates only at the top portion of weld bead. Thus, appropriate joint design (gap opening between the plates) enables the molten filler metal to reach the root of the weld [63,65,69].

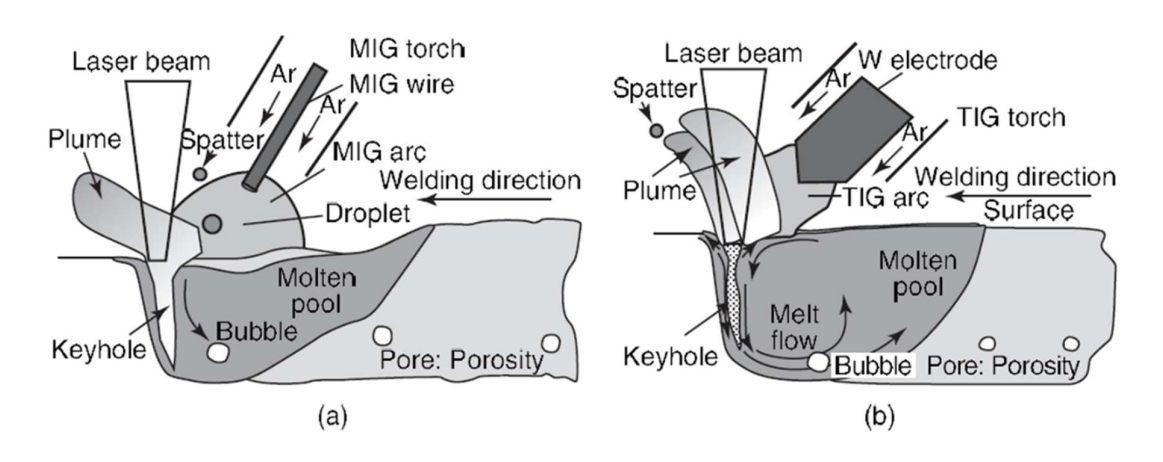


Figure 1.11. Schematic representation of (a) laser-MIG hybrid and (b) laser-TIG hybrid welding processes [69]

1.9.2 Hybrid Laser-TIG welding process:

In this hybrid-TIG welding system, a non-consumable tungsten electrode is used as a secondary heat source. In this process, addition filler metal may require due to use of non-consumable W electrode. However, the rate of deposition of metal is significantly less as compared to that of hybrid-MIG welding system, due to only a fraction of arc heat is utilized to melt the filler metal in this process. Laser-TIG hybrid welding process schematically shown in Figure 1.11b. The major issues encountered during this process are, tungsten electrode contamination, erosion of tungsten tip and high affinity towards oxygen for tungsten electrode. Similar to hybrid-MIG welding process, hybrid-TIG process improves are stability due to addition of laser heat source [63,64,69].

1.9.3 Hybrid Laser-Plasma welding process:

In this plasma arc hybrid welding (PAW) system, a constricted plasma arc is considered as a secondary heat source. A non-consumable W electrode is recessed in the welding torch in this process. Heat is generated between a constricted arc established between the non-consumable W electrode and the workpiece. The melt area and the W electrode are protected from the contamination by shielding gas as well as additional orifice gas. The arc in PAW is constricted or collimated and more stable and doesn't deflect more easily as in TIG process, due to converging nature of the orifice gas nozzle and thus allow arc to expands slightly with increase in arc length. The hybridization between laser and plasma improves the weld penetration depth, welding speed and stabilizes the plasma arc [63,69].

1.10 Statistical Modelling applied for Welding

Notwithstanding that any process development requires cumbersome experimentation with repeated analysis of experimentation and optimization of numerous processing parameter, a suitable design of experiments approach is always required to co-relate influence of various critical process parameters on relevant output responses. Response surface methodology (RSM) is one such mathematical technique often utilized to optimize the process parameters by proper identification and estimating control input parameter's quantitative influence [70]. In recent times, statistical modelling with design of experiments (DOE) approach were found to be extensively used successfully on variety of science and engineering problems to optimize the process parameters, thus, facilitating vast reduction in experiments. DOE is an analytical or experimental approach which is generally used to statistically indicate the relationship between input variables or parameters with output responses. Among the most conspicuously used DOE, RSM with Box-Behnken Design (BBD) method is one such suitable and effective method that allow researchers to effectively understand the influence of process variables, particularly in situations where several process inputs potentially influence process response such as in deep penetration laser welding process of thick sections. Since influence of one parameter depend on level of other interdependent parameters, simultaneous effect of it needs to be investigated and as such in most RSM problems, relationship between responses and process parameters are unknown and needs to be effectively established. Although CCD method employing with addition of centre points and axial points is useful for chronological experimentation, it requires five levels that burden experimenters. On the other hand, BBD entails to use only three levels for each parameter and thereby reduce the burden on conducting many experiments. However, use of BBD confines to situations wherein predicting extreme values of response is not of utmost importance. Thus, BBD that can effectively provide high quality predictions when studying linear and quadratic interactions of the process [70,71].

1.11 Motivation and Research Objectives of the Thesis work

As advanced ultra-supercritical (AUSC) thermal power plant boilers are aimed at increasing the efficiency to 46 – 50% to withstand higher temperatures (710 – 760°C) and pressures (25 – 35 MPa), application of Ni-based super alloy such as Inconel 617 in various parts is the need of the hour with development of suitable joining technology. Inconel 617 (Ni-Cr-Co-Mo), a solid-solution strengthened and carbide hardened nickel-based superalloy is most promising candidate material for use in boiler components of coal-based thermal power plants such as superheater and reheater tubes, main steam pipes, valves, turbine rotor parts etc., owing to its superior hot corrosion/oxidation resistance coupled with creep resistance and high-temperature structural stability. As the candidate material is used in thicknesses ranging from 4 mm - 12 mm, development of a suitable low heat-input welding process, specifically for high section thickness (10 mm) is essentially required for fabrication and construction of various boiler parts and hence chosen for the present work.

Although, several conventional fusion welding processes such as SMAW, SAW, GMAW, TIG and their advanced variants are currently in use for joining thick-sectioned boiler parts, but these multi-pass welding processes characterized by their high heat input entail certain inherent disadvantages such as high component distortion, excessive filler material consumption and induced high residual stresses in the components which deteriorates the life of the components and necessitates subsequent machining for distortion correction of the components, large HAZ, poor process repeatability with cumbersome edge-preparation. Furthermore, on account of poor weldability of Ni-based superalloy, several weld imperfections and defects are encountered during thick-section welding such as lack of fusion, high propensity to hot cracking (solidification and liquation cracking) that drastically deteriorate high-temperature performance as well as vulnerability for porosity formation. In addition, it is a daunting task to obtain satisfactory appearance on surface as well as bottom of the weld during deep penetration welding of thick-sectioned materials due to occurrence of imperfections such as underfills, undercuts, spatters, and root humps.

Single-pass welding process employing laser heat source such as Autogenous Laser welding and Laser-Arc Hybrid welding are anticipated to provide great promise in these aspects due to their remarkable advantages when compared to conventional fusion welding techniques,

such as low heat input, narrow HAZ, high aspect (depth-to-width) ratio welds, high welding speed leading to higher production rate, minimal distortion and residual stress in weldments and thus provide tremendous technological and economic benefits. LHW is a fusion joining process in which a laser beam interacts with the electric arc in a same weld pool and the synergic effect between these two heat sources is gainfully employed to produce a deep and narrow weld with improved gap bridgeability.

Several reported research works attempted welding of Inconel 617 alloy employing various types of arc and laser welding processes with many-a-times unsuccessful in complex designs and thick-section welding. It was still challenging to weld high viscous Ni-based superalloy parts/components by fusion joining technique due to their critical weldability issues including formation of liquation cracks in PMZ/HAZ, surface underfills and root hump defects, lack of fusion and lack of penetration, porosity formation, weld cracking, eutectic formations, and segregation of alloying elements deteriorating the performance of the weld joint. Although, various attempts were tried to reduce weld cracking susceptibility by controlling heat-input or employing additional preheating and modification of filler-material, detailed understanding in terms of identification of low melting eutectic phases and their mechanical behavior on weld performance is still lacking. Moreover, when welding thick-section which is essential for boiler components, the satisfactory through-thickness penetration with defect-free weldment in single pass welding was still a daunting task due to formation of surface underfill / undercuts with root hump defects associated with incompatible unfavorable melting characteristics of Inconel 617 alloy. As laser-hybrid welding (LHW) with addition of an arc source (TIG, MIG etc) to laser help enhance weldability (reducing liquation cracking susceptibility) with enhanced gapbridging ability, relatively higher distortion with low processing speeds still an issue to enhance its engineering manoverability at economic costs.

Therefore, the present research work is targeted to investigate and analyze metallurgical, mechanical and corrosion behavior with comprehensive characterization of weldments produced in laser and laser-hybrid welded joints of 10-mm thick Inconel 617 superalloy in solution-annealed condition. Later, with thorough understanding of weldability with CO₂ laser alone and hybrid systems, advanced diode laser with improved beam quality is utilized to study the metallurgical and mechanical behavior of single-pass weld joints produced in butt-joint configuration. After optimization of diode laser-based welding process, a novel patented process developed with specially designed joint with two-step joining strategy for welding 10-mm thick Inconel 617 superalloy in a single pass. In order to compare engineering

advantages and economics of the process, this novel single-pass adaptive diode laser welding (ADLW) technique was compared with LHW and conventional multi-pass TIG welding process. Furthermore, comprehensive metallurgical, mechanical and corrosion properties evaluation was carried out utilizing advanced characterization techniques of EBSD, Nano-Indentation and Micro-focus XRD tools.

Various work elements constituting the thesis work include:

- a) Comprehensive study on process optimization of autogenous laser welding (ALW) and laser hybrid welding (LHW) of Inconel 617 alloy
- b) Detailed study with understanding and co-relating of weld fusion behavior with microstructure evolution and liquation cracking susceptibility in both ALW and LHW welding processes
- c) Process optimization of single-pass autogenous laser welding of 10-mm thick Inconel 617 superalloy employing high-power fiber-coupled diode laser integrated to a robotic workstation with comprehensive assessment of mechanical and metallurgical properties.
- d) Statistical modelling with multi-objective optimization employing RSM-BBD method with desirability approach for deep penetration laser welding of thick sections using DLW
- e) Setting up of an apparatus and a novel method for laser welding of thick metallic material such as Inconel 617 employing filler-wire preplacement with specific joint design and two-step welding procedure employing DLW and finally,
- f) Comprehensive comparative study of ADLW, LHW and conventional multi-pass TIG welding processes of joints with assessment of their metallurgical, mechanical and hotcorrosion behavior properties.

1.12 Overview of the Thesis

The Thesis comprises of ten chapters. Chapter 1 describes overview of technical background, with motivation and targeted objectives of the study, whereas, Chapter 2 discusses literature review on various welding methods reported on Inconel 617 alloy. Chapter 3 describes the experimental setups and conditions employing CO₂, high-power DLW, LHW and conventional TIG welding methods along with comprehensive characterization of weldment employing Optical, FESEM with EDS and Elemental Mapping, EBSD, Micro-focus XRD, High-speed Nano-Indentation System and Micro-Vickers hardness, Mechanical and corrosion

properties of the weld joints were evaluated employing Tensile / Impact testing and hightemperature corrosion test rigs. Additionally, Statistical approach of design of experiments for welding process optimization was also carried out with experimental validation. Discussion of results with analysis of the work is carried out in Chapters 4-9. Chapter 4-5 discusses comprehensive study on process optimization and understanding of mechanism of liquation cracking susceptibility during ALW and LHW processes. Chapter 6 deals with the study on process optimization of thick-sectioned single-pass autogenous laser welding using high-power fiber-coupled diode laser with assessment of weld joint properties. Chapter 7 describes the process optimization of thick-sectioned DLW by employing statistical analysis with RSM-BBD method with desirability approach. Chapter 8 presents the novel welding method developed employing robot-integrated fiber-coupled diode laser welding apparatus for laser welding of thick metallic materials with joint design and two-step welding strategy. Chapter 9 discuss comprehensive comparative study on single-pass ADLW and LHW welding processes with conventional multi-pass TIG welding process with assessment of their metallurgical, mechanical and high temperature corrosion behavior. Chapter 10 summarizes the work with conclusions drawn from the study and projecting direction for future investigations.

1.13 References

- Shingledecker, J. P. "The US DOE/OCDO A-USC materials technology R&D program." In Materials for Ultra-Supercritical and Advanced Ultra-Supercritical Power Plants, pp. 689-713. Woodhead Publishing, 2017.
- 2. Viswanathan, R., and W. Bakker. "Materials for ultrasupercritical coal power plants—Boiler materials: Part 1." Journal of materials engineering and performance 10, no. 1: 81-95, 2001.
- 3. Osgerby, S. "Steam turbines: Operating conditions, components and material requirements." In Structural Alloys for Power Plants, pp. 22-35. Woodhead Publishing, 2014.
- 4. David, Stan A., John A. Siefert, and Zhili Feng. "Welding and weldability of candidate ferritic alloys for future advanced ultrasupercritical fossil power plants." Science and Technology of Welding and Joining 18, no. 8: 631-651, 2013.
- 5. Di Gianfrancesco, Augusto, ed. Materials for ultra-supercritical and advanced ultra-supercritical power plants. Woodhead Publishing, 2016.
- Fukuda, Masafumi. "Advanced USC technology development in Japan." In Materials for Ultra-Supercritical and Advanced Ultra-Supercritical Power Plants, pp. 733-754. Woodhead Publishing, 2017.
- 7. Mathur, Alok, O. P. Bhutani, T. Jayakumar, D. K. Dubey, and S. C. Chetal. "India's National AUSC Mission—Plan and Progress." ASM International, 2013.
- 8. FTSE, Dongke Zhang, ed. Ultra-supercritical coal power plants: materials, technologies and optimisation. Elsevier, 2013.
- 9. Bhatt, N. C., Maneesh Batrani, Jatinder Mohan, V. Gopalakrishnan, and M. K. Verma. "Indian AUSC Steam Turbine Program—Current Status and Future Program." 2015.
- 10. Abe, F. "Development of creep-resistant steels and alloys for use in power plants." In Structural alloys for power plants, pp. 250-293. Woodhead Publishing, 2014.

- 11. David, Stan A., John A. Siefert, and Zhili Feng. "Welding and weldability of candidate ferritic alloys for future advanced ultrasupercritical fossil power plants." Science and Technology of Welding and Joining 18, no. 8 (2013): 631-651.
- 12. Siefert, J. A., and S. A. David. "Weldability and weld performance of candidate austenitic alloys for advanced ultrasupercritical fossil power plants." Science and Technology of Welding and Joining 19, no. 4: 271-294, 2014.
- 13. David, Stan A., J. A. Siefert, J. N. DuPont, and J. P. Shingledecker. "Weldability and weld performance of candidate nickel base superalloys for advanced ultrasupercritical fossil power plants part I: fundamentals." Science and Technology of Welding and Joining 20, no. 7: 532-552, 2015.
- 14. Wheeldon, J. M., and J. P. Shingledecker. "Materials for boilers operating under supercritical steam conditions." In Ultra-supercritical coal power plants, pp. 81-103. Woodhead Publishing, 2013.
- 15. Agarwal, D. C. "Nickel and nickel alloys." Handbook of Advanced Materials (2004): 217.
- 16. Romanosky, Robert. "A comprehensive overview of the United States advanced ultrasupercritical (USC) materials research program." In Conference of Advanced ultrasupercritical coal-fired power plants. 2012.
- 17. Abe, Fujio. "Research and development of heat-resistant materials for advanced USC power plants with steam temperatures of 700 C and above." Engineering 1, no. 2: 211-224, 2015.
- 18. Wheeldon, J. M., and J. P. Shingledecker. "Materials for boilers operating under supercritical steam conditions." In Ultra-supercritical coal power plants, pp. 81-103. Woodhead Publishing, 2013.
- 19. Special Metals Corporation. Inconel740 bulletin. Special Metals Corporation, Huntington, WV, USA, 2005.
- 20. Xie X S, Zhao S Q, Dong J X: An investigation of structure stability and its improvement on new developed Ni-Cr-Co-Mo-Nb-Ti-Al superalloy. Materials Science Forum; 475: 613-516, 2004.
- 21. Xie X S, Zhao S Q, Dong J X: A new improvement of Inconel alloy 740 for USC power plants. Proc of Advances in Materials Technology for Fossil Power Plants, ASM, 2008.
- 22. Z. Liu, H. Bao, G. Yang, S. Xu, Q. Wang, Y. Yang. Material advancement used for 700 °C AUSC-PP in China. In: D. Gandy, J. Shingledecker, eds. Advances in Materials Technology for Fossil Power Plants: Proceedings from the Seventh International Conference. Materials Park, OH: ASM International: 171–179, 2013.
- 23. Xie, Xishan, Yunsheng Wu, Chengyu Chi, and Maicang Zhang. "Superalloys for Advanced Ultra-Super-Critical Fossil Power Plant Application." Superalloys; InTech: Rijeka, Croatia (2015): 51-76.
- 24. Klöwer, J. "Alloy 617 and derivatives." In Materials for Ultra-Supercritical and Advanced Ultra-Supercritical Power Plants, pp. 547-570. Woodhead Publishing, 2017.
- 25. Mankins, W. L., J. C. Hosier, and T. H. Bassford. "Microstructure and phase of INCONEL alloy 617 stability." Metall. Trans 5: 2579-2590, 1974.
- 26. VdTÜV-Blatt 485 (VdTÜV Material Data Sheet 485), Dec. 2009
- 27. ASME International: Standard Specifications B-166/B-168, ed. 2010
- 28. F. Schubert, H.J. Penkalla, G. Ullrich, in: Proc. Conf. High Temperature Metallic Materials for Application in Gas-Cooled Reactors, Wien, 1981.
- 29. Ren, Weiju, and Robert Swindeman. "Preliminary consideration of alloys 617 and 230 for generation IV nuclear reactor applications." In ASME Pressure Vessels and Piping Conference, vol. 42843, pp. 371-384. 2007.

- 30. R. Blum, R.W. Vanstone, Materials development for boilers and steam turbines operating at 700°C, in Materials for Advanced Power Engineering, in: Proceedings of the 8th Liege Conference, pp. 41–60, 2006.
- 31. J. Klower, R.U. Husemann, M. Bader, Development of nickel alloys based on alloy 617 for components in 700°C power plants, Proc. Eng. 55, 226–231, 2013
- 32. Chetal, S. C., T. Jayakumar, and A. K. Bhaduri. "Materials research and opportunities in thermal (Coal-based) power sector including advanced ultra super critical power plants." In Proc. Indian Natl. Sci. Acad, vol. 81, pp. 739-754. 2015.
- 33. Inconel 617 alloy datasheet, Special metals corporation, 2005.
- 34. Gariboldi, Elisabetta, Marcello Cabibbo, Stefano Spigarelli, and Dario Ripamonti. "Investigation on precipitation phenomena of Ni–22Cr–12Co–9Mo alloy aged and crept at high temperature." International Journal of Pressure Vessels and Piping 85, no. 1-2: 63-71, 2008.
- 35. Wu, Quanyan, Hyojin Song, Robert W. Swindeman, John P. Shingledecker, and Vijay K. Vasudevan. "Microstructure of long-term aged IN617 Ni-base superalloy." Metallurgical and materials transactions A 39, no. 11: 2569-2585, 2008.
- 36. Wenjie, R.; Fenggui, L.; Renjie, Y.; Xia, L.; Zhuguo, L. Liquation Cracking in Fiber Laser Welded Joints of Inconel 617. J. Mater. Proc.Technol, 226, 214–220, 2015.
- 37. Idowu, O. A.; Ojo, O. A.; Chaturvedi, M. C. Effect of Heat Input on Heat Affected Zone Cracking in Laser Welded ATI Allvac 718Plus Superalloy. Mater. Sci. Eng. A, 454-455, 389–397, 2007.
- 38. Huali, X.; Wen, L.; Fenggui, L.; Peng, W.; Yuming, D. Evolution of Carbides and Its Characterization in HAZ during NG-TIG Welding of Alloy 617B. Mater. Charac, 130, 270–277, 2017.
- 39. Shanlin, L.; Kejian, L.; Mengjia, H.; Yao, W.; Zhipeng, C.; Jiluan, P. The Mechanism for HAZ Liquation of Nickel-Based Alloy 617B during Gas Tungsten Arc Welding. Metals, 10(1), 94, 2020.
- Zhang, Mingjun, Genyu Chen, Yu Zhou, and Shenghui Liao. "Optimization of deep penetration laser welding of thick stainless steel with a 10kW fiber laser." Materials & Design 53: 568-576, 2014.
- 41. Zhang, Mingjun, Zheng Zhang, Kun Tang, Cong Mao, Yongle Hu, and Genyu Chen. "Analysis of mechanisms of underfill in full penetration laser welding of thick stainless steel with a 10kW fiber laser." Optics & Laser Technology 98: 97-105, 2018.
- 42. J. O. Milewski and E. Sklar, "Narrow gap laser welding," Google patent US5760365 A (June 1998)
- 43. "Laser wire-filled welding method for thick plate with narrow gap" Google patent CN103801833A, (May 2014)
- 44. "Butt laser welding method of welded plate material", Google patent JP6255314B2, (Dec 2017)
- 45. "Large-size structural member laser welding tool, system and method", Google patent CN112570888A, (Mar 2021)
- 46. Sun, Junhao, Wenjie Ren, Pulin Nie, Jian Huang, Ke Zhang, and Zhuguo Li. "Study on the weldability, microstructure and mechanical properties of thick Inconel 617 plate using narrow gap laser welding method." Materials & Design 175 (2019): 107823.
- 47. Kou, Sindo. "Welding Metallurgy, A John Wiley & Sons." Inc., Hoboken, New Jersey: 17-20. 2003.
- 48. M. B. Henderson, D. Arrell, R. Larsson, M. Heobel and G. Marchant, Science & Technology of Welding & Joining, vol. 9, no. 1, pp. 13-21, 20049
- 49. Norrish, John. Advanced welding processes. Springer Science & Business Media, 1992.
- 50. Ahmed, Nasir, ed. New developments in advanced welding. Taylor & Francis US, 2005.

- 51. Steen, William M., and Jyotirmoy Mazumder. Laser material processing. springer science & business media, 2010.
- 52. O'Brien, R. "Welding Handbook: Welding Processes; Miami: American Welding Society." ISBN 0-87171: 110-116, 1991.
- 53. Z. Sun, A. S. Salminen and T. J. I. Moisio, Journal of Materials Science Letters, vol. 12, no. 14, pp. 1131-3, 1993.
- 54. Gao Z, Ojo O. Modeling analysis of hybrid laser-arc welding of single-crystal nickel-base superalloys. J Acta materialia.;60(6-7):3153-3167, 2012.
- 55. Helm, Johanna, Adrian Schulz, Alexander Olowinsky, Andreas Dohrn, and Reinhart Poprawe. "Laser welding of laser-structured copper connectors for battery applications and power electronics." Welding in the World 64, no. 4 (2020): 611-622.
- 56. Tsukamoto, S. "Developments in CO2 laser welding." In Handbook of Laser Welding Technologies, pp. 17-46. Woodhead Publishing, 2013.
- 57. Eboo, M., W. M. S., Clarke, J. "Arc -augmented laser welding," Proceedings of fourth International Conference of advances in welding processes. Harrogate, Yorks, England, 1, Abington, pp. 9-11, 1978.
- 58. Quintino, L., A. Costa, R. Miranda, David Yapp, V. Kumar, and C. J. Kong. "Welding with high power fiber lasers—A preliminary study." Materials & Design 28, no. 4: 1231-1237, 2007.
- 59. Katayama, Seiji. "Fundamentals and Features of Laser Welding." In Fundamentals and Details of Laser Welding, pp. 35-55. Springer, Singapore, 2020.
- 60. Li, Lin. "The advances and characteristics of high-power diode laser materials processing." Optics and lasers in engineering 34, no. 4-6: 231-253, 2000.
- 61. Parker, Keith. "Welding with high power diode lasers." Coherent, Inc. 2012.
- 62. Steen, William M. "Arc augmented laser welding." Metals Constr. 21, no. 7: 332-335, 1979.
- 63. Acherjee, Bappa. "Hybrid laser arc welding: State-of-art review." *Optics & Laser Technology* 99: 60-71, 2018.
- 64. Shenghai, Zhang, Shen Yifu, and Qiu Huijuan. "The technology and welding joint properties of hybrid laser-tig welding on thick plate." *Optics & Laser Technology* 48: 381-388, 2103.
- 65. Fellman, Anna, and Veli Kujanpaa. "The effect of shielding gas composition on welding performance and weld properties in hybrid CO2 laser-gas metal arc welding of carbon manganese steel." *Journal of Laser Applications* 18, no. 1: 12-20, 2006.
- 66. Ono, Moriaki, Yukio Shinbo, Akihide Yoshitake, and Masanori Ohmura. "Development of laser-arc hybrid welding." Nkk Technical Report-Japanese Edition: 70-74, 2002.
- 67. Ribic, B., T. A. Palmer, and T. DebRoy. "Problems and issues in laser-arc hybrid welding." International materials reviews 54, no. 4 (2009): 223-244.
- 68. Victor, Brian M. "Hybrid laser arc welding. Edison Welding Institute".
- 69. Olsen, Flemming Ove, ed. Hybrid laser-arc welding. Elsevier, 2009.
- 70. Montgomery, Douglas C. Design and analysis of experiments. John wiley & sons, 2017.
- 71. Prasad, K. Siva, Ch Rao, and D. Nageswara Rao. "Application of design of experiments to plasma arc welding process: a review." Journal of the Brazilian Society of Mechanical Sciences and Engineering 34, no. 1: 75-81, 2012.

CHAPTER 2 LITERATURE REVIEW

As discussed in the previous chapter, Advanced-ultra-supercritical (AUSC) boiler is an extension of ultra-supercritical boiler by increasing the steam temperature and pressure for enhancement of coal-based thermal power plant efficiency and at the same decreased the CO₂ emissions to preserve the environment. Ni-based superalloy Inconel 617 is considered as one of the outstanding candidate material to meet the proposed AUSC boiler steam conditions due to its outstanding oxidation, hot corrosion, and creep resistant properties [1,2]. Fusion welding is an essential joining process for fabrication and construction of various structural and functional parts of the AUSC boiler. Conventional welding techniques often makes deleterious effects due to high heat input, need for multiple weld passes that entail excessive filler material consumption, low welding speed, large HAZ, poor process repeatability with cumbersome edge-preparation, high component distortion and high residual stresses and necessitates subsequent machining for distortion correction of the components [3,4]. Further, on account of poor weldability of Ni-based superalloy a several weld imperfections and defects are encountered during thick-sections single/multi-pass conventional/high energy beam welding such as lack of fusion, high propensity to hot cracking (solidification and liquation cracking) that drastically deteriorate high-temperature performance, and porosity formation [4].

In addition, it is a daunting task to obtain satisfactory appearance on surface as well as bottom of the weld during single-pass autogenous laser welding of thick plates as several studies reported occurrence of imperfections such as underfills, undercuts, spatters, and root humps [5,6]. Thus, successful development of the welding process and utilisation of moderately thick-sectioned Ni-based superalloy materials is one of the critical engineering challenge for improving efficiency and maintenance of the plant. Hence, welding and weldability of Inconel 617 superalloy materials in AUSC boilers becomes vital. Inconel 617 superalloy can be welded by various conventional joining techniques such as tungsten inert gas (TIG), hot-wire narrow gap (NG-TIG), metal inert gas (MIG), submerged arc welding (SAW), plasma arc welding (PAW) and high-energy beam processes including Laser beam welding (LBW) and Electron beam welding (EBW). Many researchers focused their studies on the joining of Inconel 617 using different arc and laser-based welding processes. Therefore, a comprehensive literature review on various conventional/laser-based single/multi-pass

welding processes for joining Ni-based superalloy along with their weldability issues has been undertaken. Furthermore, literature review on statistical modelling approach in laser welding process are also summarized in this chapter.

2.1 Welding of Inconel 617

Wen Liu et al, investigated the influence of five different thermal cycle with similar heating and cooling rate but with variation in peak temperature ranging from 1150 to 1350°C to simulate HAZ during Inconel 617 welding by employing Gleeble simulation methodology as shown in Figure 2.1a thermal cycle. Figure 2.1b shows the typical micrograph constitutes of weld and HAZ obtained in TIG welded joint. They found peak temperature possess significant effect on the secondary carbides evolution in HAZ during welding. At low peak temperature of 1150°C, they observed no adverse effect on simulated HAZ microstructure compare to base material as a result the microstructure was similar to base material. However, at intermediate peak temperature range between 1200°C and 1250°C (shown in Figure 2.1c), coarsening of carbides along the GBs (grain boundaries) were observed in simulated HAZ.

Further raising the peak temperature to beyond 1300°C and within 1350°C, the carbides present inside the grains dissolved completely and lamellar eutectic type of microstructure were observed at the GBs in simulated HAZ as depicted in Figure 2.1d. Furthermore, micro-hardness distribution analysis indicated that the simulated HAZ had no visible hardness variation as compared to base material as a result of similar average grain size to that of base material. However, tensile strength was found to be decrease with increasing the peak temperature owing to the formation of continuous lamellar eutectic microstructure with coarsened carbides at grain boundaries at high simulated peak temperature [7]. Therefore, it can infer from this study that the lamellar type eutectic structure could be realized when peak temperature crosses 1300°C and these type of structure at HAZ has significant influence on tensile properties of the weldments.

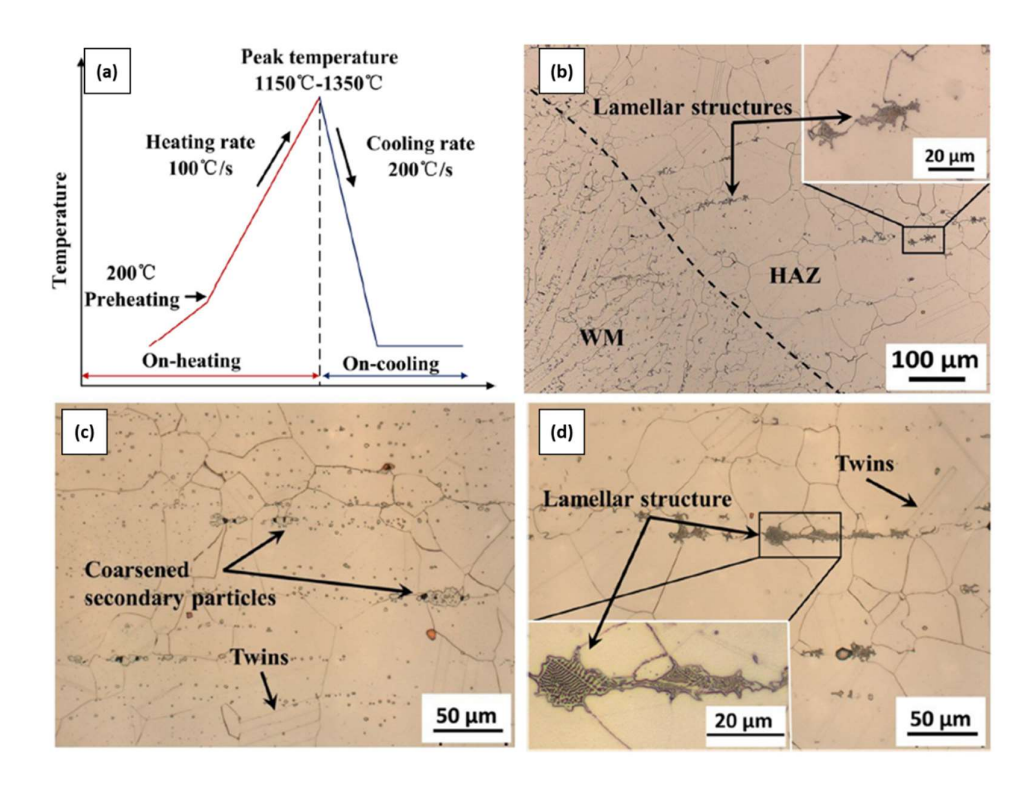


Figure 2.1. (a) Thermal cycle utilized in simulated HAZ study and (b) Micrograph showing lamellar type structure in TIG welded joint and micrographs of thermal simulated HAZ at (c) 1250°C and (d) 1300°C [7]

Further, Huali and co-researchers systematically studied the evolution of $M_{23}C_6$ carbides in HAZ of superalloy 617B with varying distance from fusion boundary during narrow gap-TIG welding processing. They found that when the peak temperature close to the fusion boundary in HAZ reach the Cr,Mo-rich $M_{23}C_6$ carbides solvus temperature, then these carbides become unstable and undergo partial dissolution and liberate Cr and Mo into the adjacent matrix. Due to low diffusivity of Mo in γ -matrix as compared to Cr, Mo segregated at the interface of γ / $M_{23}C_6$ and form M_6C carbides and Cr diffused into the surrounding matrix causing formation of Cr-depletion region as shown in Figure 2.2. On further heating above eutectic temperature, Cr,Mo-rich $M_{23}C_6$ carbides reacts with the γ -matrix and thereby forming detrimental liquid film of eutectic composition. On cooling, typical lamellar eutectic type of microstructure constitutes of Cr-rich $M_{23}C_6$, Mo-rich M_6C multi-carbides and γ -Ni matrix forms in HAZ [8]. Therefore, it can infer from this study that the lamellar type eutectic structure ($M_{23}C_6 + M_6C$ multi-carbides + γ -Ni) could be formed in the vicinity to the fusion boundary in HAZ, where peak temperature crosses eutectic temperature.

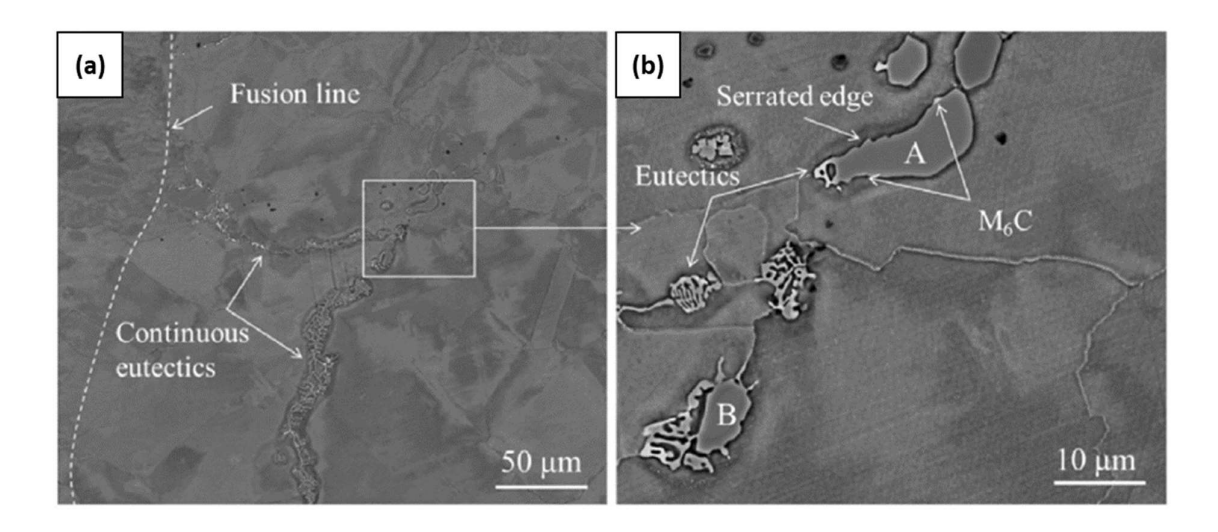


Figure 2.2. NG-TIG welded Inconel 617 (a) HAZ and (b) magnified view [8]

Similar observations were made in the study conducted by Shanlin Li et al. on welding of Inconel 617B during multi-layer Narrow gap-TIG welding processing. They found by thermal simulation study that the constitutional liquation of micron-size M23C6 carbides occurred when the peak temperature in HAZ reaches to 1300°C which is responsible for the evolution of eutectics and micro-fissures along GBs in HAZ. However, they observed slight softening of HAZ region owing to microstructural variation and weakening of strengthening mechanism caused by welding process [9]. Similarly, constitutional liquation of Cr, Mo-rich M₂₃C₆ carbides were observed in simulated HAZ of Alloy 617B during multi-layer GTAW processing and were found to be responsible for HAZ liquation of the alloy 617B welded joint study conducted by Shanlin Li et al. Rapid heating during welding provides insufficient time for diffusion of solute atoms into the surrounding matrix, thus causing a eutectic reaction to occur between M₂₃C₆ carbides and γ-Ni matrix. However, fine M₂₃C₆ carbides form in Cr supersaturated region due to experiencing lower peak temperature and sufficient time for Cr to precipitate from the γ -Ni matrix by subsequent multiple weld thermal cycle. TEM analysis of the network eutectic microstructure further confirms that the presence of M₆C carbide in eutectic network resulting in ternary phase formation. Therefore, eutectic network is composed of three distinct constituents ($M_{23}C_6 + M_6C$ multi-carbides + γ -Ni) with different morphologies [10].

Liquation cracks are predominant in multi-pass welds where the initial weld passes become the HAZ for the subsequent weld passes. Since these types of cracks are formed in weld FZ, hence the name as weld-metal liquation cracking. Therefore, in addition to the HAZ liquation cracking, multi-pass weldments are susceptible to weld metal liquation cracking as well. Fink et al. studied weldability of Inconel 617 alloy employing reduced heat-input modified dip arc welding processes such as cold metal transfer (CMT) and pulsed-mix processes and with conventional pulsed-arc welding processes. All welds (CMT, pulsed-mix and pulsed-arc) showed surface cracks present on the top weld layer and attributed to the high amount of restraint during welding. Moreover, all weld fusion zones exhibited few microcracks in the upper half region of the bead cross-section which occurred just beneath the first layer and observed significant enhancement of Mo content at the liquid film enable liquation cracking. Figure 2.3 shows the micrograph of the Inconel 617 alloy welded joint showing typical liquation cracking in underlying weld bead. Additionally, few liquation microcracks were observed in the vicinity to the fusion boundary in the HAZ and connected to the carbide stringers present in the base material microstructure. They concluded that the formation of micro-cracks in multi-layer weld bead as well as in HAZ is highly unpredictable in these arc welding processes [11].

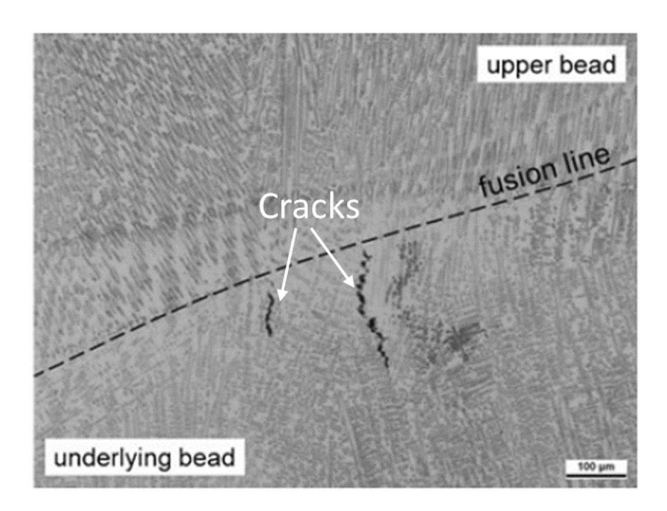


Figure 2.3. Micrograph showing weld metal liquation cracking [11]

Wenjie et al. found that extensive HAZ liquation cracks occur in fiber-laser weldments of Inconel 617 due to the constitutional liquation reaction between Cr,Mo-rich $M_{23}(C,B)_6$ carbides and γ matrix. They suggested to maintain either high heat input condition or induce preheating to reduce the liquation-cracking susceptibility by suppression of continuous grain boundary GB resolidified phase formation. Figure 2.4 shows the reduction of GB resolidified phase and total crack length with increment in heat-input as well as preheating temperature owing to reduction in liquid film thickness and inducement of low thermal stresses. Suppression of continuous grain boundary GB resolidified phase formation along with low

thermal stresses are found to be significant factors in reducing the liquation cracking susceptibility [12].

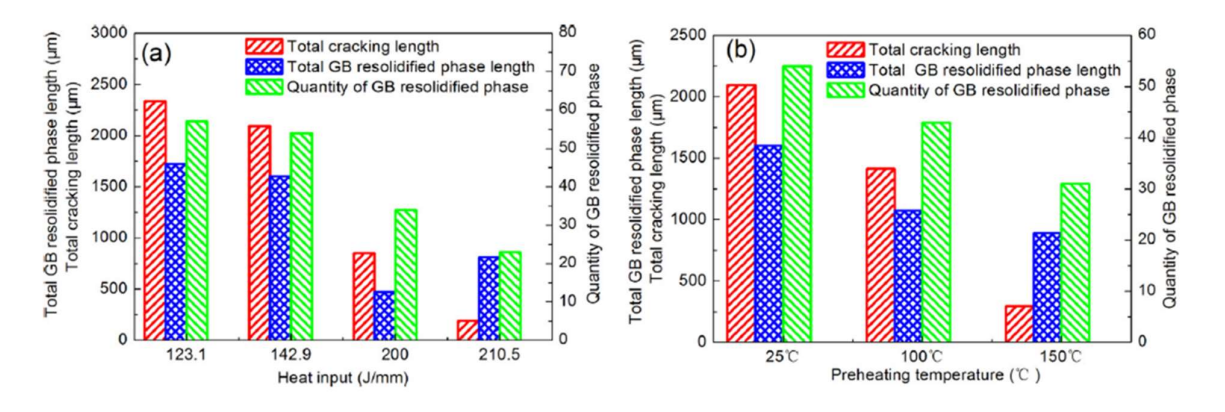


Figure 2.4. Variation of total GB resolidified phase and total crack length as a function of heat input and preheating temperature [12]

Few studies focused their studies on liquation cracking susceptibility during laser welding although for various other alloys. A study conducted by Osaba et al. on microstructural analysis of laser welded Haynes 282 superalloy in conjunction with Gleeble simulation of HAZ. Their research study indicated that increasing the heat input in laser welding results in increase in the depth of penetration, aspect (depth to width) ratio, areas of fusion and HAZ. However, this alloy was found to be susceptible to HAZ liquation cracking and that HAZ cracking is attributed to the degradation of hot ductility of the alloy due to the presence of subsolidus GB liquation which diminishes the ability to accommodate the weld thermal stresses. Figure 2.5a shows the typical micrographs showing HAZ cracks and these types of cracking were found to be decrease with increase in heat input as shown in Figure 2.5b [13].

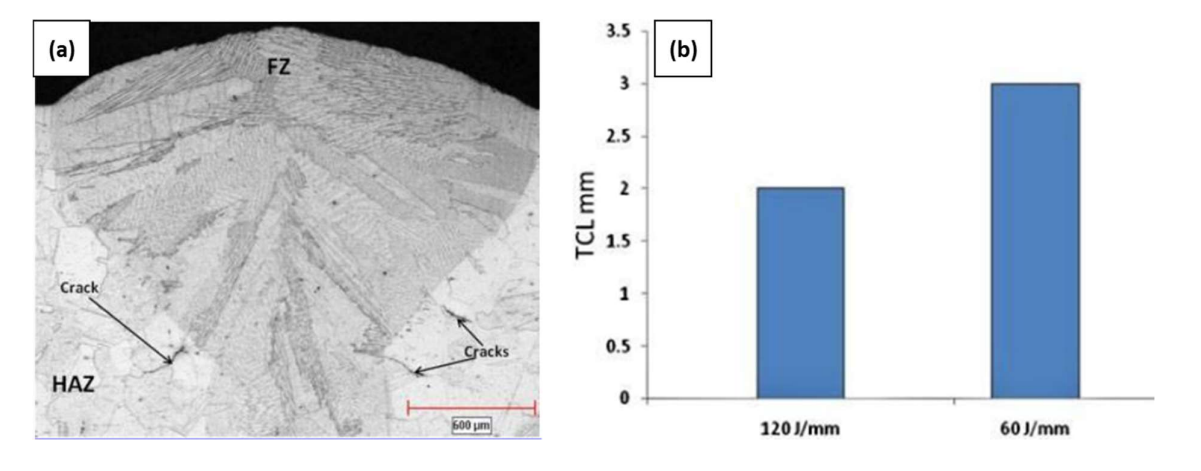


Figure 2.5. (a) Optical micrograph showing cracks in HAZ and (b) variation in total crack length with heat input [13]

Furthermore, Yan et al. investigated the influence of various heat input on liquation cracking susceptibility in HAZ during laser welding of GH909 superalloy. Their results indicated that susceptibility to liquation cracking was found to be increase with increase in the heat input (welding speed and laser power) as shown in Figure 2.6. The formation of such cracks in laser welded GH909 alloy was attributed to the coarsening of microstructure which deteriorates the hot ductility of this alloy and cause significant reduction in binding forces between the adjacent grains and formation of large tensile stress during weld cooling. The presence of cracks not only affect the hot-ductility of the alloy but also reduces the tensile strength of the material [14].

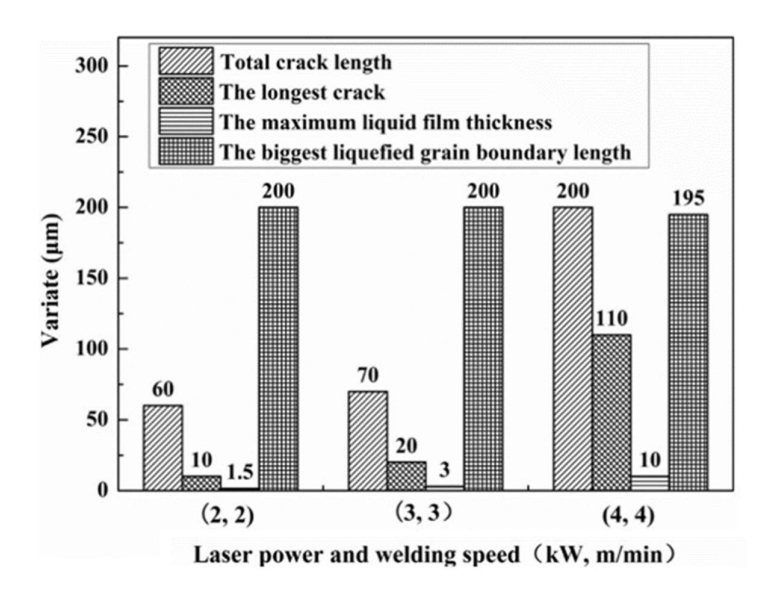


Figure 2.6. Effect of welding speed and laser power on cracking phenomena [14]

Although many reports on laser welding of Inconel 617 and various other superalloys, occurrence of liquation cracking at PMZ/HAZ was found to most common and also attributed to weld bead profile formation and their subsequent associated microstructural and stress changes. A study conducted by Luo et al. on thermal elastic-plastic behaviour of the laser welding of Ni-based superalloy by finite elemental analysis. They found that welding speed (heat input) and weld bead shape (radius of curvature at neck zone of nail-head type laser weld bead profile) has significant influence on occurrence of HAZ liquation cracking. They observed that at low welding speed (high heat input), liquation cracks in HAZ were minimized and attributed to the decrease in the elevated temperature plastic strain associated with effect of penetration shape i.e, radius of curvature [15].

Shinozaki et al. investigated the weldability of precipitation hardened Ni-based superalloy Inconel 718 more specifically the influence of weld bead cross-sectional profile on liquation cracking. They found that the weld bead cross-sectional shape changes according to the laser scanning speed and laser-power adopted. At scanning speed of 1.5 m/min or less and a laser power of 3 kW, the bead shape obtained was like a champagne glass shape, whereas at higher scanning speed in the range of 2-5 m/min the bead shape changes to nail head type. However, various weld defects such as underfills, porosity etc were observed in laser welded superalloy. They also observed that the liquation cracking in HAZ always occurs and mostly found in the neck zone of the weld bead cross-section. Their study indicated that the radius of curvature of the fusion boundary at neck zone in nail-head type laser-welded Inconel 718 influenced liquation cracking greatly and suggested that there exists a critical radius of curvature over which cracking can be effectively controlled [16].

Nishimoto et al. systematically examined the weldability of Inconel 718 alloy during laser welding and discussed the relationship between processing parameters, weld bead shapes and occurrence of weld defects. More importantly discussed the factors influence the HAZ liquation cracking susceptibility in this alloy. Their observations indicated that at scanning speed of 1.5 m/min or less and a laser power of 4.5 kW, the bead cross-sectional shape obtained was like a wine cup shape (type-W), whereas at higher scanning speed of 2.5 m/min the bead shape changes to nail head type (type-N) attributed to the interaction time. Underfill and porosity are predominant weld defects in laser welded superalloy and mostly found at high laser power and low scanning speed. They found HAZ liquation cracking being predominant at neck-like waist zone over the weld bead cross-section and closely related to the weld bead profile, more particularly degree of the waist at neck zone termed as radius of curvature. This type of cracking is attributed to the higher amount of GB liquation remained during weld cooling cycle and subsequent imposition of higher amount of tensile strain acted perpendicular to the grain boundary liquation region. Figure 2.7 indicated that the cumulative length of HAZ liquation cracking significantly increased with a decrease in radius of curvature. They concluded that the susceptibility to liquation cracking could be suppressed by increasing the radius of curvature and by refining the grain size and homogenization heat treatment. It is also interested to note from Figure 2.7 that the liquation cracking is predominant in nail head type (type-N) than compared to wine cup shape (type-W) [17]. It is also an indication that the shape of bead profile has significant influence on cracking susceptibility and nail head type generally obtained in most of the laser welds, whereas wine cup shape bead profile mostly formed in laser + arc hybrid weld. Thus, most of the studies identified that the hybrid welding is more beneficial in terms of resistance to liquation cracking susceptibility which will be discussed later in this chapter.

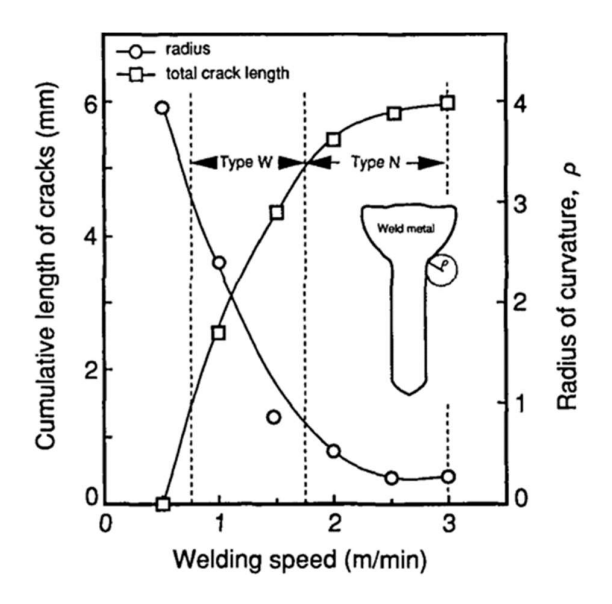


Figure 2.7. Relation between HAZ liquation cracks and radius of curvature at neck zone [17]

Further, to understand in detail the cause for HAZ liquation cracking in laser welded superalloy, an FEM analysis was conducted by Nishimoto et al. their study indicated that neck zone over the cross-sectional weld is more prone to heat accumulation than compared to top and bottom regions (Region 2 shown in schematic Figure 2.8). Susceptibility to HAZ liquation cracking was found to be more in region 2 (neck region) over the weld bead cross-section and attributed to the large liquation temperature width occurred on heating, thus longer time is required for cooling (different cooling rate than compare to other regions) under loading by high tensile plastic strain [18]. In recent times, Laser-Arc Hybrid welding has gained widespread importance for joining thick sections for various high temperature and high-pressure applications in comparison to multi-pass arc welding techniques due to its capability to produce welds with deeper penetration, low thermal distortion and minimal residual stress on account of high welding speed, low heat input, narrow weld bead and HAZ [19,20]. Few studies also reported on the liquation cracking susceptibility of the Ni-based superalloy using laser hybrid techniques.

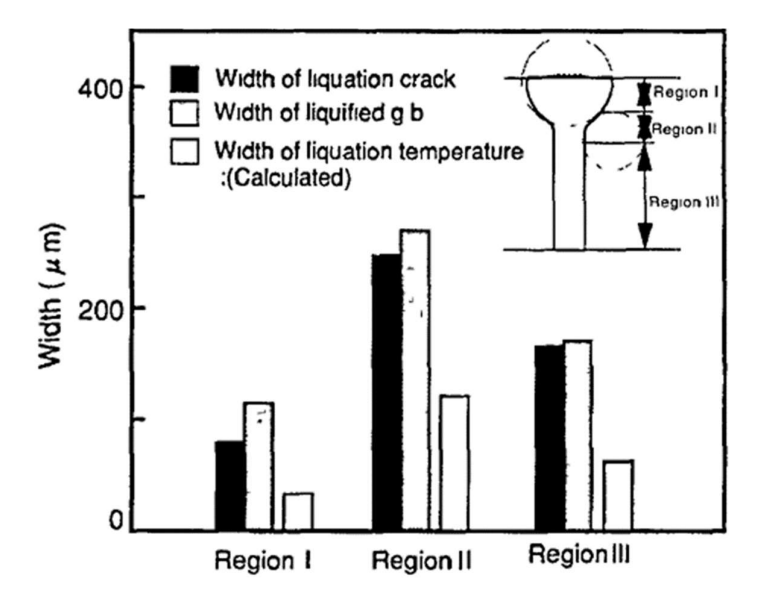


Figure 2.8. Variation of liquation cracks and liquated grain boundary in different regions of laser weld cross-sectional [18]

Z. Gao, in his numerical modelling study on laser and laser-hybrid welding of Ni-based superalloy, concluded that weld bead shape, especially at neck zone strongly influenced liquation cracking susceptibility. Figure 2.9 shows the influence of laser and laser hybrid welding processes on strain rate gradient in the vicinity to the fusion boundary for assessing liquation cracking susceptibility. He observed that the addition of arc heat source with laser in case of a hybrid process alters the temperature and strain rate distribution in the vicinity to the fusion line and the cooling rate will be much lower in case of Laser-GMA hybrid process than autogenous laser welding process. Their study concluded that laser-GMA hybrid welding process is beneficial over the autogenous laser welding process by minimizing HAZ liquation cracking susceptibility [21].

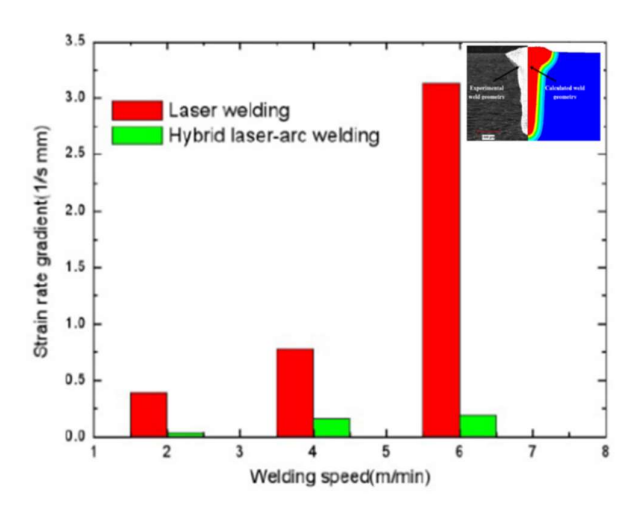


Figure 2.9. Variation in strain rate gradient as a function of welding speed [21]

Hu et al. utilized the laser as well as hybrid processes to weld high-strength aluminium alloys. They found vast number of solidification cracks in the weld FZ. Microscopic analysis of these cracks indicated that such type of cracks occurred in welds when the FZ was in the semi-solid state. Thermal cycles at various process conditions were systematically measured experimentally and co-related with thermo-mechanical modeling study, indicated that cracking phenomena is connected to the temperature distribution which causes transverse tensile strains to produce during cooling cycle. They concluded that, cracking susceptibility can be reduced by utilizing an additional heat source as in case of MIG addition to laser in hybrid welding process helps in altering the temperature distribution and thus reducing this cracking tendency [22].

Gebhardt et al. studied the laser-GMA hybrid welding of thick-walled tubes made of S460NH steel. Various experiments were designed and conducted by adopting the design of experiments methodology in order to investigate and optimize the welding process parameters on formation of hot cracks in the weldments. Their results indicated that hot cracking susceptibility found to be decreased with high levels of GMA power. However, cracking tendency enhances with increase in the laser power [23]. Moore et al. demonstrated the welding of various pipeline steels using autogenous laser and laser-arc hybrid welding processes. They found that, it is possible to improve the microstructural and mechanical performance of the weldments by utilizing the metal-cored filler material in laser-arc hybrid welding process at an optimized welding parameters and joint geometry in place of laser welding alone. Moreover, rapid cooling and subsequent formation of solidification cracks during autogenous laser welding can be resolved by using a hybrid welding process [24]. However, attempts were tried to reduce weld cracking susceptibility by controlling heat-input during welding, employing additional preheating and modification of filler-material. Complete understanding in terms of identification of low melting eutectic (LME) and their mechanical behavior is still inadequate with experimental validation, more specifically, influenced by low heat input welding processes.

2.2 Thick-Sections Welding

Zhang et al. investigated the deep-penetration autogenous laser welding of thick section stainless steel materials using fiber laser. Their results indicated that, focal point position is a main parameter for deep penetration autogenous laser welding of thick sections and they concluded that the focal point position must be inside the specimen surface coupled with optimized welding speed for obtaining good full penetration welds. However, at inadequate welding parameters, the resultant weld bead obtained with deep underfill and huge root hump defects as shown in Figure 2.10 [25].

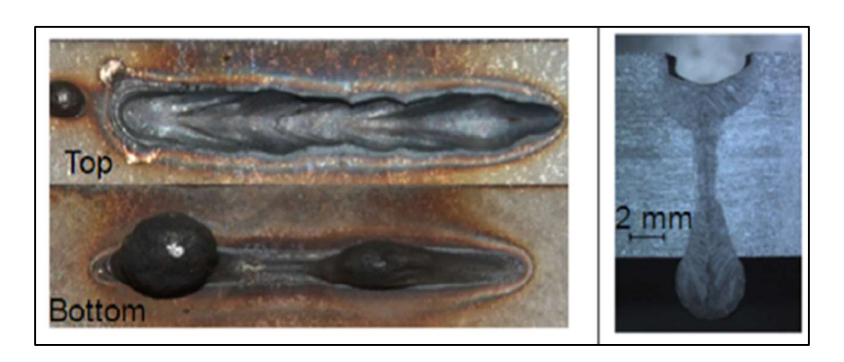


Figure 2.10. Deep-penetration laser weld top and bottom bead along with weld cross-sectional showing huge underfill and root hump defects [25]

Another study by same authors Zhang et al. studied the mechanism of underfill defects formation during laser welding of thick sections. They observed that, high-speed downward flow of molten metal accompanied with high recoil pressure and localized vaporization decisively resulted in occurrence of surface underfill and root hump defects. Once the melt pool is fully penetrated, the molten metal in the bottom melt pool flows rearward i.e., opposite to the welding direction and accumulates significantly at the bottom surface resulting in droplet formation. When this molten droplet achieve significant volume may begin to sag due to gravity and grows continuously. Thus, droplets of mass solidified in the form of hump at the bottom surface of weld processed with inadequate welding parameters [26].

A study conducted by S. Li et al. on relation between formation of spatters and dynamic melt pool behavior under various process parametric conditions while deep-penetration high-power laser welding of SUS 304 stainless steel. Their research study indicated that an increase in the laser power causes significant increase in the formation of spatters as a result of intense vaporization. However, the focal point position is the key to control the welding defects such as underfill, undercuts, spatters and porosity. They obtained sound weld joint when the focal point position was inside the base metal [27]. Another study by Kawahito et al. on fiber laser welding of stainless steels 304, identified that the weld bead profile depicts a keyhole penetration in all adoptable welding speed ranges from 0.6 – 10 m/min, and the depth of penetration was shallower with increase in the welding speed. However, some welding defects

were found at lower welding speeds, whereas huge underfills with spatters were observed at higher welding speeds. Formation of surface underfill cause by the inadequate welding speed and attributed to the metal ejection from the molten weld pool during high-power thick-sections laser welding [28,29].

Another study conducted by Guo et al. carried out on comparison between flat and horizontal laser welding position of thick sections made of S700 high strength steels. Their study identified that several weld defects including lack of penetration, underfill/undercuts, and root sagging are most common during single-pass autogenous laser welding of thick sections in flat position and are attributed to the gravity-induced fluid flow towards the root side of the weld joint. However, by employing horizontal position during laser welding, appropriate balance between surface tension forces, gravity pressure (hydrostatic) and recoil-pressure due to intense vaporization can be maintained and thus can mitigate the formation of undercuts and root sagging [30].

Furthermore, a study conducted by Matsumoto et al. on influence of laser focusing properties and various other welding parameters on deep penetration laser welding of high strength steel. In their study, they adopted two different optical systems with different power density distributions and focal depths (2 mm and 4 mm) to carry out the deep penetration welding. They obtained sound weld joints by employing a 4 mm focal depth optical system at lower scanning speed of 25 – 50 mm/s and attributed to the stable keyhole without large fluctuations and bubbles formation in the keyhole as observed by high-speed video camera. However, some welding defects like surface underfill and root hump were obtained in shorter focal depth optical system and attributed to the fluctuation of laser keyhole [31]. It can infer from the literature review that it is more challenging to obtain a satisfactory weld with no underfill and root hump defects especially in highly viscous thick-sectioned Inconel 617 alloy wherein deep penetration required with single pass.

2.3 Recent developments on welding techniques for Inconel 617 superalloy material

2.3.1 Arc welding processes:

Few studies reported on welding of Inconel 617 superalloy employing various arc welding processes. Fink et al. have joined 12-mm thick Inconel 617 alloy plates by employing reduced heat input modified dip arc welding processes such as cold metal transfer (CMT) and

pulsed-mix processes and compared with conventional pulsed-arc welding processes in terms of metallurgical and mechanical aspects. The results showed that modified dip arc welding processes reduced 30 - 50 % production time with retention of good bead appearance and comparable mechanical properties to that of conventional pulsed arc welding methods as shown in Figure 2.11a. However precise positioning of the filler wire during welding of first layer must be properly controlled to avoid lack-of-fusion defects. 14 weld passes were utilized to complete 12-mm thick Inconel 617 alloy plates by employing these processes. Figure 2.11b shows the typical weld bead cross-section obtained by CMT process.

Fusion zone microstructure constitutes completely of austenitic dendritic structure with random distribution of secondary precipitates. However, slightly finer dendritic microstructure was observed in modified dip arc weldments owing to higher cooling rates associated with reduced heat input. Moreover, HAZ for all weldments were characterized by the dissolution of carbides as a result of rapid heating during welding process. Modified dip arc weldments exhibited a finer HAZ as compared to pulsed-arc weldments and attributed to the high heat input. Moreover, weld tensile and impact properties of the modified dip arc welds are comparable to pulsed arc weldments [11].

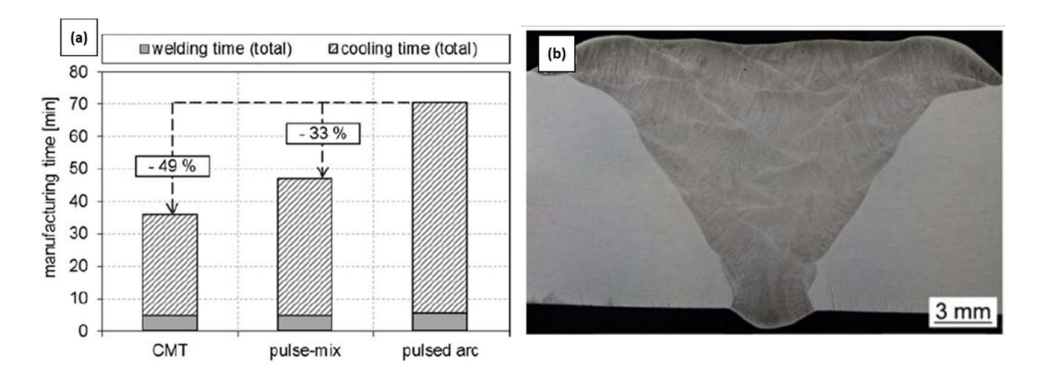


Figure 2.11. (a) Graph showing manufacturing time for CMT, pulse-mix and pulse arc processes and (b) Optical macrograph of CMT welded joint [11]

Farahani et al. welded Inconel 617 alloy by using continuous current (CC-GTAW) and pulsed current GTAW (PC-GTAW) processes. Total three weld passes were utilized to complete 11-mm thick Inconel 617 alloy plates by employing these welding processes. Figure 2.12 depicts the photographs of two weld beads produced by CC-GTAW and PC-GTAW processes. It indicates that the welds produced by PC-GTAW process constitutes of smaller fusion zone and HAZ as compared to CC-GTAW process owing to lower heat input of the process and pulsed current effects. Fusion zone microstructure consisted of larger columnar

grains with dendritic structure and wider spacing between dendrites in CC-GTAW welded specimen as compared to finer dendritic spacing in PC-GTAW welded specimen. HAZ for both weldments were characterized by the dissolution of carbides and grain growth. However, grain refinement occurred in fusion zone of PC-GTAW welded specimen and results in superior mechanical properties (tensile and impact) owing to lower heat input and subsequent faster cooling rates as compared to CC-GTAW [32,33].

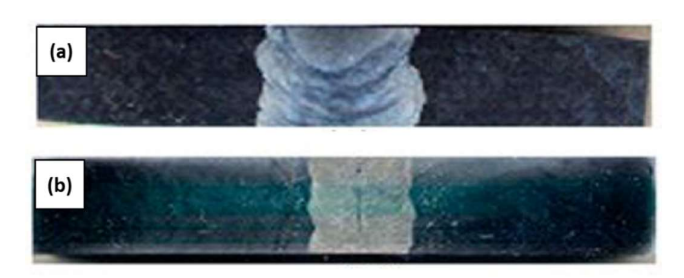


Figure 2.12. Welded samples (a) Continuous current and (b) Pulsed current GTAW [33]

Park et al. joint Inconel 617 alloy by using conventional TIG welding process. Total eight weld passes were utilized to complete 12-mm thick Inconel 617 alloy plates by employing this welding process. Sound weld joint were obtained at an optimized welding conditions and parameters. HAZ of alloy 617 weldments did not show any obvious variation in microstructure and composition as compared to substrate. However, weld metal showed coarse grain microstructure as compared to substrate and HAZ. Fusion zone microstructure consisted of dendritic structure with major constituents such as Ni, Cr, Co and Mo dispersed in the matrix. Further, tensile and bend strength conducted at RT and at 700°C of the weldments indicated 10 – 11% reduction in tensile and bend strength of the welds at 700°C as compared to room temperature [34].

Moreover, Mageshkumar et al. examined the microstructural features and mechanical performance of the pulsed current gas tungsten arc welded (PC-GTAW) Inconel 617 alloy weldments. Total four weld passes were utilized to complete 5-mm thick Inconel 617 alloy plates by using PC-GTAW welding process. Macrostructural analysis confirmed that the sound weld joint was obtained at an optimized welding conditions and parameters of PC-GTAW process. Further, microstructural analysis of weld fusion zone indicated that the FZ microstructure constitutes of fine columnar dendritic structure and presence of fine equiaxed dendrites were also seen. There is also evidence of migrated grain boundaries in the fusion zone owing to solute distribution during weld solidification due to multi-pass welding. Cr-rich M23C6 and Mo-rich M6C carbides were observed in the interdendritic sites of the FZ

microstructure. However, there were no unmixed zone was observed at the weld interface and attributed to the similar composition and melting point of base and filler metals. They observed superior weld joint strength as compared to substrate material and the bend test of the weldments revealed defect free welds obtained by pulsed current GTAW process [35].

Furthermore, Liu et al. studied the microstructural features and mechanical performance of the conventional TIG welded Inconel 617 alloy joint. The results showed that the weld metal constitutes of fully austenite with a dendritic morphology with obvious growth direction and carbide precipitates dispersed in the fusion zone matrix. Elemental analysis indicated that weld zone has significant local depletion of Ni and Co in the vicinity to the solidification and sub-solidification grain boundaries. Microhardness and tensile test at high temperature of base and weld metal indicated that weld metal has slightly higher hardness than compared to base metal and attributed to the strengthening effect of sub-solidification grain boundaries and observed that maximum tensile strength of weldments at high temperature are close to substrate material. Further, the fracture position of the tensile test specimen was found to be in the center of the weld metal owing to grain boundary failure [36].

Shanlin Li et al. investigated room and high temperature mechanical properties of multi-layer Narrow gap-TIG welded Inconel 617B. Furthermore, thermal simulation of the HAZ was conducted to explain the behavior of M₂₃C₆ carbides during welding operation. They observed slight softening of HAZ region owing to microstructural variation due to eutectic formation and weakening of strengthening mechanism caused by welding process. Figure 2.13 shows the room and high temperature tensile properties of base and welded Inconel 617 alloy at various temperatures. Y.S and UTS of both weld and base metal was found to be decreased with increase in temperature. Y.S of the welded joint at room temperature is superior to the base metal, however, UTS of the welded joint is found to be less compare to base metal [9].

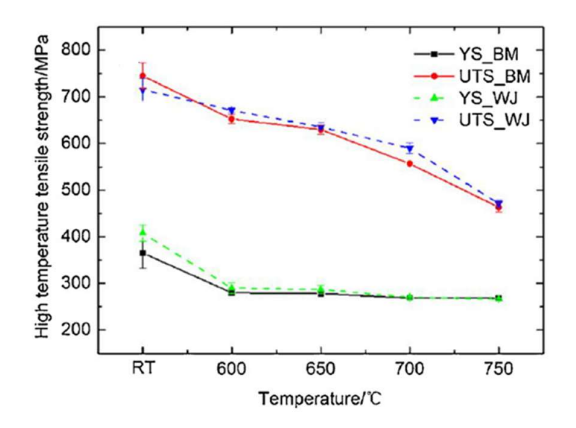


Figure 2.13. Room and high temperature tensile properties of base and welded Inconel 617 alloy [9]

Furthermore, Xiaogang Li et al. investigated fracture toughness of the narrow-gap TIG weldments of Inconel 617B at 700° C temperature for AUSC boiler applications. They found that the fracture toughness of the base metal and HAZ was found to be higher as compared to weld metal of NG-TIG welded Inconel 617B alloy. The higher fracture toughness is attributed to the presence of vast quantity of annealing twins (Σ 3 boundaries) coupled with lots of coincidence site lattice (CSL) boundaries inside grains causes less serious strain localization in base metal and HAZ [37].

A study conducted by Yuan Gao el al. on investigation of fracture toughness of NG-TIG welded Inconel 617 alloy at room temperature as well as high temperatures at 650°C, 700°C and 750°C. Research work identified that the fracture toughness of the weld lower than that of substrate material owing to coarse columnar dendritic microstructure, misorientation differences and the precipitated phases. However, at higher temperature both weld and base metal showed similar fracture toughness values and attributed to the decreased in the weld joint strength. Although, weld metal possesses lower fracture toughness, but still weld metal showed interestingly stable microstructure at elevated temperature as compared to substrate material. It is due to the grain boundary weakening and precipitated phases fractured at elevated temperature in substrate material [38].

Kim et al. studied the tensile and creep properties of GTAW welded Inconel 617 alloy at elevated temperature. Their results indicated that the weld metal has superior YS, but lower UTS and % elongation as compared to substrate material at RT. However, at temperature of 800°C, the YS and UTS of base and weld metal are approximately similar. Weld metal showed a longer creep rupture life but lower creep rate and rupture ductility than that of substrate material. However, at higher exposure time of 36,800h, the creep life of Inconel 617 weldments was similar to that of base [39]. Furthermore, B. J. Kim et al. utilized small punch creep test for evaluating creep behaviour at 700°C of Inconel 617 alloy TIG weldments for future AUSC boiler applications. To identify the creep properties of the weakest portion in Inconel 617 alloy weldments, test specimen of small sizes extracted from cross-weldments as shown in Figure 2.14 from weld, HAZ and substrate base metal. They found that the among weld, HAZ and base metal, HAZ was the weakest portion of the weldments by showing shortest rupture life

and attributed to the transition of the microstructure at the interface boundary causing premature failure of this region [40].

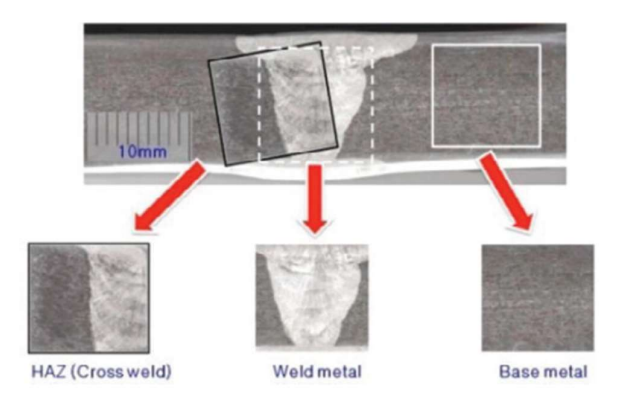


Figure 2.14. Small punch creep test specimens extracted from Inconel 617 TIG weldments [40]

Totemeier et al. studied the creep-fatigue interaction of GTAW Inconel 617 alloy weldments and base metal at elevated temperatures. They found that Creep-Fatigue lives were decreased with increase in holding time for both weld and base metals, however Inconel 617 weldments lives were found to be significantly low as compared to that of substrate material. Cracks were found to be in the fusion zone which followed interdendritic paths in case of cross-sectional weldments constitutes of fusion, HAZ and unaffected base metal [41].

2.3.2 Laser-based welding processes

Few studies were reported on welding of Inconel 617 alloy by utilizing laser-based welding processes. Wenjie et al. conducted a comparative study on fiber and CO₂ laser welding of 5-mm thick Inconel 617 alloy plates. Results indicated that the heat input required to obtain full penetrating welds is relatively lower in fiber laser welding than with CO₂ laser welding. Weld bead shape in fiber laser welding changed from Y to I shape with reduction in heat input, whereas no apparent change in shape of bead profile was observed in CO₂ laser welded joints as shown in Figure 2.15. Fusion zone microstructure of all welds depicts the columnar dendrites grown perpendicular to the fusion boundary due to the direction of heat flow. Alloying elements like Cr, Mo and Ti etc were segregated into the interdendritic regions in both welding processes with highest being in CO₂ laser as compared to fiber laser welds [42].

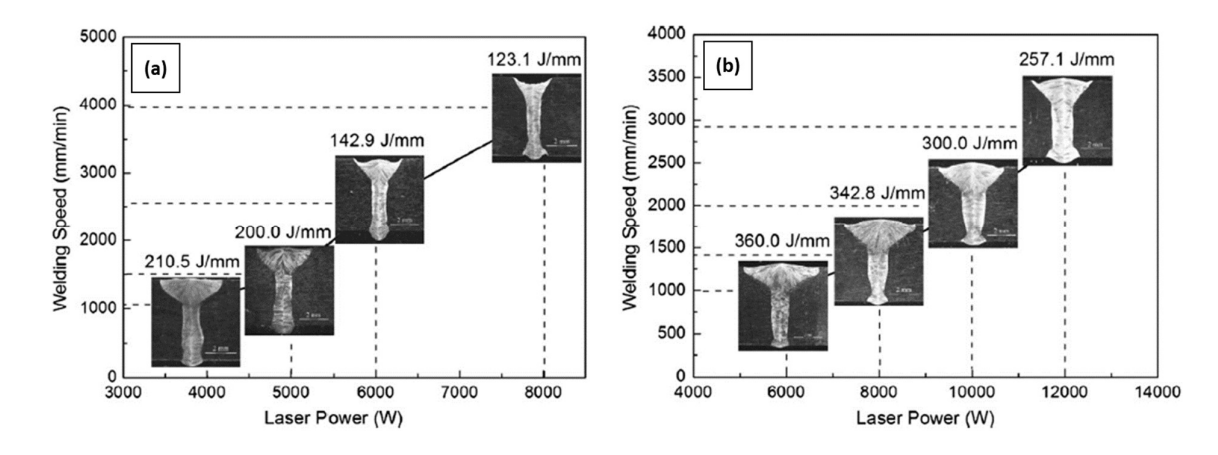


Figure 2.15. Variation in weld bead profile with heat input in (a) Fiber and (b) CO₂ laser welding of Inconel 617 alloy [42]

Adamiec et al. examined the microstructural features and mechanical performance of laser welded 3-mm thick Inconel 617 superalloy plates. They found that continuous weld bead with defect free welds could obtained at an optimized processing parameters of laser power and transverse welding speed. However, inappropriate increase in the laser power causes excess insignificant penetration in the welds. Hardness of the laser welded fusion zone were higher as compared to that of substrate material and attributed to the fast-cooling rate associated with laser heating cycle [43].

Cheng et al. investigated the welding position on weld quality of laser welded Inconel 617 alloy. The research results indicated that, the welding position had significant influence on quality of welds in terms of porosity formation and subsequent mechanical properties when high heat input was employed. However, keyhole-induced porosity are predominant welding defects in horizontal and vertical-down position welds and are the causes for the reduction in tensile properties of the weldments as compared to other welding positions [44]. Furthermore, Wenjie et al. investigated the nucleation of liquation cracks in fiber laser-welded Inconel 617 alloy under various heat input and pre-heating conditions as explained previously in section 2.3 [12]. In recent study conducted by Wenjie Ren et al. on effect of thermal exposure upto 7000 hours at 750° C on microstructural characteristics and mechanical performance of Inconel 617 superalloy laser weldments. They found that various secondary carbides such as M_{23} C6 and M_{6} C, Ti (C,N), TCP (topologically close phase) μ phase and γ precipitate phase (Ni₃Al) were presents in the Inconel 617 laser welds after thermal exposure at 750° C. Further, volume fraction of M_{23} C6 and M_{6} C carbides as well as γ precipitate phase after 7000 hours exposure

caused significant increase in the hardness and reduction of impact toughness of the Inconel 617 alloy weldments [45].

Few studies focused their studies on individual and comparative study between Laser, and Laser hybrid welding processes although for various alloys. In recent study conducted by Palanivel et al. studied microstructural features and mechanical performance of Incoloy 800 superalloy during laser welding. They observed that weld bead profile significantly influenced by the laser scanning speed and hourglass-shaped weld profile with slight wider width at top obtained at optimal process condition during laser welding of superalloy. Columnar dendritic structure with coarse austenitic grains was observed in the weld fusion zone that grown perpendicular to weld line during solidification. Equiaxed dendrites were observe in the weld center more predominantly in higher welding speed welds. HAZ region did not show any obvious grain size as compared to base metal, however, significant phase changes were observed in HAZ. EBSD analysis indicated that austenitic grain size decreases with increase in the welding speed. A 99 % of joint efficiency was obtained in laser welding of Incoloy 800 [46].

Zhang et al. systematically investigated the weldability of the laser welded GH909 superalloy under different welding speeds and laser powers. Their study indicated that the bead profile in laser welded GH909 superalloy was transformed from Y-shape to hourglass-shape and again to Y-shape bead profile under low laser power and welding speed or high types. This is attributed to the increased power density which causes heat adsorption and thus increased melting area [47]. Jaing et al. investigated the fiber laser welding of solid solution strengthened Ni-based superalloy GH3535 under continuous and pulsed wave mode of welding. They found that large number of porosities were observed in the bottom of the continuous wave welded joint as compared to pulsed wave. Although, the fusion zone of both welds was constituting of γ-Ni matrix and M₆C carbides dispersed in the matrix, but grain size of the pulsed wave was found to be significantly low as compared to continuous wave welds. Further, the presence of large number of pores in continuous wave welds caused significant reduction in tensile strength [48].

Alcock et al. examined the feasibility of high-power diode laser for deep penetration laser welding of 10-mm thick SS 304L thick plates. Results indicated that the full penetration was achieved in butt joint configuration at an optimized processing parameter. They demonstrated that high power diode laser is capable of welding thick plates in keyhole mode

and the joint properties obtained are comparable to other high power density laser-based welding processes [49]. Malchus et al. utilized high power diode laser for welding 13-mm thick L485MB steel plates in butt-joint configuration. Homogenous weld bead without any fusion zone cracks entailed successful welding of thick joints with vertical edge offsets up to 3 mm. Compared to other laser systems, high power diode laser with wider spot size provides advantages for high gap-bridgeability and leverage in precision fit-up requirements [50].

Nobuyuki Abe et al. successfully used high-power density diode laser for welding SUS 304 stainless steel plates of thickness ranging from a minimum 0.15 mm to a maximum of 10 mm. Results indicated that full penetration in 10-mm thick plates was achieved without cracks and pores at an optimized process parameters by employing top-hat shape intensity distribution beam of diode laser. It was found that the weld quality obtained by this process are on par to the joints produced with high power CO₂ and Nd:YAG lasers [51]. Cao et al. successfully demonstrated the laser-arc hybrid welding for joining thick sections of HSLA steels. Their results indicated that full penetration welds were obtained in single pass using laser hybrid welding techniques at an optimized groove design, geometry and processing parameters. They found that addition of MAG arc to the laser results in wider and deeper weld beads with improved penetration depth and gap tolerance. Laser-leading hybrid welding process produced higher quality welds due to presence of less underfill and porosities defects as compared to Arc-leading hybrid method. On comparing the multi-pass MIG welds with single-pass hybrid welds, the laser-leading hybrid process produced welds with low distortion [52].

Roepke et al. investigated the influence of laser power, GMAW arc power, and distance between laser and arc on weld characteristics during hybrid welding of DH36 and EH36 steels. Their study indicated that full joint penetration with uniform fusion zone characteristics in top and bottom regions were obtained at an optimized process parameters regardless of the laser power adopted. However, decrease in the distance between the gap of laser and arc heat sources results in increased the total penetration [53]. Frostevarg et al. investigated the various types of undercuts formation during laser, arc and hybrid welding processes. They found that curved, rounded bottom and centre line are the basic three types of undercuts can form during laser bead welding, whereas single or double sided curved and crack like or micro flaw undercuts could be realized in GMAW. However, total six different types of undercuts can be formed during laser-arc hybrid welding process due to addition of two heat sources. In this study, they optimized the hybrid welding process parameters and conditions to obtain an undercut free weld [54]. Gao et al. demonstrated the laser-MIG hybrid welding of mild steel under various

process conditions. They found that laser-MIG hybrid welds are composed of two distinct regions; upper wider zone and narrower nether zone, which are similar to arc and laser zones. Microstructural and hardness distribution analysis of these zones indicated that elemental distribution and microhardness varied in these two zones as a result of differences in their cooling rates. As a result, laser zone has smaller HAZ, finer grain size, low segregation and higher hardness of laser fusion zone as compared to arc zone [55].

Guoxiang et al. investigated the comparative residual stress study on 12-mm thick ultragrained steel components in single-pass hybrid and multi-pass GMAW by employing finite element analysis. The hybrid weld was developed by combining the Laser and GMAW arc heat sources in which Laser beam and GMAW arc were modeled by using a conical and double-ellipsoidal body heat sources respectively. Study indicated that the weld distortion and magnitude of residual stresses in hybrid welds are much smaller than compared to multi-pass GMAW processes as a result of low heat input [56]. Pan et al. studied the effect of laser power, weld transverse speed and root gap during hybrid welding of thick sections high strength steel plates on depth of penetration, weld geometry and welding defects. Results indicated that occurrence of weld defects such as underfill/undercuts, root humps can be avoided during hybrid welding of thick-sections by proper implementation of process parameters [57].

2.4 Recently developed narrow-gap multi-pass laser welding methodology

Moon et al. (US4527040) patented a laser welding method that entails weld joints applicable to navy for improved fracture toughness. The novelty of the disclosure lies in utilizing ad additional through-thickness insert between the parts with fusion by 15-kW CO₂ laser beam [58]. Tsukamoto et al. (US8481885B2) disclosed a novel laser welding method in which a narrow groove design was implemented with simultaneous melting of solid filler material along with metallic parts under controlled laser heat input, appropriate alignment of laser spot to filler interaction position and shielding atmospheric conditions [59]. Milewski et al. developed a unique multipass narrow gap laser welding method with addition of filler wire for joining thick sections with moderate laser powers (material). The developed welding method obviated the need of costlier high-power lasers and the leavay in fit up requirements [60]. In 2014, a further improved laser welding method disclosed (CN103801833A) adopting a positive defocusing fiber laser beam under conductive mode to successfully producing weld joints in thick metallic sections (up to 60 mm) in which laser beam irradiated (multi-layer) in the bottom and sidewall of the narrow groove to form a molten pool in a thermal conductive

welding mode. Subsequently, the filler wire is fed into the molten pool resulting in melting of wire and the gap filled to effectively form a sound weld joint. Indeed, defects generally prone in thick-section welding such as sidewall fusion, porosity, undercuts etc. were positively handled to produce defect-free weldments [61].

In another patented work (JP6255314B2), a specific double groove design, both at opening upper side as well as bottom root, in the metallic plates with multi-pass/multi-layer welding with edge and design-configuration preparation concurrently for thicknesses up to 30 mm employing multiple laser beams of appropriate input and processing conditions. Although, these disclosed laser welding methods successfully welded thick-metallic materials, additional specific fabrication methods with design of groove and edge preparation, simultaneous feeding of filler during welding, utilization of multiple laser beams and multi-layer/multi-pass welding add to the cost of capital investment, cumbersome edge preparation with design of welding method and precision in control of heat input and fit ups [62]. In another recently disclosed invention (CN112570888A), a comprehensive laser welding system with integration of laser welding tool to a workstation with magnetic fixturing setup was utilized for fabricating large sized metallic structural parts [63].

Notwithstanding the above-mentioned inventions, few published works are also available in literature employing multi-pass narrow-gap (MP-NG) laser welding technique for joining thick-sections of Ni-based superalloy. Junhao et al. welded thick Inconel 617 alloy plates by using a MP-NG laser welding technique. 5 weld passes were utilized to complete the 11-mm thick Inconel 617 alloy plates by this technique as shown in macrographs of Figure 2.16a. The research results indicated that superior mechanical properties with reduced heat input, number of filling passes and filler metal consumption obtained by multi-pass narrow-gap technique as compared to other multi-pass arc welding processes. However, precise control of the distance between the filler wire and laser beam spot is necessary, to avoid lack of fusion and porosity during V-shaped filling pass (shown in Figure 2.16b) [64].

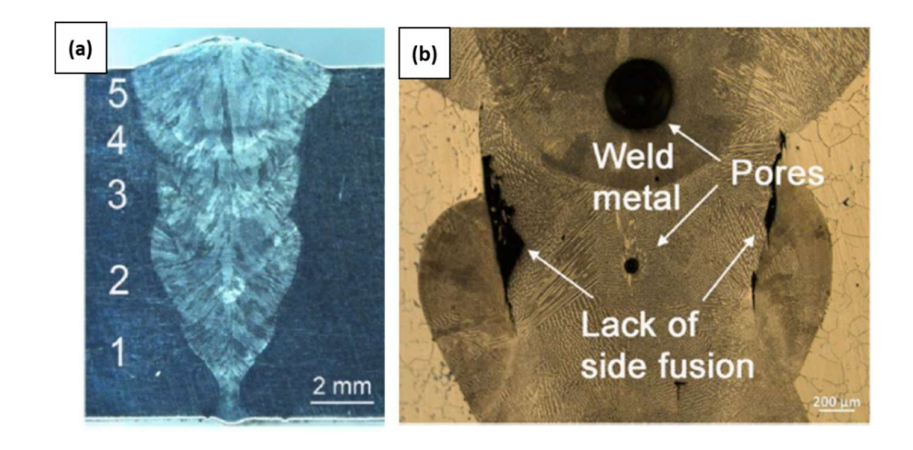


Figure 2.16. (a) Multi-pass narrow-gap laser weld joint and (b) Defects in Y-shaped weld bead [64]

Kessler et al. demonstrated welding of 140-mm thick Inconel 617 alloy pipe by utilizing a MP-NG laser welding technique with very low laser power and energy per unit length. Figure 2.17a depicts the weld seam of 140-mm thick Inconel 617 alloy pipe produced by Laser multipass narrow gap technique. Results showed that this technique are capable of producing welds of 140 mm wall thickness pipes free from cracks and bonding defects with reduced heat input and porosity at an optimal condition. Furthermore, lack of fusion defects was also found to be reduced and the weld fusion and HAZ showed not much variation in alloying elements as a result enhanced high temperature properties of the weldments. Further, magnified micrograph of the weld interface constitutes of weld and HAZ along with EBSD analysis shown in Figure 2.17b indicated proper bonding at the interface [65].

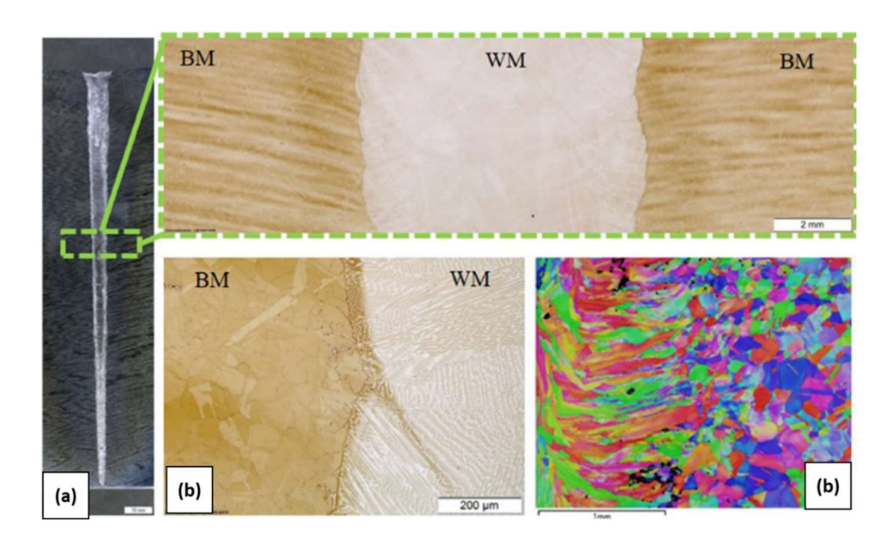


Figure 2.17. (a) Laser multi-pass narrow gap of 140-mm thick Inconel 617 alloy pipe, (b) magnified view of weld interface and (c) EBSD analysis [65]

Zhang et al. investigated the welding of 50-mm thick SUS316L ASS plates using narrow-gap laser welding methodology. They found that the solidification cracks in fusion zone could be reduced by controlling the alloying element of the filler wire, thus, by controlling the ferrite content of the weld fusion zone in an appropriate range. Further, the maximum tensile stress of the narrow gap laser weldments was found to be significantly as compared to conventional TIG weldments [66]. Zhao et al. successfully utilized the MP-NG laser welding method to weld HSLA low alloy thick steel plates under different process conditions such as laser power, scanning speed and wire feed rate. Their study indicated that defect free welds can be obtained under optimized processing parameters by employing narrow-gap multi-pass laser welding technique [67].

Guo et al. systematically investigated the interactions of process parameters such as welding speed, laser power and wire feed rate during MP-NG laser welding of high strength steels. Their study indicated that at an optimized process parameter, a 8-mm thick plates can be weld by two filling passes, whereas 13-mm thick plated can be welded by three filling passes. Further, tensile strength of the weldment produced by this technique is found to be similar to that of substrate material [68]. Yu et al. studied the welding of 17-mm low-carbon steel plates using narrow-gap laser welding methodology. They observed that the groove design has significant role in determining the quality of welds during MP-NG laser welding. When the laser beam and filler wire can approach smoothly to the root of the groove, by employing a small groove design and size helps in reducing the filler material consumption as well as reduce the filler wire deflection in the narrow gap. This helps in improving the fusion of the complete groove and reduce lack of side-wall fusion defects [69].

2.5 Hot corrosion behavior of superalloy materials

As high temperature corrosion is one significant issue associated with the boiler tubes during operation of thermal power plant. It is due to the combined effect of coal-ash and flue gas environment encountered in thermal power plant boilers which causes premature failure of the boiler components. Few studies reported on high-temperature corrosion behaviour of Inconel 617 alloy in various environment. Hari et al. conducted a comparative study on alloy 617 OCC material between air and synthetic coal-ash environment simulated in laboratory at a temperature of 700°C. In their study, laboratory simulation was done by coating the Inconel alloy specimens with synthetic salt constitutes of 5% Na₂SO₄, 5% K₂SO₄, 30% Fe₂O₃, 30% Al₂O₃ and 30% SiO₂. Additionally, high temperature oxidation test also conducted at same

temperature in air environment for comparative study purpose. These samples were exposed for total time of 5000 hours with thermal cycling at each 500 hours of exposure time. Further, change in weight was monitored after each thermal cycle of 500 hours to understand the corrosion kinetics. Their results indicated that, corrosion product formed after exposed to air during oxidation test over the entire exposure time range was found to be Cr₂O₃ completely. However, various other corrosion products form in addition to Cr₂O₃ such as Fe₂O₃ and spinel oxide – NiCr₂O₄ during exposed to salt environment. No significant change in weight was observed after oxidation test owing to the presence of protective Cr₂O₃ layer, however, change in weight was significant in case of coal-ash (salt) environment caused due to the reaction of Cr₂O₃ with Ni-content and formed spinel oxide phase NiCr₂O₄. Thus, it indicated that the corrosion rate enhanced for synthetic coal-ash environment as compared to air environment [70].

Hari et al. conducted comprehensive comparative study between synthetic salt mixture environment and synthetic salt mixture + flue gas environment simulated at laboratory on Nibased superalloy 617. Laboratory simulation was done by coating the Inconel alloy specimens with synthetic salt constitutes of Na₂SO₄, K₂SO₄, Fe₂O₃, Al₂O₃ and SiO₂ and exposed it to the flowing gas mixture constitutes of 15% CO₂, 3.5% O₂, 0.25% SO₂ and the rest N₂ (Vol%) at a temperature of 700 °C. Additionally, high temperature corrosion test also carried out at same temperature and salt coated condition but without gas mixture for comparison purpose. They found that the SO₂ content present in the flue gas in case of salt + flue gas environment plays a dominant role and accelerated the corrosion rate due to sulfidation both internally and externally. Cr contents exist in the alloy reacts with the S-containing species in the salt + flue gas environment and leads to form chromium sulfide [71].

Aung et al. investigated high temperature corrosion behavior of Inconel 740 alloy in a synthetic coal-ash environment at various temperatures of 700, 750 and 800° C. Their study indicated that rate of corrosion increases with increase in exposure temperature specially at 750° C and above temperatures. High tendency to form TiS contents in the internal sulfidation stage in the alloy during high temperature caused significant enhance the hot corrosion both internally and externally [72]. Stein-Brzozowska et al. systematically investigated the hot corrosion behavior of various Ni-based superalloy including Alloy 263, Inconel 617 and Inconel 740 at a temperature range of $640 - 760^{\circ}$ C and with an exposure time of 1000 hours. In laboratory furnace, they found that sulphur-containing species induced hot corrosion on Inconel 617 alloy after 1000 hours of exposure. It is due to the presence of highest Molybdenum

and lowest Titanium contents Inconel 617 alloy as compared to alloy 263 and 740. However, during power plant exposures, all these three superalloys reveal similar corrosion rates [73]. El-Awadi et al. systematically examined the high temperature corrosion behavior of two different superalloys such as Inconel 617 and 738 at different exposure temperatures of 700, 800 and 900°C with an exposure time of 100 hours. Corrosive media was utilized in their study was the mixture of Nacl and Na₂SO₄ which were sprayed on the test specimens prior to testing. They found that the corrosion process was endothermic and increased spontaneously with increase in temperature in both the alloys. However, various other corrosion products form in addition to Cr₂O₃ such as spinel oxides of NiCr₂O₄ and CoCr₂O₄ during exposed to salt environment [74].

Furthermore, Naghiyan et al. investigated the high temperature corrosion behavior of Ni-based superalloy Inconel 738 substrate coated with Inconel 625 produced by Nd:YAG laser and TIG cladding techniques. The high temperature corrosion test was conducted at 900°C for 36 hours by exposing the specimens to salt mixture constitutes of Na₂SO₄-60wt%V₂O₅. Microstructural analysis of the exposed specimens revealed a series of cracks present both on the surface as well as at substrate-coating interface of cladded specimens produced by TIG method. However, no such cracks and pores were found in cladded specimens produced by Laser beam. It indicated that the hot corrosion resistance of laser-cladded specimens was found to be superior as compared to TIG-cladded specimens owing to the dense, stable and porousfree protective coating present on the surface of the laser-cladded specimens [75]. Wang et al. studied the corrosion behavior of H1 and H2 steels substrate coated with Hastelloy C22 by employing diode laser technique. Their results indicated that the corrosion resistance of coated specimens is found to be superior as compared to that of substrate specimen and attributed to the differences in chemical composition. Thus, it indicated that the corrosion resistance of H1 and H2 steel substrates are enhanced by Hastelloy coating coated by laser technique. Further, increase in the laser scanning speed resulted in improvement in corrosion resistance of Hastelloy coating owing to finer microstructure [76].

2.6 Statistical modelling applied for welding process optimization

Further to previous section, the welding defects of underfill and root sag hump could not be completely eliminated in deep penetration high-power laser welding process due to complexity of the weld pool dynamics pertaining to influence of multiple process parameters. Response surface methodology (RSM) is often utilized to optimize the process parameters by

proper identification and determining the control input parameters' quantitative effect [77]. Thus, using numerical approach by utilizing RSM methodology helps for effective optimization of the welding processing parameters in order to obtain satisfactory weld beads. Few published reports are available in literature on RSM method on fusion welding process to determine the influence of various welding parameters on resultant weld bead formation. Moradi et al. investigated the effect of autogenous laser welding process parameters on weld bead profile of Nickel based superalloy Rene 80 by using RSM methodology. Laser power, transverse speed, defocusing distance and inert gas pressure were considered as the input parameters, whereas output responses such as weld area, weld width at top and middle depth, undercuts and drop off were considered. Based on the analysis using statistical techniques, they found that the heat input and other laser input parameters considered in the design model has significant effect on weld bead profile. More specifically, welding speed was found to be more significant input parameters with negative influence on output responses. Laser power has a direct effect on all output responses. High inert gas pressure leads to cause welding geometrical defects [78].

Srinivas et al. utilized RSM to optimize the plasma arc welding (PAW) processing parameters including weld current, transverse speed and plasma gas flow rate to obtain satisfactory weld bead characteristics as output responses like weld bead width and weld bead height. ANOVA results indicated that the developed models are statistically adequate. Results indicated that high depth-to-width ratio welds were obtained at an optimized process parameter. It has found that the both current and transverse speed possess significant influence on weld bead width and weld bead height, however, plasma gas flow rate was insignificant for selected range. The regression equations were found to be forecast weld bead width and height with good accuracy [79].

Benyounis et al. utilized RSM approach to optimize butt-welding parameters employing CO₂ laser in joining 5-mm steel plates. Laser power, transverse speed, and defocusing distance were considered as input parameters in the design model. The goal for the RSM model to set the process variables at optimum conditions in order to obtain desired welds with maximum weld penetration, reduced heat input, minimal width of weld and HAZ. Predicted results obtained from desirability approach were found to be in good agreement with the experimental ones [80]. Similarly, Vijayan et al. examined the influence of welding process parameters by employing CO₂ laser in gaussian mode to weld low carbon steel plates using RSM approach. Three processing parameters such as laser power, transverse speed and

defocusing distance was considered as input variables. ANOVA indicated that at an optimized process parameters based on the predicted model are found to be adequate in order to produce a desired sound good quality weld. Further validation of the model developed was done by conducting the actual experiments and found to be in good agreement [81].

Khan et al. optimized Nd:YAG laser welding process parameters to weld ferritic AISI 430 and austenitic 304L stainless steel using design of experiments approach employing RSM. Three process parameters such as laser power, welding speed and incident laser angle was considered as input variables as these parameters influence the weld bead profile significantly. The criteria were considered as maximize the weld resistant length and shearing force, whereas weld radial penetration must be minimum. Regression analysis indicated that the all-input parameters were optimized to obtain desired weld bead [82]. Sahil et al. utilized the RSM to optimize the conventional MIG welding process parameters to weld 5-mm thick mild steel plates. MIG arc current, voltage and gas flow rate was considered as input variables in the present model. Their results indicated that all three input parameters significantly affect the hardness of the weldments, in which welding voltage is the highest significant factor followed by gas flow rate and current. At an optimized process parameter, the resultant hardness of the weldments was found to be increased by 29.21% [83].

Furthermore, optimization of the pulsed laser-TIG hybrid welding processing parameters in joining 5.6-mm thick 316LN SS plates were conducted by Ragavendran et al. Laser power, pulse duration and frequency, TIG current were considered as input variables in the RSM model. Weld penetration, fusion zone area, and weld bead width were considered as the output responses. Results indicated that all four input variables have significant effect on resultant weld bead formation. Maximum penetration depth was obtained at an optimized process parameters predicted by the developed statistical model [84]. Shi et al. systematically investigated and optimize the MP-NG laser welding process parameters with addition of filler-wire using 10-kW Nd:YAG laser to weld 20-mm thick high strength steel plates by employing statistical methods. Three process parameters such as laser power, transverse speed and wire feed rate was considered as input variables as these process parameters influence the weld bead profile significantly in this technique. The responses were considered as transversal area of additional metal, weld bead width and height and the ratio weld bead width to height. Validation experiments were conducted based on the optimized parameters provided by the model and found that all these input variables significantly affect the output responses withing

the factor domain. Macro and microstructural analysis of the cross-sectional weld bead indicated that this method produced weld with fewer welding defects [85].

2.7 References:

- Hosseini HS, Shamanian M, Kermanpur A. Characterization of microstructures and mechanical properties of Inconel 617/310 stainless steel dissimilar welds. J Materials characterization. 2011;62(4):425-431.
- Mankins W, Hosier J, Bassford T. Microstructure and phase stability of Inconel alloy 617. J Metallurgical Transactions. 1974;5(12):2579-2590.
- 3. Di Gianfrancesco A. Materials for ultra-supercritical and advanced ultra-supercritical power plants. Woodhead Publishing; 2016
- 4. Keßler B, Brenner B, Dittrich D, et al., editors. Laser multi-pass narrow-gap welding-a promising technology for joining thick-walled components of future power plants. MATEC Web of Conferences; 2019: EDP Sciences
- Zhang, Mingjun, Shun Chen, Yingzhe Zhang, Genyu Chen, and Zhuming Bi. "Mechanisms for improvement of weld appearance in autogenous fiber laser welding of thick stainless steels." Metals 8, no. 8 (2018): 625.
- Zhang, Mingjun, Kun Tang, Jian Zhang, Cong Mao, Yongle Hu, and Genyu Chen. "Effects of processing parameters on underfill defects in deep penetration laser welding of thick plates." The International Journal of Advanced Manufacturing Technology 96, no. 1 (2018): 491-501.
- 7. Wen, L.; Fenggui, L.; Renjie, Y.; Xinhua, T.; Haichao, C. Gleeble Simulation of the HAZ in Inconel 617 Welding. J. Mater. Proc. Technol. 2015, 225, 221–228.
- 8. Xu, Huali, Wen Liu, Fenggui Lu, Peng Wang, and Yuming Ding. "Evolution of carbides and its characterization in HAZ during NG-TIG welding of Alloy 617B." Materials Characterization 130 (2017): 270-277.
- 9. Li, Shanlin, Kejian Li, Zhipeng Cai, and Jiluan Pan. "Behavior of M23C6 phase in Inconel 617B superalloy during welding." Journal of Materials Processing Technology 258 (2018): 38-46.
- 10. Li, Shanlin, Kejian Li, Mengjia Hu, Yao Wu, Zhipeng Cai, and Jiluan Pan. "The mechanism for HAZ liquation of nickel-based alloy 617B during gas tungsten arc welding." Metals 10, no. 1 (2020): 94.
- 11. Fink, Carolin, and Manuela Zinke. "Welding of nickel-based alloy 617 using modified dip arc processes." Welding in the World 57, no. 3 (2013): 323-333.
- 12. Ren, Wenjie, Fenggui Lu, Renjie Yang, Xia Liu, and Zhuguo Li. "Liquation cracking in fiber laser welded joints of inconel 617." Journal of Materials Processing Technology 226 (2015): 214-220.
- Osoba, L. O., and O. A. Ojo. "Influence of laser welding heat input on HAZ cracking in newly developed Haynes 282 superalloy." *Materials Science and Technology* 28, no. 4 (2012): 431-436.
- Yan, Fei, Chongjing Hu, Xiong Zhang, Yuanzheng Cai, Chunming Wang, Jun Wang, and Xiyuan Hu. "Influence of heat input on HAZ liquation cracking in laser welded GH909 alloy." Optics & Laser Technology 92 (2017): 44-51.
- 15. Luo, X., K. Shinozaki, H. Kuroki, S. Yoshihara, Y. Okumoto, and M. Shirai. "Analysis of temperature and elevated temperature plastic strain distributions in laser welding HAZ study of laser weldability of Ni-base superalloys (Report 5)." (2002): 385-392.

- Shinozaki K, Kuroki H, Luo X, et al. Effects of welding parameters on laser weldability of Inconel 718. Study of laser weldability of Ni-base, heat-resistant superalloys (1st Report). Welding international. 1999;13(12):945-951.
- 17. Nishimoto K, Woo I, Ogita T, et al. Factors affecting HAZ cracking susceptibility of laser welds. Study of weldability of Inconel 718 cast alloy (4th report). Welding International. 2001.
- 18. Nishimoto, K., I. Woo, and M. Shirai. "Analyses of temperature and strain distributions in laser welds study of the weldability of Inconel 718 cast alloy (Report 6)." (2002): 284-292.
- 19. Bagger, Claus, and Flemming O. Olsen. "Review of laser hybrid welding." Journal of laser applications 17, no. 1 (2005): 2-14.
- 20. Eboo, Ghulam Mohammed, W. M. Steen, and J. Clarke. "Arc augmented laser welding." (1979): 257-265.
- 21. Gao, Z, Numerical Modeling to Understand Liquation Cracking Propensity during Laser and Laser Hybrid Welding (I). Int. J. Adv. Manuf. Tech. 2012, 63(1), 291–303.
- 22. Hu, B., and I. M. Richardson. "Mechanism and possible solution for transverse solidification cracking in laser welding of high strength aluminium alloys." Materials Science and Engineering: A 429, no. 1-2 (2006): 287-294.
- 23. Gebhardt, M. O., Andrey Gumenyuk, and Michael Rethmeier. "Solidification cracking in laser GMA hybrid welding of thick-walled parts." Science and technology of welding and joining 19, no. 3 (2014): 209-213.
- 24. Moore, P. L., D. S. Howse, and E. R. Wallach. "Microstructures and properties of laser/arc hybrid welds and autogenous laser welds in pipeline steels." Science and Technology of Welding and Joining 9, no. 4 (2004): 314-322.
- 25. Zhang, Mingjun, Genyu Chen, Yu Zhou, and Shenghui Liao. "Optimization of deep penetration laser welding of thick stainless steel with a 10kW fiber laser." Materials & Design 53 (2014): 568-576
- Zhang, Mingjun, Zheng Zhang, Kun Tang, Cong Mao, Yongle Hu, and Genyu Chen. "Analysis
 of mechanisms of underfill in full penetration laser welding of thick stainless steel with a 10kW
 fiber laser." Optics & Laser Technology 98 (2018): 97-105.
- S. Li, G. Chen, S. Katayama, Y. Zhang, Relationship between spatter formation and dynamic molten pool during high-power deep-penetration laser welding, Appl. Surf. Sci. 303 (2014) 481–488.
- 28. Q. Pan, M. Mizutani, Y. Kawahito, S. Katayama, High power disk laser-metal active gas arc hybrid welding of thick high tensile strength steel plates, J. Laser Appl. 28 (2016) 012004 (9p).
- Y. Kawahito, M. Mizutani, S. Katayama, Elucidation of high-power fibre laser welding phenomena of stainless steel and effect of factors on weld geometry, J. Phys. D: Appl. Phys. 40 (2007) 5854–5859
- 30. W. Guo, Q. Liu, J.A. Francis, D. Crowther, A. Thompson, Z. Liu, Comparison of laser welds in thick section S700 high-strength steel manufactured in flat (1G) and horizontal (2G) positions, CIRP Ann.–Manuf. Technol. 64 (2015) 197–200.
- 31. N. Matsumoto, Y. Kawahito, K. Nishimoto, S. Katayama, Effects of laser focusing properties on weldability in high-power fiber laser welding of thick high-strength steel plate, J. Laser Appl. 29 (2017) 012003 (9p).
- 32. Farahani, E. " Material characterization of direct and pulsed current gas tungsten arc welding of Inconel 617." International Welding and Joining Conference, 2012.
- 33. Farahani, E., M. Shamanian, and F. Ashrafizadeh. "A comparative study on direct and pulsed current gas tungsten arc welding of alloy 617." International Journal on Manufacturing and Material Science 2, no. 1 (2012): 1.

- 34. Park, Young Su, Hyo Sik Ham, Sang Myung Cho, and Dong Ho Bae. "An assessment of the mechanical characteristics and optimum welding condition of Ni-based super alloy." Procedia Engineering 10 (2011): 2645-2650.
- 35. Mageshkumar, K., P. Kuppan, and N. Arivazhagan. "Investigation on microstructure and mechanical properties on pulsed current gas tungsten arc welded super alloy 617." In IOP Conference Series: Materials Science and Engineering, vol. 263, no. 6, p. 062032. IOP Publishing, 2017.
- 36. Liu, Wen, Fenggui Lu, Xinhua Tang, Renjie Yang, and Haichao Cui. "The microstructure evolution and element segregation of Inconel 617 alloy tungsten inert gas welded joint." Journal of Materials Research 31, no. 4 (2016): 435-442.
- 37. Li, Xiaogang, Kejian Li, Shanlin Li, Yao Wu, Zhipeng Cai, and Jiluan Pan. "Microstructure and high temperature fracture toughness of NG-TIG welded Inconel 617B superalloy." Journal of Materials Science & Technology 39 (2020): 173-182.
- 38. Gao, Yuan, Chendong Shao, Haichao Cui, Ninshu Ma, and Fenggui Lu. "Study on fracture toughness of 617 Ni-based alloy welded joint under different elevated temperatures." Journal of Materials Research 35, no. 14 (2020): 1790-1802.
- 39. Kim, Woo-Gon, Jae-Young Park, I. M. W. Ekaputra, Sung-Deok Hong, Seon-Jin Kim, and Yong-Wan Kim. "Comparative study on the high-temperature tensile and creep properties of Alloy 617 base and weld metals." Journal of Mechanical Science and Technology 27, no. 8 (2013): 2331-2340.
- 40. Kim, B. J., Y. B. Sim, J. H. Lee, M. K. Kim, and B. S. Lim. "Application of small punch creep test for Inconel 617 alloy weldment." Procedia Engineering 10 (2011): 2579-2584.
- 41. Totemeier, Terry C. "High-temperature creep-fatigue of Alloy 617 base metal and weldments." In ASME Pressure Vessels and Piping Conference, vol. 42878, pp. 255-260. 2007.
- 42. Ren, Wenjie, Fenggui Lu, Renjie Yang, Xia Liu, Zhuguo Li, and Seyed Reza Elmi Hosseini. "A comparative study on fiber laser and CO2 laser welding of Inconel 617." Materials & Design 76 (2015): 207-214.
- 43. Adamiec, Janusz, and Robert Kocurek. "Effect of autogenous laser weld on microstructure and mechanical properties of Inconel 617 nickel alloy." In Solid State Phenomena, vol. 226, pp. 43-46. Trans Tech Publications Ltd, 2015.
- 44. Cheng, Hao, Li Kang, Jincheng Pang, Boce Xue, Dong Du, and Baohua Chang. "Effect of the welding position on weld quality when laser welding Inconel 617 Ni-based superalloy." Optics & Laser Technology 139 (2021): 106962.
- 45. Ren, Wenjie, Yuan Chen, Ling Lan, Fenggui Lu, and Zhuguo Li. "Thermal Exposure Effect on the Microstructural and Mechanical Properties of a Laser-Welded Inconel 617 Joint in an Air Environment." Journal of Materials Engineering and Performance 30, no. 6 (2021): 4328-4340.
- Palanivel, R., I. Dinaharan, R. F. Laubscher, and Ibrahim M. Alarifi. "Effect of Nd: YAG laser welding on microstructure and mechanical properties of Incoloy alloy 800." Optics & Laser Technology 140 (2021): 107039.
- 47. Zhang, Xiong, Zhengwu Zhu, Xiuquan Ma, Chunming Wang, Gaoyang Mi, and Shuye Zheng. "Solidification features and tensile performance altered by increased welding speed during laser welding GH909 superalloy." Materials Characterization 181 (2021): 111488.
- 48. Jiang, Zhenguo, Wang Tao, Kun Yu, Caiwang Tan, Yanbin Chen, Liqun Li, and Zhijun Li. "Comparative study on fiber laser welding of GH3535 superalloy in continuous and pulsed waves." *Materials & Design* 110 (2016): 728-739.
- 49. Alcock, J. A., and B. Baufeld. "Diode laser welding of stainless steel 304L." Journal of Materials Processing Technology 240 (2017): 138-144.

- 50. Malchus, Joerg, Volker Krause, Georg Rehmann, Michael Leers, Arnd Koesters, and David G. Matthews. "A 40kW fiber-coupled diode laser for material processing and pumping applications." In High-Power Diode Laser Technology and Applications XIII, vol. 9348, p. 934803. International Society for Optics and Photonics, 2015.
- 51. Abe, Nobuyuki, Ritsuko Higashino, Naoki Nakagawa, Masahiro Tsukamoto, Shoji Miyake, Shuichi Noguchi, and Masakazu Hayashi. "Welding and forming of thick steel plates with a high-power density diode laser." In International Congress on Applications of Lasers & Electro-Optics, vol. 2000, no. 1, pp. A16-A23. Laser Institute of America, 2000
- 52. Cao, X., P. Wanjara, J. Huang, C. Munro, and A. Nolting. "Hybrid fiber laser–Arc welding of thick section high strength low alloy steel." Materials & Design 32, no. 6 (2011): 3399-3413.
- 53. Roepke, C., S. Liu, S. Kelly, and R. Martukanitz. "Hybrid laser arc welding process evaluation on DH36 and EH36 steel." Welding Journal 89, no. 7 (2010): 140-149.
- 54. Frostevarg, Jan, and Alexander FH Kaplan. "Undercuts in laser arc hybrid welding." Physics Procedia 56 (2014): 663-672.
- 55. Gao, Ming, Xiaoyan Zeng, Jun Yan, and Qianwu Hu. "Microstructure characteristics of laser—MIG hybrid welded mild steel." Applied Surface Science 254, no. 18 (2008): 5715-5721.
- 56. Xu, Guoxiang, Haichao Pan, Peng Liu, Pengfei Li, Qingxian Hu, and Baoshuai Du. "Finite element analysis of residual stress in hybrid laser-arc welding for butt joint of 12 mm-thick steel plate." Welding in the World 62, no. 2 (2018): 289-300.
- 57. Pan Q, Mizutani M, Kawahito Y, Katayama S (2016) High power disk laser-metal active gas arc hybrid welding of thick high tensile strength steel plates. J Laser Appl 28(1):012004
- 58. Moon et al. "Method of laser welding", Google patent US4527040 (July 1985).
- 59. Tsukamoto et al. "Laser narrow groove welding apparatus and welding method", Google patent US8481885B2 (July 2013).
- 60. J. O. Milewski and E. Sklar, "Narrow gap laser welding," Google patent US5760365 A (June 1998).
- 61. "Laser wire-filled welding method for thick plate with narrow gap" Google patent CN103801833A, (May 2014).
- 62. "Butt laser welding method of welded plate material", Google patent JP6255314B2, (Dec 2017)
- 63. "Large-size structural member laser welding tool, system and method", Google patent CN112570888A, (Mar 2021).
- 64. Sun, Junhao, Wenjie Ren, Pulin Nie, Jian Huang, Ke Zhang, and Zhuguo Li. "Study on the weldability, microstructure and mechanical properties of thick Inconel 617 plate using narrow gap laser welding method." Materials & Design 175 (2019): 107823.
- 65. Kessler, Benjamin, Dirk Dittrich, Berndt Brenner, Jens Standfuss, and Christoph Leyens. "Extension of the process limits in laser beam welding of thick-walled components using the Laser Multi-Pass Narrow-Gap welding (Laser-MPNG) on the example of the nickel-based material Alloy 617 occ." Welding in the World 65, no. 7 (2021): 1359-1371.
- 66. Zhang X, Ashida E, Tarasawa S, Properties of welded joint for narrow gap laser welding of austenitic stainless steels. In: 29th International Congress on Applications of Lasers and Electro-Optics. ICALEO 2010, Anaheim, (2010) pp 632–637.
- 67. Zhao, Y., F. Su, J. Huang, J. S. Zou, and Y. X. Wu. "Microstructure and Mechanical Properties of a 10CrNi3MoV Thick Plate Welded Joint Using Narrow Gap Laser Welding with Filler Wire." Lasers in Engineering (Old City Publishing) 41 (2018).
- 68. Guo, Wei, Dave Crowther, John A. Francis, Alan Thompson, and Lin Li. "Process-parameter interactions in ultra-narrow gap laser welding of high strength steels." The International Journal of Advanced Manufacturing Technology 84, no. 9 (2016): 2547-2566.

- 69. Yu, Y. C., S. L. Yang, Y. Yin, C. M. Wang, X. Y. Hu, X. X. Meng, and S. F. Yu. "Multi-pass laser welding of thick plate with filler wire by using a narrow gap joint configuration." Journal of Mechanical Science and Technology 27, no. 7 (2013): 2125-2131.
- Hari, P. R., N. Arivazhagan, M. Nageswara Rao, and A. H. V. Pavan. "Comparative studies on corrosion of alloy 617 OCC at 700 C in air and simulated coal ash environments." Materials Today: Proceedings 5, no. 5 (2018): 11452-11459.
- 71. Hari, P. R., N. Arivazhagan, M. Nageswara Rao, and A. H. V. Pavan. "High temperature corrosion of alloy 617 OCC at 700° C in simulated USC power plant environment." Materials Research Express 6, no. 7 (2019): 076557.
- 72. Aung, Naing Naing, and Xingbo Liu. "Effect of temperature on coal ash hot corrosion resistance of Inconel 740 superalloy." Corrosion Science 82 (2014): 227-238.
- 73. Stein-Brzozowska, Gosia, Diana M. Flórez, Jörg Maier, and Günter Scheffknecht. "Nickel-base superalloys for ultra-supercritical coal-fired power plants: Fireside corrosion. Laboratory studies and power plant exposures." Fuel 108 (2013): 521-533.
- 74. El-Awadi, G. A., S. Abdel-Samad, and Ezzat S. Elshazly. "Hot corrosion behavior of Ni based Inconel 617 and Inconel 738 superalloys." *Applied surface science* 378 (2016): 224-230.
- 75. Fesharaki, Mohammad Naghiyan, Reza Shoja-Razavi, Hojjat Allah Mansouri, and Hossein Jamali. "Evaluation of the hot corrosion behavior of Inconel 625 coatings on the Inconel 738 substrate by laser and TIG cladding techniques." Optics & Laser Technology 111 (2019): 744-753.
- Wang, Qin-Ying, Yang-Fei Zhang, Shu-Lin Bai, and Zong-De Liu. "Microstructures, mechanical properties and corrosion resistance of Hastelloy C22 coating produced by laser cladding." Journal of alloys and compounds 553 (2013): 253-258.
- 77. Šibalija, Tatjana V., and V. D. Majstorovic. Advanced Multiresponse Process. Optimisation. Berlin, Germany: Springer, 2016.
- 78. Moradi, Mahmood, and Majid Ghoreishi. "Influences of laser welding parameters on the geometric profile of NI-base superalloy Rene 80 weld-bead." The International Journal of Advanced Manufacturing Technology 55, no. 1 (2011): 205-215.
- 79. Srinivas, K., Vundavalli, P. R., & Hussain, M. M. (2018, July). Modeling of Plasma Arc Welding of Inconel 617 Super Alloy Plates using RSM. In IOP Conference Series: Materials Science and Engineering (Vol. 390, No. 1, p. 012048). IOP Publishing.
- 80. Benyounis, K. Y., Abdul-Ghani Olabi, and M. S. J. Hashmi. "Optimizing the laser-welded butt joints of medium carbon steel using RSM." Journal of Materials Processing Technology 164 (2005): 986-989.
- 81. Vijayan, K., and P. Ranjith Kumar. "Investigation of Process Parameters for Laser Welding of Low Carbon Steel using RSM." *Asian Journal of Research in Social Sciences and Humanities* 6, no. 8 (2016): 2005-2018.
- 82. Khan, M. M. A., Luca Romoli, Marco Fiaschi, Gino Dini, and F. Sarri. "Multiresponse optimization of laser welding of stainless steels in a constrained fillet joint configuration using RSM." The International Journal of Advanced Manufacturing Technology 62, no. 5 (2012): 587-603.
- 83. Angaria, Sahil, P. S. Rao, and S. S. Dhami. "Application of RSM to optimize MIG welding process parameters for hardness." Int J Emerg Technol Eng Res 5, no. 9 (2017): 31-36.
- 84. Ragavendran, M., N. Chandrasekhar, R. Ravikumar, Rajesh Saxena, M. Vasudevan, and A. K. Bhaduri. "Optimization of hybrid laser–TIG welding of 316LN steel using response surface methodology (RSM)." Optics and Lasers in Engineering 94 (2017): 27-36.

85. Shi, Hao, Ke Zhang, Zhengyi Xu, Tianyu Huang, Liwen Fan, and Weining Bao. "Applying statistical models optimize the process of multi-pass narrow-gap laser welding with filler wire." The International Journal of Advanced Manufacturing Technology 75, no. 1 (2014): 279-291.

3.1 Methodology of Experiments

This chapter discuss the detailed description of materials utilized for welding experimentation, welding processes such as CO₂ laser - MIG arc hybrid welding (LHW), conventional tungsten inert gas (TIG) and high-power diode laser welding (DLW) experimental setup, process conditions, joint configurations, methodology adopted, visual inspections, characterization tools for analyzing the macro and microstructural features in weldments and assessments of mechanical and corrosion properties of the weldments. Figure 3.1 illustrates the comprehensive methodology of welding experimentation and joint quality analysis adopted for the entire work in flow chart form.

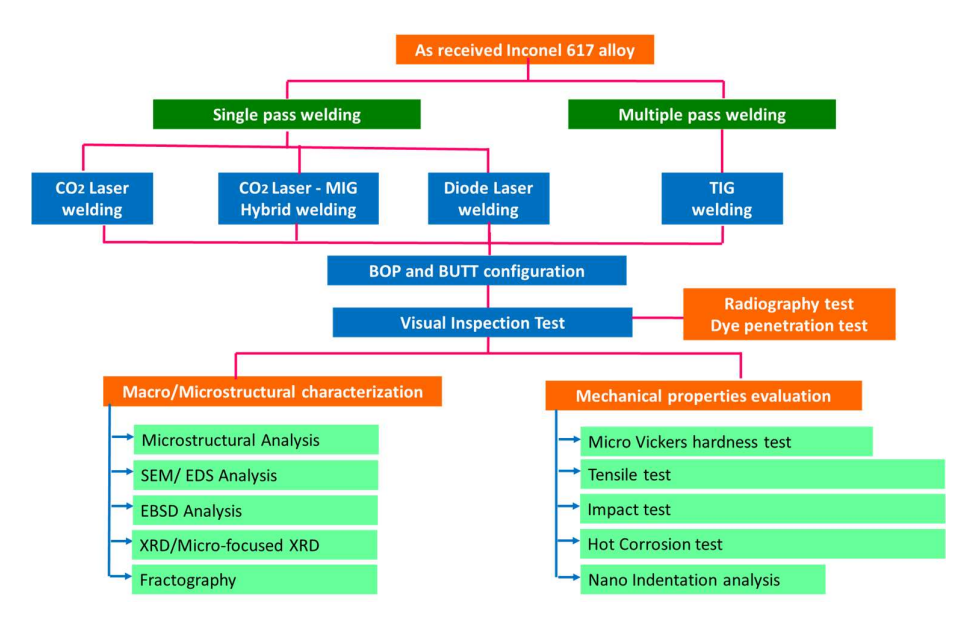


Figure 3.1. Flow chart of methodology adopted for welding experimentation and weld quality analysis

3.2 Materials

The base material selected for the present investigation is a solid-solution strengthened Nickel based superalloy Inconel 617 with a nominal composition of Cr - 20 - 23%, Mo - 8 - 10%, Co - 10 - 13%, Al - 0.6 - 1.5% and Ti - 0.2 - 0.5% [1-3] in the form of 8 - 12 mm thick plates. The as-received base metal received was hot-rolled and solution-annealed at a

temperature of 1140°C followed by water quenching. ER NiCrMo-4 filler wire with two different sizes (1.2 mm and 3.2 mm dia) was used as filler materials. The chemical composition of both superalloy base metal and filler material was analyzed by Inductively coupled plasma-Optical emission spectroscopy (ICP-OES) chemical analysis and tabulated in Table 3.1.

Table 3.1. Chemical composition (wt. %) of Inconel 617 base and filler metal

Inconel 617	Cr	Со	Мо	Al	Ti	Fe	В	Ni
Base Metal	22.4	11.9	8.55	1.28	0.41	0.59	0.0049	Bal
Filler	21.4	10.8	8.28	1.37	0.39	0.48	0.0047	Bal

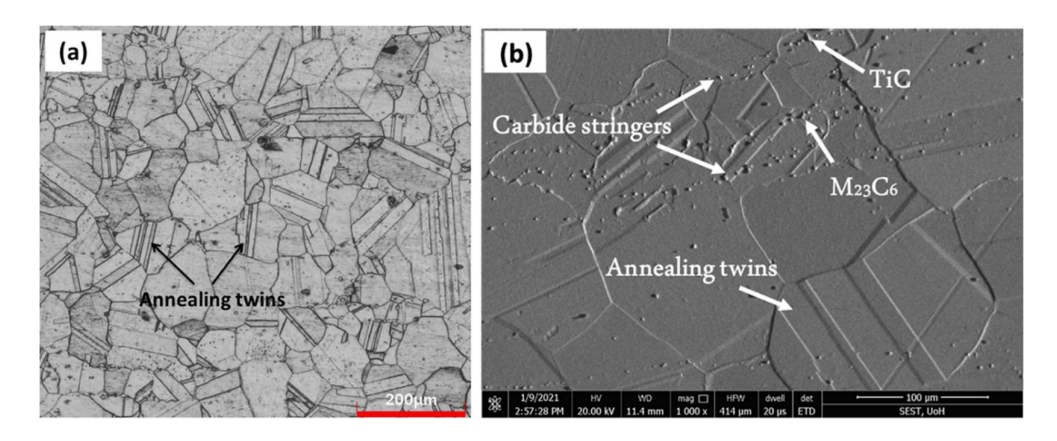


Figure 3.2. As-received microstructure of Inconel 617 alloy (a) optical and (b) FESEM

Figure 3.2 shows the as-received base metal (BM) microstructure of Inconel 617 alloy observed by optical and high-magnification scanning electron microscope (FESEM). In solution-annealed condition microstructure constitutes of fully austenitic grains with presence of numerous carbide stringers along rolling direction and plenty of annealing twins inside the grains that would have originated during solution-annealing treatment [4]. Large number of discrete various types and morphology carbide particles of Cr, Mo, Ti etc. are randomly distributed along the grain boundaries as well as inside the austenitic grains as marked by arrows in Figure 3.2b. EDS spot analysis of these selected particles shown in Table 3.2, confirms that the carbides in the BM were black block-shaped particulates were TiC-type and globular grey particulates were Cr, Mo-rich M₂₃C₆ carbides, whereas white particles were Morich M₆C-type carbides [5,6].

Table 3.2. EDS analysis (wt. %) of the carbides and surrounding matrix in BM

Phase	Cr	Mo	Ni	Co	Al	Ti
(Cr, Mo)-rich M ₂₃ C ₆	61.23	14.90	12.34	5.87	0.21	0.32
TiC	19.67	4.78	9.25	3.98	0.15	59.45
Matrix	24.32	8.83	49.81	12.19	0.42	0.58

X-ray diffraction (XRD) analysis of as-received BM shown in Figure 3.3, further confirms that the BM of Inconel 617 alloy consists of γ (Ni-Cr-Co-Mo) as matrix along with predominant Cr,Mo-rich M₂₃C₆ carbides phase. However, low-intensity diffraction peaks were also observed for Mo-rich M₆C carbides and TiC carbides as well but to a meagre amount. This low intensity is plausibly due to lower volume fraction of the carbides present in this condition. Apart from these phases, few M₂C phases could also be realized in as-received BM. These analyses results were in consistent with the observations made by several researchers [5-7].

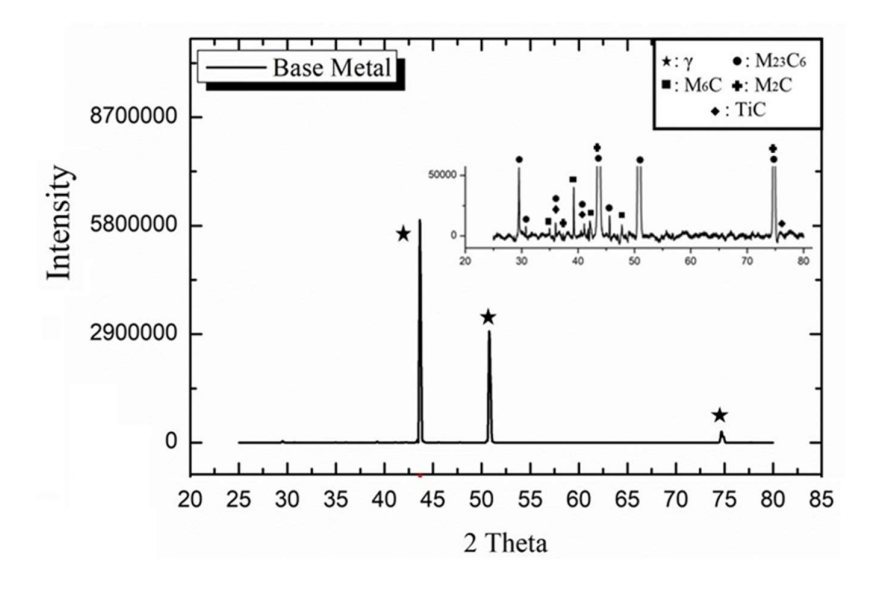


Figure 3.3. XRD of as-received Inconel 617 alloy BM

3.3 Design of Joint configurations

A generic Y-groove edge configuration with root face height of 4.5 mm and total included angle of 15° was designed for LHW methods. Similarly, a Y-groove butt joint with larger total included angle of 60° and a root face height of 1.5 mm was designed and utilized for multi-pass TIG welding purpose. DLW experiments was performed on square butt joint configuration plates. Distance between the plates for LHW, TIG and DLW were maintained was 0.2, 3 and 0 mm respectively. Joint configurations for LHW, TIG and DLW welding

processes are shown in Figure 3.4. All weldments were configured to butt-joint configuration for mechanical properties evaluation, whereas, bead-on-plate (BOP) configuration utilized for process optimization experiments.

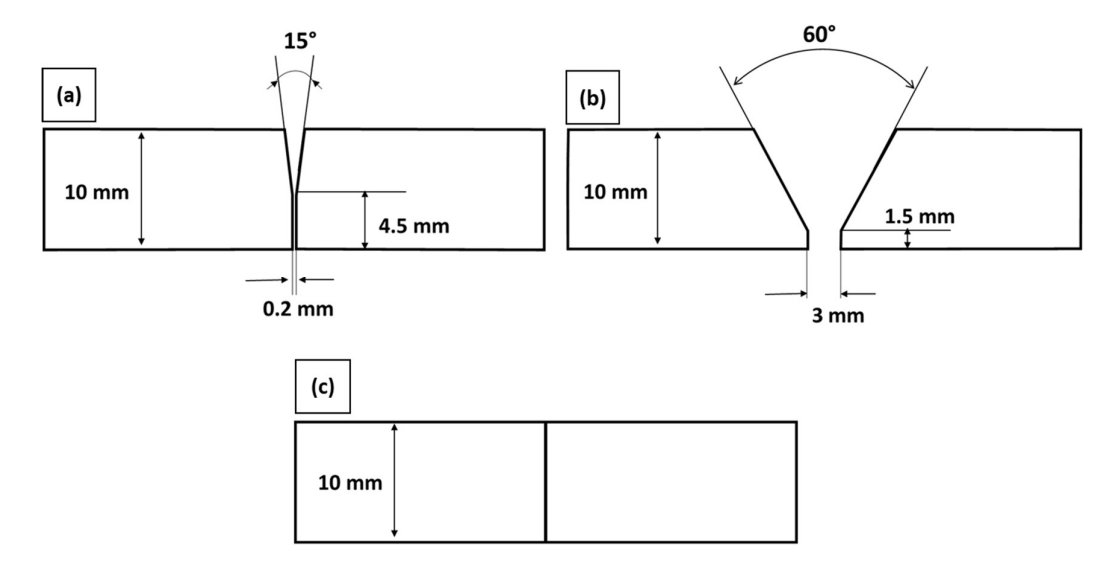


Figure 3.4. Joint configuration of (a) LHW, (b) TIG, and (c) DLW

3.4 Welding Systems and Setup Conditions

Initially laser welding experiments has been carried out using a Slab CO_2 Laser in continuous wave (CW) utilizing a gaussian beam intensity profile with a spot diameter of 180 6 μ m. Later, a MIG arc heat source has been combined with CO_2 Laser to perform Laser-MIG hybrid welding experiments.

3.4.1 Slab CO₂ laser:

In CO₂ Laser system mixture of gases like carbon dioxide, helium, and nitrogen in the ratio of 1:2:8 is used for lasing. This type of laser is electrically excited by use of a gas discharge, which can operate either with DC or AC or in the RF (radio frequency) domain to produce the laser beam with higher wavelength of 10.6 μm. CO₂ Laser is classified based on the type of heat removal method and the flow direction of the lasing medium. Slab CO₂ Laser system is of slow flow laser types. The lasing medium is excited by RF in a narrow space (around 2 mm) between two wide electrodes. These electrodes are arranged in the form of a slab, hence named as Slab CO₂ Laser. The wide slab discharge area with small distance between electrodes permits effective heat removal via the water-cooled electrodes directly and hence allows high-power with sufficiently high-beam quality (k > 0.9) laser to be produced.

ROFIN Slab CO₂ Laser system utilized in the present study is shown in Figure 3.5a and its schematic representation is shown in Figure 3.5b. Slab CO₂ Laser is integrated to a 4-axis CNC workstation for movement in X,Y,Z with maximum allowable distances of 3000, 1500 and 300 mm respectively and a rotational axis.

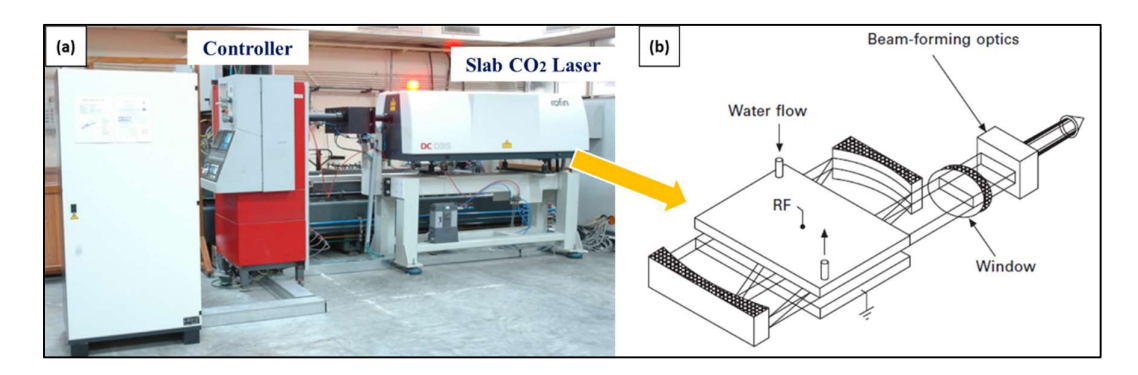


Figure 3.5. (a) Slab CO₂ laser system setup and (b) Schematic of Slab CO₂ laser

Table 3.3. Slab CO₂ laser system variables

CO ₂ Laser					
Laser type	Slab CO ₂ (DC-035 Rofin, Germany)				
Wavelength	10.6 μm				
Laser beam spot size	180 μm dia (circular)				
Mode of processing	Continuous wave (CW)				
Power	3.5 kW				
Laser beam angle	3° to vertical				
Focal distance	300 mm				

3.4.2 Metal Inert gas (MIG) welding equipment:

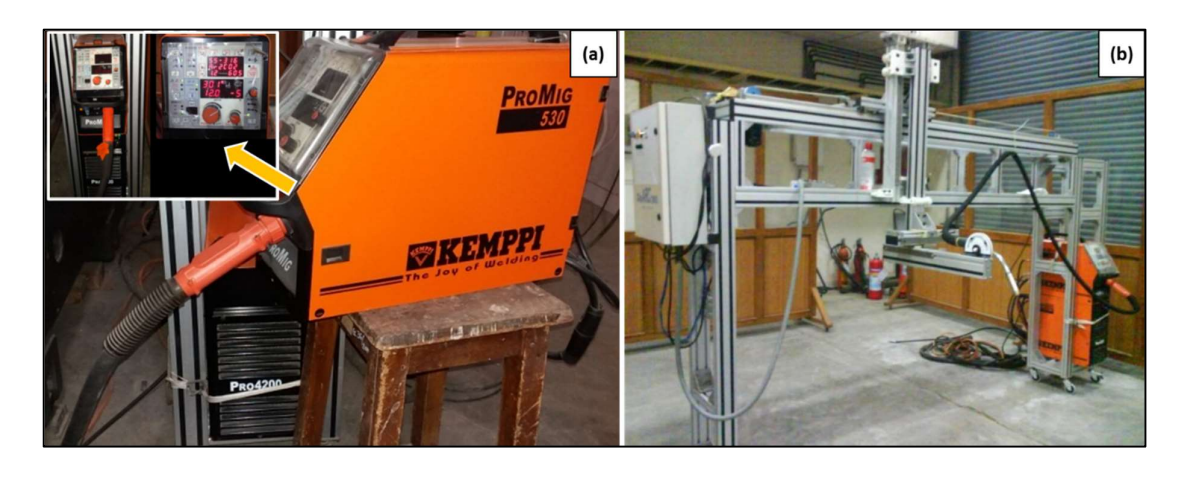


Figure 3.6. (a) KEMPPI MIG welding equipment with zoom in inset image of controller and (b) Standalone workstation with wheel base

Figure 3.6 shows the MIG welding system constitute of KEMPPI Pro 4200 Evolution power source and Pro-MIG 530 wire feeder. This power source is inverter based and capable of operating in multi-operation power sources for MIG, Pulsed-mode MIG as well as TIG welding in DC. This type of welding system can be operated both in automatic and robotic mode. The filler wire electrode is fed through the rollers from a coil at a constant feeding speed provided according to set wire feed rate. The max. welding voltage that can be achieved is 46 V at a 400 A current. It is utilized in synergic-pulsed mode of operation in the present study.

3.4.3 CO₂ laser - MIG arc hybrid welding (LHW):

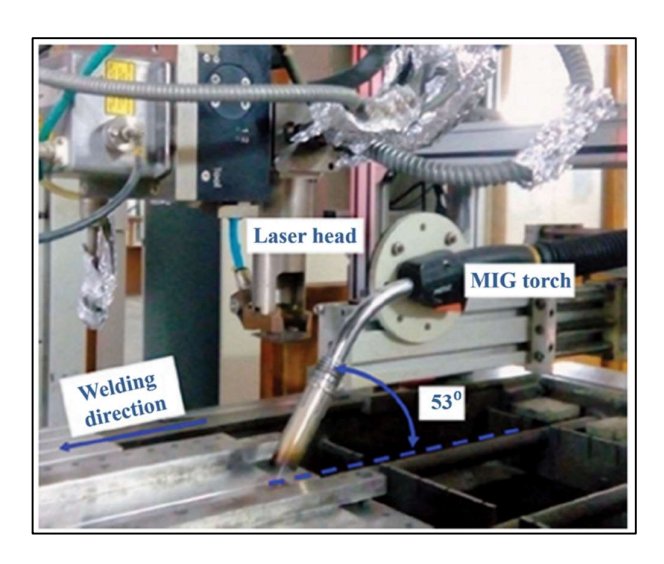


Figure 3.7. CO₂ laser – MIG hybrid welding setup

Table 3.4. Process variables for LHW

Laser	MIG				
Type – Slab CO ₂ laser	Torch Stand-off distance – 12 - 15 mm				
Wavelength – 10.6 μm	MIG Torch angle – 56 - 60°				
Laser beam spot dia – 180 μm Mode of Processing – CW	Metal Transfer mode –Pulsed Synergic				
Laser Power – 3.5 KW	MIG wire feed rate – 7 - 8 m/min				
Focal length – 300 mm	Filler wire – ER NiCrMo-4, Ø 1.2 mm				
Laser – MIG hybrid					

Distance between sources – 2 - 3 mm

Process orientation- Laser leading

Welding Speed – 1, 0.8 and 0.6 m/min

Shielding gas – 100 % Helium @ 15 lpm

Laser-MIG arc hybrid welding (LHW) experiments were performed by combining a 3.5 kW Slab CO₂ Laser (Model: DC-035 Rofin, Germany) integrated to a 4-axis CNC workstation with a MIG torch (Kemppi Pro 4200 Evolution MIG). Figure 3.7 shows the experimental setup for LHW process. CO₂ laser was operated in continuous wave mode, whereas MIG arc was used in pulsed-synergic mode. A 300 mm laser focal distance was fixed to obtain a laser beam spot of dia 180 µm of gaussian distribution profile. The distance between the MIG electrode and the laser beam spot maintained was 2 - 3 mm and they were oriented in such a way that the laser beam is always in front and the MIG torch is behind i.e., laser leading the MIG arc. Angle between the laser beam and MIG torch with horizontal plane were approximately 90° and 53° respectively. 100% helium was used as a shielding gas and fed through the MIG torch to protect the weld pool from contamination. Base plates were clamped using clamps, stiffeners and screws with manual hand tightened to avoid distortion during experimentation. Details of LHW process parameters are provided in Table 3.4. Further, the heat input calculation was carried out as defined in mathematical Equations 3.1 – 3.3 and the efficiency values were taken from the references [8-11].

$$Q_l = \eta_l \frac{P_l}{s} \qquad eqn (3.1)$$

$$Q_{MIG} = \eta_{MIG} \frac{V * I}{s}$$
 eqn (3.2)

$$Q_{Hybrid} = Q_l + Q_{MIG} \qquad eqn (3.3)$$

Where Q_l , Q_{MIG} and Q_{Hybrid} – Heat input of laser, MIG, and hybrid processes, respectively

 P_l – Laser power

 η_l and η_{MIG} – Efficiencies of the laser and MIG process respectively

V and I - Arc voltage and current

s - Welding speed

3.4.4 Conventional TIG welding:

A Conventional Tungsten Inert gas (TIG) welding equipment was employed for performing welding experiments. Figure 3.8 illustrates the manual TIG welding setup utilized for experimentation. Prior to welding, base plates were cleaned with acetone and clamped by specially designed fixtures to avoid distortion during experimentation. Filler wire of 3.2 mm dia was utilized for weld passes. A sum of six weld passes were utilized to successfully complete the 10-mm thick superalloy plate welding. Argon shielding gas was utilized to shroud the weld pool to avoid contamination. An Inter-pass temperature of 150°C was maintained between interpass weld depositions. The temperature between the weld passes was checked with the pyrometer. After each weld pass, the surface of the welds was cleaned with wire brush and acetone. Welding current and voltage maintained were kept in the range of 130 – 140 amp and 11.5 – 13.5 volts respectively with welding speed being maintained between 50 – 60 mm/min. All welding passes carried out manually by the same welder and the welding was done in a single session. After welding, the weldments were subjected to dye penetrant and radiographic examination to check any surface or internal defects.



Figure 3.8. Manual TIG welding experimental setup

3.4.5 Fiber-coupled high-power diode laser welding (DLW):

Diode lasers are advantageous over CO₂ lasers on account of this specific quality such as shorter wavelength, high absorptivity, high energy conversion efficiency, high reliability, longer serviceability and portability and low capital cost. Diode lasers constitutes of semiconductor diodes (for example: GaAs) with equal facets at the end of the splits of the optical cavity. Semiconducting materials of GaAs compounds produces electromagnetic radiations (laser light) in near I.R region when excited with electrical device. Therefore, it infers that the semiconducting device converts electrical energy directly into laser light. An individual emitter in diode laser bars produces a few watts of output power. Diode laser bars

consists of numerous emitters in the form of horizontal and vertical stacks to generate diode lasers with maximum output power in tens of hundreds of kilowatts range. Figure 3.9 shows the high-power fiber-coupled diode laser system. In which, laser is generated from the laser source and passed through the optical fiber. The laser welding system further includes a processing controller to operate the 6-axis robot which is further configured to hold the optical module. Optical module is configured to receive the laser beam from the laser source through optical fiber. Furthermore, the robot's 6th arm is configured to travel along X-Y-Z axes to guide the optical module to focus and scan the laser beam on the sample pieces. The movement of the 6-axis robot in any user-defined direction is controlled by a processing controller.

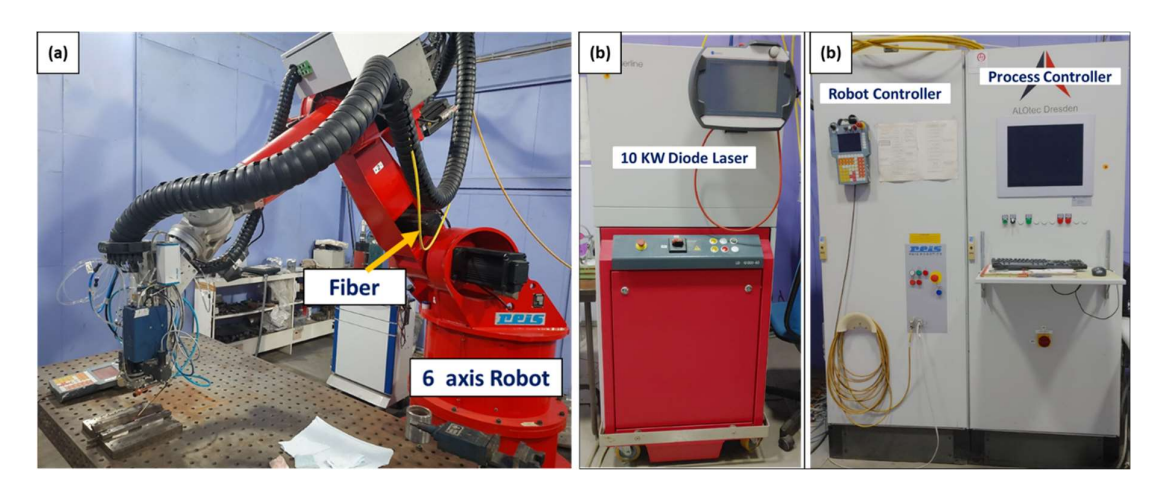


Figure 3.9. (a) High power fiber-coupled Diode Laser system setup (b) 10 kW diode laser and (c) Robot and process controller

In the present study, diode laser welding (DLW) experiments were performed by using a high-power fiber-coupled diode laser system (Model: LDF-10000-60 VGP, Laserline GmbH, Germany) integrated to a 6 + 2 axis robotic workstation (Model: RV40-RSV, Reis Robotics, Germany) and an optical head tailored to deliver circular laser beam spot of 0.9 mm diameter in multi-mode spacial intensity distribution. The laser beam was delivered through an optical fiber of 600 µm core diameter (NA:0.22) fixed to the 6th axis of the robot. The experimental setup used in the study for autogenous single-pass laser welding employing high power fiber-coupled diode laser is shown in Figure 3.9 and the details of process variables and conditions employed are described in Table 3.5. Figure 3.10 shows the optical setup utilized in the present study along with schematic representation of overview of diode laser welding fixturing and process setup.

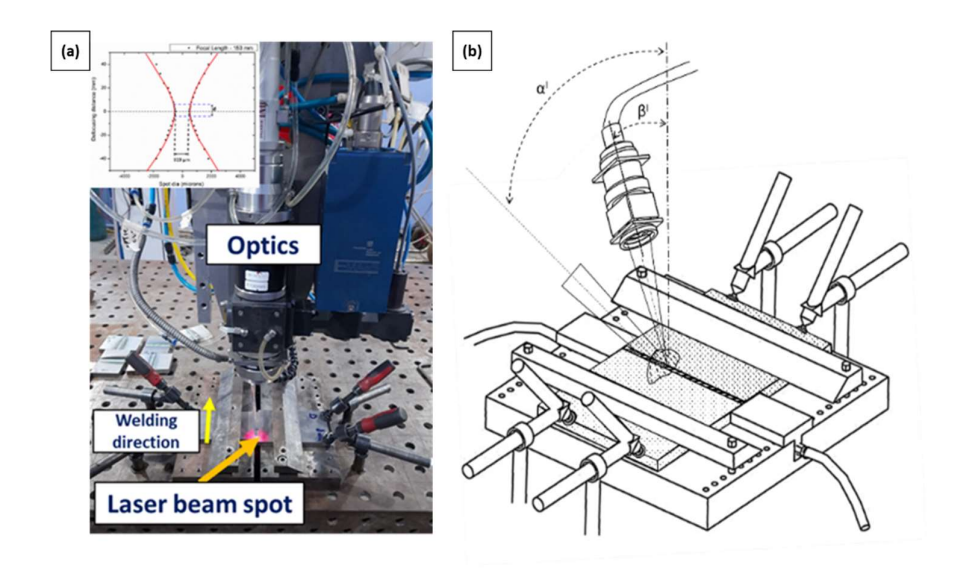


Figure 3.10. (a) Optical setup with inset image of variation in laser spot diameter with defocusing distance and (b) Schematic representation of overview of diode laser welding fixturing and process setup

A combination of collimating focusing optics were arranged in the optical head to produce laser beam spot of 0.9 mm diameter at a fixed working distance of 150 mm (focal length of 150 mm) on the surface of the metal plates to be joined. The defocusing distance in laser welding is generally defined as the distance between the focal plane and the surface of the material. A positive or negative defocus is obtained when laser focal point is above or below the surface of the material and a zero defocus entails focal point exactly impinging on surface of the material.

Table 3.5. Diode Laser welding process variables

Laser type Wavelength Optical fiber Laser beam spot size (Circular) BPP Mode of processing Laser beam angle Focal length	Fiber coupled diode laser 900 – 1070 nm 0.6 mm core dia with NA: 0.22 0.9 mm dia 66 mm mrad CW 3° to vertical 150 mm
Shielding gas Shielding gas pressure Angle of shielding gas nozzle Shielding gas working distance Shielding gas flow rate	Helium 3 bar 45° to vertical 40 mm 3 bar pressure

Prior to conducting experiments, it was felt important to calculate focal depth theoretically (using equations Eqns 3.4 - 3.6) [12-15] and experimentally of the laser beam used for experimentation employing the optical head of the system constituting fiber and collimating/focusing lenses. Wavelength considered as average of 900 - 1070 nm in calculation. The measurement of the laser beam spot size was evaluated by measuring the spot size by measuring burnt spot profile of laser at low power of 100W for a pulse duration of 100 ms passing though the black photographic print paper. Inset image in Figure 3.10 illustrate variation in laser spot diameter with defocusing distance in both directions of positive and negative distances from the focal plane. Laser spot analysis based on photographic print paper burns provided a close approximation in laser spot diameter analysis with focusing distance. Thus, focal depth of the 0.92 mm (measured spot diameter at focus) laser beam measured was found to be 9.8 mm as per burnt spots on photographic prints paper. In Eq 3.6, the tolerance factor p (associated with the condition of laser system and optical setup) could be realised as 1.75 from the approximate variation in spot size by 75% higher to that of spot dimeter at focus with retention of its size within Rayleigh length of the optical system. Substituting this value in the Eq. 3.6, the focal depth of the laser beam could be realised as 9.3 mm. Indeed, values obtained as per burnt spots on photographic paper (9.8 mm) are close to approximation of 9.3 mm focal depth obtained from theoretical assessment using Eq 3.6.

$$M^{2} = BPP.\frac{\pi}{\lambda} \qquad \text{eqn (3.4)}$$

$$Spot \, size \, (s) = \frac{4\lambda f M^{2}}{\pi D} \qquad \text{eqn (3.5)}$$

$$Depth \, of \, focus \, (d) = \frac{8\lambda M^{2}}{\pi} \sqrt{\rho^{2} - 1} \left(\frac{f}{D}\right)^{2} \qquad \text{eqn (3.6)}$$

$$Where, \lambda - \text{wavelength}$$

$$BPP = Beam \, parameter \, product$$

f = Focal length

D = Input beam diameter

ρ = Tolerance factor

Welding was performed by tilting laser beam to an angle of 3° with vertical for effective protection of sensitive optics from the damage due to possible plasma plume and laser beam back-reflections. An additional cross-jet was also provided at the end of optical head with supply of nitrogen gas perpendicular to laser beam to protect optics from dangerous back-reflection effects as well as spatters that are usually generate during welding. A shielding gas

nozzle was attached to the laser head with an angle of 45° with helium gas supply at a 3-bar pressure through its orifice (6 mm diameter) to shield the weld pool from atmospheric contamination. A 40 mm working distance from laser beam spot maintained to provide adequate spread on weld pool for effective protection and at the same time not to exert any force on melt pool. Laser head and shielding gas nozzles were oriented in such a way that the laser leads shielding nozzle during experimentation.

3.5 Response surface methodology (RSM) based statistical modeling:

As RSM statistical modelling of fusion welding processes are well reported in literature, statistical analysis on deep penetration high-power fiber-coupled diode laser welding of thick sections is unknown. Therefore, the present work aims to optimize the deep penetration diode laser welding process parameters to obtain full penetration welds with complete elimination of welding defects such as underfill, undercuts, root sag humps. In this study, laser welding experiments were conducted by using RSM-BBD (Box-Benkhen Design) methodology with three-factor and three-level methodology as shown in Table 3.6. High-power fiber-coupled diode laser welding experimental setup (similar to as explained previously) is shown in Figure 3.11. The statistical analysis software Design-Expert V-11 was utilized for the purpose to generate the design matrix for three-factor and three-level and subsequent analysis of the experimental data.

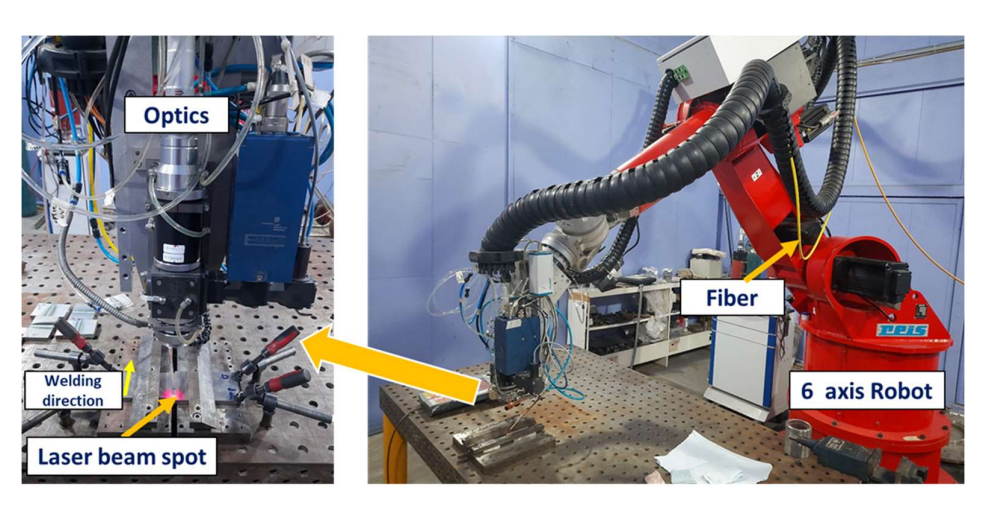


Figure 3.11. High power Diode Laser welding setup and zoom-in image of optics and fixturing setup

Table 3.6. Input process parameters with 3-factors and 3-levels used for BBD experiments

Level	Laser Power (kW)	Welding speed (mm/s)	Defocus distance (mm)	
-1	5	6	-2	
0	5.5	10	0	
+1	6	14	+2	

A sum of 15 experiments were performed based on the three-factor and three-level matrix obtained from RSM-BBD method and their results obtained as shown in Table 3.7. Laser welding critical process parameters such as Laser power (LP), Welding speed (WS) and Defocusing distance (DF) were considered as input variables while other laser welding processing conditions and parameters were maintained constant during experimentation. Analysis of variance (ANOVA) technique was utilized to examine the significance of the developed model and the output responses were corelated with input variables using regression equation [16,17]. The upper bead width (UBW), weld penetration (WP), fusion zone area (FZA) and radius of curvature (ROC) was considered as output responses. Indeed, step-wise regression method during ANOVA technique eliminates the insignificant terms automatically (terms being F<1 and P>0.05) for the developed mathematical model [16,17]. Furthermore, the adequacy of the developed model and its significant terms on linear and quadratic and their interactions were analyzed. Finally, these statistical developed models were utilized to identify the optimize welding process parameters to ensure the desired weld bead. Indeed, full penetration weld with reduced surface underfill and root hump defects and increase ROC to as maximize as possible is the desired criteria in this study.

Table 3.7. Experiments obtained from BBD method based on 3-factors and 3-levels and their results

	Factor 1	Factor 2	Factor 3	Response 1	Response 2	Response 3	Response 4
				Upper	Weld	Fusion	Radius of
	A: Power	B: Speed	C: Defocus	bead width	Penetration	zone area	curvature
Run	kW	mm/s	mm	mm	mm	mm ²	mm
1	6	6	0	8.01	10	34.41	1.64
2	5.5	10	0	6.61	7.23	22.34	1.09
3	5.5	10	0	6.2	7.06	20.3	0.76
4	5	14	0	5.48	5.59	13.37	0.47
5	6	14	0	6.13	6.73	16.66	0.66
6	5.5	10	0	7.28	6.78	20.97	0.66
7	5	6	0	7.72	7.71	26.27	1.24

8	6	10	2	7.17	6.64	19.67	1.06
9	5.5	14	2	6.06	5.54	13.86	0.65
10	5.5	6	2	8.88	6.91	28.71	1.2
11	5	10	2	6.77	5.37	15.84	0.68
12	5.5	14	-2	5.53	6.91	17.33	0.62
13	6	10	-2	6.62	7.76	23.62	1.07
14	5	10	-2	5.93	7	19.06	0.69
15	5.5	6	-2	6.96	10	38.01	1.23

As well known in any welding process optimization, weld bead profile characteristics such as Upper bead width (UBW), Fusion zone area (FZA), and Weld penetration (WP) are known to play a pivotal role in assessing influence of processing parameters on weld quality and joint efficiency. Furthermore, Radius of curvature (ROC) forms at neck zone of weld bead cross-section in laser welded joint is an important bead profile characteristic for assessing liquation cracking susceptibility in Ni-based superalloy. Indeed, higher the ROC lowers the liquation cracking susceptibility [18,19]. Therefore, UBW, FZA, WP and ROC were comprehensively assessed and considered as output responses in the present statistical analysis. Figure 3.12 shows the schematic representation of these four responses evaluated from the resultant cross-sectional macrographs. In order to analyze the weld bead profile characteristics such as UBW, WP, FZA and ROC, welded samples were cut in the transverse direction after laser welding experiments using EDM wire cut and prepared the surfaces according to the metallographic procedure. Macrostructural examination of these cross-sectional metallographic welds was analyzed by employing Opto-digital microscope integrated to imaging software.

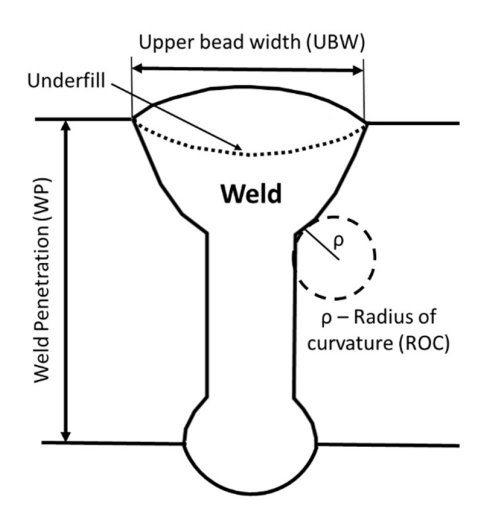


Figure 3.12. Schematic representation of laser weld bead profile showing various weld bead characteristics

3.6 Design of novel joint with setting up of diode laser apparatus for development of novel welding process (ADLW):

As various welding defects such as underfill, undercuts, root sag humps, laser-induced porosity, lack of penetration, lack of fusion and various other metallurgical defects could be realized during deep penetration laser welding of thick Ni-based superalloy. A method for complete elimination of these defects is the need of the hour. Thus, to develop a novel method for diode laser welding of thick sections with complete elimination of welding defects, work to setup high-power diode laser welding has been taken up. The present novel welding method utilize a high-quality high-power diode laser integrated to a 6 + 2 axis robotic workstation (similar to that explained previously), additional fixturing and shielding setup as illustrated in Figure 3.13, for joining thick-section metal plates using a newly designed butt joint configuration for preplacement of solid filler wire / rod followed by two welding steps.

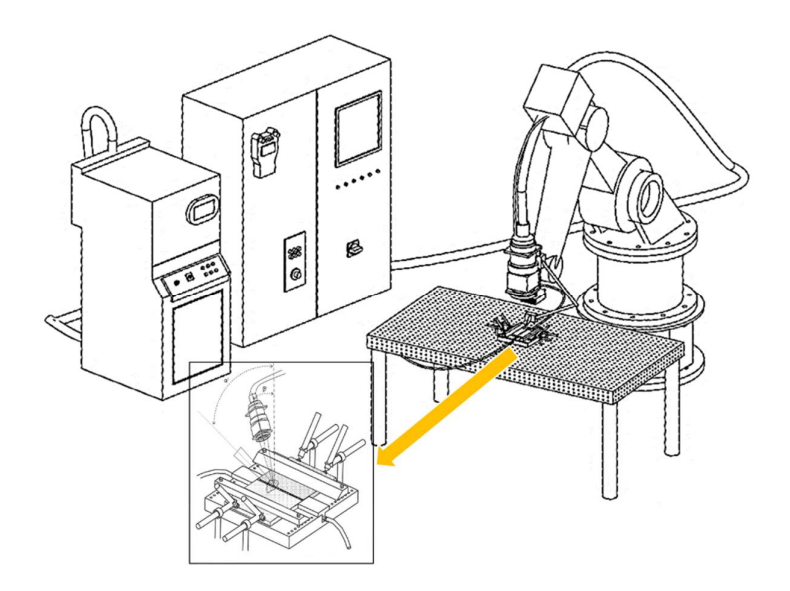


Figure 3.13. Schematic overview of the high-power fiber-coupled diode laser welding experimental setup

Firstly, the edges of the pair of metallic materials plates of similar thicknesses (8 – 12 mm) were machined with suitable joint configuration to form a special top and bottom narrow groove depending on the wire/rod size (Ø 1.2 - 3.2 mm) as shown in Figure 3.14a. A total included angle of a top and bottom groove chosen was $45 - 75^{\circ}$ and $90 \pm 5^{\circ}$ respectively. The depth of the top groove was 1 - 4 mm (based on the filler wire/rod size) so that at least half of the filler wire diameter insert inside the plate-thickness, while the depth of the bottom groove was 0.05 times of plate thickness. Then, a solid filler wire / rod of same type akin to work piece

was aligned and fixed into the top narrow groove with specially designed fixturing setup as shown in Figure 3.14b. Furthermore, typical size of the solid filler wire was \emptyset 1.2 – 3.2 mm diameter depending on plate thickness and groove design. Details of optimized parameters including filler type, size and groove geometry utilized in the present study to weld 10-mm thick Inconel 617 alloy plates is presented in Table 3.8.

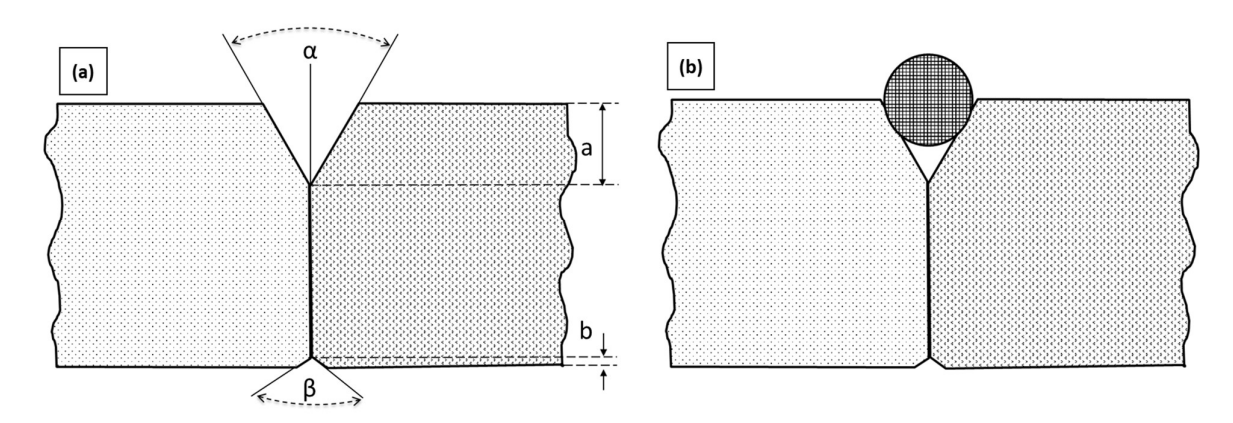


Figure 3.14. Schematic illustration (a) Design of joint configuration and fit up, (b) Filler wire pre-placed in the groove

Table 3.8. Optimized variables for joint configuration and filler wire

Parameters	Values		
Base metal plates	Inconel 617 alloy		
Thickness	10 mm		
Filler material	ER NiCrMo-4		
Filler material size	Ø 3.2 mm		
Included top groove angle (α)	60°		
Included bottom groove angle (β)	90 °		
Depth of top groove (a)	3.6 mm		
Depth of bottom groove (b)	0.5 mm		

Appropriate fixturing setup designed and fabricated with shielding setup for the purpose as shown in inset image in Figure 3.13. Inert shielding gas (helium) was provided by a shielding nozzle to protect from atmospheric oxidation during welding. Furthermore, a backpurging shielding setup was also provided by supplying the same type of shielding gas at the root side of the weld during laser welding. Further, the included angle between the shielding nozzle and its vertical was in the range of $45 - 50^{\circ}$. The developed method involved two-step

welding procedure (tack welding and seam welding). In the first step, filler wire/rod was tack-welded with suitable laser processing parameters (pre-determined laser power and defocusing distance) and conditions (based on plate thickness, groove-design, filler-wire type and size) so that wire/rod completely get spot-welded in between the grooves. The distance between the tacks maintained was in the range of three to four times that of weld tack spot diameter. The filler wire/rod was melted by the defocused laser beam in continuous or pulsed mode with laser power varying in the range of 0.5 - 3 kW, depending upon the size and type of the filler wire utilized under appropriate shielding condition. Figure 3.15 depicts schematic illustration of laser tack welds overview of sample plates. The tack welding was performed in a way that filler wire fuses with minimal melting of work piece plates/parts to the extent sufficiently to entail metallurgical bonding between the wire and the plates without absence of any undulations throughout the groove of the plates and smooth edge fit up.

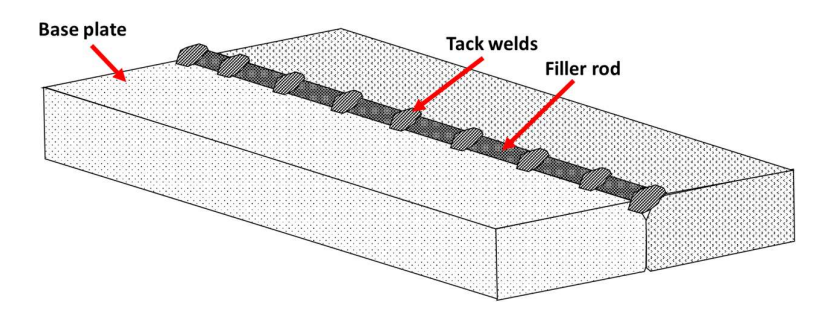


Figure 3.15. Schematic illustration showing Tack welded plate

After laser tack welding, the plates/parts were cleaned with acetone and wire-brush to remove any defects or un-melted or oxidized particles formed if any during tack welding operation. Subsequent to appropriate shielding setup, a specific profiled laser beam of 0.5-0.9 mm diameter is scanned with pre-determined laser power, scanning speed in welding direction and defocusing distance on the assembly constituting tack-welded wire and both plates. Further, the power of the laser beam used in either continuous or modulated mode with 5-6 kW along the weld seam. The schematic setup for laser seam welding process is shown in inset image in Figure 3.13 while schematic illustration of the enlarged portion of laser seam welded overview after producing effective joint is shown in Figure 3.16.

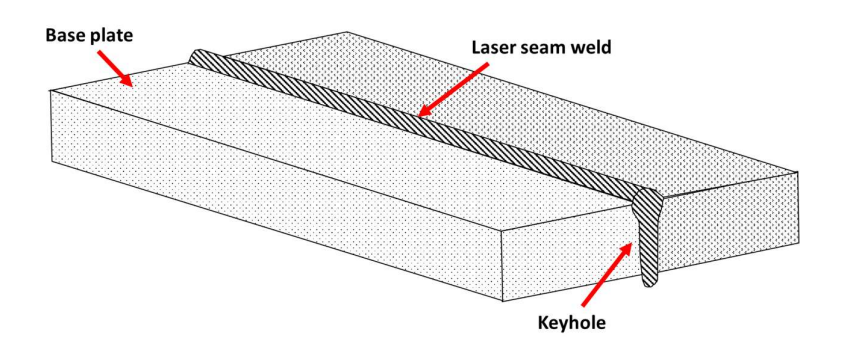


Figure 3.16. Schematic illustration showing Laser seam welded plate

Table 3.9. Optimized process parameters for laser tack and seam welding experiments

OPTIMIZED WELDING PROCESSING PARAMETERS						
Laser	Fiber-coupled diode laser					
Laser spot dia	0.9 mm					
Laser power for Tack welds	2.5 kW					
Defocusing distance for tack welding	1 mm inside wire					
Pulse width	150 ms					
Laser power for seam welding	6 kW					
Defocusing distance for seam welding	1.5 mm inside wire					
Welding speed	6 mm/s					
Shielding gas	100% Helium					
Gas pressure	3 bar					
Defocusing distance for seam welding Welding speed Shielding gas	1.5 mm inside wire 6 mm/s 100% Helium					

After successful laser seam welding operation, the welded coupons were subjected to visual weld quality inspection as well as non-destructive testing (NDT) evaluation employing dye penetrant and radiography methods, followed by metallographic analysis, tensile testing and hardness distribution analysis.

3.7 Characterization of weldments

Subsequent to welding experiments, visual and radiography examination of welds were carried out to check any internal or surface welding defects present in the weldments. Distortion in weldments on both sides of the welds were measured using height gauge. However, magnitude of distortion may not be appropriate by manual calculating method due to clamping of the base plates during welding. After these analyses, the welded samples were cut in

transverse direction to the weld using an EDM wire cut machine and cross-sectional metallographic samples were prepared and polished employing standard metallographic preparation procedure followed by etching using a Kalling's reagent (100ml HCl + 100ml C₂H₅OH + 5g CuCl₂). Welded surface and cross-sectional samples were subjected to various macro, microstructural analysis, hardness distribution and other properties evaluations. The techniques used for characterization and the description are given in the Table 3.10.

Table 3.10. Details of various characterization tools used in the present study

	Facility	Purpose	Model	Manufacturer
1)	Optical Microscope with Image analyzer	Macrostructural analysis (50X 500X)	SZ2-ILST	Olympus Corporation, Japan
2)	Opto-Digital Microscope with Image analyzer	Microstructural analysis (5X 5000 X)	DSX-510	Olympus Corporation, Japan
3)	FE-SEM attached with EDS and EBSD unit	Microstructure, EDS, Elemental Mapping and EBSD analysis	Nova NanoSEM 450	FEI, Netherland
4)	XRD System	Phase analysis	D8 Advance	Bruker AXS, Germany
5)	Micro-focused XRD system	Micro Phase analysis	RAPID-II-D/MAX	RIGAKU Corp., Japan
6)	Automatic Hardness Tester	Vickers hardness measurement	VMH 104	Leica GmbH, Germany
7)	Nano Indentation	Nano hardness measurement	Nano Inc	Oak Ridge, USA
8)	Universal testing machine for Tensile testing	Tensile properties	KUT-40	INSTRON, USA
9)	Impact testing	Impact properties	IT-30	FIE, India
10)	Horizontal tubular furnace Controller – Eurotherm Nanodac TM	Hot corrosion	EPC3016P1	Carbolite Gero, Germany

3.7.1 Bead profile analysis

Figure 3.17 illustrate a typical cross-sectional weld bead profile that is generally obtained in a Laser-based welding processes in Ni-based superalloy with indications of various regions of interest marked schematically. Three distinguishably different regions of interest apart from unaffected base metal (BM) namely, Fusion Zone (FZ) constituting fully melted and resolidified region, partially melted zone (PMZ) constituting dark etched region with eutectic formation next to FZ and finally grey-etched Heat Affected Zone (HAZ) region wherein transformed microstructure without involvement of melting generally form in a typical

weld bead of superalloy material such as Inconel 617. For the ease of understanding to account critical neck zone region of the weld bead profile from other zones, it was felt pertinent to segregate the weld cross-section into three distinguishably different regions longitudinally according to the definition provided in [20], namely upper region, neck region and lower region. Various other weld bead profile characteristics such as weld penetration (WP), upper bead width (UBW), neck bead width (NBW), lower bead width (LBW), Fusion Zone Area (FZA) and radius of curvature (ROC-ρ) were also indicated in Figure 3.17.

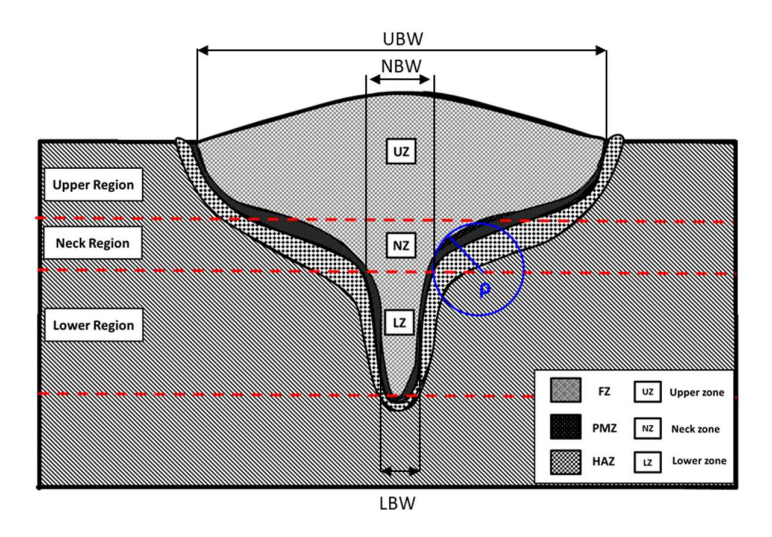


Figure 3.17. Schematic representation of laser-based weld bead profile showing various weld bead characteristics

3.7.2 Macro and Microstructural analysis

For Macro and Microstructural analysis, cross-sectional metallographic welds were etched using Kalling's reagent solution. Prior to analysis, these samples were cleaned ultrasonically to remove any deleterious particles. Then, macro and microstructural examination of these weldments was analyzed by employing Stereo Microscope (Olympus, Model SZ2-ILST, Japan) and Opto-digital microscope (Model DSX-510, Japan) integrated to imaging software and High magnification microstructural analysis were carried out using field emission scanning electron microscopy FESEM (Model FEI Nova NanoSEM 450, Netherlands) equipped with EDS (shown in Figure 3.18) for elemental compositional analysis at different zones of interest comprising fusion zone (FZ), Partially melted zone (PMZ), Heat Affected Zone (HAZ) and Base Metal (BM) as described in Figure 3.17. EDS attached to FESEM was utilized to analyze compositional variation in dendritic boundary, interdendritic region in fusion zone, eutectics in PMZ, partially dissolved carbides in HAZ and surrounding

matrix by using spot-analysis and elemental mapping analysis. Furthermore, EBSD attached to FESEM was utilized to comprehensive study the grain size and grain size distribution in weldments. Image analysis software were utilized to evaluate quantitatively the weld bead characteristics described in Figure 3.17 as well as other critical characteristics such as percentage of phases in fusion zone, quantification of grain boundary re-solidified phases and liquation crack length in PMZ region, grain size and secondary dendritic arm spacing (SDAS).



Figure 3.18. Field emission scanning electron microscope (FESEM) attached to EDS/EBSD

SDAS was evaluated in fusion zone microstructure based on method "D" suggested by Vandersluis et al. [21]. Eqn. 3.7 illustrates the assessment of SDAS.

$$SDAS = \frac{L}{N-1} \qquad eqn (3.7)$$

 $\label{eq:where L-Length of primary arm (center-center) of counted secondary arms and N-Number of secondary arms$

Then by using SDAS values, the cooling rates in the fusion zones were calculated by using the empirical Eqn. 3.8 [7].

$$\lambda = K.R^n \qquad eqn (3.8)$$

Where λ – SDAS, R – Cooling Rate, K and n are material constants.

3.8 Phase analysis

3.8.1 Conventional X-ray diffraction (XRD)

Phase analysis in as-received base material and weldments of Inconel 617 alloy produced by CO₂ laser, diode laser, laser hybrid and conventional TIG methods was carried out using X-ray diffraction system (Bruker AXS, Germany). XRD technique utilizes the patterns obtained from the scattered electrons diffracted from lattice plane of the exposed surface. Each of the crystal plane will diffract with different intensity depending on orientation in the plane. The apparatus is equipped with auto divergence and convergence slit assemblies for constant area analysis, apart from normal fixed slits. The instrument was fine-tuned to high-resolution mode to detect even very low concentration phases and enable accurate positional measurements of Bragg peaks. XRD was performed using a Cu-kα target in the 2θ range of 25 - 80° with a step size of 0.02° under slow scanning speed of 0.1°/ min. For XRD analysis, samples were first cut into a size of 10 x 10 mm at weld center using low-speed Isomet saw and polished with silicon carbide paper and Al₂O₃. Later electro-polishing was performed using a Struers' standard A2 electrolyte solution for ten seconds.

3.8.2 Micro-focused X-ray diffraction (XRD):

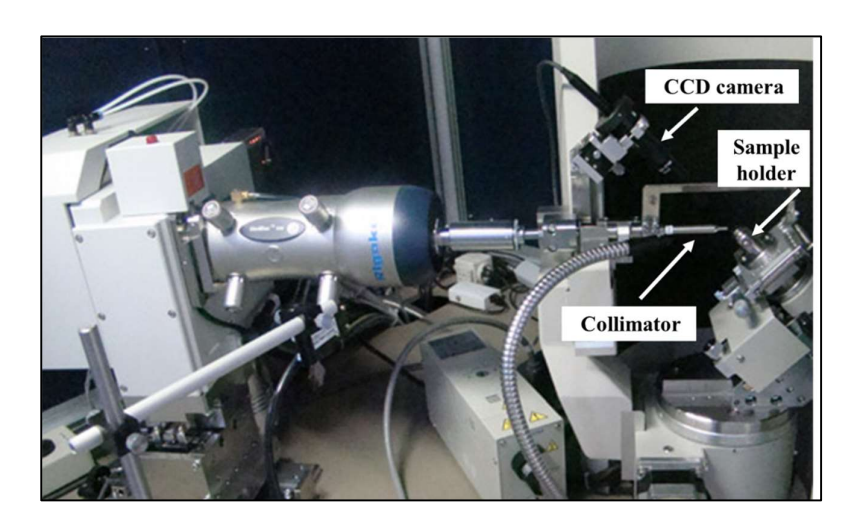


Figure 3.19. Micro-focus X-ray diffraction system (XRD)

Further, to comprehensively identify phases present in critical small regions of weldments, micro-focused X-ray diffraction system was utilized since it assesses with high precision and accuracy. This is the most adaptable laboratory scale XRD system. This system is equipped with high intensity micro-focus rotating anode X-ray source-(Rigaku MicroMax 007HF) with high brightness at the focus point position. This system also constitutes of high sensitive and large image plate based 2D detector, which provides a full scan starting from -47 to +163 degree for 20 in a single exposure even with very small duration of time. In this system,

X-ray beam can focus to a very fine spot in the order of 10, 50, 100 μm and so on (dia) which helps in identifying phases in localized areas. This system can be operated in reflection, transmission and glancing incidence configuration. Further, it also has ability to perform fully automated area mapping using auto stage. This micro-focused XRD system used to evaluate various characteristics such as phase analysis, texture, residual stress, trace phase detection (for phase fraction of 0.1-1% or less) in micro/macro-area apart from thin film analysis in the glancing incidence mode. In the present study, micro-XRD scans were carried out by using D/MAX RAPID II Rigaku Smart Lab system (RIGAKU Corp., Tokyo, Japan) XRD shown in Figure 3.19 with Cu-Kα target and with a spot size of spot of 100 μm diameter. Xrd scans were done both in FZ as well as critical small regions of PMZ and HAZ.

3.9 Mechanical Properties of Weldments

3.9.1 Hardness analysis:

3.9.1.1 Conventional: Microhardness testing at 200gf load with a diamond base pyramid indenter on as-received base material as well as welded samples of Inconel 617 alloy carried out with an automatic digital Vickers micro-hardness testing facility (Model VMH 104, Lieca GmbH, Germany) as mentioned in Table 3.10. The system is equipped with various indenter (Vickers and Knoop) and can be used with loads ranging from 1 – 2000gf and variable objective lens (10 – 100X). Hardness measurements were carried out across the fusion, PMZ/HAZ and BM with a dwell time of 15 sec. An average of three readings reported for the purpose. A minimum of three times of indentation diagonal distance was always maintained between two indents every time when hardness measurements were undertaken in the samples.

3.9.1.2 Nano Indentation:

Nano indentation also known as depth sensing indentation techniques was first proposed and developed by Oliver and his co-workers [22]. It works on the basis of the theory of elastic-mechanic contacts. This test measures the mechanical properties of any materials by impinging the Berkovich indenter into the surface of the test specimen under predefined load and hold it before unloading. Based on the load-displacement curve, the hardness and elastic modulus of the material can be evaluated by taking the slope of the unloading curve and the ratio of the peak force to the projected contact area of the indent respectively. This technique is not only a simple extension of conventional micro-hardness test but also various other information such as creep, fracture toughness and residual stress etc at nano level can be

evaluated from load-displacement data. Nano indentation testing is now become popular for evaluating hardness of the thin film coatings as it limits the depth of indentation to remove the surface effects and other surface mechanical characteristics [23].

In the present study, as hardness of the localized micro-level regions such as Low-Melting Eutectics (LME) and GB carbides is difficult to measure by Vickers hardness tester, high speed Nano-indentation testing was carried out using advanced Nano-Indentation system (Nano mechanics Inc., Oak Ridge, USA) as shown in Figure 3.20 at an applied load of 2 mN. The distance between the indents maintained was one micrometer. Nano indentation maps of area $30 \times 30 \ \mu m^2$ constituting 900 indents per map were collected and analyzed for understanding phase distributions. Additionally, elastic modulus maps were also measured to assess mechanical strength of individual phases present in weld microstructures.



Figure 3.20. High speed Nano Indentation system

3.9.2 Tensile and Impact tests:

Joint efficiency with tensile properties evaluation of welded joints as well as substrate material were evaluated by subjecting to room temperature tensile testing employing a universal tensile testing machine (INSTRON Model 5584) shown in Figure 3.21a. Crosshead speed of 1 mm/min was maintained constant during testing. Prior to tensile testing, butt joint specimens were subjected to surface grinding to remove surface defects of underfill/root sag and camber present if any. Welded as well as substrate tensile test coupons were prepared according to ASTM E8 standard. Welded samples were extracted perpendicular to the weldment as shown in Figure 3.21b and the details of sample dimension is shown in Figure 3.21c. After tensile test,

fractured samples were examined using FESEM to assess mechanism of fracture and its morphology.

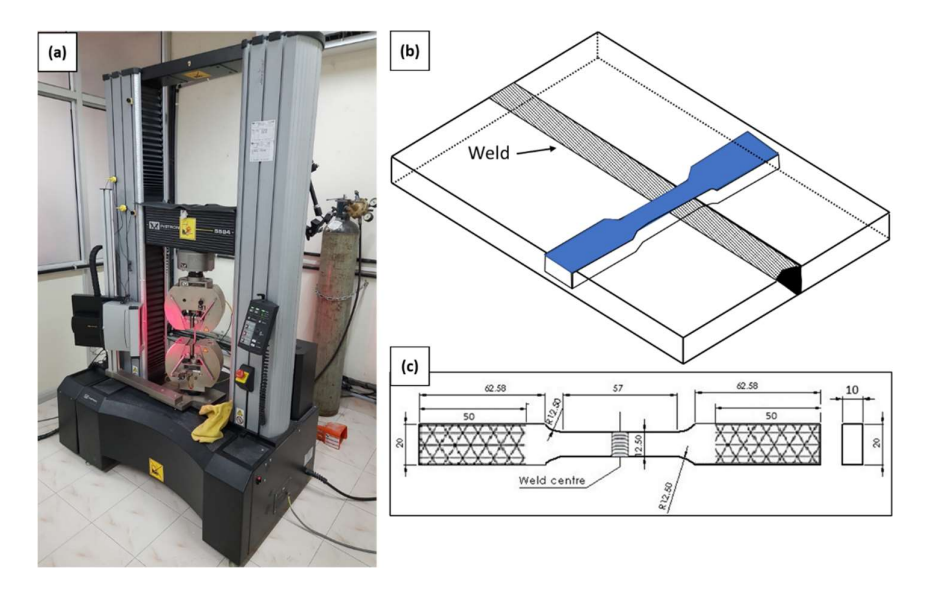


Figure 3.21. (a) Universal tensile testing machine, (b) Samples extracted from welded plates and (c) Transverse tensile test specimen as per ASTM E8 (All dimensions in mm)

Furthermore, the Impact energy of the cross-weld specimens along with as-received BM were evaluated by using Impact testing machine as shown in Figure 3.22a. Amount of energy required for sample failure were recorded for each sample. Average of three samples were considered. The test specimens were prepared according to the ASTM E23-18 standard and the dimensions are shown in Figure 3.22b.

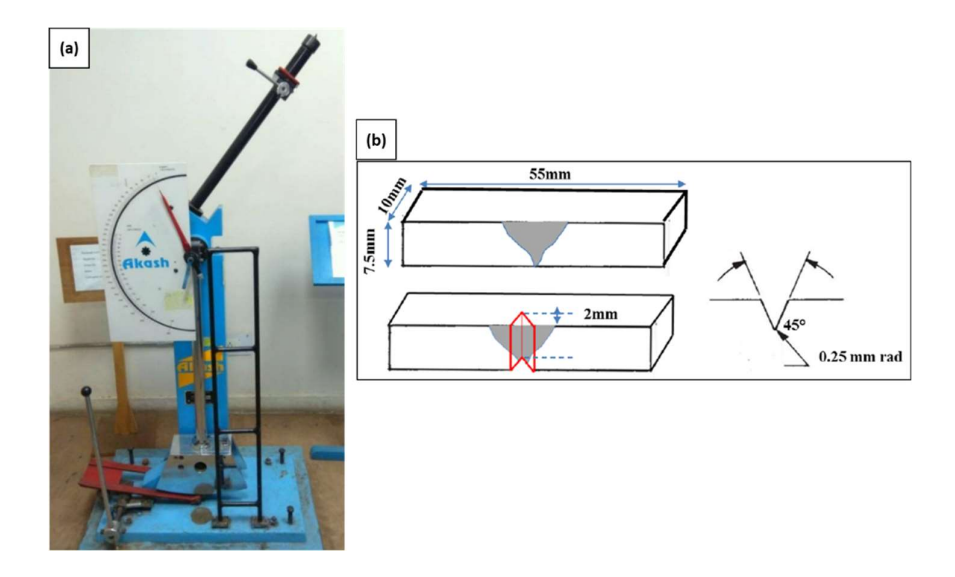


Figure 3.22. (a) Impact testing machine, (b) Impact test specimen as per ASTM E23-18 (All dimensions in mm)

3.10 Hot corrosion analysis of weldments

As mentioned, Inconel 617 superalloy intended to be used in future boiler components such as superheater, reheater tubes wherein high-temperature corrosion is one of the important characteristics to be assessed. Therefore, high-temperature corrosion behaviour under coal-ash and salt-environments of the weldments as well as as-received base metal were studied in a horizontal tubular furnace as shown in Figure 3.23 simulating boiler power plant environment. The USC power plant environment was simulated by combining synthetic coal-ash and a flowing synthetic flue gas mixture. The synthetic coal-ash consisted of Fe₂O₃ (6 %) + 1.6 % $K_2SO_4 + Al_2O_3$ (30 %) + SiO₂ (60 %) + 0.4 % $Na_2SO_4 + TiO_2$ (2 %). The salt composition consisted in the ratio of Na_2SO_4 : K_2SO_4 : NaCl - 75:24:1. The synthetic flue gas mixture composed in the ratio of CO_2 cylinder – N_2 : CO_2 : $O_2 - 75.99$: 3.44: 20.57 and SO_2 cylinder – SO_2 : $N_2 - 0.134$: 99.866. The synthetic flue gas mixture was passed through the furnace tube at a flow rate of 100 ml/min.

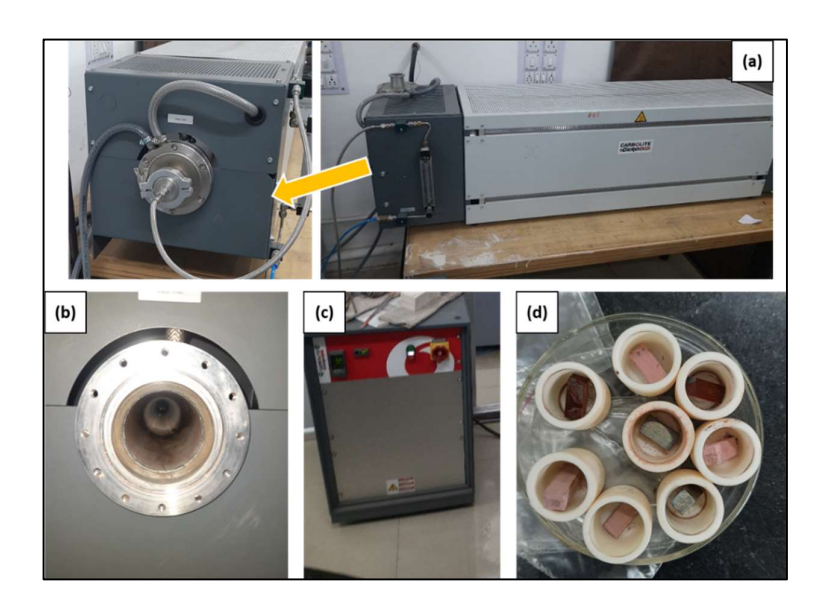


Figure 3.23. (a) Horizontal tubular furnace for hot corrosion study (b) inside view, (c) controller and (d) samples placed in the crucible

Initially, samples were cut using an EDM wire cut machine of size 20 x 7 x 5 mm cross-sectionally to the weldments. Then each sample was polished metallographically by using SiC emery grit papers upto 1000, followed by rinsed with distilled water and then cleaned with acetone. The synthetic coal-ash was prepared by mixing with distilled water and then subjected to ultrasonicator to form a slurry with proper mixing of the ingredients. Then the samples for coal-ash coated study were coated with coal-ash slurry by using a smooth painting brush.

Weight of the slurry on each sample must be atleast 3-5 mg/cm² of the specimen surface area. Subsequent to coating, the coated specimens were subjected to preheating at a temperature of 200°C to remove moisture. After preheating, the samples were placed in alumina crucible (shown in Figure 3.23d) and weight prior to expose in the furnace. Similar procedure was applied for salt-coated specimens. After measuring weight of each sample along with crucible, the samples were placed in the furnace for corrosion study. Cyclic hot corrosion test was carried out at a temperature of 600°C for 1000 hours with 5 cycles (200, 400, 600, 800 and 1000 hours). After each exposure cycle the weight change was measured with 0.1 mg accuracy analytical weighing balance. After 1000 hours exposure time, each test specimens were thoroughly analyzed using XRD, SEM and EDS. The corrosion rate was determined in terms of thickness of corroded layer formed at the end time and its characteristic in terms of elemental phase analysis and composition assessed by employing XRD and EDS.

3.11 References

- 1. Klöwer, J. "Alloy 617 and derivatives." In Materials for Ultra-Supercritical and Advanced Ultra-Supercritical Power Plants, pp. 547-570. Woodhead Publishing, 2017
- 2. Inconel 617 alloy datasheet, Special metals corporation, 2005
- 3. SB168, Section II, Part B, Nonferrous material specifications, ASME Boiler and Pressure Vessel Code, 2010, 213–226.
- 4. Pavan, A. H. V., K. S. N. Vikrant, R. Ravibharath, and Kulvir Singh. "Development and evaluation of SUS 304H—IN 617 welds for advanced ultra-supercritical boiler applications." Materials Science and Engineering: A 642 (2015): 32-41.
- 5. Tytko, Darius, Pyuck-Pa Choi, Jutta Klöwer, Aleksander Kostka, Gerhard Inden, and Dierk Raabe. "Microstructural evolution of a Ni-based superalloy (617B) at 700 C studied by electron microscopy and atom probe tomography." Acta materialia 60, no. 4 (2012): 1731-1740.
- 6. Sun, Junhao, Wenjie Ren, Pulin Nie, Jian Huang, Ke Zhang, and Zhuguo Li. "Study on the weldability, microstructure and mechanical properties of thick Inconel 617 plate using narrow gap laser welding method." Materials & Design 175 (2019): 107823.
- 7. Ren, Wenjie, Fenggui Lu, Renjie Yang, Xia Liu, Zhuguo Li, and Seyed Reza Elmi Hosseini. "A comparative study on fiber laser and CO2 laser welding of Inconel 617." Materials & Design 76 (2015): 207-214.
- 8. Benyounis, K. Y., A. G. Olabi, and M. S. J. Hashmi. "Effect of laser welding parameters on the heat input and weld-bead profile." Journal of materials processing technology 164 (2005): 978-985.
- 9. Kou, Sindo. "Welding metallurgy." New Jersey, USA 431, no. 446 (2003): 223-225.
- 10. Üstündağ, Ömer, Sergej Gook, Andrey Gumenyuk, and Michael Rethmeier. "Hybrid laser arc welding of thick high-strength pipeline steels of grade X120 with adapted heat input." Journal of Materials Processing Technology 275 (2020): 116358.
- 11. Fuerschbach, P. W. "Measurement and prediction of energy transfer efficiency in laser beam welding." Welding Journal 75, no. 1 (1996)
- 12. Steen, William M., and Jyotirmoy Mazumder. Laser material processing. springer science & business media, 2010.

- 13. Wandera, C., and Veli Kujanpää. "Optimization of parameters for fibre laser cutting of a 10 mm stainless steel plate." Proceedings of the Institution of Mechanical Engineers, Part B: Journal of Engineering Manufacture 225, no. 5 (2011): 641-649.
- 14. online website http://www.rsoptics.com/zznlshow.asp?id=223.
- 15. O'Neill, W., M. Sparkes, M. Varnham, R. Horley, M. Birch, S. Woods, and A. Harker. "High power high brightness industrial fiber laser technology." In International Congress on Applications of Lasers & Electro-Optics, vol. 2004, no. 1, p. 301. Laser Institute of America, 2004.
- 16. Montgomery, Douglas C. Design and analysis of experiments. John wiley & sons, 2017.
- 17. A. Khorram, M. Ghoreishi, CO2 laser welding of Ti6Al4V alloy and the effects of laser parameters on the weld geometry, Lasers Eng. 21 (2011) 135–148.
- 18. Nishimoto, K., I. Woo, T. Ogita, and M. Shirai. "Factors affecting HAZ cracking susceptibility of laser welds. Study of weldability of Inconel 718 cast alloy (4th report)." (2001): 965-972.
- 19. Gao Z. Numerical modeling to understand liquation cracking propensity during laser and laser hybrid welding (I). The International Journal of Advanced Manufacturing Technology. 2012;63(1):291-303.
- 20. Shinozaki K, Kuroki H, Luo X, et al. Effects of welding parameters on laser weldability of Inconel 718. Study of laser weldability of Ni-base, heat-resistant superalloys (1st Report). Welding international. 1999;13(12):945-951
- 21. Vandersluis E, Ravindran C. Comparison of measurement methods for secondary dendrite arm spacing. J Metallography Microstructure and Analysis. 2017;6(1):89-94
- 22. Oliver WC, Pharr GM. An improved technique for determining hardness and elastic modulus using load and displacement sensing indentation experiments. J Mater Res. 1992;7(6):1564–83
- 23. Wang, Haidou, Lina Zhu, and Binshi Xu. Residual stresses and nanoindentation testing of films and coatings. Springer, 2018.

Comprehensive study on process optimization of CO₂ Laser and CO₂ Laser-MIG Arc Hybrid welding of Inconel 617 alloy

4.1 Introduction

The first task was to assess the feasibility of welding Inconel 617 alloy by employing autogenous CO₂ laser welding (ALW) and CO₂ laser + MIG hybrid welding (LHW) techniques. Hence, bead-on-plate (BOP) welding configurations used to assess the influence of heat input in both ALW and LHW processing. Optimization of laser and laser-hybrid welding processes of this superalloy has been carried out using comprehensive microstructural and hardness distribution analyses of weldment employing ALW and LHW techniques. Study taken up to investigate the effect of heat input on both ALW and LHW of Inconel 617 alloy. Thus, comprehensive analysis of various weld bead profile characteristics along with critical Radius of Curvature (ROC) has been taken up in this chapter (as it determines liquation cracking susceptibility at neck zone) akin to several studies reported on superalloy [1-6]. Subsequent to welding, analysis of various bead profile characteristics such as weld bead width, weld penetration depth, fusion zone area, depth-to-width aspect ratio, along with fusion zone microstructure, secondary dendritic arm spacing (SDAS), cooling rates, hardness distribution, and width of HAZ is comprehensively explained in this chapter.

4.2 Experimental Methodology

The base material selected for the entire present investigation is a solid-solution strengthened Nickel based superalloy Inconel 617 in a form of plate of thickness 10 mm in solution-annealed condition with a nominal composition as tabulated in Table 3.1. Bead on plate (BOP) welding experiments were carried out using Autogenous CO₂ laser welding (ALW) and CO₂ laser + MIG hybrid welding (LHW) processes. The Laser-MIG hybrid welding setup employed for the experimentation was shown in Figure 3.7 and the process variables were depicted in Table 3.4. Welding process parameters with a fixed laser power of 3.5 kW (maximum available with CO₂ laser system) and varying welding speed in the range of 0.6 – 1.0 m/min employed for BOP welding experiments is presented in Table 4.1. Further, heat input calculations were done by using equations 3.1 – 3.3 and SDAS and cooling rates were evaluated by using equations 3.7 and 3.8 respectively as showed in chapter 3.

Table 4.1. Process parameters of LHW and ALW BOP welding experiments

Process	Sample ID	Laser Power (kW)	Welding speed (m/min)	Wire feed rate (m/min)	Heat Input (J/mm)
Lagar MIC	LHW 1		1		480
Laser–MIG Hybrid	LHW 2	3.5	0.8	8	630
	LHW 3		0.6		820
Autogonoug	ALW 1		1		190
Autogenous Laser	ALW 2		0.8	-	260
	ALW 3		0.6		315

4.3 Bead profile analysis

Cross-sectional weld bead profile analysis in any fusion weld joint is essential for understanding its strength and weldability. Detailed bead profile analysis by cross-sectional macroscopy has been taken up for the purpose. As the principal aim of the study is to assess the influence of heat input on weld bead profile characteristics, wide variation of heat input in the range of 190 - 820 J/mm was adopted for experimentation under bead-on-plate configuration with employment of both ALW and LHW methods. Further to explain influence of mode of welding (conduction/keyhole) with type of welding process (ALW/LHW) on weld bead profile in conjunction with heat input, it was felt pertinent to explain the mechanism of weld bead formation at various stages with schematic representation as depicted in Figure 4.1. Indeed explaining this schematic at various stages in bead profile help facilitate evaluating an important critera termed as ROC, determined as "\rho" in our case, as it was observed to directly affect liquation cracking suceptability at neck zone as reported by several studies on superalloy [3-6].

Figure 4.1 (e) illustrate a typical weld bead profile that is generally obtained in a LHW process involving two heat sources of laser and conventional MIG or TIG. Three distinguishably different regions of interest namely, FZ constituting fully melted and resolidified region, PMZ constituting dark etched region with eutectic formation next to FZ and finally grey-etched HAZ region wherein transformed microstructure without involvement of melting generally form in a typical weld bead of superalloy material such as Inconel 617. The bead profile will be generally of wine-cup shape in high energy density welding processes such as LHW with wide face at top and narrow bottom. The laser source being intense and high

intensity allow for deep and narrow penetration with keyhole, whereas, MIG source induce lateral spread in fusion bead with predominantly conduction mode. Thus bead width at upper face region (Wupper) will be wider with low depth-to-width aspect ratio in LHW as compared to that of ALW, although depending on the heat input and material coupling, the bead profile varies to a great extent. Apart from the specified cross-sectional weld bead profile dimensions of FZ, other characteristics such as FZ area, depth-to-width aspect ratio, PMZ and HAZ characterictics are also found to greatly influence strength of joint and other properties of the weldment.

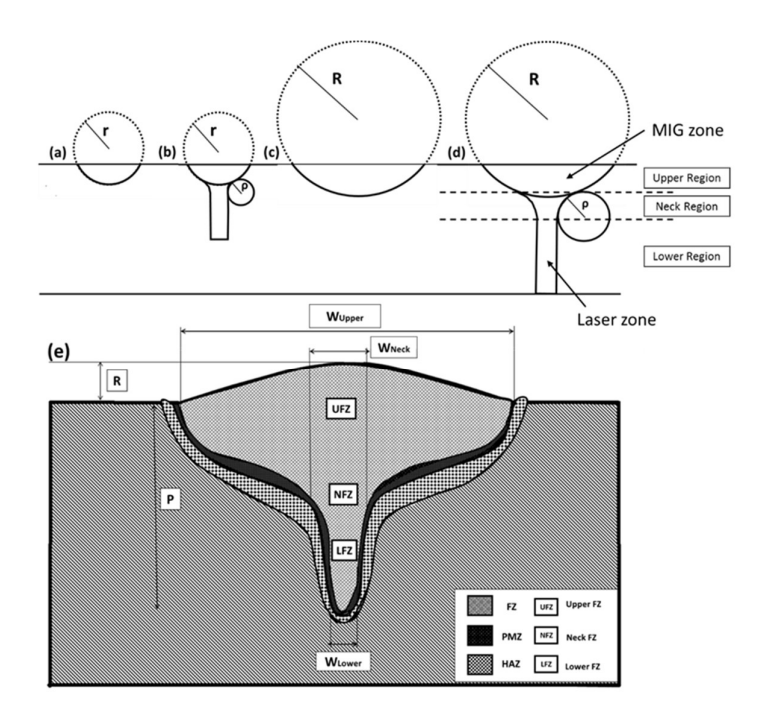


Figure. 4.1: Schematic representation of (a) Laser conduction mode (b) Laser keyhole mode, (c) MIG arc mode (d) Laser-MIG Hybrid mode, and (e) Laser-MIG hybrid weld bead geometry

Notwithstanding the influence of various bead profile charcateristics, ROC was found to be most influencing in laser and laser-hybrid welding process, more specifically when the material involved is a Inconel 617 superalloy due to PMZ formation and susceptibility to liquation cracking. Figures 4.1 (a-d) illustrate typical schematic profiles that could evolve at various stages in ALW and LHW methods. Figure 4.1 (a) illustrate typical weld bead that forms in case of autogenous laser welding when processed in conduction mode with no protrusion of keyhole (absence of "\rho", the ROC at neck zone) and hypothetical radius (r) produced in this case will be generally low. When the energy density increase due to increase in heat input to a

level beyond threshold level wherein strong evaporation occurs on the melt surface, the recoil pressure developed will be sufficient to induce a deep narrow depression through the thickness of material, indicating keyhole effect. In such case, ROC " ρ " will evolve at the neck zone intersecting conduction and keyhole modes of fusion zones (depicted in Figure 4.1 (b)). A keyhole in laser welding is a unique phenomenon which includes various factors such as multiple reflections, Fresnel absorption, recoil pressure and pressure due to surface tension [7]. Welds obtained by keyhole mode welding entail high aspect ratio (depth-to-width). However, in case of LHW processes, as two different heat sources of laser and MIG act simultaneously onto the material surface, a broadened weld bead width with deeper weld penetration profile evolve as shown in Figure 4.1 (d) as compared to a simplified semispherical bead in case of only MIG welding with reasonably low heat input energy (as depicted in Figure 4.1 (c)).

For the ease of understanding to account critical neck zone region of the weld bead profile from other zones, it was felt pertinent to segregate the weld cross-section into three distinguishably different regions longitudinally according to the definition provided in [4], namely upper region, which extended from the upper bead surface to the upper point of contact between the two circles lying on fusion line. The upper region is a wide fusion region predominantly comprising of MIG effect in case of LHW and laser alone in ALW. Neck region extends from the curved contour region of upper circle and lower points of contact between the two circles of the bead cross-section. In case of LHW, neck zone is considered to be the combined effect of laser as well as MIG, whereas in case of ALW it is alone due to laser heat source. Lower region is the narrow region with heat effect of predominantly laser induced penetration region covering the remaining region from the lower point of contact. Apart from the above geometrical features of weld bead profile, area of FZ, area of HAZ, depth-to-width aspect ratio, width of HAZ at maximum heat stagnation (near neck region), defined as HAZ_{max}, intersecting conduction and keyhole regions of ALW or laser and MIG FZs of LHW are also evaluated to comprehensively understand the effects due to heat input variation and heat sources. Evaluation of these profile parameters were assessed based on the criteria adopted by several studies reported on laser and laser-hybrid welding of various materials [3-6].

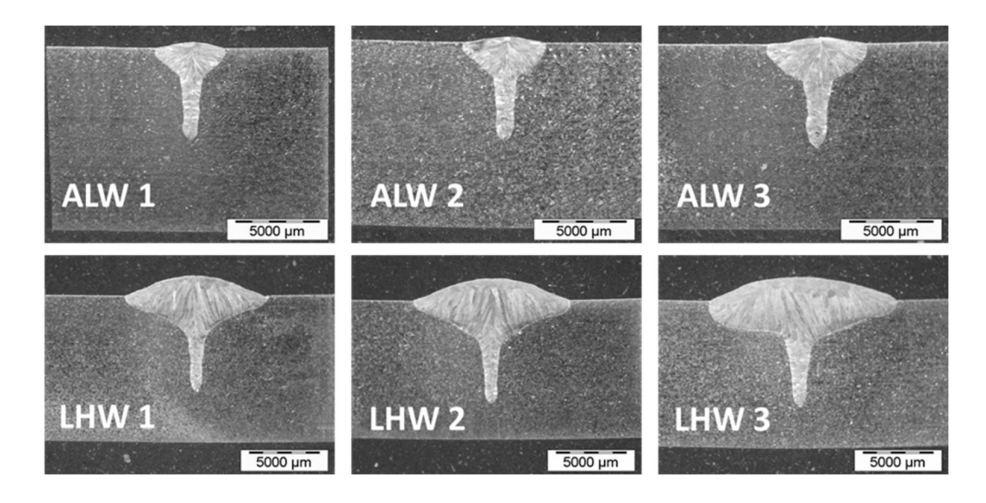


Figure. 4.2: Macrographs of ALW and LHW welds at different heat input conditions

Figure 4.2 depicts the cross-sectional weld bead macrographs obtained in both ALW and LHW processes with variation of heat input ranging from 190 – 315 J/mm in former and 480 – 820 in later. Table 4.1 depicts processing parameters employed for bead-on-plate experimentation. As welding speed affects the weld quality more than that of laser power since it influences weld bead profile, all experiments were conducted at a fixed laser power of 3.5 kW, maximum available with the CO₂ laser system, in case of both ALW and LHW and varying welding speed of 0.6 - 1.0 m/min. The influence of two different welding processes of ALW and LHW, on weld bead formation is clearly discernible in macrographs presented in Figure 4.2. In LHW, bead profile illustrates a typical "wine-cup" shape with the wider and shallower upper zone which is of similar morphology to that of the arc welds and a narrow deeper lower zone which is in accordance to that of laser welds is due to the combined synergitic effect of laser and arc sources. ALW bead profile shows a typical Y-shape bead, shallower at top and narrower at the root, plausibly, due to the small concentrated CO₂ laser beam of diameter 180 μm. Weld bead profiles obtained in the processes are associated with intensity distribution profiles of heat sources as reported by several works involving laser and laser-hybrid welding of metallic materials [8-10].

Figure 4.3 illustrates the influence of heat input in both ALW and LHW processes on various bead profile geometrical features evaluated constituting weld bead widths and depth of penetration as well as areas of FZ and HAZ zones obtained from the weld cross-sectional macrographs. It is clear that due to the addition of MIG source in LHW, the upper fusion zone (UFZ) width obtained was three times larger than that of ALW, although with a sluggish extent of depth of penetration. Indeed the marginal improvement of 1.2-1.3 mm in penetration depth

due to the addition of laser source in LHW is discernible on account of narrow laser-focus based heat input as compared to that of ALW. Marginal improvement of penetration depth in LHW even when the heat input is enhanced by combining MIG arc with laser beam indicated that the MIG arc merely heats up the metal surface, whereas laser determines depth of penetration.

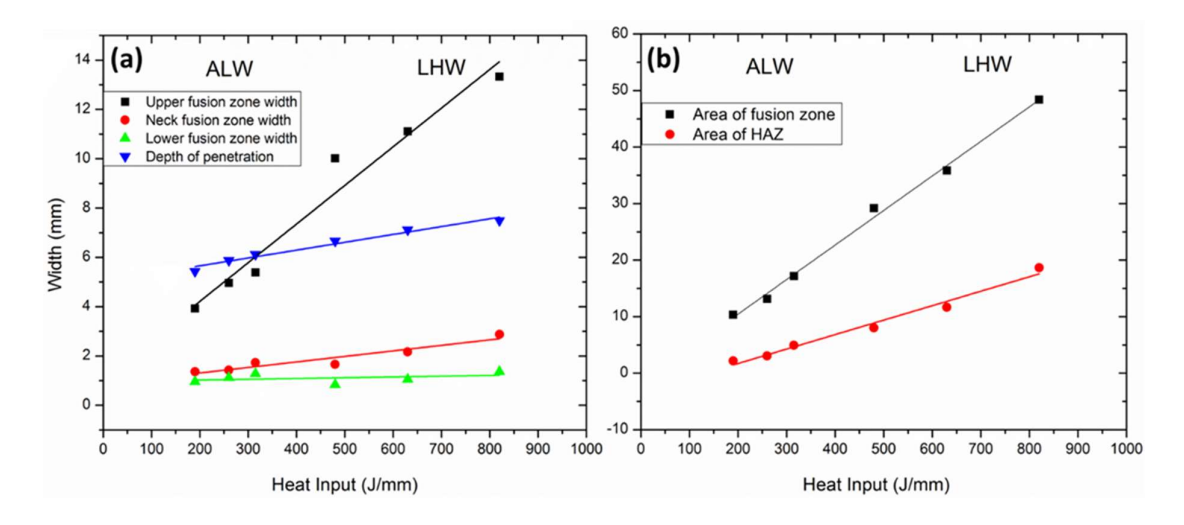


Figure. 4.3: Effect of heat input on (a) weld bead geometry, and (b) Area of fusion zone and HAZ

Apparently, the reinforcement was also found to be higher in LHW (can be seen in Figure 4.2) as compared to that of ALW weld beads. This can be attributed to the filler addition in case of LHW. Apparently, bead width evaluated at all zones of upper, lower and neck regions of FZ and depth of penetration increased with increase in heat input. However, the extent of increase was gentler in case of penetration depth and neck/lower fusion widths associated with laser source effect with not much effect of depth-to-width aspect ratio. Indeed, due to marginally small variation in welding speed (0.6-1.0 m/min), significant attenuation in laser beam energy by plasma could be visualized. Consequently, stabilization of weld pool obtained could be optimum with variation in heat input within the range adopted for experimentation for better weld quality and seam consistency. Other researchers also reported similar effects of weld bead geometry with variation in heat input in laser and laser-hybrid processes [8-10].

Despite with production of defect-free weld joints, it is well known that the cross-sectional area of FZ and HAZ surrounding it greatly influence joint properties of strength, stress condition and distortion. Thus, the influence of heat input and type of welding process on weld bead profile in terms of weld FZ and HAZ (surrounding both PMZ and HAZ) areas are calculated and presented in Figure 4.3b. It is clear that both FZ and HAZ areas are found to

increase with the increase in heat input as a direct consequence in both ALW and LHW processes. FZ area nearly doubled from 10 sq. mm to 17 sq. mm with an increase in heat input from 190 to 315 J/mm in case of ALW, whereas it enhanced from 29 sq.mm to 48 sq.mm with an increase in heat input from 480 to 820 J/mm in LHW. Indeed, a small amount of FZ area with high aspect (depth-to-width) ratio is the unique characteristic of laser beam welding process on account of keyhole effect with highly concentrated laser energy source. Large amount of weld metal in LHW as compared to that of ALW resulting in wider upper bead width help facilitate in gap bridegability at the expense of joint strength. A similar trend could be observed in variation of HAZ area with respect to heat input. Despite high variation in FZ area in LHW, the extent of increase in penetration is rather monotonic and slow as compared to that observed in ALW. This could be attributed to less hindrance of plasma in ALW as compared to that of LHW. In other words, the small plasma/vapor absorption does not interrupt laser energy penetration into the substrate effectively in the ALW process. Similar observations to the effect of weld bead profiles in terms of fusion and HAZ area with variation in heat input were reported in several welding studies [8-10]. Indeed, these aspects are found to greatly influence thermal gradient profile, stress-strain distribution, and ROC along solid-liquid fusion boundary and microstructure explained later.

4.4 Microstructure and hardness distribution analysis

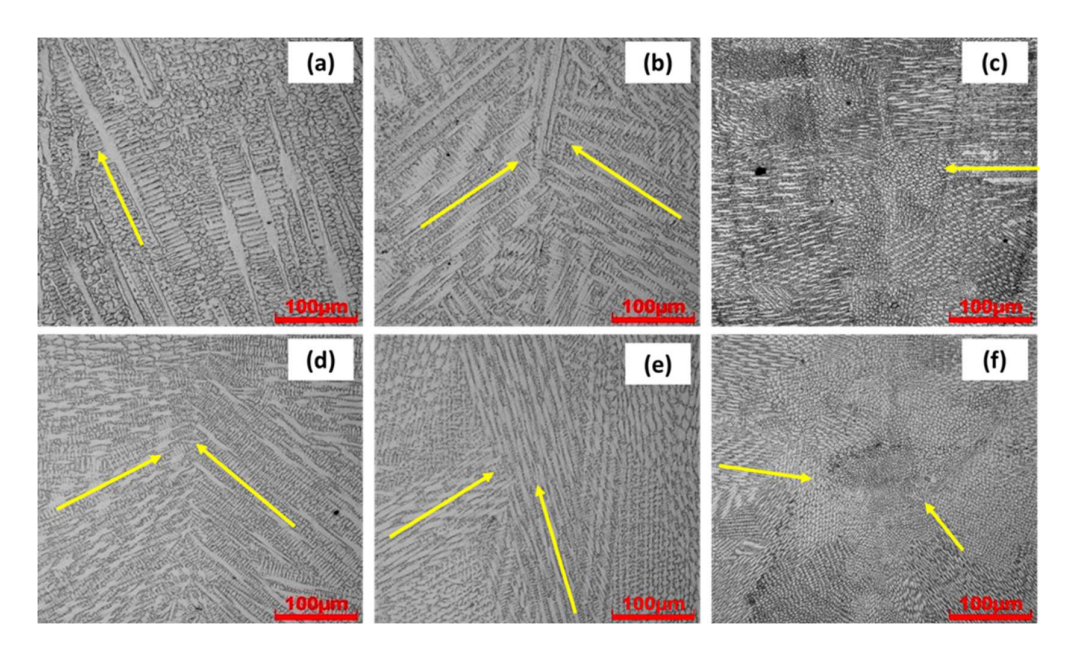


Figure. 4.4: Optical micrographs in various regions (a) UFZ, (b) NFZ, (c) LFZ of LHW, (d) UFZ (e) NFZ, and (f) LFZ of ALW,

UFZ – Upper fusion zone, NFZ - Neck fusion zone, LFZ – Lower fusion zone

Figure 4.4 elucidates optical micrographs of various regions of upper, lower and neck within central weld fusion line in both ALW and LHW. It can be seen that columnar/cellular dendrites of γ-Ni grew in direction of welding and converged towards the weld central line as in the direction of heat flow. However, the coarser columnar/cellular dendritic microstructure was observed in UFZ of LHW in comparison with UFZ of ALW, presumably, due to prevailing high peak temperature and low cooling rate in LHW than ALW as reported study by Tomasz Kik [11]. The cooling rate evaluated from SDAS and explained previously facilitated in understanding its influence on microstructural coarsening and segregation effects. Indeed, LHW process induced 25% higher peak temperature and thereby extended cooling time by three-times as compared to that of ALW. Thus, FZ microstructure, morphology of dendrites, and micro-segregation of elements in inter-dendritic regions influenced by cooling rate, presented in Figure 4.5, are found to vary distinguishably different due to variation in heat inputs associated with LHW and ALW processes. It is clear from Figure 4.5e that the cooling rate decrease with increase in heat input in both LHW and ALW. In the UFZ, the cooling rate is in the range of $0.2 - 0.35 \times 10^5 \text{ K/s}$ in LHW and $1.25 - 1.55 \times 10^5 \text{ K/s}$ in ALW, which are in good agreement with the previously reported studies on Inconel 617 alloy [8]. Significant reduction of cooling rate in UFZ of LHW (0.22 x $10^5 - 0.35$ x 10^5 K/s) as compared to that of ALW $(1.26 \times 10^5 - 1.54 \times 10^5 \text{ K/s})$ on account of addition of MIG arc in case of LHW process. Apparently, no obvious variation in cooling rates observed between lower fusion zones (LFZ) of LHW and ALW welds. Whereas, variation of cooling rate still observed in NFZ between LHW and ALW processes (shown in Figure 4.5e), indicating that the NFZ of LHW is the combined effect of MIG and Laser resulting in lower cooling rates compared to NFZ of ALW.

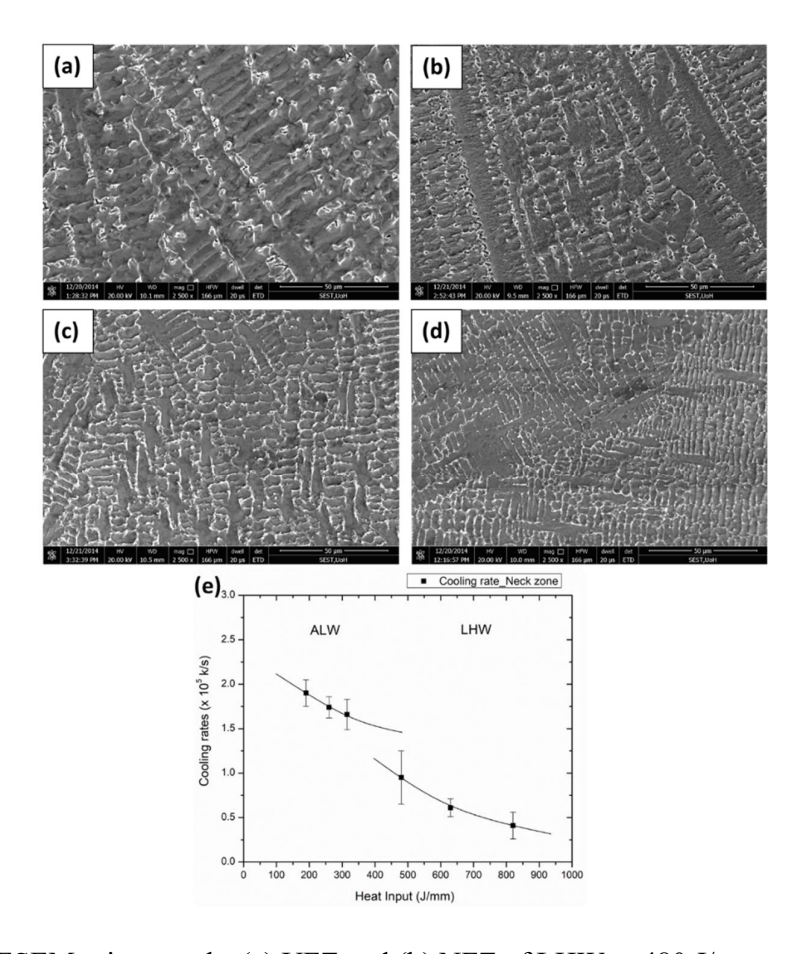


Figure 4.5. FESEM micrographs (a) UFZ and (b) NFZ of LHW at 480 J/mm and (c) UFZ and (d) NFZ of ALW at 190 J/mm heat input and (e) Cooling rates vs heat input in NFZ of ALW and LHW

Table. 4.2. Chemical composition of the Interdendritic region (IR) and the Dendrites (D) as determined by EDS analysis (wt %)

Heat input (J/mm)	Sample	Region	Cr	Mo	Ni	Со	Al	Ti
	I IIW I IE7	IR	25.48	14.12	43.29	9.23	0.48	0.76
490	LHW_UFZ	D	23.80	8.57	50.14	11.33	0.31	0.51
480	LIIW MEZ	IR	24.3	11.24	44.42	10.4	0.65	0.57
	LHW_NFZ	D	23.19	8.07	50.75	11.63	0.57	0.46
	ALW HEZ	IR	24.44	12.53	43.06	11.2	0.31	0.61
100	ALW_UFZ	D	23.59	7.91	51.84	12.15	0.21s	0.43
190	ALW NEW	IR	23.98	11.09	44.12	11.04	0.55	0.58
	ALW_NFZ	D	23.12	8.43	49.95	12.65	0.44	0.54

Figures 4.5 (a-d) elucidate the influence of cooling rate on FZ microstructures of UFZ and NFZ in both LHW and ALW. As well known, the cooling rates in laser and laser hybrid welded FZs influence the micro-segregation of alloying elements into the inter-dendritic regions during solidification. Thus, to quantify segregation behavior in welded FZs due to heat input and type of welding method, SEM/EDS spot analysis was carried out at weld central line along with EDS spot analysis (depicted in Table 4.2) of both LHW and ALW FZs. Results indicated that inter-dendritic region carbides formed in both LHW and ALW FZs are found to be enriched with Mo (nearly doubled), Cr and Ti (marginally increased) as compared to the surrounding matrix. The segregation of Cr and Mo into the inter-dendritic region results in the formation of Cr, Mo-rich secondary carbides upon solidification. It is the lower solubility of Mo content in the γ -Ni matrix, micro-segregation enhances into inter-dendritic region of both LHW and ALW FZs. The micro-segregation of Mo into the inter-dendritic region of ALW is quite lower than compared to that of LHW and could be attributed to the high cooling rate and prevailing low-temperature gradient in ALW.

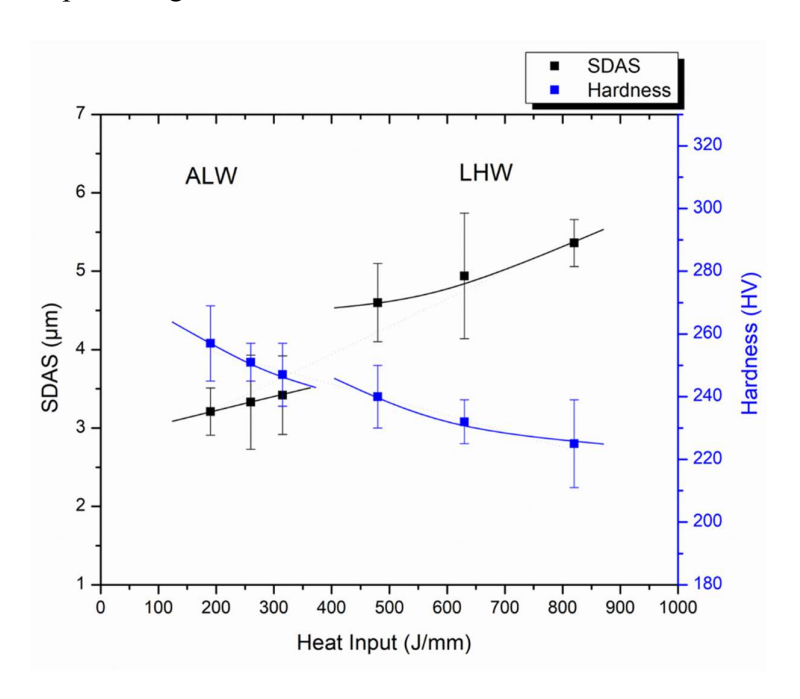


Figure. 4.6: SDAS and Hardness distribution as a function of heat input in Neck fusion zone (NFZ) of ALW and LHW

The SDAS and micro-hardness values of ALW and LHW in NFZs under different heat input conditions are shown in Figure 4.6. SDAS in the UFZ and NFZs is higher than that observed in the lower fusion zone (LFZ) of both LHW and ALW. Apparently, SDAS increases with increase in the heat input in both LHW and ALW as a consequence of temperature

gradients and cooling rate effects. In LHW, the SDAS of UFZ is 2.5-3 times higher than LFZ is plaussibly due to the presence of lower cooling rates in UFZ ($0.22 \times 10^5 - 0.35 \times 10^5 \text{ K/s}$) as compared to LFZ ($2.30 \times 10^5 - 2.65 \times 10^5 \text{ K/s}$). High heat input in LHW can drive the secondary dendritic arms to grow at the expense of the lower cooling rate in UFZ. The cooling rate variation within UFZ and LFZ in ALW is relatively unperturbed, and as a result, the extent of variation of SDAS is significantly low.

Consistent with microstructural variation observed due to heat input and type of welding process involved, microhardness of weld FZ decreases with increase in heat input in both LHW and ALW welds. The hardness of UFZ and NFZ in LHW was found to be slightly lower than that of UFZ and NFZ in ALW. It is clear that the average hardness in UFZ of LHW is influenced by the low cooling rates associated with MIG arc resulting in coarser SDAS and low hardness than compared to ALW. LFZ of both LHW and ALW welds showed the highest hardness. This distinguishable hardness difference in LFZ, despite with similar composition, could be attributed to the microstructural refinement (finer SDAS) accompanied with laser-induced melting involving high cooling rate in ALW as compared to that of high heat-input LHW process. Similar observation of reduction in average hardness distribution as heat input decreased attributed to the finer SDAS at the expense of higher cooling rates of fiber and CO₂ laser welded Inconel 617 has been reported in the study conducted by Ren et al. [8].

4.5 HAZ and ROC analysis at neck zone

As reported by several studies on high energy concentrated fusion welding process involving superalloy prone for liquation cracking, analysis of PMZ/HAZ and ROC at neck region were found to play a pivotal role in understanding the cracking phenomena [7,12,13]. In a study involving welding of Inconel 617, assessment of metallurgical factors including GB liquation and mechanical factors of elevated temperature plastic strain or strain rate were found to greatly influence strength of joints [5,6]. These liquation cracks were predominantly found in the neck zone of weld bead cross-section where HAZ is widest and is more liable to heat accumulation [3]. Therefore, in the present work, HAZ width has been evaluated in the neck zone of both LHW and ALW welds and the results are depicted in Figure 4.7. The inset micrograph of LHW interface in Figure 4.7 shows the measurement of HAZ width.

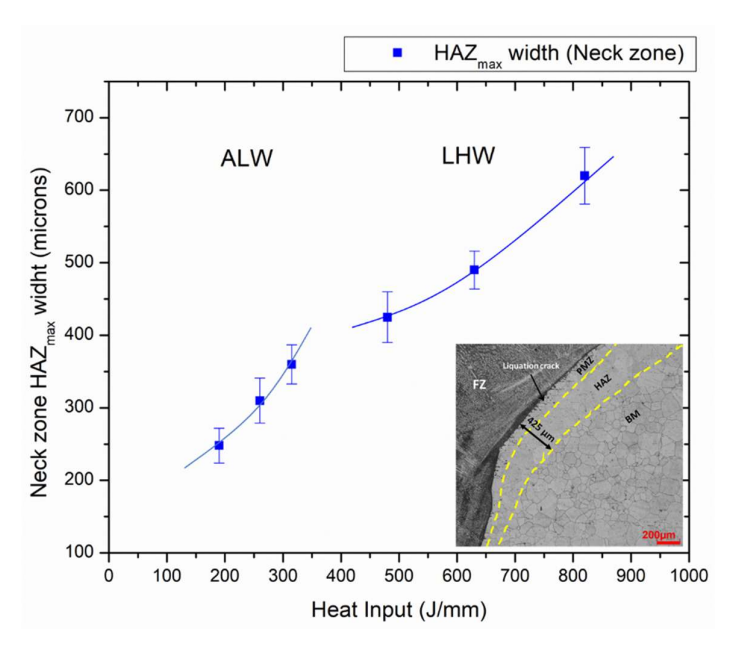


Figure. 4.7: Width of HAZ_{max} (microns) at neck zone of both ALW and LHW with inset microstructure of LHW interface

The width of HAZ was found to increase with increase in heat input in both LHW and ALW welds. However, the widest width of HAZ was obtained in LHW which is in the range of 425 – 620 µm for the heat input of 480 to 820 J/mm, whereas the HAZ width for ALW was found to be in the range of 245 – 395 µm for the heat input of 190 – 315 J/mm. This infers that the width of the HAZ at neck zone in LHW is quite wider than in ALW and plausibly due to the fact that, the neck zone of weld bead is more liable to heat accumulation and has a gentler temperature gradient as a result widest width of HAZ at neck zone than in the other zones. However, the widest HAZ width in LHW is due to the additional MIG arc heat and deposition of molten metal from filler wire resulting in an extended region of upper bead width, thereby increasing the ROC which in turn increases the width of HAZ in neck zone. Thus, the width of HAZ in the neck zone primarily depended on degree of waist at neck zone i.e, the ROC. Therefore, ROC for both LHW and ALW weld beads has been evaluated and presented in Figure 4.8. The inset schematic image in Figure 4.8 shows the measurement of ROC.

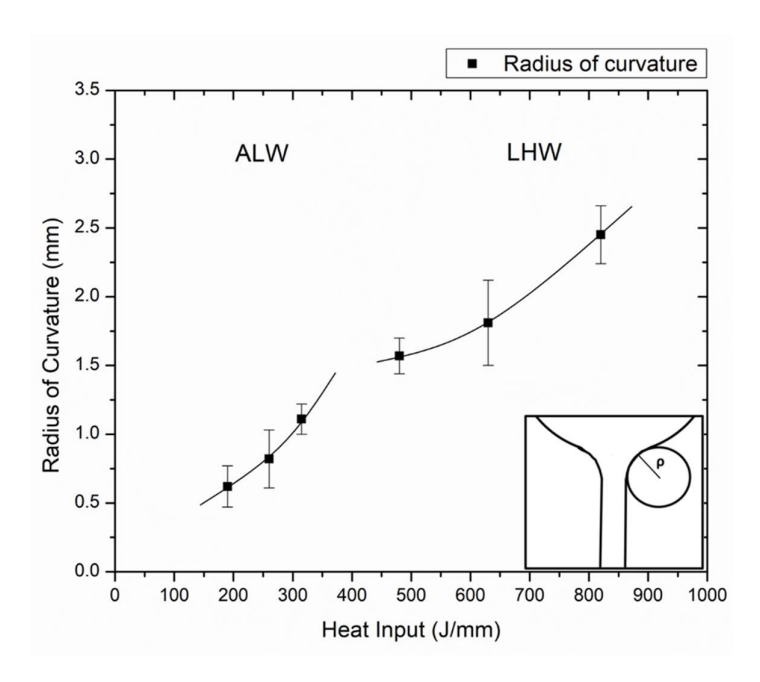


Figure. 4.8: Effect of heat input on radius of curvature of both ALW and LHW

It is clear that the ROC increases with an increase in heat input in both ALW and LHW due to increase in the interaction time. It can also be seen that the ROC in wine-cup bead shape LHW is quite larger than that in Y-type bead shape of ALW and associated with prevailing heat inputs. The huge differences in depth and width of laser and arc penetration shape and separation of these two heat sources at neck zone in LHW leads to an increase in the ROC, whereas in ALW, the ROC obtained is due to the single concentrated CO2 laser beam heat source of diameter 180 µm with high energy density. In a similar study on laser and laserhybrid welding performed by Gao et al. [6], reported strong detrimental effect of ROC on PMZ/HAZ liquation cracking susceptibility due to high heat accumulation and larger solidification time occuring at neck zone of weld bead cross-section. They found that laserhybrid welding process alters the temperature and strain distributions in the vicinity to fusion line which in turn ameliorates the cooling rates in the neck zone with magnitude of cooling rates being lower than that in laser alone welding. Thus, LHW due to addition of two heat sources causing wider HAZ in neck zone and larger ROC that envisaged reduction of cooling rate in LHW than that of ALW and thereby resulting in less susceptibility to liquation cracking. As shown in Figure 4.5e, that the cooling rates at neck FZ in ALW are higher $(1.65 \times 10^5 1.91 \times 10^5 \text{ K/s}$) than compared to LHW (0.52 x $10^5 - 0.69 \times 10^5 \text{ K/s}$). Therefore, the ongoing results suggested that the LHW process is beneficial over ALW process in terms of resistance to liquation cracking susceptibility and the ROC formation to primarily determine occurrence of liquation cracking or weakening of strength at interface PMZ region.

On the whole, in the present study, weld bead profile analysis with microstructure and micro-hardness distribution co-related well with cooling rates associated with type of welding process involved and heat input condition. However, in certain heat input conditions, liquation cracking being observed in the vicinity to the fusion boundary. Therefore, it is a necessary study to be undertaken to understand the nucleation of liquation cracking in Inconel 617 alloy weldments during welding with laser-based welding process.

4.6 Conclusions

Two different welding processes including ALW and LHW were utilized in the present bead-on-plate welding study of Inconel 617 with varying heat input. Results indicated that the weld bead profile depends on the type of welding process employed. LHW weld bead profile showed a typical wine-cup shape, whereas ALW produced a Y-shape bead profile on account of differences in the number of heat sources and their intensities profiles.

Weld bead width, penetration depth, and FZ area were found to increase with an increase in heat input of both LHW and ALW processes. The FZ area of LHW was three times larger than that of ALW, although, heat input in LHW involved was 2.5 times higher in ALW. LHW showed a 6 – 8 mm wider UFZ due to the presence of MIG arc and 1.25 – 1.35 mm greater depth of penetration than compared to that of ALW weld beads. Thus, it can be inferred that the addition of MIG arc with a laser heat source in case of the LHW process helps in obtaining wider weld bead width with marginally improved depth of penetration. LHW fusion weld showed coarser dendritic microstructure with significant enhanced SDAS resulting in low average hardness. Wider width of HAZ observed at neck zone due to heat stagnation be observed in both ALW and LHW.

ROC at neck zone increased with increase in heat input and significantly larger in LHW due to extended wide weld bead obtained by employing an additional MIG arc. Magnitude of cooling rates in neck FZ were found to be less in LHW than in ALW and thereby leading to microstructural coarsening with relatively higher micro-segregation of carbides in LHW than ALW. On the whole, weld bead profile analysis with microstructure and micro-hardness distribution co-related well with cooling rates associated with type of welding process involved and heat input condition.

4.7 References

- 1. Nishimoto, K., I. Woo, and M. Shirai. "Analyses of temperature and strain distributions in laser welds study of the weldability of Inconel 718 cast alloy (Report 6)." (2002): 284-292.
- Yan, Fei, Chongjing Hu, Xiong Zhang, Yuanzheng Cai, Chunming Wang, Jun Wang, and Xiyuan Hu. "Influence of heat input on HAZ liquation cracking in laser welded GH909 alloy." Optics & Laser Technology 92 (2017): 44-51.
- 3. Nishimoto K, Woo I, Ogita T, et al. Factors affecting HAZ cracking susceptibility of laser welds. Study of weldability of Inconel 718 cast alloy (4th report). Welding International. 2001.
- 4. Shinozaki K, Kuroki H, Luo X, et al. Effects of welding parameters on laser weldability of Inconel 718. Study of laser weldability of Ni-base, heat-resistant superalloys (1st Report). Welding international. 1999;13(12):945-951.
- 5. Luo X, Shinozaki K, Kuroki H, et al. Analysis of temperature and elevated temperature plastic strain distributions in laser welding HAZ study of laser weldability of Ni-base superalloys (Report 5). welding International. 2002.
- 6. Gao Z. Numerical modeling to understand liquation cracking propensity during laser and laser hybrid welding (I). The International Journal of Advanced Manufacturing Technology. 2012;63(1):291-303.
- 7. Gao Z, Ojo O. Modeling analysis of hybrid laser-arc welding of single-crystal nickel-base superalloys. J Acta materialia. 2012;60(6-7):3153-3167.
- 8. Ren W, Lu F, Yang R, et al. A comparative study on fiber laser and CO₂ laser welding of Inconel 617. J Materials and design 2015;76:207-214.
- 9. Ono M, Shinbo Y, Yoshitake A, et al. Development of laser-arc hybrid welding. Nkk Technical Report-Japanese Edition. 2002:70-74.
- 10. Ragavendran M, Vasudevan M. Laser and hybrid laser welding of type 316L (N) austenitic stainless steel plates. J Materials Manufacturing Processes. 2020;35(8):922-934.
- 11. Kik T, Górka J. Numerical simulations of laser and hybrid S700MC T-joint welding. J Materials. 2019;12(3):516.
- 12. Ren W, Lu F, Yang R, et al. Liquation cracking in fiber laser welded joints of inconel 617. J Materials Processing Technology. 2015;226:214-220.
- 13. Arata Y, Terai K, Nagai H, et al. Fundamental Studies on Electron Beam Welding of Heatresistant Superalloys for Nuclear Plants (Report II): Correlation between Susceptibility to Weld Cracking and Characteristics in Hot Ductility and Trans-Varestraint Test. J Transactions of JWRI. 1977;6(1):69-79.

Investigations on liquation cracking susceptibility of Inconel 617 alloy during CO₂ Laser and CO₂ Laser-MIG Arc Hybrid welding processes

5.1 Introduction

Further to the previous study on influence of processing parameters on weld bead characteristics of both ALW and LHW process with liquation cracking being observed in the vicinity to the fusion boundary, it was felt necessary to understand mechanism of liquation cracking susceptibility and mitigate its effect with detailed study. Therefore, the present investigation is aimed at analyzing the phenomena of liquation cracking in autogenous Laser and Laser-MIG hybrid welded thick sections of Inconel 617 alloy by employing advanced characterization techniques such as micro focused X-ray diffraction (XRD) and Nano-Indentation which greatly facilitate in this understanding. Thus, comprehensive analysis of influence of ALW and LHW weld bead profile on liquation cracking susceptibility with detailed understanding the nucleation of liquation cracks employing FESEM with EDS and Elemental mapping has been undertaken and correlated phase analysis by Micro-XRD technique with mechanical behaviour of low melting eutectics (LME) using Nano Indentation technique. Furthermore, mechanism of liquation cracking phenomena in thick-section laserbased welded Inconel 617 alloy is proposed in this chapter. Moreover, influence of heat input in both ALW and LHW on grain boundary resolidified phase and total liquation crack lengths were quantified and compared understand underlying mechanism effectively.

5.2 Experimental Methodology

As explained previously in chapter 3, the base material used in the study is a solid-solution strengthened Nickel based superalloy Inconel 617 in a form of plate of thickness 10 mm in solution-annealed condition with a nominal composition as tabulated in Table 3.1. Bead on plate (BOP) welding experiments were carried out using Autogenous CO₂ laser welding (ALW) and CO₂ laser + MIG hybrid welding (LHW) processes is used in this study. The Laser-MIG hybrid welding setup employed for the experimentation was shown in Figure 3.7 and the process variables were depicted in Table 3.4. Welding process parameters with a fixed laser power of 3.5 kW (maximum available with CO₂ laser system) and varying welding speed in the range of 0.6 – 1.0 m/min employed for BOP welding experiments is presented in Table 4.1.

High speed Nano-indentation testing was carried out using advanced Nano-Indentation system (Nano mechanics Inc., Oak Ridge, USA) with a Berkovich indenter as shown in Figure 3.20. Micro-focused X-ray diffraction system (D/MAX RAPID II Rigaku Smart Lab system, Tokyo, Japan) shown in Figure 3.19 was utilized for precise analysis of phases present in localized areas such as PMZ and HAZ as well as fusion zones of both ALW and LHW by employing a spot size of 100 μm diameter.

5.3 Bead profile analysis

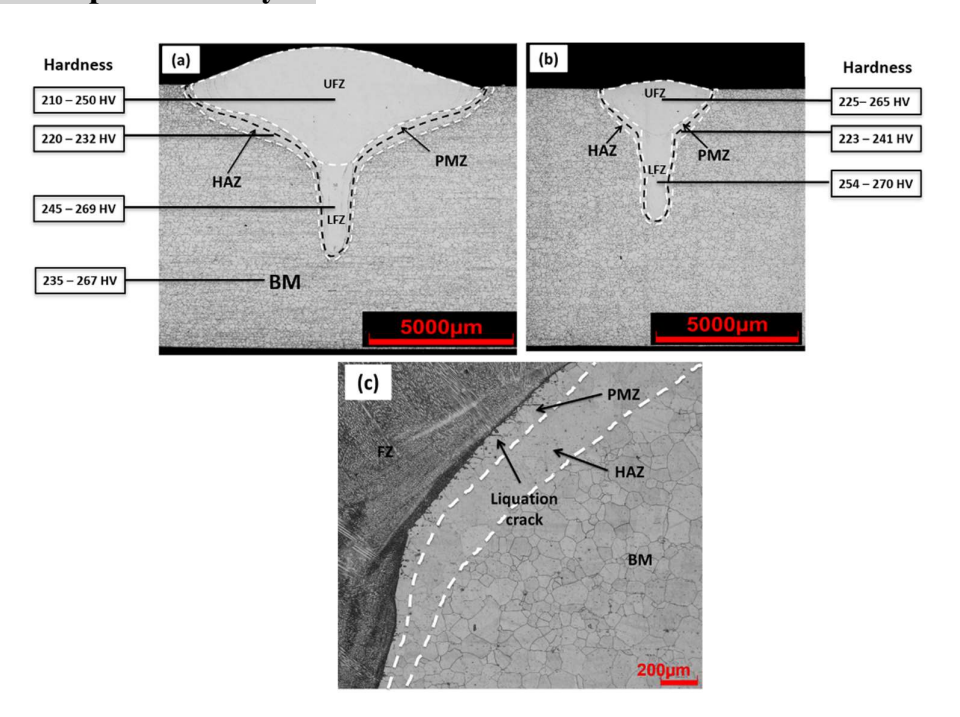


Figure 5.1. Macrographs of (a) Laser-MIG hybrid weld (LHW) processed at 480 J/mm and (b) Autogenous Laser weld (ALW) processed at 190 J/mm with vickers hardness values and (c) Micrograph of LHW Inconel 617 alloy interface processed at 480 J/mm

Figure 5.1 shows the macrographs of two different weld cross-sections which clearly reveal the influence of Laser and Laser + MIG hybrid heat sources on the weld bead profile. Macrograph of LHW presented in Figure 5.1(a) shows a typical "wine-cup" morphological bead profile with wider and shallower upper fusion zone (UFZ) region which is with morphology akin to that of arc-weld profile and a narrow and deeper lower fusion zone (LFZ) similar to that of a laser-weld bead profile. As can be seen from LHW weld bead profile, the UFZ of LHW is three times larger with nearly semi-hemispherical geometry as compared to that of narrow UFZ in ALW with Y-type bead which clearly illustrates MIG effect in LHW. The LFZ of both LHW and ALW are more or less of similar geometrical and dimensional features as evident from Figure 5.1 with finger-like shape, which could be presumably due to

deeper penetration effects associated with laser keyhole. These weld bead profiles are found to be of similar morphological and geometrical features as reported in several studies involving laser-MIG hybrid and Laser welding processes [1,2]. Thus, it is clear that an increase in heat input directly enhances weld bead fusion as evident from the melting of more metal in LHW than in ALW [3].

Table 5.1. Cross-sectional bead profile analysis of Autogenous Laser (ALW) and Laser-MIG hybrid (LHW) weldments

Welding Process	Heat Input (J/mm)	Penetration (P) mm	FZ Area (sq.mm)
Lagar MIC	480	6.66	29.17
Laser–MIG Hybrid	630	7.12	35.84
	820	7.43	48.39
Autogenous Laser	190	5.43	10.34
	260	5.88	13.13
	315	6.12	17.19

Table 5.1 depicts the effect of heat input on calculated FZ area and weld penetration depth. FZ area nearly doubled from 10 sq. mm to 17 sq. mm in increase in heat input from 190 to 315 J/mm in case of ALW, whereas FZ area increased from 29 sq.mm to 48 sq.mm in increase in heat input from 480 – 820 J/mm in case of LHW process. On the whole, the FZ area was found to be a direct consequence of heat input, ranging from 10 sq.mm in the process involving 190 J/mm heat input to 48 sq.mm in case of 820 J/mm heat input. However, the extent of variation of penetration depth with heat input was found to be insignificant compared to that of FZ area variation. The depth of penetration enhanced from 5.4 to 7.4 mm with an increase in heat input from 190 J/mm to 820 J/mm. Figure 5.1(c) displays the optical micrograph of Laser-MIG hybrid weld bead cross-section. It can be visualized that the weld cross-section consists of various zones of interest formed due to thermal and compositional gradients namely FZ, PMZ, HAZ and unaffected BM. The distinguishable difference between PMZ and HAZ is the presence of low-melting eutectics, resolidified phase in PMZ and numerous liquation cracks sometimes penetrating in to the FZ/HAZ.

5.4 X-ray Phase Analysis

Further, to qualitatively assess various phases present in FZ, PMZ, HAZ and BM, an advanced micro-focused X-ray diffraction analysis was utilized. Figure 5.2 illustrates XRD patterns of various regions of interest obtained in both LHW and ALW weld beads. It is evident from the XRD patterns that phases significantly varied in FZ, PMZ and HAZ regions as compared to those of BM in both the welding processes. The unaffected BM of Inconel 617 consisted of predominantly γ -Ni matrix and certain amounts of carbides $M_{23}C_6$ (M = Cr, Mo) and M_2C (M = Cr, Mo). Low-intensity diffraction peaks from these carbides could be observed at 2 Θ of 37°, 42° and 48° (the zoomed inset image) in BM, although to a very meagre extent. Indeed, in few reported studies, these carbides were detected by TEM and XRD analyses, although observed in lesser amounts [4-6].

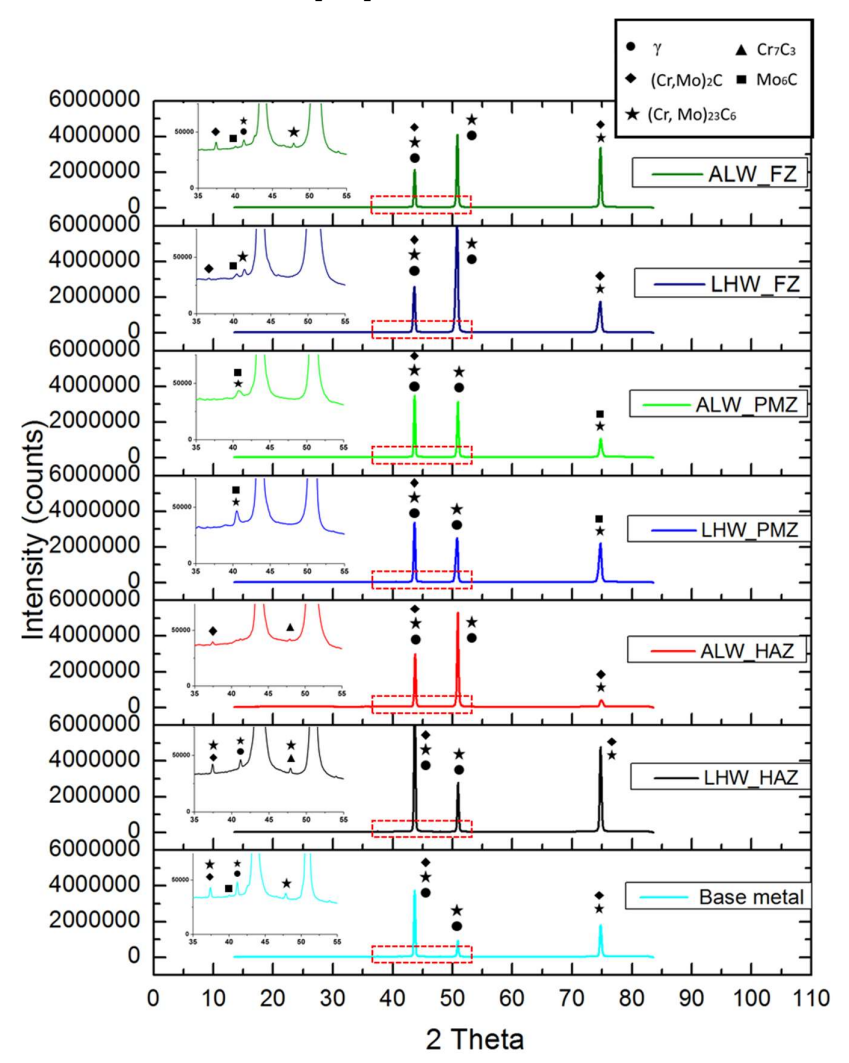


Figure 5.2. Micro XRD patterns of ALW and LHW in FZ, PMZ, HAZ and base metal Comparing XRD peaks of BM with HAZ regions in case of both ALW and LHW welds,

predominantly M₂₃C₆ carbides) could be observed with its predominant presence at 2Θ of 48°, although their amounts varied significantly between ALW and LHW welds. Apparently the deconvoluted 2Θ peak at 75° of the HAZ regions of both welds revealed its presence with significant peak broadening being observed. Formation of such different chromium carbides could be attributed to the transformation of principal carbides into newer precipitated carbides such as Cr₇C₃ from Cr₂₃C₆ as the HAZ region may experience high temperature with sufficient diffusion (different thermal cycle) from the prevailing process condition. In a similar study involving heat treatment of Inconel 617, similar effects of transformation of Cr₇C₃ from Cr₂₃C₆ (at temperature ranging between 1200-1250°C) was observed and reported [7-9].

Moving further close to the fusion boundary with presence of cracks and eutectic morphological microstructure region (as revealed by high-resolution SEM micrograph explained later), termed as partially melted zone (PMZ), XRD patterns clearly showed elimination of Cr_7C_3 phase with formation of new carbide phase identified as M_6C (M being Mo). Indeed, identification of this phase at 20 of 42° (that could be observed in zoomed inset portion) corroborates its formation, plausibly associated with more Mo-rich carbide precipitation in the ternary eutectic comprising γ -Ni and carbides of $M_{23}C_6$ and M_6C . In a similar study involving TIG welding of Inconel-617B alloy, formation of such Mo-carbides in the liquated HAZ was revealed by TEM analysis and attributed to the weld thermal cycle experienced close to the fusion boundary [10]. Further, by comparing X-ray diffraction patterns of PMZ and FZ regions, it is clear that not much secondary precipitates of $M_{06}C$ could be observed in FZ with microstructure predominantly being comprised of γ -Ni dendrites and interdendritic boundary constituting Cr and Mo rich carbides of $M_{23}C_6$ types. Apparently few lowintensity peaks of Cr and Mo rich $M_{20}C$ carbides could still be observed in the diffraction pattern of FZ regions of both LHW and ALW welds.

5.5 Hardness distribution Analysis

Furthermore, hardness distribution presented in Figure 5.1 clear that the average hardness remained more or less similar in the FZ of both LHW and ALW weld beads but with insignificant reduction as compared to that of BM. The microhardness was found to be in the range of 210-265 HV in FZ regions as against 232-267 HV in BM. However, microhardness reduced further in HAZ to the level of 220-241 HV from the BM values. The wide scatter in hardness values of all these regions of FZ and BM regions could be attributed to significant variations in inter-dendritic/grain boundary carbides. Indeed presence of relatively soft

chromium and molybdenum enriched carbides transformed from primary carbides in HAZ, as evidenced from the XRD analysis envisage its reduction in hardness as compared to that of BM. Although hardness variations across the upper fusion zone (UFZ), lower fusion zone (LFZ), neck zone (NZ) and HAZ of weld bead exhibited similar effects in both welds processed with different heat inputs, marginal enhancement in hardness of fusion region of LFZ (both in ALW and LHW) could be observed as compared to that of BM. This distinguishable difference in LFZ, despite the similar composition, could be attributed to the microstructural refinement (dendritic grain size) accompanied with laser induced melting involving high cooling rate as compared to that of high heat-input MIG process.

5.6 Fusion zone Microstructural Analysis

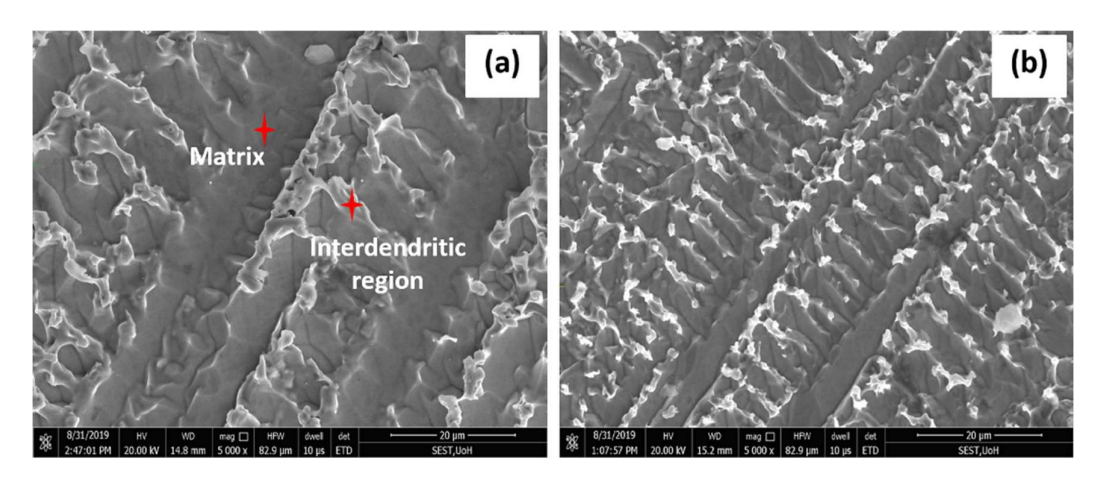


Figure 5.3. FESEM micrographs of fusion zone in different regions (a) LHW and (b) ALW

Figure 5.3 shows the SEM micrographs of FZ microstructures of both LHW and ALW welds. It can be seen that the columnar dendrites of γ -Ni had grown perpendicular to fusion boundary (evident from high magnification SEM micrographs of FZ/PMZ interfaces presented in Figure 5.3 (a,b) and got converged towards the weld center, a typical weld FZ microstructure in the direction of heat flow as reported by several studies involving welding of Inconel 617 [2,11.12]. In comparison with ALW, LHW showed coarser columnar/cellular dendrites, although with a varied morphology. Presumably, high peak temperatures (25% higher in LHW than that of ALW as per calculations based on model predicted by Tomasz Kik and co-workers [13]) with extended duration in cooling time (tripled in LHW to that of ALW) facilitate in dendritic coarsening with significant compositional variation in interdendritic region carbides. The primary and secondary dendrites constituting γ -Ni matrix in the fusion zone microstructures are richer in Ni and Co, whereas interdendritic carbides are relatively rich in

Mo (nearly doubled) and Cr (marginally increased) compared to surrounding matrix as per EDS spot analysis. As solubility of Mo in γ -Ni is lower than that of Cr, segregation of Mo-rich carbides in interdendritic boundary enhances. These metallic carbides were observed to be of $M_{23}C_6$ and M_2C (M being Cr and Mo) type as analysed by XRD.

5.7 Analysis of PMZ and HAZ

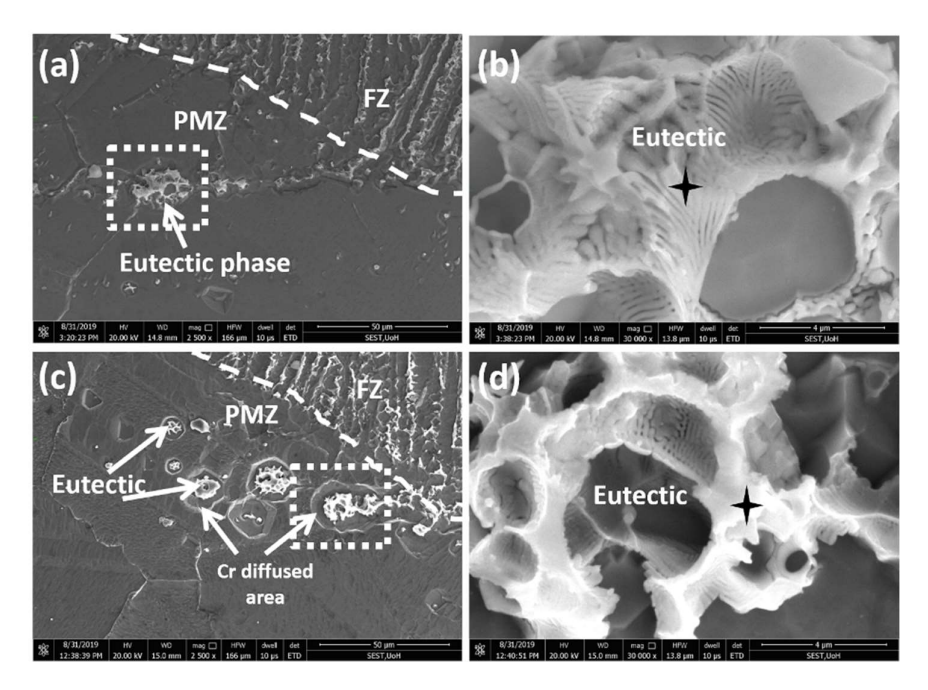


Figure 5.4. FESEM images of PMZ of (a) LHW specimen (b) magnified view of eutectic phase marked as a dotted box in (a) and (c) ALW specimen (d) magnified view of eutectic phase marked as a dotted box in (c)

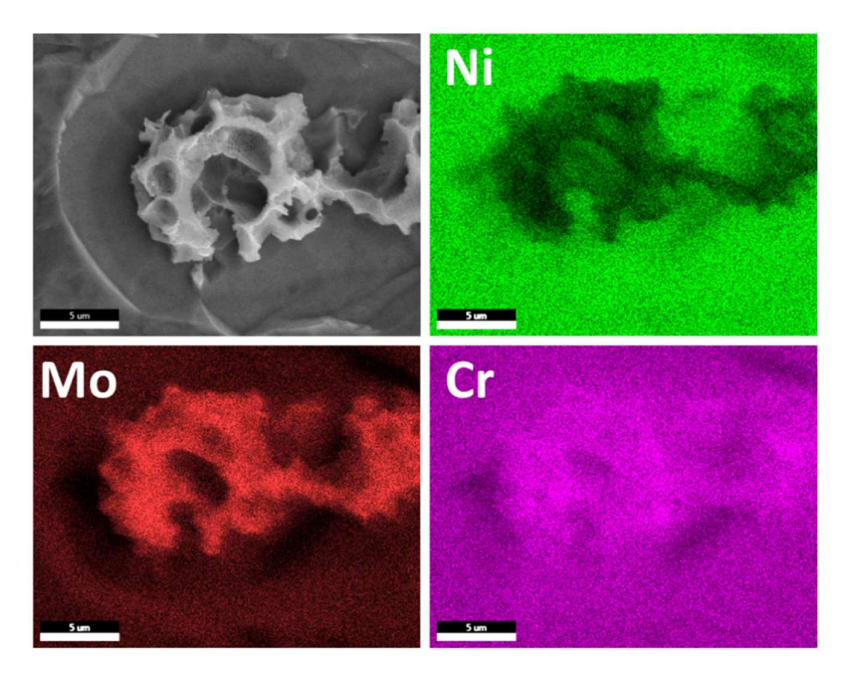


Figure 5.5. Element map analysis of the eutectic phase

Table 5.2. EDS analysis in wt % of the eutectic phase and surrounding matrix in PMZ of LHW and ALW

	Region	Cr	Mo	Ni	Co	Al	Ti
	Eutectic	47.42	29.75	11.73	3.97	0.37	1.11
LHW_PMZ	Matrix	24.60	8.74	50.64	12.32	0.32	0.65
	Diffused area	27.49	8.49	49.73	12.01	0.42	0.96
AIW DM7	Eutectic	43.91	24.66	17.64	5.26	0.31	1.18
ALW_PMZ	Matrix	24.93	8.63	49.59	12.76	0.34	0.54
	Diffused area	26.67	8.12	48.91	12.11	0.47	0.88

Figure 5.4 shows FESEM micrographs of PMZ constituting austenite grains and pockets of network structure with fine particulates in the GBs in both welds. Indeed further high magnification images (Figures 5.4(b) and (d)) of these networks with EDS analysis indicate that they are plausibly formed due to eutectic reaction with multiple phases enriched with Cr and Mo. Elemental mapping of the eutectic network structure in PMZ microstructure depicted in Figure 5.5 shows that the eutectic network constitutes carbides of both Cr and Mo. Indeed, nearly doubling of weight percentage of Cr and tripling of Mo with depletion of Ni and Co as compared to austenite matrix as evident from EDS analysis. Correlating these eutectic networks with compositional variations in terms of enrichment of Cr and Mo and XRD analysis, it can be the outcome of the formation of ternary eutectic comprising γ -Ni+M₆C/M₂₃C₆. The eutectic network was observed to be doubled with wider PMZ in neck region of LHW than ALW, indicating the direct influence of heat input. Greater the heat input, higher is the quantity of low melting eutectic network formation in the grain boundary of the PMZ. Furthermore, higher level of diffusion of Cr and Mo in eutectics of LHW than ALW is discernible as evident from EDS analysis. In a similar study involving GTA welding of Nibased 617B alloy, presence of Mo₆C carbide in eutectic network resulting in ternay phase formation was observed and confirmed by TEM analysis [10]. Thus pockets of eutectic network microstructure could be observed in PMZ, wherever constitutional liquation associated with compositional changes in terms of Cr and Mo occurred during welding thermal cycle. Indeed, nano-indentation cluster map presented in Figure 5.6 further fortifies these effects.

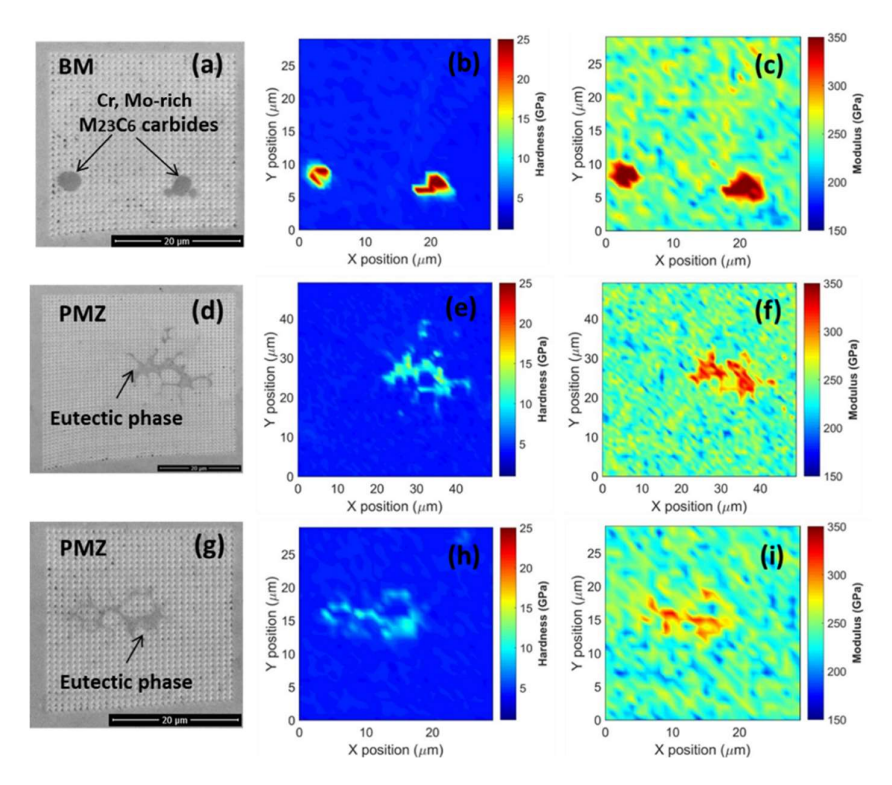


Figure 5.6. (a), (d) and (g): FESEM images of Base material (BM) carbides, LHW_LME (Low melting eutectic), and ALW_LME respectively.

(b), (e) and (h): Hardness contour map of BM, LHW and ALW respectively(c), (f) and (i): Modulus map of BM, LHW and ALW respectively obtained by Nano Indentation technique

Table 5.3. Nano hardness range (GPa) of the eutectic phases, carbide in base material, HAZ, FZ and surrounding matrix of LHW and ALW specimens

Phases	γ-Matrix (Grains/Dendrites)	Eutectic	GB/ Interdendritic carbide
LHW_PMZ	3.3 - 4.1	10.4 – 12.2	-
ALW_PMZ	2.9 - 3.5	8.3 - 10.4	-
LHW_HAZ	3.5 - 4.7	-	22.5 - 25.4
ALW_HAZ	3.2 - 4.3	-	21.2 - 23.6
LHW_FZ	5.5 - 7.1	-	18.3 - 22.2
ALW_FZ	5.7 - 6.6	-	17.6 - 19.5
BM	4.4 - 5.3	-	24.3 - 28.1

The dissolution of Cr and Mo in the eutectic network resulted in phases with low hardness of 8-11 GPa nanohardness as against hard intermetallic carbides in BM comprising Cr, Mo-rich $M_{23}C_6$ and M_2C carbides with 24-28 GPa nanohardness. Furthermore, diffusion

of Cr into the eutectic network and formation of Mo-rich carbide precipitates enabled reduction in hardness of austenite grains as evident from the reduction of nanohardness from 4-5 GPa to 3 – 4 GPa. Thus the constitutional liquation process associated with rapid thermal heating enables insufficient diffusion of solute atoms with incomplete dissolution of hard M₂₃C₆ (previously present in base metal) carbides leading to eutectic reaction between the surviving carbides of M₂₃C₆ and austenite matrix when the eutectic temperature is attained. The liquid formed in due course gets rapidly frozen into eutectic network comprising Mo-rich and Cr-rich carbides of M₂₃C₆ and M₆C types, depending on the concentration of Cr and Mo. Similar observation of constitutional liquation occurring in the liquated HAZ of TIG-welded IN 617B has been reported in the study conducted by Li and co-workers [10] and attributed to the prevailing heating cycle, although with absence of any cracking. Indeed, high temperature gradient with low cooling rate that prevails in LHW caused a significant enhancement in nanohardness of eutectic network of LHW than that of ALW (10 – 12 GPa in LHW and 8 – 10 GPa in ALW) and is attributed to dissolution of Mo (visualized from the EDS analysis). Apparently, variation in modulus values of these phases in PMZ regions of both LHW and ALW and depicted in cluster maps of Figure 5.6 corroborate these effects.

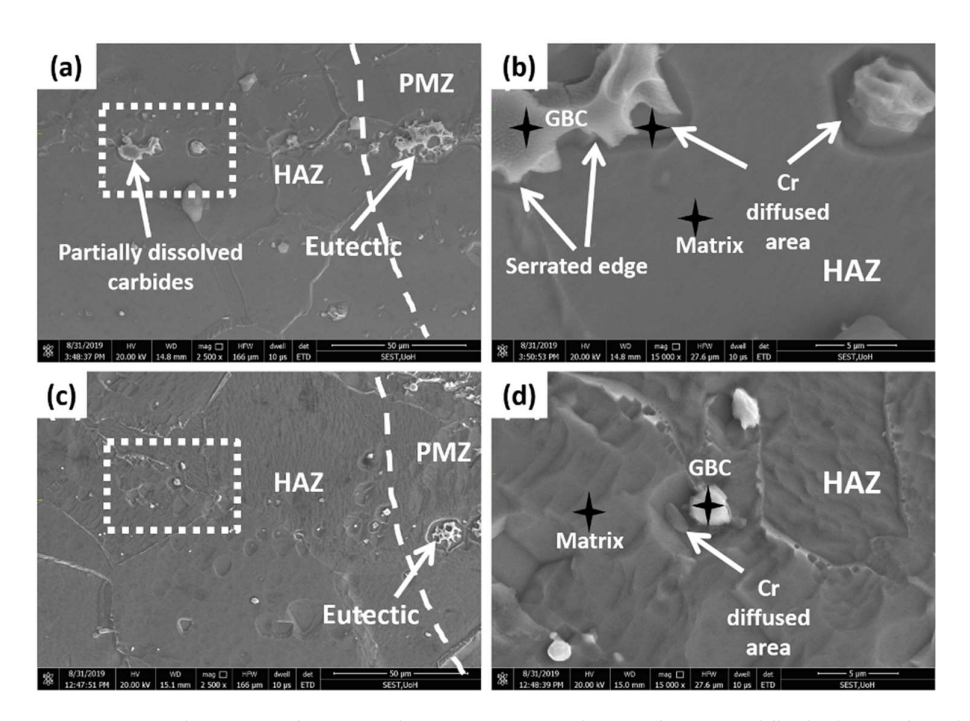


Figure 5.7. FESEM images of HAZ of (a) LHW specimen (b) magnified view of carbides marked as a dotted box in (a) and (c) ALW specimen (d) magnified view of carbides marked as a dotted box in (c)

Table 5.4. EDS analysis in wt % of the grain boundary (GB) carbide and surrounding matrix in HAZ of LHW and ALW

	Region	Cr	Mo	Ni	Co	Al	Ti
LHW_HAZ	GBC	41.3	19.18	15.48	5.94	0.3	0.86
	Matrix	24.37	8.75	49.64	12.13	0.39	0.62
	Diffused area	29.39	8.29	47.24	11.30	0.14	0.84
ALW_HAZ	GBC	58.21	17.35	13.52	6.02	0.45	1.47
	Matrix	24.11	8.89	49.62	12.83	0.46	1.16
	Diffused area	27.04	7.94	48.66	11.11	0.16	0.56

The HAZ microstructures of LHW and ALW welds below the PMZ regions depicted in Figure 5.7 clearly indicate slightly modified microstructure as compared to that of BM with absence of any low melting eutectics. Some pockets of partially dissolved carbide precipitates could be observed in the region. As peak temperatures experienced in HAZ will be well below 1250°C, beyond the solvus temperature of carbides of Cr and Mo, only partial dissolution could be visualized and as a result serrated carbides with different morphologies could be observed in the microstructures shown in Figure 5.7. Furthermore, selective EDS point analysis (shown in Table 5.4) at diffused area indicated that these regions comprised of slightly higher amount of Cr than that of the pre-existing γ -matrix grains. Thus variation in nano-hardness of γ -matrix grains in HAZ as compared to that of BM is evident from the values depicted in the Table 5.3. However, these modified carbides of M₂₃C₆ (morphologies) observed in GB were relatively Cr- and Mo- lean than that of GB carbides of BM as evident from higher nano-hardness values of 20 – 25 GPa, slightly lesser than that of GB carbides of BM whose nano-hardness was in the range of 24 – 28 GPa with high-Cr and high-Mo contents. Furthermore, as previously observed, these carbide clusters at grain boundary may plausibly comprise of M₇C₃ – type as per micro-XRD analysis. Indeed, significant peak temperature that prevails at HAZ region facilitates dissolution of more Cr and thereby modifies the carbide phase with compositional variation. Apparently there is not much variation in γ -matrix grains and as a result no significant variation in nano-hardness and FCC crystal structure of austenite. Although microstructural scatter exists from the PMZ interface to unaffected BM in both weldments, deeper structural changes could be observed in HAZ region of LHW than ALW owing to higher heat input effects.

5.8 Mechanism of Liquation cracking susceptibility in Laser weldments

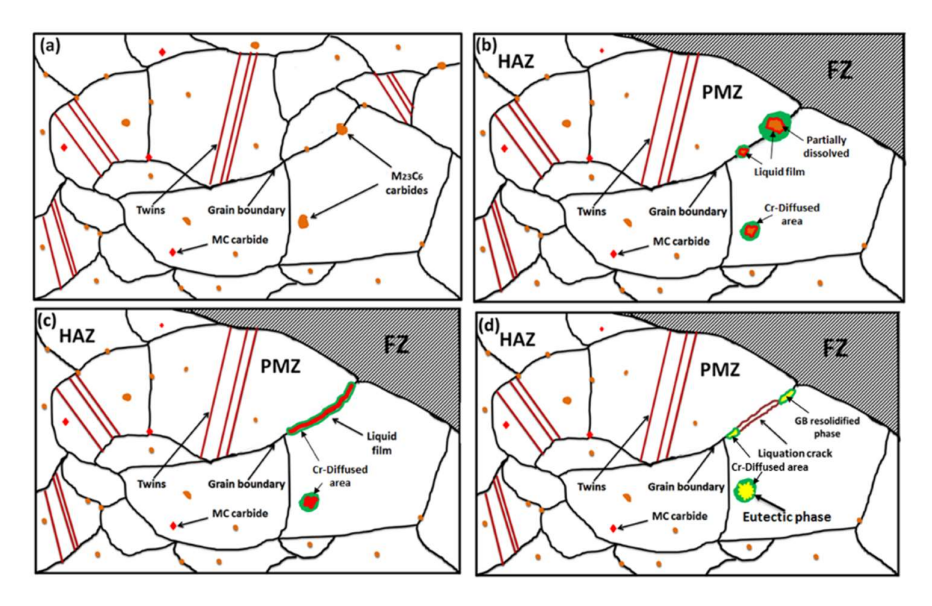


Figure 5.8. Schematic illustration of Liquation cracking phenomena

The susceptibility of constitutional liquation cracking in superalloy welds is governed by the critical PMZ regions formed due to the welding method adopted. Several researchers attributed the cracking phenomena to the formation of the continuous liquid film along the grain boundaries and the thermal stresses induced by weld thermal cycle [14,15]. It is, however, important to consider the factors responsible for its formation in our present Inconel 617 superalloy. Figure 5.8 shows one such schematic illustration proposed for the occurrence of liquation cracking phenomena. Initially, the BM of Inconel 617 superalloy in solution-annealed condition comprises of several (Cr, Mo)-rich M₂₃C₆ carbides with distinguishably different morphology and size dispersed along GBs and within austenitic grains as depicted in Figure 5.8 (a). As the temperature during welding cycle reaches these carbides solvus temperature, adjacent to the fusion boundary, they become unstable and undergo partial dissolution. This phenomena when subjected to rapid heating conditions such as laser or arc welding result in liberation of solute elements such as Cr and Mo with partial dissolution of these carbides, especially more predominantly at PMZ region. These Cr atoms diffuse into the surrounding γ matrix and Mo segregates at the boundary of γ / M₂₃C₆ due to its lower diffusion coefficient [16]. I

n this way, the surrounding γ matrix gets enriched by Cr, causing the compositional gradient at the network between the decomposed (Cr, Mo)-rich $M_{23}C_6$ carbides and matrix. This surrounding Cr-rich area is considered as Cr-diffused area in Figure 5.8 (b). Segregation of Mo contents resulting in the formation of Mo-rich M_6C carbides at the junction of γ / $M_{23}C_6$. Thereby resulting injunction consisting γ matrix and $M_{23}C_6/M_6C$ carbides. As soon as the

temperature reaches to eutectic point, then a proportion of liquid film form as shown in Figure 5.8 (b) by a eutectic reaction between γ matrix and $M_{23}C_6/M_6C$ carbides. This constituional intergranular liquid film connects with the adjacent liquid pockets and spread along the GBs in PMZ as shown in Figure 5.8 (c).

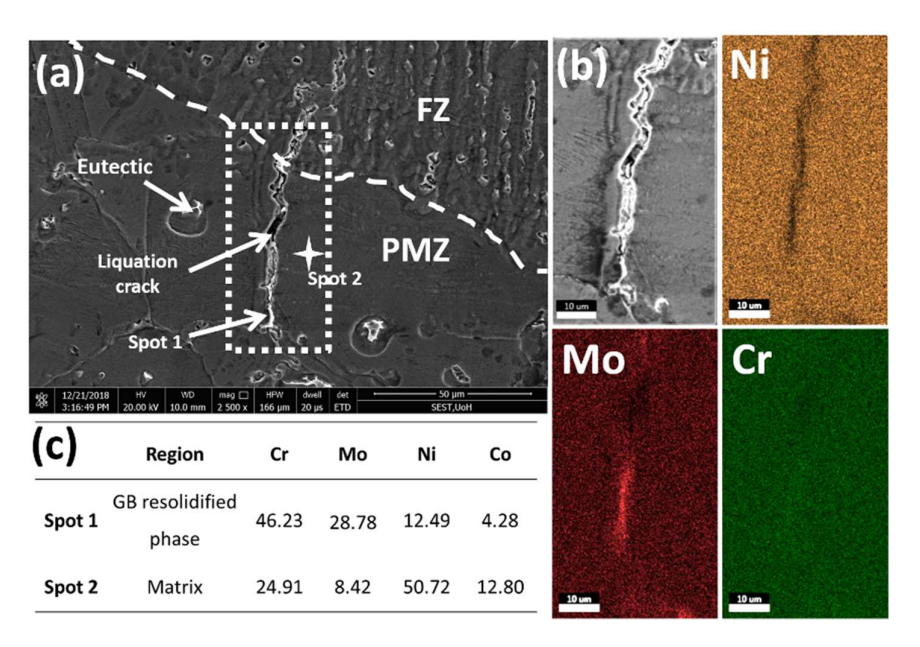


Figure 5.9. (a) PMZ liquation crack in neck zone region (b) Elemental mapping analysis (c) EDS results of GB resolidified phase and matrix of LHW

Subsequent to the solidication of weld during cooling cycle of the process, the constitutional liquid film at PMZ may get strained and degrade the ability to accommodate thermal stress developed at boundary and therby result in cracking with decohesion along the solid-liquid interface. These cracks are generally referred to as liquation cracks surrounding the eutectic microstructure which are enriched with Cr and Mo contents. Sometimes, these cracks were observed to propagate in FZ/HAZ depending on the amount of heat input and the rate of cooling involved in the welding thermal cycle.

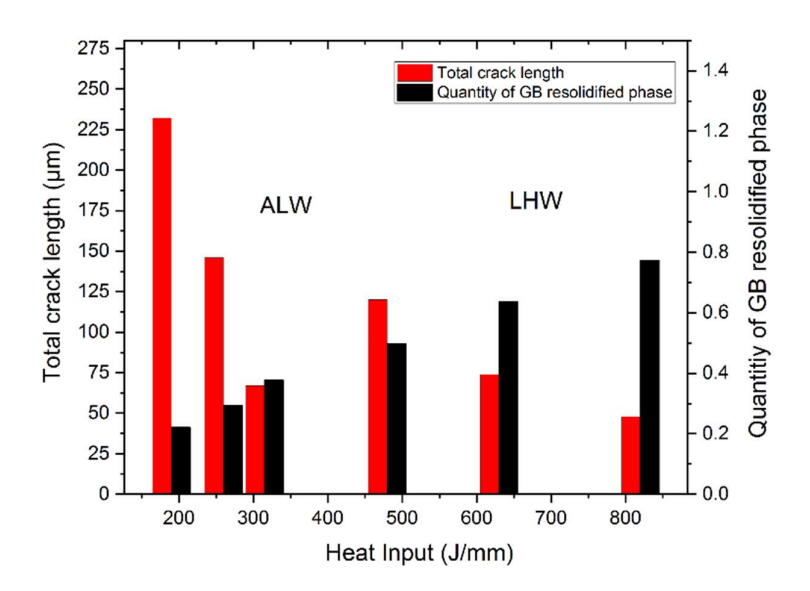


Figure 5.10. Variation of total crack length (TCL) and quantity of grain boundary (GB) resolidified phase (%) of LHW and ALW under different heat input

Figure 5.9 illustrates one such PMZ region of LHW bead with liquation crack formed along the grain boundary with irregular and zigzag morphology (processed with 630 J/mm heat input). However, the liquation cracks were propagated into the HAZ and FZ in some of the heat input conditions. EDS point analysis and elemental mapping shown in Figure 5.9 (b) and (c) show that this GB resolidified phase consists of 3.5 times higher amount of Mo (28.78 wt%) and 2 times higher amount of Cr (46.23 wt%) than the surrounding austenite matrix. This indicates that the GB resolidified phase is highly enriched with Mo than Cr along with depletion in Ni and Co contents. Further, to assess the influence of heat input by adopting different welding methods (laser and laser-hybrid) on the amount of GB resolidified phase and density of cracking (measured in terms of total crack length (TCL)) were analyzed and depicted in Figure 5.10. With the decreased heat input, the TCL increased steadily in both ALW and LHW processes. LHW showed nearly 50% reduction in TCL than ALW, whereas the quantity of GB resolidified phase enhanced by 50% in LHW than ALW. The relatively low heat-input process with high cooling rate such as ALW was found to produce less quantity of GB resolidified phase, but higher TCL due to higher thermal stresses associated with high cooling rate of the laser cycle. On the contrary, even though the high heat input in LHW process results in generation of higher quantity of GB resolidified phase, the occurrence of liquation cracking is less due to lower thermal stresses associated with low temperature gradient. At high heat input, the LHW and ALW welds showed the lowest TCL values that imply that the susceptibility to liquation cracking in both LHW and ALW could be reduced with an increase in heat input.

Alternatively, increasing heat input, by employing a different process such as LHW may enhance higher resolidified eutectic phases but with less susceptibility to liquation cracking on account of vast reduction in temperature gradients with slow cooling rate.

5.9 Conclusions

Two different joining techniques, namely, laser-hybrid welding (LHW) and autogenous laser welding (ALW) processes, on Inconel-617 with emphasis on understanding the mechanism of PMZ liquation cracking have been comprehensively studied. Cracking susceptibility was co-related with microstructure and hardness analysis by employing advanced characterization techniques like Micro-XRD and Nano-Indentation, along with standard OM, SEM and EDS characterization tools. The study indicated that bead profile changes with the type of welding technique employed. Ternary eutectic network phase constituting γ -Ni + M₂₃C₆ + M₆C has formed on account of eutectic reaction associated with constitutional liquation with cracking in PMZ region of both welds, with amount of network being high in LHW than ALW, accompanied with reduced cracking rate. Higher the welding speed, lower the weld penetration in both welding processes. As expected, wine-cup shaped penetration was observed in LHW, whereas ALW produced deep-penetration narrow weld bead on account of the intensity-profiles involved in the process. Higher amount of low melting eutectic phases at the neck region with higher diffusion of Mo-rich M₆C carbides (with lower hardness) segregation was observed in LHW bead than ALW counterpart.

Susceptibility to PMZ liquation cracking was found to be higher in ALW than LHW and attributed to high cooling rate that prevails in laser cycle. Apparently with increase in heat input susceptibility to liquation cracking reduced in both the processes. High heat-input in LHW process produces low temperature gradient and therby promoting higher diffusion of solute elements (Cr and Mo) released from the (Cr, Mo)-rich M₂₃C₆ carbides into γ matrix. As the thermal gradient in ALW is much greater than LHW, which significantly enhances the thermal stresses and thus contribute to cracking susceptibility, although low amount of eutectics in partially melted region could be produced. Thus it can be inferred that the addition of MIG arc to the laser heat source (LHW) helps to improve the resistance to liquation cracking by modifying the thermal cycle with enhanced stress relaxation in PMZ even at low heat input conditions. The LHW process could be beneficial over Autogenous laser welding (ALW) process in terms of resistance to liquation cracking.

5.10 References

- 1. Acherjee, B., Hybrid laser arc welding: State-of-art review. Opt. Laser. Tech. 2018, 99, 60-71.
- 2. Wenjie, R.; Fenggui, L.; Renjie, Y.; Xia, L.; Zhuguo, L.; Elmi Hosseini, S. R., A comparative study on fiber laser and CO2 laser welding of Inconel 617. *Mater. Des.* 2015, 76, 207-214.
- Colegrove, P.; Ikeagu, C.; Thistlethwaite, A.; Williams, S.; Nagy, T.; Suder, W.; Steuwer, A.; Pirling, T., Welding process impact on residual stress and distortion. Sci. Tech. of Weld. Join. 2009, 14 (8), 717-725.
- 4. Tytko, D.; Choi, P.; Klöwer, J.; Kostka, A.; Inden, G.; Raabe, D., Microstructural evolution of a Ni-based superalloy (617B) at 700°C studied by electron microscopy and atom probe tomography. *Act. Mater.* 2012, *60* (4), 1731-1740.
- Takahashi, T.; Fujiwara, J.; Matsushima, T.; Kiyokawa, M.; Morimoto, I.; Watanabe, T., Analysis of precipitated phase in heat treated inconel alloy 617. *Trans. Iron. Steel. Inst. Jpn.* 1978, 18 (4), 221-224.
- Singh, A.; Moitra, A.; Bhaskar, P.; Sasikala, G.; Dasgupta, A.; A.K.Bhaduri, Effect of Longterm Thermal Exposure on Microstructure Evolution and Mechanical Properties of Alloy 617.
 J. Mat. Sci. Tech.: 2016.
- 7. Chun, Y. B.; Mao, X.; Han, C. H.; Jang, J., Microstructural evolution and tensile properties of oxide dispersion strengthened Alloy 617 at elevated temperatures. *Mater. Sci. Eng. A.* 2017, 706, 161-171.
- 8. Chaturvedi, M. C. In *Liquation cracking in heat affected zone in Ni superalloy welds*, Mater. Sci. Forum., Trans Tech Publ: 2007; pp 1163-1170.
- 9. Weiss, B.; Grotke, G.; Stickler, R., Physical metallurgy of hot ductility testing. *J. Weld.* 1970, 49 (10), 471s.
- Shanlin, L.; Kejian, L.; Mengjia, H.; Yao, W.; Zhipeng, C.; Jiluan, P., The Mechanism for HAZ Liquation of Nickel-Based Alloy 617B During Gas Tungsten Arc Welding. *Metals*. 2020, 10 (1), 94-94.
- 11. Sun, J.; Ren, W.; Nie, P.; Huang, J.; Zhang, K.; Li, Z., Study on the weldability, microstructure and mechanical properties of thick Inconel 617 plate using narrow gap laser welding method. *J. mater. Des.* 2019, *175*.
- 12. Pavan, A. H. V.; Vikrant, K. S. N.; Ravibharath, R.; Singh, K., Development and evaluation of SUS 304H IN 617 welds for advanced ultra supercritical boiler applications. *Mater. Sci. Eng.*: A. 2015, 642, 32-41.
- 13. Tomasz, K.; Jacek, G., Numerical Simulations of Laser and Hybrid S700MC T-Joint Welding. *Materials*. 2019, *12* (3), 516-516.
- 14. Wenjie, R.; Fenggui, L.; Renjie, Y.; Xia, L.; Zhuguo, L., Liquation cracking in fiber laser welded joints of inconel 617. *J. Mater. Proc. Tech.* 2015, 226, 214-220.
- 15. Idowu, O. A.; Ojo, O. A.; Chaturvedi, M. C., Effect of heat input on heat affected zone cracking in laser welded ATI Allvac 718Plus superalloy. *Mater. Sci. Eng. A.* 2007, 454-455, 389-397.
- 16. Yin, H.; Gao, Y.; Gu, Y., Evolution of the microstructure and microhardness of the welding joint of IN 740H alloy with IN 617 as filler metal. *Mater. Charac.* 2017, *127*, 288-295.

Optimization of high-power fiber-coupled diode laser process parameters for deep penetration welding of Inconel 617 superalloy

6.1 Introduction

Although LHW using CO₂ laser could effectively reduce liquation cracking susceptibility as observed in previous study, employing single laser heat source with enhanced coupling efficiency under relatively low heat input condition can effectively improve the weldability of Inconel 617 alloy thick-sections. Due to limited availability of CO₂ laser power for welding thick-sections and low coupling with superalloy due to high wavelength, it was felt pertinent to attempt welding using latest high-quality high-power fiber-coupled diode laser under controlled heat input. Therefore, the current study is aimed to optimize the high-power diode laser welding (DLW) process parameters for 10-mm thick Inconel 617 alloy. However, based on the literature review on deep penetration autogenous laser welding of thick sections it was observed that, it is a daunting task to obtain satisfactory appearance on surface as well as bottom of the weld employing a single-pass autogenous laser welding process in thick plates as several literature studies reported occurrence of imperfections such as underfills, undercuts, spatters, root humps, porosity, lack of side-wall fusion etc. [1-3]. Moreover, no studies have been reported so far on high power diode laser welding of thick Inconel 617 superalloys. This entails the crucial need to investigate the feasibility of using latest high-quality high-power diode laser for single-pass welding of thick Inconel 617 superalloy with comprehensive understanding on the influence of critical processing parameters on weld characteristics and joint efficiency.

6.2 Experimental Methodology

In the present study, diode laser welding (DLW) experiments were performed by using a high-power fiber-coupled diode laser system (Model: LDF-10000-60 VGP, Laserline GmbH, Germany) integrated to a 6 + 2 axis robotic workstation (Model: RV40-RSV, Reis Robotics, Germany) as shown in Figure 3.9 and an optical head tailored to deliver circular laser beam spot of 0.9 mm diameter in multi-mode spacial intensity distribution shown in Figure 3.10. As identifying effective laser focal point to enable maximum coupling efficiency is a primary step to optimize any laser processing method, firstly, bead-on-plate (BOP) welding experiments

were performed with varying focusing distance from -14 to +10 mm with an appropriate laser power of 6 kW and welding speed of 5.5 mm/s. BOP study was principally aimed to investigate the effect of focusing distance for the laser beam spot used for welding with comprehensive analysis of various bead profile characteristics such as Upper bead width (UBW), Fusion zone area (FZA), Weld penetration (WP), and aspect ratio (depth to width). Later, with optimized focusing distance from BOP study, welding experiments were carried out in square butt-joint configuration (shown in Figure 3.4c) by varying the welding speed in the range of 4 – 18 mm/s. The details of process parameters for BOP and Butt joint study are shown in Table 6.1. Base material utilized for the present study is a solid-solution strengthened Nickel based superalloy Inconel 617 in a form of plate of thickness 10 mm in solution-annealed condition with a nominal composition as tabulated in Table 3.1.

Laser Welding speed Configuration Defocusing distance (mm) power (mm/sec) (kW) -14, -10, -8, -6, -4, -2, 0, **BOP** 6 5.5 +2, +4, +6, +8, +10 Butt 5.5 4, 6, 10, 14, 18 -2

Table 6.1. Laser welding process parameters

6.3 Weld bead profile analysis

In any welding process optimization, weld bead profile is known to play a pivotal role in assessing influence of processing parameters on weld quality with joint efficiency assessment for fabrication application. Foremost, in a laser welding process, it is the power density that determines the penetration possible in the material and its thickness. As heat input in laser welding process is determined by the laser power and welding speed, laser power of 6.0 kW for 0.9 mm diameter spot that can deliver power density of $\approx 9.5 \text{ X } 10^5 \text{ W/cm}^2$ and a welding speed of 5.5 mm/s were fixed to entail keyhole mode welding and melt-runs generated on plate in BOP configuration. Prior to optimization of welding speed, it was necessary to locate the focus position for optimizing the process for maximizing melt efficiency. Thus, initial BOP welding experiments were conducted by varying focusing distance from -14 to +10 mm to assess weld bead formation and evaluated weld bead profile characteristics. Later on, after optimization of focus position, actual welding experiments on plates were performed in

square butt-joint configuration with variation in welding speed in the range of 4 - 18 mm/s. Table 3.5 and Table 6.1 illustrate setup conditions and processing parameters utilized for the study. Although, the focal position is known theoretically and experimentally (with earlier experimental works with other materials), it is necessary to optimize focusing position for each material and thickness involved in welding as coupling efficiency depends on various factors of thermophysical properties of material, material thickness, joint design, optical system and condition of the laser system delivering 3D intensity profile distribution. Additionally, poor consistency in laser beam quality and maintenance aspects of optical modules in diode lasers entails the optimization of focusing distance every time when new experiment for welding the material. As laser spot parameters of focus shift, Rayleigh length and focus diameter in diode laser welding setup depends on wavelength combination, laser power and conditions of laser system and optics, it is mandatory to optimize the defocusing parameter [4-10]. Comprehensive analysis of bead profile taken up to assess influence of focusing position both in positive and negative defocusing distance in the range of -14 mm to +10 mm from the zero-focus position (focal plane) from the surface of the metal plate. The range chosen in a way to cover the focal depth of approximately 10 mm evaluated both experimentally (9.8 mm as per burn prints of spot diameter measurement) and theoretically (9.3 mm as per Eq. 3.6). Thus, after fixing optimum defocusing position (-2.0 mm below the surface) experiments were conducted by varying welding speed in the range of 4 – 18 mm/s and a fixed laser power of 5.5 kW for flatbutt joint configuration.

Various critical cross-sectional weld bead profile characteristics such as WP, UBW, NW, RSW and FZA were evaluated in weld joints by employing image analysis software. Figure 3.12 elucidates schematic illustration of these characteristics that form in a typical deep penetration laser welded joint. Underfill at the top of the bead as well as and root sag hump at the bottom are found to be more prevalent in joints involving high thickness deep penetration welding [1-3]. Apart from these, process inter-dependent and weld quality characteristics of underfill/root sag defects, aspect ratio, FZA, and surface finish/appearance were also evaluated and assessed their influence with variation of defocusing distance and welding speed.

6.3.1 Influence of defocusing distance on melt-runs in BOP configuration

In any laser welding process optimization, it is the laser beam spot size and its energy intensity profile distribution that governs laser-material interaction and its melt behaviour that eventually determine joint efficiency. Although, once the laser system along with its optical

setup and laser power is fixed, it is presumed that its power density will envisage easy understanding of weld behaviour. In actual practice, the conditions of the laser source and optical elements does not remain same and hence assuming power density of a defined laser spot remains elusive. Thus, identifying focusing position becomes most important in optimizing a laser-based welding process. Furthermore, in a thick-section welding, it becomes further critical due to material thickness, joint design and their associated heat-transfer and melt-pool thermodynamics. In fact, many studies involving laser welding of moderate-to-thick sections reported consideration of focus shift few millimeters below the focal plane (negative defocusing) for effective penetration with melt-pool stability [4,10-16]. Furthermore, focus shift with variation in focal depth was observed to profoundly effect when processing using diode laser and attributed to the fluctuating power efficiency of the laser and its poor-quality maintenance [4]. Thus, optimization of focusing distance is mandatory before optimizing other processing conditions of laser power, welding speed and other setup conditions.

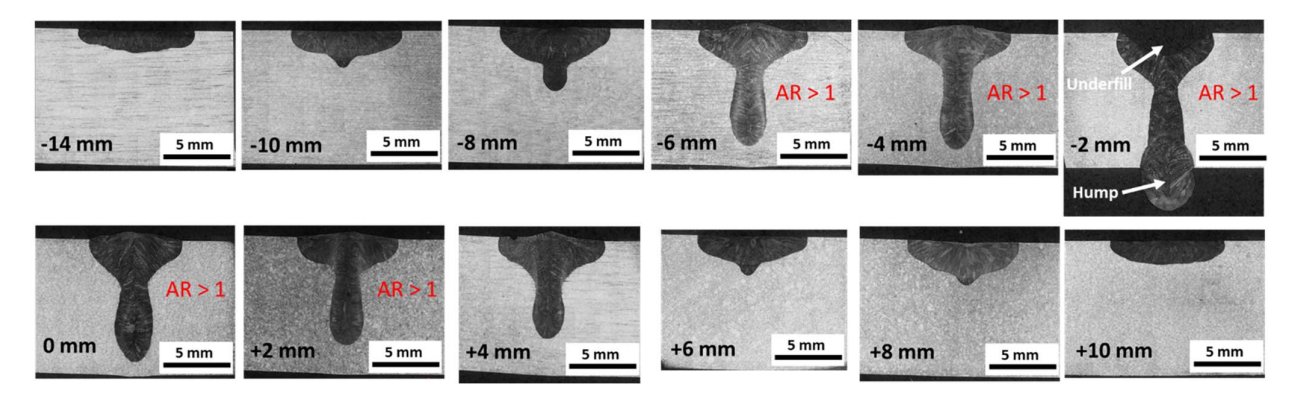


Figure 6.1. Cross-sectional optical macrographs of BOP welds at different defocusing distances

Figure 6.1 illustrates cross-sectional macrographs of melt-runs obtained in BOP welding configuration when processed with a fixed laser power of 6 kW and a fixed welding speed of 5.5 mm/s. The power density at focus was observed to be $9.5 \times 10^5 \text{ W/cm}^2$, sufficient enough for inducing keyhole welding using fiber-coupled diode laser with 66 mm-mrad beam parameter product (BPP) quality. Further to cover entire effective focal depth of nearly 10 mm (measured from spot size calculation as well as mathematical calculation following Eq. 3.6), experiments were performed at every step of 2 mm defocusing in both positive and negative distance of the focal plane (zero focus) amounting -14 mm to +10 mm. It is clear that bead profile with melt volume efficiency (determined by weld fusion zone area) varied significantly with defocusing distance. This elucidates the effect of laser spot diameter variation in zee direction (both positive and negative directions) governed by the laser beam quality of focal

depth and its intensity distribution profile. Figure 6.2 depicts results of measured bead profile characteristics constituting UBW, WP and FZA as a function of defocusing distance. It is clear that defocusing distance induce significant effect on weld bead profile and melt efficiency (FZA) on account of their associated effects of power density, spot size, intensity distribution and energy coupling behaviour of laser-material interaction. Indeed, the mode of welding shifted from conduction mode at defocusing distance beyond focal depth (above +4 mm and below -6 mm) with depth-to-width Aspect Ratio (AR) below 1.0 to effective fully transitioned keyhole mode (AR \geq 1.0) when processed within the range of focal depth of \approx 10 mm.

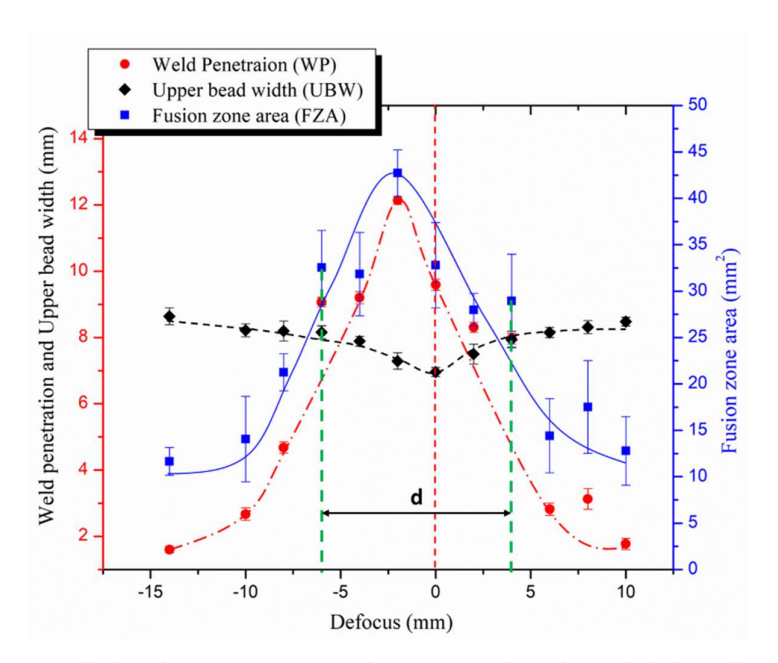


Figure 6.2. Variation in WP, UBW and FZA as a function of defocusing distance

A close observation of weld FZA clearly indicated more or less constant within 30-40 mm² when processed within the focal depth region of 10 mm (approximately), i.e., -6 mm to +4 mm, evident from the bead profiles. This FZA reduced by half $(11-20 \text{ mm}^2)$ with AR falling below 1.0 (0.18-0.57) when processed beyond the focal depth with focusing distance beyond -6 mm and +4 mm. Thus, the approximate defocusing distance in both directions could plausibly lie between 6 mm below focus and 4 mm above focus with focal depth approximating to 10 mm. Indeed, calculated aspect ratio also fell above 1.0 indicating keyhole mode of welding with focus spot diameter falling within focal depth range (evaluated experimentally and calculated mathematically). Consistent to the aspect ratio observation, power density observed was also within the range of $10^5 - 10^6$ W/cm². In conjunction with the effect, laser spot diameter was also observed to fall within in the range of 0.91 mm - 1.56 mm (1.75 times), a tolerance factor (ρ) based on the measured experiments of beam profile (Inset of Figure 3.10).

Indeed, the measured and calculated focal depth fell within the range of experimental result with 6% error. In fact, the results of focal depth evaluation matched well with that of result obtained in the study reported by Alcock and Baufeld using laser intensity measurements and calculations in welding of 10 mm stainless steel using similar fiber-coupled diode laser and optical setup. In their study, diameter of the focus spot varied with output power and Rayleigh length in conjunction with the brilliance and multi-mode quality (top-hat in slow axis and Gaussian in fast axis) of the diode laser beam [4].

A close observation of bead profile further indicates smooth transition of mode of welding from fully conduction mode (nearly hemispherical bowl shape bead) without any keyholing protrusion (in case of melt-run processed with -14 mm and +10 mm focusing distances) to fully penetrated keyhole mode (Y-shape bead) with violent melt pool turbulence and excessive evaporation resulting in heavy underfill and root sagging (in case of melt-run processed with -2 mm defocusing distance) be observed with beyond-thickness weld penetration and maximum AR (1.66) in weld processed with -2.0 mm defocusing distance. As evident from Figure 6.1, the maximum weld penetration of beyond material thickness (12 mm that includes root sagging) with maximum FZA of 42 mm² obtained in case of weld processed a negative defocus of 2.0 mm as against the weld processed with zero defocus. Although UBW obtained was slightly higher (7.3 mm) in weld processed with -2 mm defocus, as against UBW of 7.0 mm in weld with zero defocus, maximum penetration beyond thickness of material could be obtained with highest aspect ratio of 1.66. It is plausible that at a considerable negative defocussing distance, laser beam entering into keyhole converged gradually to the focal point imposing optimum power density with maximum intensity inside the material than that of weld processed with zero focussing on surface of the material. Various similar studies involving laser welding of thick materials, a defocusing of -2 mm exhibited highest depth of penetration over the surface-focusing (at focus) attributing to enhanced laser energy transfer enabling deeper weld penetration [17,18]. However, for positive defocus, this phenomenon gets deteriorated owing to attenuated intensity associated with outwardly diverging laser beam entering into the keyhole through the surface of the material and thereby resulting in shallow penetration. At negative defocus, power density induced in the laser keyhole wall with inward beam divergence is higher than that of outward beam divergence at positive or zero defocusing [2].

Theoretically, focal depth is defined by the Rayleigh length of the optical system, a distance from focal point to the position at which the laser beam diameter increases by a factor

of square root of two. Change in laser beam diameter is governed by the laser and its beam quality (divergence) quality and thereby determines its power density variation along its focal depth. Indeed, high brilliance and high beam quality (beam parameter product of 66 mm-mrad) with advanced collimation and focusing optics entailed large focal depth in the present fibercoupled diode laser as compared to previously used diode lasers with high divergence and poor focusability. This is evident from producing a partially keyhole penetration in weld processed even with -8 mm and +6 mm defocusing distances, indicating availability of sufficient power density at large focal distance and thereby providing high leverage in welding with zee direction variation. On the whole, an optimum defocusing distance of -2 mm entailed maximum penetration with highest aspect ratio and melt efficiency (maximum FZA and WP). Another contrasting feature that can be observed, is, formation of defects such as huge underfill (2 mm) and large root sag (3 mm) in weld processed with optimum defocusing position as compared to that of other welds with absence of such defects. It appears, there exists a threshold power density limit defined by focal position, material-thickness and thermophysical properties over which the recoil pressure developed by the violent keyhole envisages depression with massive evaporation at surface and root sag due to excessive drag of melt. Nevertheless, the study on the influence of defocusing distance employing 10-mm thick viscous material such as Inconel 617 superalloy suggests that effective focal depth not only influence melt efficiency but also induction of under-filling / root sagging defects on account of varied laser-material interactions governing melt pool stability. Similar observations in weld defects were also reported in high power laser welding studies employing thick metallic materials [1,2,19]. Thus, after optimizing the focusing distance with BOP experimentation, further optimization to effectively produce defect-free through-thickness weld (without underfill and root sag) by varying welding speed undertaken with experiments conducted on square-butt joint configuration.

6.3.2 Influence of welding speed on welds of square-butt joint configuration

Subsequent to the optimization of defocusing distance employing BOP configuration, experiments were conducted in square butt joint configuration with same 10-mm thick Inconel 617 superalloy plates with variation in welding speed ranging from 4 – 18 mm/s. A fixed laser power of 5.5 kW and defocusing distance of -2 mm was utilized for all experiments to study the influence of welding speed with comprehensive analysis of bead profile, microstructure and hardness distribution. The reason to maintain a fixed power of 5.5 kW, although lower to that of BOP experimentation, was to produce similar effects of melt efficiency in butt joints. It is well known that amount of material to melt will be lower in butt-joint as compared to melt-

run on BOP owing to air gap existence between plates that facilitate deeper power distribution in vertical direction. Additionally, butt-joint configuration entail enhanced laser energy utilization with improved keyholing effects as compared to BOP configuration [8]. Subsequent to optimization of welding speed leading to formation of defect-free weld joint with full penetration, tensile properties of the joint were compared vis-à-vis substrate material by subjecting to uniaxial tensile testing with sectioning of the joints from the butt-welded plates produced.

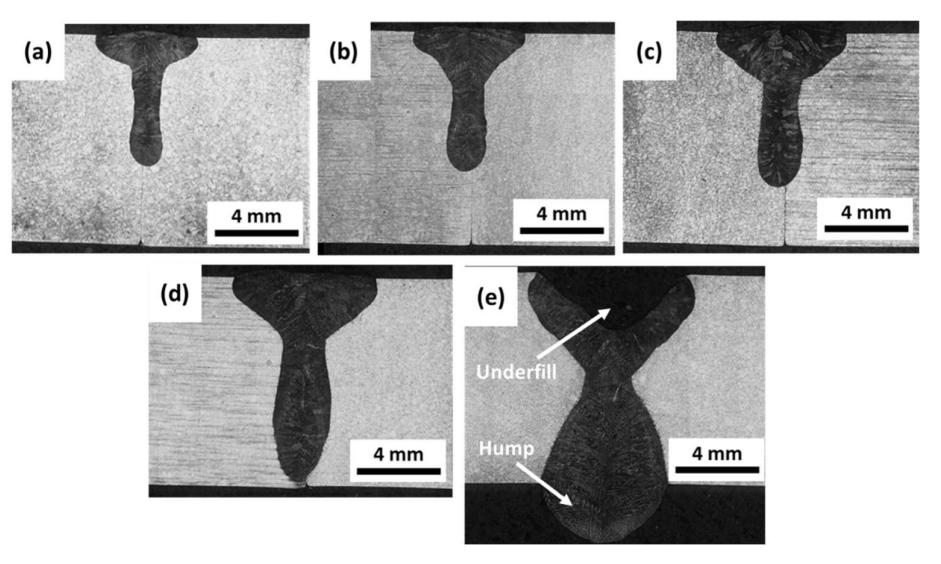


Figure 6.3. Cross-sectional optical macrographs of butt welds at various welding speeds (a) 18 mm/s, (b) 14 mm/s (c) 10 mm/s, (d) 6 mm/s and (e) 4 mm/s

Figure 6.3 shows the cross-sectional macrographs of butt welds processed with different welding speeds. As similar to previous observation in defocusing distance experimental analysis, here again deep underfill with heavy root sag bump observed in through-thickness penetrated joint and no such defects in other partially penetrated welds. Indeed, application of sufficient fixed laser power density of 8.3 x 10⁵ W/cm² entailed keyhole welding in all welds with aspect ratio being maintained greater than 1.0. Figure 6.4 summarizes various bead profile characteristics of UBW, WP, FZA and Aspect Ratio AR (depth to width) obtained as a function of welding speed. It is clear that welding speed greatly influences weld bead profile on account of heat input (interaction time). Increase in welding speed from 4 mm/s to 18 mm/s resulted in reduction of penetration in non-linear way with depth of penetration becoming halved and aspect ratio reducing from 1.6 to 1.3. FZA associated with melt volume per unit length also increased gradually in non-linear way from 13 mm² to 52 mm² with reduction in welding speed from 18 mm/s to 4 mm/s. Thus, all these aspects of increase in WP and FZA are in line with decrease in welding speed as reported by several studies on laser

welding [4,14,20]. Apparently, extent of increase in UBW was relatively lower to that of weld penetration depth with enhancement of heat input by virtue of weld interaction time, typical of a laser welding process.

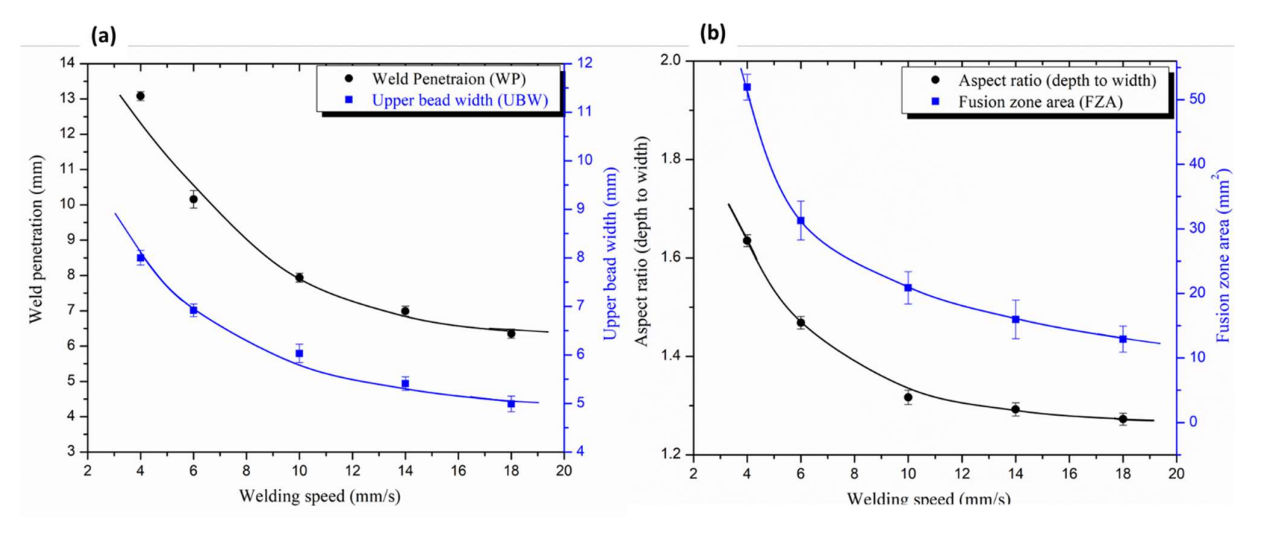


Figure 6.4. Variation in (a) WP and UBW and (b) Aspect ratio (depth to width) and FZA as a function of welding speed

At lowest welding speed of 4 mm/s, beyond-thickness penetration was obtained with underfill and root hump defects as compared to partially penetrated weld (6.4 mm weld penetration depth) with no such defects in bead processed with 18 mm/s. Defect-free nearly full penetration (9.75 mm) bead without any underfill/root hump was obtained in case of butt joint processed with 6 mm/s welding speed. Welds with surface underfills/undercuts and root hump defects not only affect the surface integrity but also deteriorates the weld mechanical properties. It is noteworthy to observe such underfill and root hump defects were only observed in case of fully penetrated weld, whereas no such defects were observed in partially penetrated welds in high power diode laser welding of Inconel 617 alloy. This observation was similar to that observed in previous experimental results of melt-runs in BOP with variation in defocusing distance. Similar effect of producing underfill/root hump only in full penetration welds as compared to partially penetrated ones were reported in few studies involving laser welding of thick steels [2,3,14]. A possible reason for such defects in full penetration welds be attributed to melt pool dynamics and keyhole behaviour when processed under specific heat input condition determined by welding speed.

The dynamics of melt pool in keyhole laser welding are governed by the combination of parameters comprising heat input (laser power, welding speed and beam intensity profile), joint design (thickness and butting edges design) and thermophysical properties of the material involved. If the heat input is sufficiently low with high welding speed resulting in partial penetration, the molten pool may not behave violently due to prevailing stable keyhole solidification process, although with trapped porosity. In contrast, when heat input by virtue of low welding speed increase to a threshold level (governed by laser energy, joint design and material properties) that result in violent fluctuation of melt flow, the weld metal at the rear end may billow down to form hump at the bottom and also generate underfill at top due to spatter. Thus, producing such defects of underfill or root sag or undercut or humps when keyholing remains unstable with rapid solidification. Further to these conditions, if highly viscous material such as Ni-based superalloy, fluctuating melt pool becomes violent and unstable leading to high difficulty in control and as a result producing weld defects of underfill/undercut (excessive localized evaporation and spatter) and root hump (excessive melt flow rearwards leading to droplet formation). Thus, root humps in weld bead are more prone in butt-joint configuration than in BOP and attributed to melt drag in the gap and air plume. Thus, such defects of underfill/root humps were not observed in partially penetrated weld when processed at welding speed beyond 4 mm/s, whereas, when processed with 4 mm/s, huge underfill and root hump defects appeared in the weld bead. Indeed, high-speed downward flow of molten metal accompanied with high recoil pressure and localized vaporization decisively resulted in occurrence of surface underfill and root hump defects [1,2,15,21].

Once the melt pool is fully penetrated, the molten metal in the bottom melt pool flows rearward i.e., opposite to the welding direction and accumulates significantly at the bottom surface resulting in droplet formation. When this molten droplet achieve significant volume may begin to sag due to gravity and grows continuously. Thus, droplets of mass solidified in the form of hump at the bottom surface of weld processed with 4 mm/s is clearly discernible. Similar welding defects were observed in several studies of deep penetration laser welding and attributed to keyhole instability [1-3,10]. Thus, process optimization by controlling welding speed (6 mm/s) entailed nearly full penetration weld joint with complete avoidance of underfill and root hump effects as through-thickness penetration welding in 10-mm thick superalloy Inconel 617 became elusive. Similar effects of such defects were reported in YAG, diode and fiber laser welding studies of thick metallic materials and suggested to control heat input by virtue of laser defocusing and welding speed parameters [12,14,16].

6.4 Microstructure and hardness distribution analysis

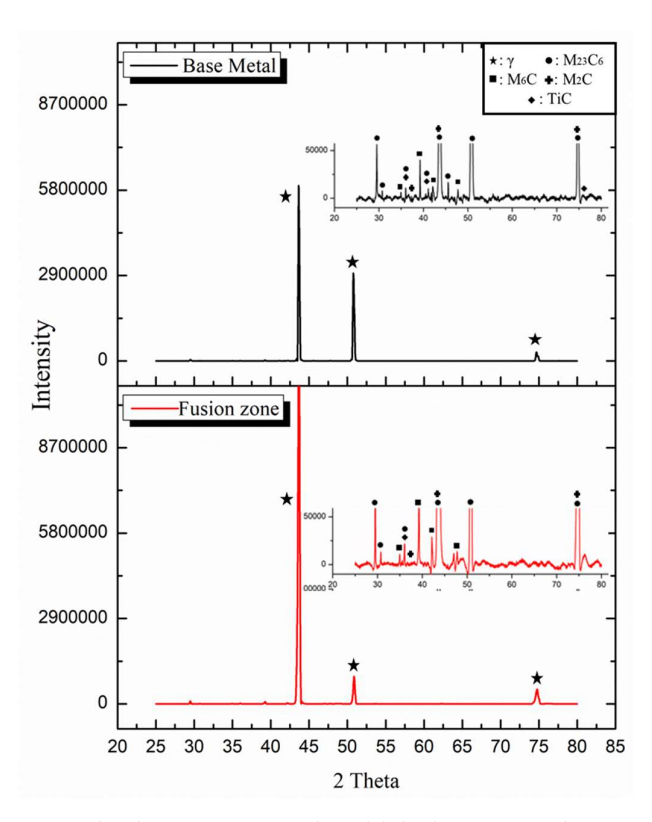


Figure 6.5. XRD of substrate BM and weld fusion zone of Inconel 617 alloy

Since, the butt joint processed with 5.5 kW laser power, 6 mm/s welding speed and -2.0 mm defocusing produced defect-free nearly full penetration weld (9.75 mm), the same was subjected to tensile testing and comprehensive analysis of its microstructure and hardness distribution employing FESEM, EDS, XRD and Vickers Hardness Test undertaken and compared with substrate. Prior to detailed microstructure analysis, phases formed in both weld fusion and substrate regions were first analyzed by employing XRD technique with slow scanning. Figure 6.5 shows the XRD patterns obtained in fusion zone of laser welded butt-joint specimen processed with 6 mm/s welding speed as well as as-received substrate material. The diffraction peaks located at 43.5°, 51° and 75° for weld fusion zone correspond to γ-(Ni-Cr-Co-Mo) matrix akin to that of as-received base material (BM), although in varied quantity. A zoomed-in inset image of XRD pattern presented in Figure 6.5 further confirms enhanced intensity of secondary peaks of carbides of chromium and molybdenum in weld fusion zone as compared to that of base metal. These phases were observed to be of M_2C (M = Cr, Mo) and M_6 C-type (M = Mo) as reported by several studies on welding of Inconel 617 alloy. Apparently, reduced peak intensities of M₂₃C₆-type of chromium carbides could be observed in fusion region as compared to that of base metal. Indeed, precipitation of Mo-rich carbides of M₂C and M₆C types from dendritic matrix (γ) accompanied with partial dissolution of chromium

carbides resulted in such fusion zone microstructure of laser welded Inconel 617 alloy [22]. Furthermore, significant peak broadening of the X-ray diffraction patterns of γ -(Ni-Cr-Co-Mo) in weld fusion zone as compared to that of BM indicates dendritic refinement due to the prevailing high cooling rate of laser welding cycle. Indeed, elemental distribution analysis of these microstructures of fusion and base metal by employing FESEM/EDX depicted in Figure 6.6 corroborated this aspect. Weld metal microstructure composed of columnar dendrites of γ (Ni-Cr-Co-Mo) symmetrically distributed around its weld centre following the direction of thermal gradient of laser welding cycle. Indeed, formation of such columnar dendritic structure along the laser energy distribution line in laser welding process is attributed to the prevailing high cooling rate and large thermal gradient in deep penetration laser welding process [2,20]. Furthermore, growth of dendrites perpendicular to the fusion boundary and directed towards the weld centre opposite to the direction of heat flow is clearly discernible from high magnification weld interface micrograph depicted in Figure 6.6b.

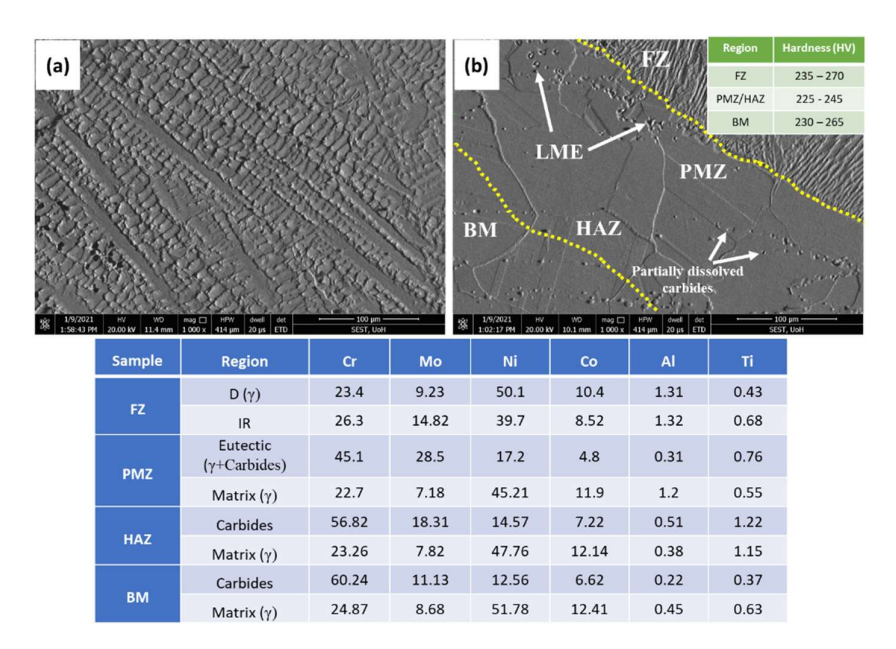


Figure 6.6. FESEM micrographs of (a) weld fusion zone and (b) weld interface with an inset image showing Micro-Vickers hardness values and EDS results (D – Dendritic core, IR – Interdendritic)

It is common in any weldment of alloy with carbide forming elements, microsegregation along interdendritic region following weld solidification that determine its joint strength to a great extent. As Inconel 617 is more prone to liquation cracking, understanding microstructural variations throughout the weld region encompassing FZ, PMZ and HAZ becomes tantamount. Figure 6.6 illustrating high magnification micrographs of central weld fusion region and interface boundary along with micro-hardness distribution and elemental

spot analysis (Table of Figure 6.6) help facilitate in understanding microstructure and distribution of carbides in dendritic core (D) and interdendritic (IR) regions. Results indicate that distinguishable elemental segregation existed in both FZ and PMZ regions of laser welded Inconel 617 alloy. The dendritic core constituting γ (Ni-Cr-Co-Mo), as indicated by XRD analysis, are richer in Ni and Co contents, whereas IR are predominantly Mo-rich and Cr-rich carbides of M₂C and M₆C (Mo being double compared to surrounding matrix). In addition, pockets of Ti-rich carbides were also found micro-segregated in the inter-dendritic region of weld metal. The results are convergent with that of phases being analyzed by XRD previously. Indeed, Mo and Ti carbides segregated strongly (as compared to that of Cr) into at IR in weld microstructure due to the fact that the Mo and Ti are powerful carbide forming elements with strong affinity. Moreover, the diffusivity of Mo and Ti into γ matrix is also significantly low and as a result segregated with expulsion from the matrix [23]. Pronounced segregation of Cr and Mo into the IR of fusion zone (identified by EDS analysis) could weaken the strength of the microstructure as previously observed in γ -Ni matrix intensity peaks by XRD analysis when compared to that of BM.

As the strength of the weld also depend on microstructure at fusion boundary and HAZ, detailed analysis with elemental distribution in PMZ and HAZ regions is necessary. Figure 6.6b depicts high magnification microstructure at fusion boundary and HAZ with elemental analysis at various regions of PMZ, HAZ and BM. Indeed, partially melted region associated with constitutional liquation of low melting eutectics (LME) is discernible in the vicinity of the boundary along with partially dissolved carbides at HAZ without involvement of melting. Formation of such LMEs is attributed to liquation reaction possible between γ-Ni matrix and secondary carbides during heating of the welding cycle as reported in laser welding of Inconel 617 alloy [24]. Indeed, EDS elemental distribution analysis presented in Table of Figure 6.6 elucidating higher amounts of Cr and Mo in LME than in matrix envisaging ternary phase constituting γ-Ni + M₂₃C₆ + M₆C as reported by our previous study employing advanced XRD and Nano-Indentation analyses [25]. However, Cr content decreased and Mo content increased in carbides of HAZ and LME in PMZ as compared to substrate BM (Table in Figure 6.6). Indeed, pronounced segregation of these carbides of Cr and Mo may cause significant reduction in strength of the joint due to weakening of the surrounding matrix. Moreover, Ding. K, et al [26] found that the continuous eutectic network along the GBs may plausibly weakens the connection between the grains leading to micro-cracking or loss of ductility that will eventually impair joint strength. Hong et al [27], observed micro-fissuring at nail head site of bead profile

during CO₂ laser welding of IN 718 and attributed to reduction of strength on account of grain coarsening and liquation cracking. Furthermore, micro-hardness evaluation of FZ, PMZ/HAZ and BM (depicted in the inset of Figure 6.6b) reconfirmed varied strength of the microstructure. FZ hardness was found to be in the range of 235 - 270 HV as against substrate BM hardness of 230 - 265 HV. A wide scatter in the BM hardness is attributed to the mixture of fine and coarse austenitic grains. Marginally improved hardness in FZ of diode laser welded Inconel 617 alloy could be attributed to the microstructural refinement (finer dendritic grain size) associated with rapid solidification with high cooling rate of the laser welding cycle. Further, HAZ including PMZ region showed slight reduction in hardness (210 – 240 HV), plausibly due to the dissolution of carbides in the austenitic grains and enrichment of alloying elements in the grain boundary carbides causing variation in solid-solution strengthening of γ -Ni matrix [28]. Overall, hardness and strength of the weld remained more or less similar to that of base metal except to the formation of low melting eutectics in PMZ of 70 - 100 micro-meters indicating optimization of the welding process.

6.5 Analysis of tensile properties of welded butt joint

Further to the microstructural analysis, tensile testing of the optimized butt welded joint (processed with optimum conditions of 5.5 kW laser power, 6 mm/s welding speed and -2.0 mm defocusing distance) conducted at room temperature to assess its joint efficiency and compared to that of BM. The engineering stress-strain curves of substrate BM and welded Inconel 617 alloy are presented in Figure 6.7 along with tensile properties evaluated.

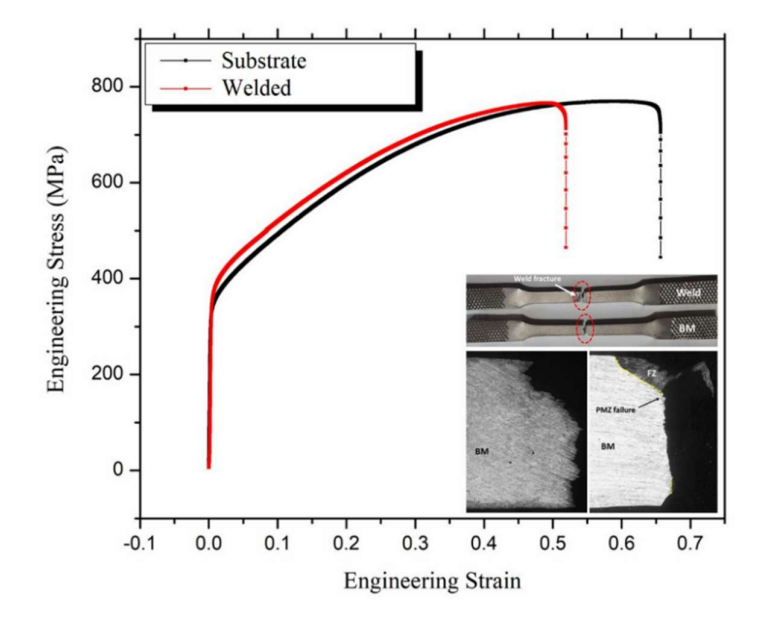


Figure 6.7. Stress-strain graphs of substrate and welded Inconel 617 alloy, with inset of fractured tensile test specimens with cross-section macrographs (yellow dash line indicates fusion boundary)

The YS and UTS of the optimized butt-welded joint are 354-360 and 745-765 MPa respectively with an elongation of 42-51 %. In contrast, BM showed YS and UTS of 325-335 and 765-769 MPa respectively with an elongation of 60-67%. A 97-99% joint efficiency could be achieved during autogenous diode laser welding at optimum conditions along with improvement in YS, although with a reduction in elongation as compared to BM. Moreover, the weld joint strength obtained in the present study is found to be comparable and slightly superior to that of reported studies of other researches adopting various multi-pass and modified advanced techniques of TIG, MIG or CMT. Fink et al. [29] obtained a joint strength of 761 MPa, 759 MPa and 764 MPa in CMT, Pulsed-MIG and Pulsed-Arc weldments of Inconel 617 alloy respectively. Moreover, Young et al. [30], obtained a joint strength of 675 MPa during multi-pass TIG welding of Inconel 617 alloy. Similarly, Shanlin et al. [31], obtained joint strength of 745 MPa in multi-layer NG-TIG welding of Inconel 617 alloy. Thus, it is evident that joint strength of high-power diode laser welded Inconel 617 alloy is stronger than that of joints produced with other arc welding methods.

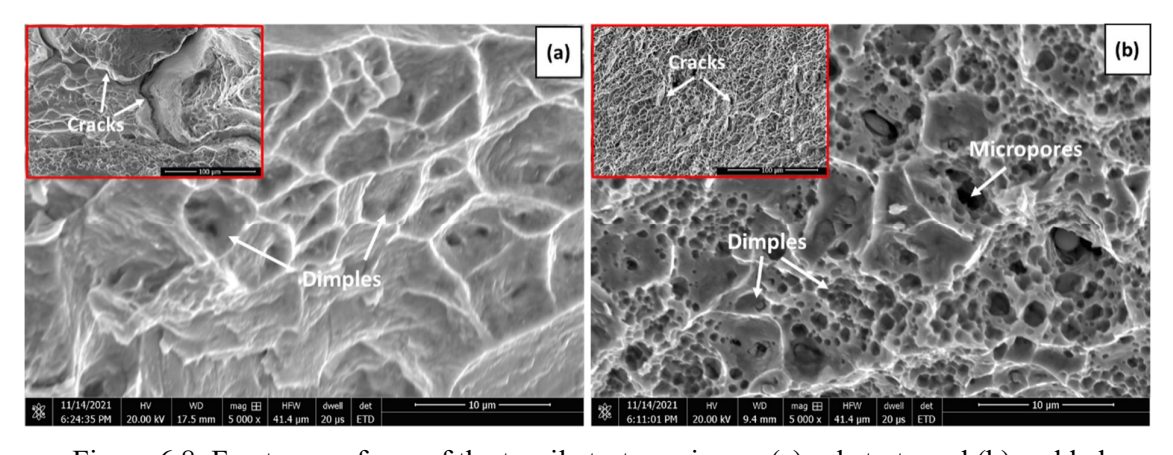


Figure 6.8. Fracture surfaces of the tensile test specimens (a) substrate and (b) welded

In order to analyze strengthening mechanism of weldment and assess fracture behaviour, cross-sectional analysis of fractured tensile test specimens was undertaken. Inset images in Figure 6.7 illustrate location failure of tensile test coupons at the end of fracture of tensile testing. It is clear from the inset macrographs of tensile specimens (Figure 6.7) that the location of failure in weldment was found to be in PMZ/FZ boundary region. The cracks during tensile loading appear to have nucleated from the weak PMZ region and propagated through the fusion boundary into the FZ. More precisely at the neck zone of weldment during tensile

loading, as it is likely to be prone to high stressed condition with loss of ductility and micro-fissuring. Similarly, presence of micro-fissures and/or liquified film formation along GBs in PMZ were observed and attributed to crack nucleation during tensile loading in several works involving welding of several alloys [27,32]. The high magnification fracture surfaces presented in Figure 6.8 further fortify ductile rupture mode of fracture in both welded and base metal specimens. However, deep dimples were observed in BM as against shallow dimples with clear micro-pores in weld fracture surface indicating higher strength with elongation in BM as compared to that of weld joint. A close look into the fractographs indicate that BM fractured with cracks being propagated along grain boundary, whereas, multiple cracking originated along the interdendritic region of refined microstructure of weld fusion region in weld joint. Indeed, strength of the 10-mm thick laser welded joint of Inconel 617 produced under optimum processing conditions with a single pass using high-quality diode laser in single pass matched with that of BM envisaging its adoption in various industry.

6.6 Conclusions

The study demonstrated successful autogenous laser welding of 10-mm thick Inconel 617 in single pass in square-butt configuration utilizing advanced high-quality diode laser. Defect-free nearly full penetration welding with 97-99% joint efficiency could be achieved with optimization of parameters of laser power, welding speed and focusing distance. Indeed, the study demonstrated the efficiency of the deep penetration welding process on par with multi-pass, multi-joint, hybrid and modified advanced welding processes employing conventional lasers as well as other fusion welding techniques with advantages of producing deeper welds with control in distortion, high speed processing and minimal melting (no filler requirement) and high productivity.

Depth of penetration, width-to-depth aspect ratio and weld bead profile in high-power diode laser welding of Inconel 617 alloy was found to principally depend on precise location of focal position and power density governed by laser power and welding speed. Indeed, there exists an optimum focal spot position over which effective laser energy coupling with material exists depending on laser, optical setup, depth of focus and material thickness/joint design. Although full penetration without underfill and hump defects could not be achieved due to ineffective precise control in keyhole melt pool stability associated with laser intensity convergence of viscous Inconel 617 alloy, optimum processing conditions of focusing distance (-2 mm) and welding speed (6 mm/s) entailed production of defect-free nearly full penetration.

The weld bead profile produced at optimum processing conditions consisted of typical Y-shape with fusion zone microstructure constituting dendrites of γ -matrix with directional solidification and segregation of Mo and Cr carbides along inter-dendritic boundary. In PMZ, in the vicinity of fusion boundary, LMEs were observed and attributed to the possible constitutional liquation of secondary phase particles during welding.

Weld joint obtained at optimized processing conditions had slightly higher yield strength as compared to base material; however, tensile strength and elongation was found to be slightly affected by the welding process due to formation of weak PMZ (70 - 100 micrometers wide) in joint with micro-porosity in fusion region. Moreover, the weld joint efficiency of diode laser welded Inconel 617 alloy was in the range of 97 - 99 % indicating suitability of its application for components of use in thermal power plant and other sectors.

6.7 References:

- 1. Zhang, Mingjun, Zheng Zhang, Kun Tang, Cong Mao, Yongle Hu, and Genyu Chen. "Analysis of mechanisms of underfill in full penetration laser welding of thick stainless steel with a 10kW fiber laser." Optics & Laser Technology 98 (2018): 97-105.
- 2. Zhang, Mingjun, Genyu Chen, Yu Zhou, and Shenghui Liao. "Optimization of deep penetration laser welding of thick stainless steel with a 10kW fiber laser." Materials & Design 53 (2014): 568-576.
- 3. Zhang, Mingjun, Shun Chen, Yingzhe Zhang, Genyu Chen, and Zhuming Bi. "Mechanisms for improvement of weld appearance in autogenous fiber laser welding of thick stainless steels." Metals 8, no. 8 (2018): 625.
- 4. Alcock, J. A., and B. Baufeld. "Diode laser welding of stainless steel 304L." Journal of Materials Processing Technology 240 (2017): 138-144.
- 5. Ullmann, C., 2016. High power diode laser in a balancing act between innovation and production technology. In: International Laser Symposium & International Symposium Tailored Joining, Dresden, Germany.
- 6. Li, Lin. "The advances and characteristics of high-power diode laser materials processing." Optics and lasers in engineering 34, no. 4-6 (2000): 231-253.
- Malchus, Joerg, Volker Krause, Georg Rehmann, Michael Leers, Arnd Koesters, and David G. Matthews. "A 40kW fiber-coupled diode laser for material processing and pumping applications." In High-Power Diode Laser Technology and Applications XIII, vol. 9348, p. 934803. International Society for Optics and Photonics, 2015.
- 8. Salminen, Antti, Anssi Jansson, and Veli Kujanpaa. "Effect of welding parameters on high-power diode laser welding of thin sheet." In High-Power Diode Laser Technology and Applications, vol. 4973, pp. 106-115. SPIE, 2003.
- 9. Abe, Nobuyuki, Ritsuko Higashino, Naoki Nakagawa, Masahiro Tsukamoto, Shoji Miyake, Shuichi Noguchi, and Masakazu Hayashi. "Welding and forming of thick steel plates with a high-power density diode laser." In International Congress on Applications of Lasers & Electro-Optics, vol. 2000, no. 1, pp. A16-A23. Laser Institute of America, 2000.

- Matsumoto, Naoyuki, Yousuke Kawahito, Koji Nishimoto, and Seiji Katayama. "Effects of laser focusing properties on weldability in high-power fiber laser welding of thick high-strength steel plate." Journal of Laser Applications 29, no. 1 (2017): 012003.
- 11. Salminen, Antti, Anna Fellman, and Veli Kujanpää. "Effect of material thickness and joint configuration on high power diode laser welding of steel." In International Congress on Applications of Lasers & Electro-Optics, vol. 2004, no. 1, p. 1202. Laser Institute of America, 2004.
- 12. Lin, Xingchen, Pengfei Wang, Hongbo Zhu, Yawei Zhang, Yongqiang Ning, and Lijun Wang. "A novel method for the welding of tailor-welded blanks with different thicknesses based on the diode laser source." Optics & Laser Technology 141 (2021): 107100.
- 13. Metelkova, Jitka, Yannis Kinds, Karolien Kempen, Charlotte de Formanoir, Ann Witvrouw, and Brecht Van Hooreweder. "On the influence of laser defocusing in Selective Laser Melting of 316L." Additive Manufacturing 23 (2018): 161-169.
- 14. Kabir, A. S. H., X. Cao, M. Medraj, P. Wanjara, J. Cuddy, and A. Birur. "Effect of welding speed and defocusing distance on the quality of laser welded Ti-6Al-4V." Mater. Sci. Technol 4 (2010): 2787-2797.
- 15. Liu, Xiu-Bo, Ming Pang, Zhen-Guo Zhang, Wei-Jian Ning, Cai-Yun Zheng, and Gang Yu. "Characteristics of deep penetration laser welding of dissimilar metal Ni-based cast superalloy K418 and alloy steel 42CrMo." Optics and Lasers in Engineering 45, no. 9 (2007): 929-934.
- 16. Sokolov, Mikhail, Antti Salminen, Mikhail Kuznetsov, and Igor Tsibulskiy. "Laser welding and weld hardness analysis of thick section S355 structural steel." Materials & Design 32, no. 10 (2011): 5127-5131.
- 17. Cheng, Hao, Li Kang, Jincheng Pang, Boce Xue, Dong Du, and Baohua Chang. "Effect of the welding position on weld quality when laser welding Inconel 617 Ni-based superalloy." Optics & Laser Technology 139 (2021): 106962.
- 18. Cao, X., P. Wanjara, J. Huang, C. Munro, and A. Nolting. "Hybrid fiber laser–Arc welding of thick section high strength low alloy steel." Materials & Design 32, no. 6 (2011): 3399-3413.
- 19. Vänskä, M., F. Abt, Rudolf Weber, A. Salminen, and Thomas Graf. "Effects of welding parameters onto keyhole geometry for partial penetration laser welding." Physics Procedia 41 (2013): 199-208.
- Ren, Wenjie, Fenggui Lu, Renjie Yang, Xia Liu, Zhuguo Li, and Seyed Reza Elmi Hosseini.
 "A comparative study on fiber laser and CO2 laser welding of Inconel 617." Materials & Design 76 (2015): 207-214.
- 21. Moosavy, Homam Naffakh, Mohammad-Reza Aboutalebi, Seyed Hossein Seyedein, Massoud Goodarzi, Meisam Khodabakhshi, Carlo Mapelli, and Silvia Barella. "Modern fiber laser beam welding of the newly-designed precipitation-strengthened nickel-base superalloys." Optics & Laser Technology 57 (2014): 12-20.
- 22. Ren, Wenjie, Fenggui Lu, Pulin Nie, Renjie Yang, Xia Liu, Kai Feng, and Zhuguo Li. "Effects of the long-time thermal exposure on the microstructure and mechanical properties of laser weldings of Inconel 617." Journal of Materials Processing Technology 247 (2017): 296-305.
- 23. Sun, Junhao, Wenjie Ren, Pulin Nie, Jian Huang, Ke Zhang, and Zhuguo Li. "Study on the weldability, microstructure and mechanical properties of thick Inconel 617 plate using narrow gap laser welding method." Materials & Design 175 (2019): 107823.
- 24. Liu, Wen, Fenggui Lu, Renjie Yang, Xinhua Tang, and Haichao Cui. "Gleeble simulation of the HAZ in Inconel 617 welding." Journal of Materials Processing Technology 225 (2015): 221-228.
- 25. Shanlin, L.; Kejian, L.; Mengjia, H.; Yao, W.; Zhipeng, C.; Jiluan, P. The Mechanism for HAZ Liquation of Nickel-Based Alloy 617B during Gas Tungsten Arc Welding. Metals. 2020

- 26. Ding, Kai, Peng Wang, Xia Liu, Xiaohong Li, Bingge Zhao, and Yulai Gao. "Formation of lamellar carbides in alloy 617-HAZ and their role in the impact toughness of alloy 617/9% Cr dissimilar welded joint." Journal of Materials Engineering and Performance 27, no. 11 (2018): 6027-6039.
- 27. Hong, J. K., J. H. Park, N. K. Park, I. S. Eom, M. B. Kim, and C. Y. Kang. "Microstructures and mechanical properties of Inconel 718 welds by CO2 laser welding." Journal of materials processing technology 201, no. 1-3 (2008): 515-520.
- 28. Liu, Wen, Fenggui Lu, Xinhua Tang, Renjie Yang, and Haichao Cui. "The microstructure evolution and element segregation of Inconel 617 alloy tungsten inert gas welded joint." Journal of Materials Research 31, no. 4 (2016): 435-442.
- 29. Fink, Carolin, and Manuela Zinke. "Welding of nickel-based alloy 617 using modified dip arc processes." Welding in the World 57, no. 3 (2013): 323-333.
- Park, Young Su, Hyo Sik Ham, Sang Myung Cho, and Dong Ho Bae. "An assessment of the mechanical characteristics and optimum welding condition of Ni-based super alloy." Procedia Engineering 10 (2011): 2645-2650.
- 31. Li, Shanlin, Kejian Li, Zhipeng Cai, and Jiluan Pan. "Behavior of M₂₃C₆ phase in Inconel 617B superalloy during welding." Journal of Materials Processing Technology 258 (2018): 38-46.
- 32. Chen, Xi, Zhenglong Lei, Yanbin Chen, Bing Han, Meng Jiang, Ze Tian, Jiang Bi, and Sanbao Lin. "Nano-indentation and in-situ investigations of double-sided laser beam welded 2060-T8/2099-T83 Al-Li alloys T-joints." Materials Science and Engineering: A 756 (2019): 291-301.

Statistical Analysis and Multi Objective Optimization of Diode Laser Welding Process by means of RSM and Desirability Approach

7.1 Introduction

As previously observed, complete elimination of underfill in DLW process remained unsolved, although full-penetration could be achieved with optimization of critical parameters of welding speed, laser power and focusing distance. Most of the defects of undercuts, porosity, root-sag could be minimized to a greater extent for joint efficiency with optimization of critical processing parameters, there seems to critical fine tuning required to minimize or eliminate underfill in the joint. Indeed, defects of underfill and root sags in weldments affect both the surface integrity, joint efficiency and thereby mechanical properties of the joints. As weld defects of underfill and root sag could not be eliminated completely by optimizing parameters of focusing distance and welding speed with full penetration in diode laser welding (DLW) process optimization previously studied in Chapter 6, it was felt necessary to assess comprehensively influence of all three critical parameters of laser power, focusing distance and welding speed to optimize weld quality employing RSM based statistical model. Thus, the present chapter critically investigate influence of critical process parameters employing statistical approach with RSM-BBD (Box-Behnken Design) methodology.

In this study, statistical methodology utilized was RSM-BBD with three-factor and three-level design of experimentation approach available with Design-Expert software with range of parameters and outputs presented in Table 3.6. High-power fibre-coupled diode laser welding experimental setup as explained previously and shown in Figure 3.11 is utilized for validation of the model. The statistical analysis software Design-Expert V-11 tool was utilized for the purpose to generate the design matrix for three-factor and three-level and subsequent analysis and co-relation with experimental outputs. The model developed is intended to effectively maximize penetration of weld joint with complete elimination of welding defect of underfill and minimization or elimination of other defects of undercuts, root sag humps and maximization of radius of curvature (ROC) for producing effective joints usable for applications. The mathematical model developed is validated with experiment conducted by employing desirability approach.

7.2 Experimental Methodology

The development of mathematical model is carried out for high-power DLW welding on 10-mm thick Inconel 617 in butt joint configuration to optimize the processing parameters that can eliminate or minimize underfill and root hump defects coupled with maximization of other weld profile parameters. Critical processing parameters such as Laser Power (LP), Welding Speed (WS) and Defocusing distance (DF) were considered as input variables while other processing conditions and parameters of laser beam size, mode of processing, shielding parameters, positioning of nozzle/optical head were retained same as used for initial works. As the principal aim of the model was to optimize these specific process variables to obtain joints with full penetration and minimal or complete elimination of critical weld defects of surface underfill/undercut and root sag hump defects, range of variation in level for the statistical model was chosen based on the optimized parameters obtained in the previous chapter.

In previous study, nearly full penetration welds with aspect (depth-to-width) ratio greater than one in bead-on-plate configuration were obtained at defocusing distances ranging from -6 to +4 mm from the entire range of study with defocusing distances from -14 mm to +10 mm. It is clear from the previous study, full penetration was obtained with occurrence of huge underfill and root hump defects at -2 mm defocusing distance and therefore in the present statistical approach, it was felt pertinent to optimize DF in the range of -2 to +2 mm. Thus, -2 to +2 mm for DF was the range considered in RSM model. Furthermore, the optimum levels of WS and LP entailing production of defect-free near full penetration welds in butt-joint configuration was observed to be 5.5 kW and 6 mm/s respectively from the previous study. Thus, a range of 5-6 kW for laser power (LP), -2 to +2 mm for defocusing distance (DF) and 6 – 14 mm/s for welding speed (WS) were considered best for developing the statistical model to envisage defect-free full penetration welds. Table 3.6 shows the range of laser welding process parameters with three-factor and three-level design approach obtained from the RSM model. A sum total fifteen experiments were required as per the three-factor and three-level matrix design obtained from RSM-BBD method (depicted in Table 3.7). Analysis of variance (ANOVA) technique was utilized to examine the significance of the developed model and the output responses were corelated with input variables using regression equation. Four important responses constituting Upper bead width (UBW), Fusion zone area (FZA), Weld penetration (WP) and Radius of curvature (ROC) were considered for output responses. The mathematical model to be developed should entail response factors to be maximized in some cases (WP and

ROC) and minimize in other (UBW and FZA). Similar high-power diode laser welding setup utilized for welding experiments as explained previously in chapter 3.

7.3 Statistical Model for upper bead width (UBW)

Table 7.1 depicts the ANOVA test result for UBW with variation of input variables such as LP, WS and DF. Results indicated that the all three input variables LP, WS and DF significantly influence UBW linearly as coded values of F and P were found to be greater than 1 and below 0.05 respectively. Interactive effects of WS and DF were also found to be significantly influence linearly UBW. Indeed, among these parameters, WS parameter influenced maximum as linear terms of WS has got highest and lowest F and P values respectively as compared to other variables effects. It suggests that the WS induced maximum influence on UBW. Indeed, it is the welding speed that governs the melt spread to a greater extent due to lateral expansion associated with the fixed laser beam spot. Further, no significant effect was observed on UBW with interaction terms between other parameters and no significant quadratic effects were seen of all three influencing parameters. The influence of DF is minimal due to the fixed laser spot size convergent with intensity profile within the range of parameters chosen. Therefore, linear terms of all input variables (LP, WS and DF) and interactive effect of WS and DF were found to be the predicting input parameters for UBW efficiently. Thus, the resultant regression equation to obtain UBW in relationships with actual variables are expressed as presented in equation 7.1:

UBW (mm) =
$$+6.5810 + 0.5075 * LP - 0.26156 * WS + 0.6743 * DF - 0.04343 * WS* DF$$

Eqn (7.1)

Table 7.1. ANOVA analysis for UBW

Source	Sum of Squares	Df	Mean Square	F-value	p-value	
Model	11.60	4	2.90	30.80	< 0.0001	Significant
A-Power	0.5151	1	0.5151	5.47	0.0414	
B-Speed	8.76	1	8.76	93.03	< 0.0001	
C-Defocus	1.84	1	1.84	19.58	0.0013	
BC	0.4830	1	0.4830	5.13	0.0469	
Residual	0.9413	10	0.0941			

Lack of Fit	0.3468	8	0.0434	0.1459	0.9816	Not significant
Pure Error	0.5945	2	0.2972			
Cor Total	12.54	14				
R ² : 92.42%; A	dj. R ² : 89.41					

Perturbation

10

9

8

B

7

A

A

1000 -0.500 0.000 0.500 1.000

Deviation from Reference Point (Coded Units)

Figure 7.1. Perturbation plot of UBW

As clearly seen from the ANOVA test result shown in Table 7.1 that the adequacy measures such as R² (0.924) and adjusted R² (0.894) values are closer to 1 for UBW, indicates the adequacy and predicting measures are found to be in good agreement and induced significant relations of input parameters. Indeed, high F and low P values of both WS and DF indicate their significant effect on formation of UBW in laser welding process. However, LP were less significant for the formation of UBW. This elucidates the effects of WS and DF on the formation of UBW, with WS more pronounced than DF. In fact, WS (interaction time) greatly influences the weld bead profile in fusion welding processes on account of heat input [1,2]. Indeed, after WS, DF is the significant term for the formation of UBW as DF induce significant effect on weld bead profile on account of their associated effects of power density, spot size, intensity distribution and energy coupling behaviour of laser-material interaction [3-6]. Furthermore, Figure 7.1 shows the perturbation plot for UBW which illustrates the comparison effect of all three input variables (LP, WS and DF) in the central point of the design space. It indicated that the influence of WS and DF on the formation of UBW are significantly more, with WS more pronounced than DF. However, LP has less significant on UBW. This is convergent with limited possibility of variation in lateral expansion of weld bead (top width) due to LP range chosen in the study and not much variation in UBW due to DF more or less remaining same with energy intensity distribution.

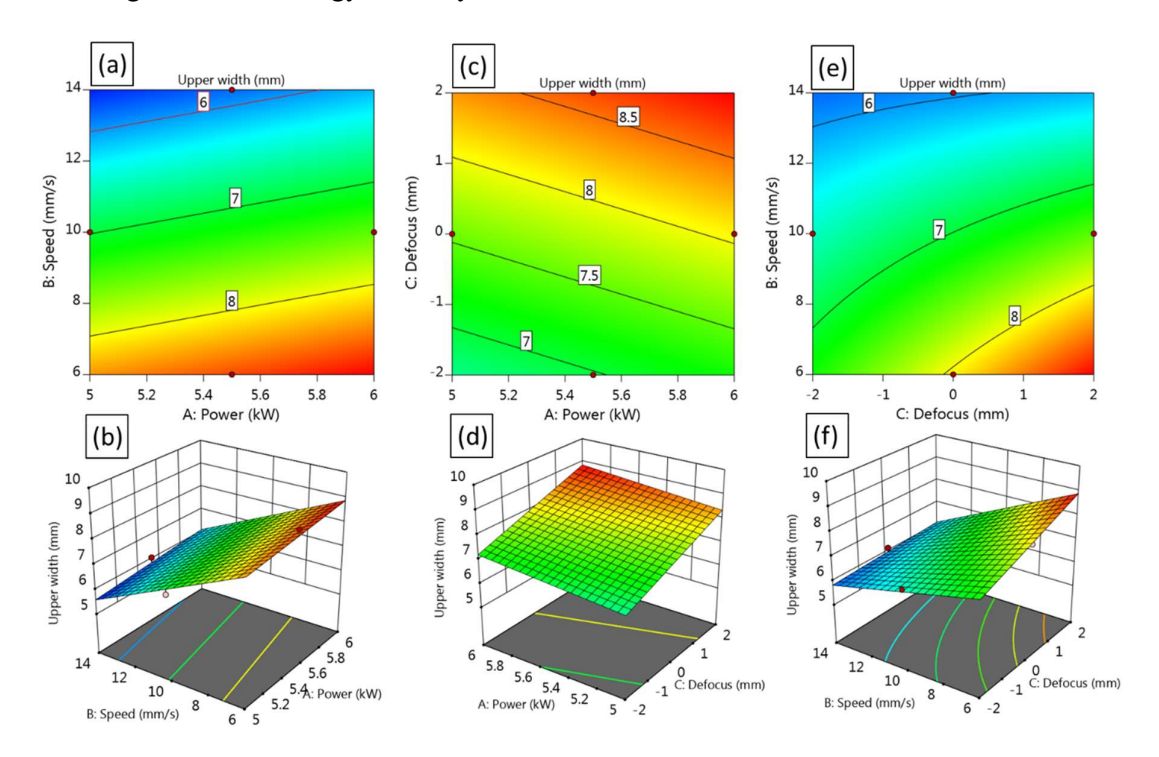


Figure 7.2. Contour plots showing influence of all three input parameters (LP, WS and DF) on UBW

Figure 7.2 shows the 2D & 3D plots of interaction of all three input parameters (LP, WS and DF) on UBW. It is clear from 2D & 3D graphs that with decreasing WS and increasing DF and LP, UBW increases. With lowest WS and highest DF and LP, maximum UBW obtained. Indeed, heat input which is a ratio of LP and WS, increases with increase in LP and decrease in WS. However, higher the positive DF, larger the spot size with outwardly diverging laser beam entering into the keyhole through the surface of the material and thereby resulting in shallow and wider UBW at positive defocus [7-9]. Similar observations were observed on model employing RSM-statistical approach in laser-based welding by various researchers [10-13]. On the whole, the regression mathematical model developed for UBW were found to be in good agreement in forecasting results in conjunctions with results obtained by experiments.

7.4 Statistical Model for weld penetration (WP)

Table 7.2. ANOVA analysis for WP

Source	Sum of Squares	Df	Mean Square	F-value	p-value	
Model	23.65	4	5.91	26.86	< 0.0001	Significant
A-Power	3.73	1	3.73	16.93	0.0021	
B-Speed	12.13	1	12.13	55.10	< 0.0001	
C-Defocus	6.50	1	6.50	29.52	0.0003	
B^2	1.30	1	1.30	5.89	0.0356	
Residual	2.20	10	0.2201			
Lack of Fit	2.10	8	0.2622	5.08	0.1749	Not significant
Pure Error	0.1033	2	0.0516			
Cor Total	25.85	14				

R²: 91.46%; Adj. R²: 88.02

Table 7.2 depicts the ANOVA test result for WP with variation of input variables such as LP, WS and DF. Results indicated that the all three input variables LP, WS and DF were significantly influenced WP linearly as F and P were found to be greater than 1 and below 0.05 respectively. Indeed, among all three input variables, WS parameter influenced maximum as linear terms of WS has got highest and lowest F and P values respectively as compared to other variables effects, similarly to the effect on UBW. It suggests that the WS induced maximum influence on WP as compared to other variables of LP and DF. In addition to this, quadratic term of WS were also found to be significantly influence WP as F and P are within desired limits of LP and DF. Further, no significant effect was observed on WP with interaction terms between any input parameters as observed in case of UBW and no more significant quadratic effects were seen between other influencing parameters. Indeed, interactive terms involving LP and DF is less decisive in influencing WP on account of the marginal effect of heat input per unit area variation involved. Therefore, linear terms of all input variables (LP, WS and DF) and quadratic term of WS were found to be the predicting input parameters for WP efficiently. Thus, the resultant regression equation to obtain WP in relationships with actual variables are expressed as presented in equation 7.2:

WP (mm) =
$$+6.0890 + 1.3650 * LP - 1.0446 * WS - 0.4506 * DF + 0.0368 * WS^2$$
 Eqn (7.2)

As clearly seen from the ANOVA test result shown in Table 7.2 that the adequacy measures of R² (0.914) and adjusted R² (0.880) are closer to 1 for WP, indicating adequacy with predictability for good agreement and induced significant relations of input parameters. Indeed, high F and low P values of WS and DF indicate their significant effect on formation of WP in laser welding process. However, LP was found more effective variable for the formation of WP but to lesser extent as compared to WS and DF as obvious from their respective F and P values. This elucidates effect of all three input variables on the formation of WP, with WS and DF more pronounced than LP. WP of the through thickness in laser welding processes depends on extent of heat input such as WS (interaction time), and LP (power density) and finally DF (intensity distribution profile governing laser-material interaction) [1,2]. WS parameter induced highest influenced on WP, it is due at the direct effect of interaction time to fuse the material for melting. After WS, DF is the significant term for the formation of WP as DF induce significant effect on weld bead profile associated with spot size and intensity distribution and energy coupling behaviour of laser-material interaction [3-6]. Indeed, small parametric range of LP selected in the space design, showed not much significant influenced on WP as obvious from the ANOVA analyses shown in Table 7.2 as compared to other parameters. Similar observations were made on welding processing employing RSM-statistical modelling by various researchers [10-13].

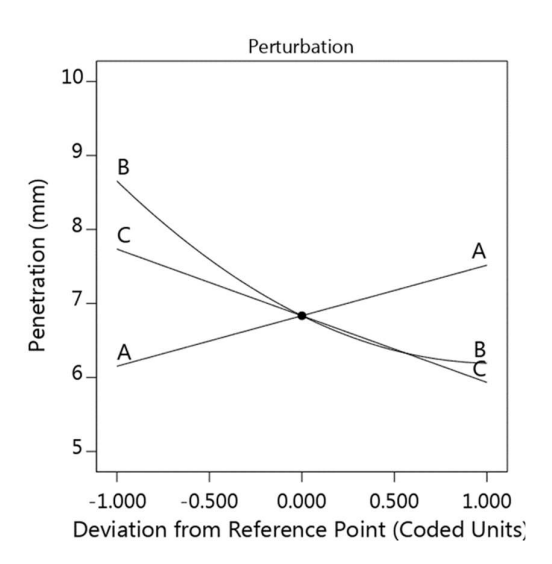


Figure 7.3. Perturbation plot of WP

Furthermore, Figure 7.3 shows the perturbation plot for the response WP which illustrates the comparison effect of all three input variables (LP, WS and DF) in the central point of the design space. It elucidates dominant negative effect of WS and DF and moderate

positive effect of LP on WP. It indicates that the WS and DF has direct effect on the response of WP of laser welded superalloy as compared to LP. As effective interaction time associated with WS has a pivotal role in determining the depth of penetration (WP). DF (negative defocus) has direct effect on WP due to the fact that at negative defocus, laser beam energy density induced in laser keyhole wall with inward laser beam divergence is comparatively high as compared to that of outward laser beam divergence at positive and zero defocusing [8,9]. However, LP has less significant on WP, due to its sluggish effect associate with the utilization of small parametric window in the design space.

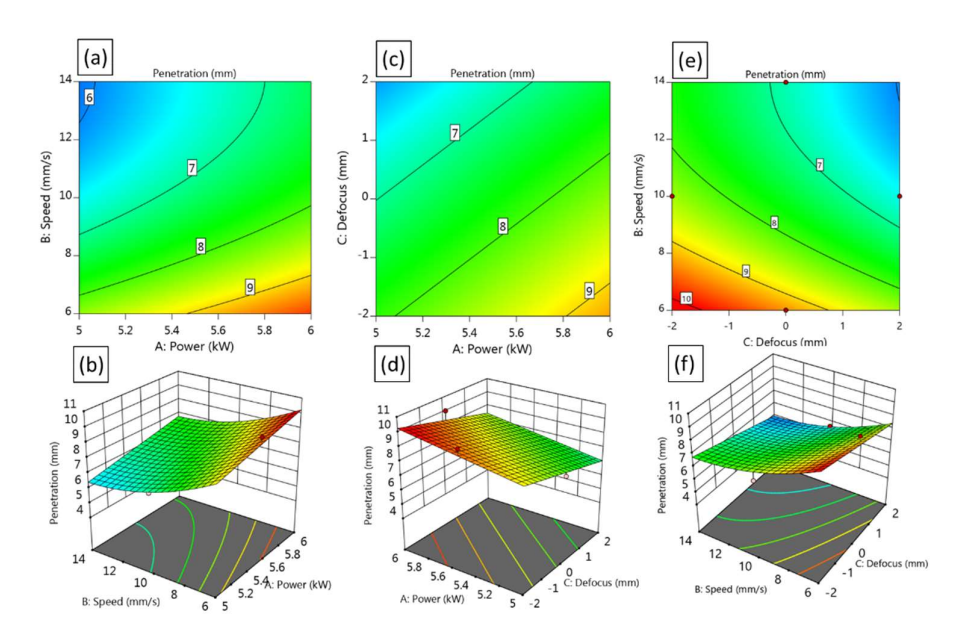


Figure 7.4. Contour plots showing influence of all three input parameters (LP, WS and DF) on WP

Figure 7.4 shows the 2D & 3D plots of interaction of all three input parameters (LP, WS and DF) on the response WP. It is clear from 2D & 3D graphs (Figure 7.4) that by decreasing WS coupled with reducing DF and by increasing LP, maximum depth of penetration (WP) could be obtained as manifest from the curving nature of 3D graphs. Indeed, either increase in LP or decrease in WS increases the heat input (heat input is a ratio of LP and WS) with extended interaction time to enhance the WP through thickness in laser welding processes [1,2,10]. However, at negative DF, laser beam enters into the keyhole wall converged gradually to the focal point imposing optimum power density with maximum intensity inside the material than that of weld processed with zero or positive focussing on surface of the material [7-9]. Similar observations were made on welding processing employing RSM-statistical modeling by various researchers [10-13]. On the whole, the regression mathematical model developed

for WP were found to be in good agreement in predicting results in conjunction with experimental values.

7.5 Statistical Model for fusion zone area (FZA)

Table 7.3. ANOVA analysis for FZA

Source	Sum of Squares	df	Mean Square	F-value	p-value	
Model	687.44	4	171.86	47.86	< 0.0001	Significant
A-Power	49.10	1	49.10	13.68	0.0041	
B-Speed	547.47	1	547.47	152.48	< 0.0001	
C-Defocus	49.70	1	49.70	13.84	0.0040	
B^2	41.16	1	41.16	11.46	0.0069	
Residual	35.91	10	3.59			
Lack of Fit	33.74	8	4.22	3.90	0.2200	Not significant
Pure Error	2.16	2	1.08			
Cor Total	723.34	14				

R²: 95.02%; Adj. R²: 93.07

Table 7.3 shows the ANOVA test result for the response FZA (to be minimized) with variation of input variables of LP, WS and DF. ANOVA test results indicated that the all three input variables LP, WS and DF significantly influence FZA linearly as F and P were found to be greater than 1 and below 0.05 respectively. Indeed, among all three input variables, response WS influenced maximum as linear terms of WS has got highest and lowest F and P values respectively as compared to other variables effects, similarly to the effect on UBW and WP. It suggests that the WS induced maximum influence on FZA as well. However, DF and LP showed almost similar effect on the response of FZA as values of F and P for DF and LP are more or less similar. In addition to this, quadratic term of WS were also found to be significantly influenced FZA as F and P are within the desired limit, similarly to the effect observed in case of WP. Furthermore, no significant effect was observed on FZA as well with interaction terms between any input parameters as observed in case of UBW and no more significant quadratic effects were seen between other influencing parameters. The result is convergent with the fact that interaction time greatly influence on melt efficiency and thereby FZA. Furthermore, the range of laser power and defocusing distance chosen may not alter the

melt efficiency due to more or less constant heat input induced for welding. Therefore, linear terms of all input variables (LP, WS and DF) and quadratic term of WS were found to be the critical predicting input parameters for FZA efficiently. Thus, the resultant regression equation to obtain FZA in relationships with actual variables are expressed as presented in equation 7.3:

$$FZA (mm^2) = +34.4381 + 4.9550 * LP - 6.2185 * WS - 1.2465 * DF + 0.2075 * WS^2$$

 $Eqn (7.3)$

As clearly seen from the ANOVA test result shown in Table 7.3 that the adequacy measures such as R² (0.950) and adjusted R² (0.930) values are closer to 1 for FZA, indicates the adequacy and predicting measures are found to be in good agreement and induced significant relations of input parameters. Indeed, highest F and lowest P values of WS indicate its significant effect on formation of FZA in laser welding process. However, DF and LP were also the significant variable for the formation of WP but to lesser extent as compared to WS as manifest from their respective F and P. This elucidates effects of all three input variables on the formation of FZA, with WS more pronounced than DF and LP. However, DF and LP showed similar effect on FZA. Similar to WP, FZA of the through thickness in laser welding processes depends on extent of heat input such as WS (interaction time), and LP (power density) and finally DF (nature of laser beam-material interaction) [1,2,10]. WS parameter induced highest influenced on FZA as evident from the ANOVA test, it is due at lower welding speed interaction time increases causes significant transfer of laser beam energy to material with prolonged duration as a result of high interaction time causing large melt fusion zone area (FZA) to form. DF and LP induced almost similar significant effect on the response FZA. After WS, DF induce significant effect on melt efficiency (FZA) on account of their associated effects of power density, spot size, intensity distribution and energy coupling behaviour of laser-material interaction [3-6]. Indeed, small parametric range of LP selected in the space design, showed not much significant influenced on FZA as manifest from their low F and high P values.

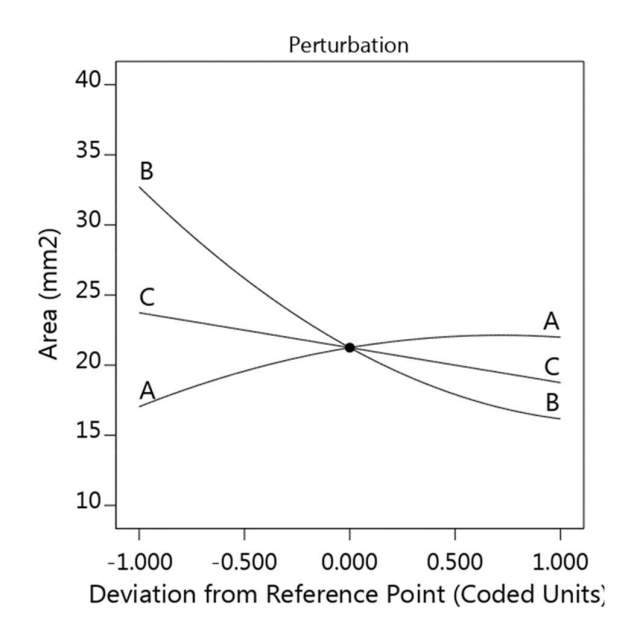


Figure 7.5. Perturbation plot of FZA

Furthermore, Figure 7.5 shows the perturbation plot for the response FZA which illustrates the comparison effect of all three input variables (LP, WS and DF) in the central point of the design space. It elucidates dominant negative effect of WS and DF and moderate positive effect of LP on FZA. It indicates that the WS has direct effect on the response FZA of laser welded superalloy followed by DF and LP. As effective interaction time associated with WS has a pivotal role in determining the melt efficiency (FZA) similar to that for WP. DF has direct influence on FZA due to the fact that at higher defocus specially at -2 mm DF, the laser beam energy interacts with the material with slightly larger spot size coupled with enhanced laser energy transfer enabling larger FZA and deeper weld penetration (WP) as explained previously. Similarly, LP has significant effect on response FZA on account of high heat input (interaction time) associated with high LP.

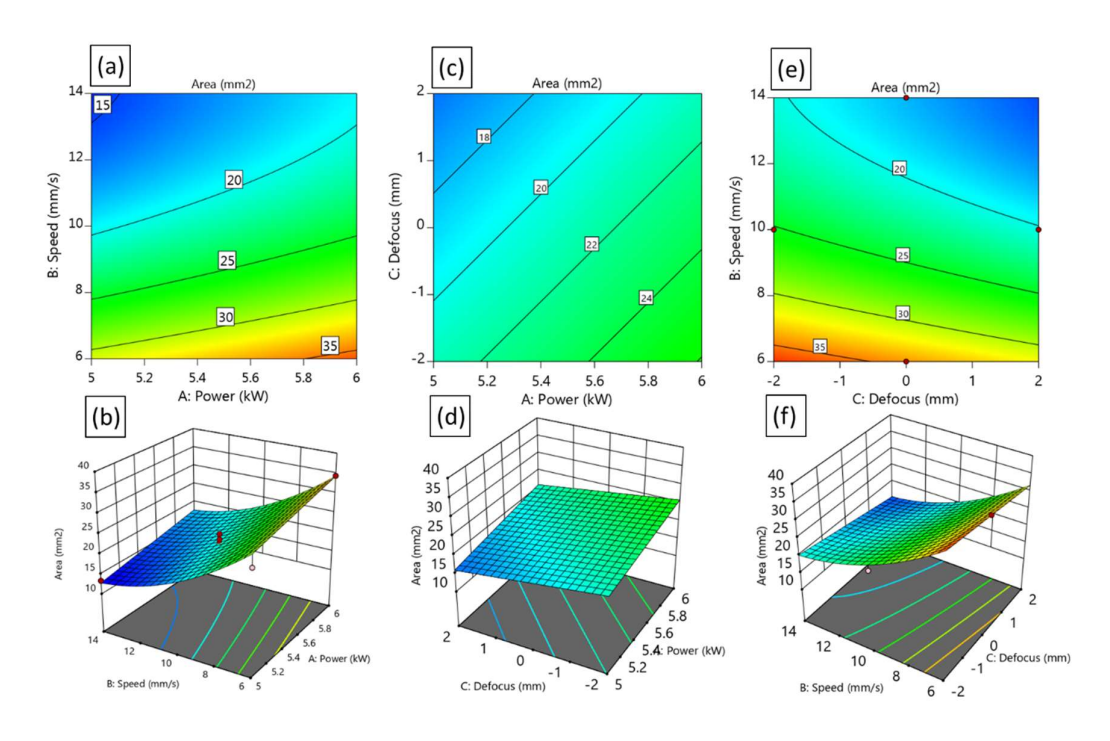


Figure 7.6. Contour plots showing influence of all three input parameters (LP, WS and DF) on FZA

Figure 7.6 shows the 2D & 3D plots of interaction of all input parameters (LP, WS and DF) on the response FZA. It is clear from 2D & 3D plots (Figure 7.6) that by decreasing WS coupled with reducing DF and by increasing LP, maximum fusion zone area (FZA) could be achieved as evident from the curvature in 3D contour plots. Indeed, either increase in LP or decrease in WS increases the heat input (heat input is a ratio of LP and WS) with extended interaction time to enhance the FZA cross-sectionally in laser welding processes [1,2,10]. Indeed, at high DF specially at -2 mm, laser beam interacts with the substrate material with slightly larger spot size coupled with enhanced laser energy transfer resulting in enhanced FZA as evident from the curvature in the contour plots (Figure 7.6). Similar observations were made on welding processing employing RSM-statistical modeling by various researchers [10-13]. On the whole, the regression mathematical model developed for FZA were found to be in good agreement in predicting results in conjunction with experimental values.

7.6 Statistical Model for radius of curvature (ROC)

Table 7.4. ANOVA analysis for ROC

Sum of Mean Source df F-value p-value Squares Square
--

Model	1.29	2	0.6432	35.69	< 0.0001	Significant
A-Power	0.2278	1	0.2278	12.64	0.0040	
B-Speed	1.06	1	1.06	58.74	< 0.0001	
Residual	0.2162	12	0.0180			
Lack of Fit	0.1150	10	0.0115	0.2271	0.9575	Not significant
Pure Error	0.1013	2	0.0506			
Cor Total	1.50	14				

R²: 85.61%; Adj. R²: 83.22

Radius of Curvature - ROC is another most important response parameter required to be assesses for this welding process since it determines susceptibility of liquation cracking at neck zone in welding superalloy [14,15]. Table 7.4 illustrates ANOVA test result for the response of ROC with variation in input variables of WS and LP. It is clear from ANOVA test results that only LP and WS induced significant effect on ROC linearly as F and P were found to be greater than 1 and below 0.05 respectively. Indeed, among the parameters of WS and LP, WS influenced maximum as linear terms of WS has got highest and lowest F and P values respectively as compared to other variables effects. However, all other parameters of linear terms (DF), quadratic as well as interactive terms influence in the selected matrix have no obvious significant effect in determining ROC as F and P were found to be beyond their required limit. This is obvious, since heat stagnation at neck-zone remains uninfluenced due to variation in DF as heat dissipation and transfer characteristics does not alter and remain constant. Thus, the resultant regression equation to obtain ROC in the laser welded cross-section in relationships with actual variables be expressed as presented in equation 7.4:

$$ROC (mm) = -0.0322 + 0.3375 * LP - 0.0909 * WS Eqn (7.4)$$

As clearly seen from the ANOVA test result shown in Table 7.4 that the adequacy measures such as R² (0.856) and adjusted R² (0.832) values are closer to 1 for ROC, indicates the adequacy and predicting measures are found to be in good agreement and induced significant relations of input parameters. Indeed, highest F and lowest P values of WS indicate its significant effect on formation of ROC in laser welding process. However, DF did not show any significant influence on ROC as compared to that of its significant influence on UBW, WP and FZA due to the utilization of small parametric window in the design space. High interaction time associated with low WS is so significant (negatively) to develop ROC as it principally

depends on the depth-to-width aspect ratio in laser welds. The effect of WS on ROC is maximum as manifest from the ANOVA analysis. Indeed, lower the WS, higher the depth-to-width ratio and as a result higher the ROC and lower will be the liquation cracking susceptibility. In contrast to the effect of WS, influence of LP on ROC found to be significant positively. Thus, higher the LP, higher is the ROC.

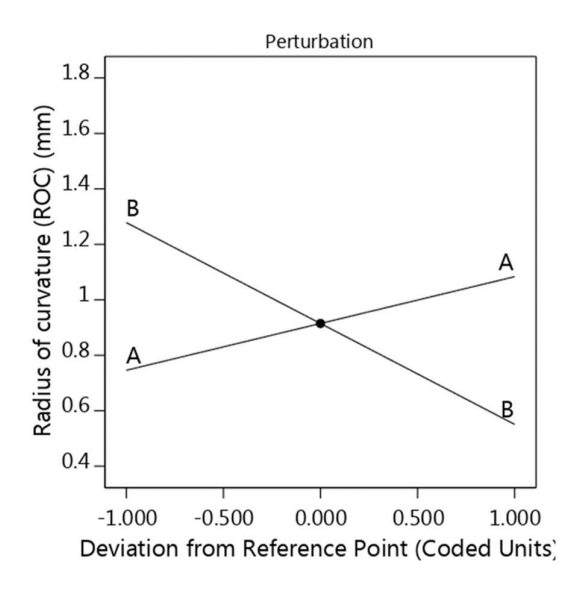


Figure 7.7. Perturbation plot of ROC

Figure 7.7 shows the perturbation plot for the response ROC which explains nearly linear converge plots (converged at central point) for both WS and LP. Therefore, higher ROC in laser welded superalloy could achieve by reducing WS (interaction time) and increasing LP. Further it is clear from Figure 7.7, that the WS has significant maximum negative influence and LP has significant positive effect on the response ROC, with effect of DF being void.

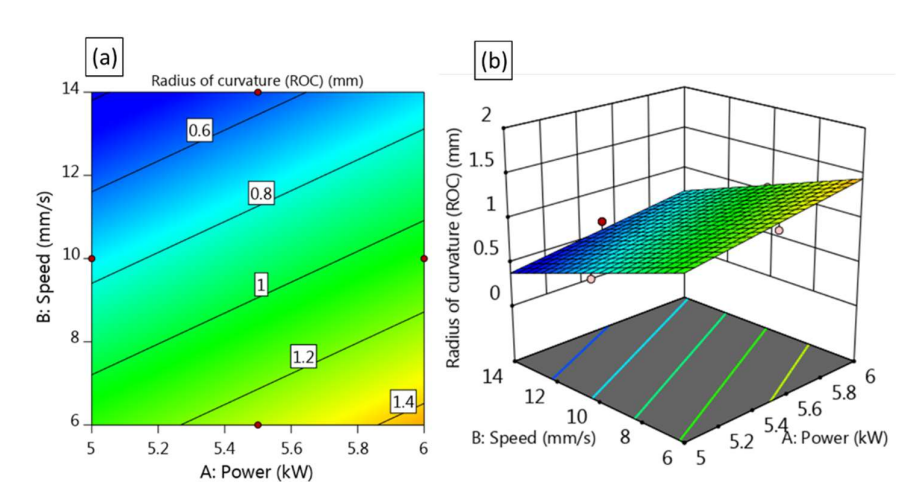


Figure 7.8. Contour plots showing influence of input parameters (LP, and WS) on ROC

Figure 7.8 shows the 2D & 3D plots of interaction parameters LP and WS on ROC. It is clear from 2D & 3D graphs (Figure 7.8) that by decreasing WS coupled with increasing LP, maximum ROC could be achieved as evident from the curvature in 3D contour plots. On the whole, the regression mathematical model developed for ROC were found to be in good agreement in predicting results in conjunction with experimental values.

7.7 Optimization using desirability approach

Table 7.5. Optimization criteria using desirability approach

Constraints	Goal	Lower Limit	Upper Limit	Importance
A: Power	is in range	5	6	3
B: Speed	is in range	6	14	3
C: Defocus	is in range	-2	2	3
UBW (mm)	is in range	5	10	3
WP (mm)	Maximize	5.37	10	5
FZA (mm ²)	is in range	13.37	38.01	3
ROC (mm)	Maximize	0.47	1.64	5

As various quadratic as well as interactive terms of the independent input variables influence output responses such as UBW, WP, FZA and ROC in the regression model, it is difficult to find the optimal processing parameters. Therefore, by applying a mutual objective optimization method using desirability function, is necessary to solve such problem. The desirability approach is a numerical method to explain and solve a combination of objective optimization problem, which satisfies all output responses and search optimal input variables with desirability values '0' indicating improper design for the output responses whereas value '1' indicates perfect design [16-18]. Table 7.5 illustrates the criteria for optimization of parameters used in this study. In this process, all input variables and the output responses such as UBW and FZA entail equal importance and kept in a range. Indeed, output responses particularly WP and ROC are kept as maximum. Indeed, higher the ROC lowers the liquation cracking susceptibility [14]. Thus, maximizing the ROC to as much as possible is the important criteria for the developing the model. As well known, critical laser welding processing parameters such as LP, WS as well as DF influence the weld bead profile (weld bead width, FZA, and WP) that effect the weld quality and joint performance. However, depth of penetration (WP) in high-energy density beam process including laser beam welding is of more

very importance to obtain high depth-to-width ratio welds. Thus, obtaining high WP without producing any defects is of primary need. Therefore, the principal aim of the model was fixed to optimize the input variables to obtain full penetration welds with minimization or complete elimination of critical welding defects generally encountered during thick sections welding such as underfill/undercut and root sag hump defects and increase ROC to as maximize as possible is the desired criteria in this study. Table 7.6 depicts the various solutions found based on the design criteria.

Number Power Speed Defocus **UBW** WP **FZA ROC** Desirability 1 6.000 6.000 -1.489 7.441 10.008 36.183 1.447 0.914 Selected 2 5.965 6.000 -2 7.212 10.191 36.647 1.435 0.908

9.499

34.774

1.382

0.863

7.908

3

6.000

6.000

-0.359

Table 7.6. Optimized solutions obtained from the model

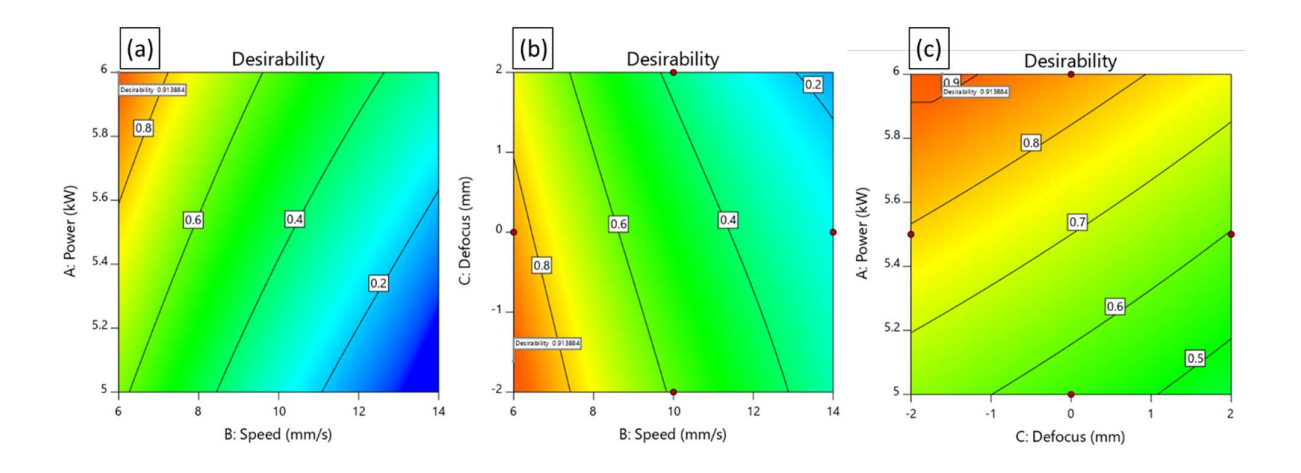


Figure 7.9. Contour plots for overall desirability for laser welding process

Further, the 2D plots shown in Figure 7.9 illustrates overall desirability of developed model with an overall desirability value of 0.914. Therefore, from desirability approach, the optimum values for high-power diode laser welding processing parameters on 10-mm thick Inconel 617 alloy are 6 kW laser power (LP), 6 mm/s WS and -1.489 mm DF. The predicted output responses from the RSM model are: weld penetration (WP) was 10.008 mm with fusion zone area (FZA) being of 36.183 mm² and upper bead width (UBW) of 7.441 mm and radius of curvature (ROC) of about 1.447 mm.

7.8 Validation of the optimum solutions

Table 7.7. Validation of experimental results with predicted one

Responses	Predicted	Desirability	Experimental	Error (%)
UBW	7.441	0.914	7.177	3.5
WP	10.008	0.914	11.127	0.1
FZA	36.183	0.914	37.69	3.9
ROC	1.447	0.914	1.411	2.4

Further the validation of the RSM model was carried out by conducting the actual laser welding experiment on 10-mm thick Inconel 617 alloy employing welding parameters obtained from the model. Then metallography samples were cut cross-sectionally, mechanically polished and etched chemically same procedure as previously described. Figure 7.10 depicts the cross-sectional macrograph of weld bead profile produced from the predicted RSM model and Table 7.7 depicts the validation of results.

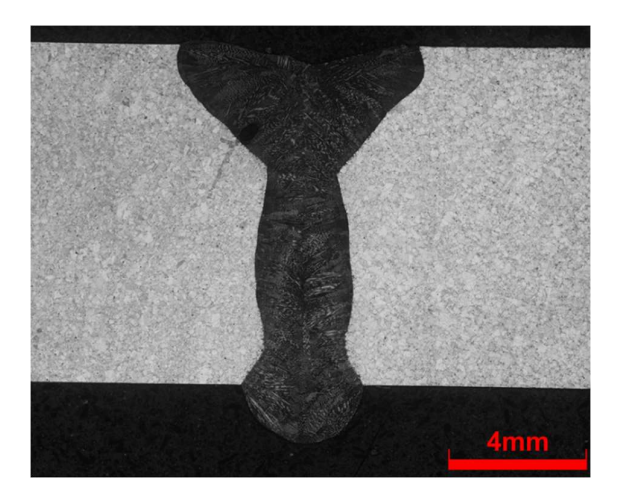


Figure 7.10. Macrograph obtained from the optimized parameters

The resulting optimized weld penetration (WP) was 11.127 mm with fusion zone area (FZA) being of 37.69 mm² and upper bead width (UBW) of 7.177 mm and radius of curvature (ROC) of about 1.411 mm. The error percentage between the optimal predicted values obtained from statistical model and actual experimental values was found to be less than 5%, which is in the acceptable range. Therefore, it can infer that the actual experimentation values are in fine agreement with the values provided by statistical approach, thus concluding that the optimum solutions obtained from the RSM model for welding thick-sections using high-power diode

laser can be applied with high precision. Although the weld bead obtained by statistical modeling approach found to be superior as compared to the welds obtained in chapter 6. However, marginal level of underfill/root humps could still be observed in deep penetration laser welding of superalloy.

7.9 Analysis of tensile properties of optimized butt joint produced by RSM

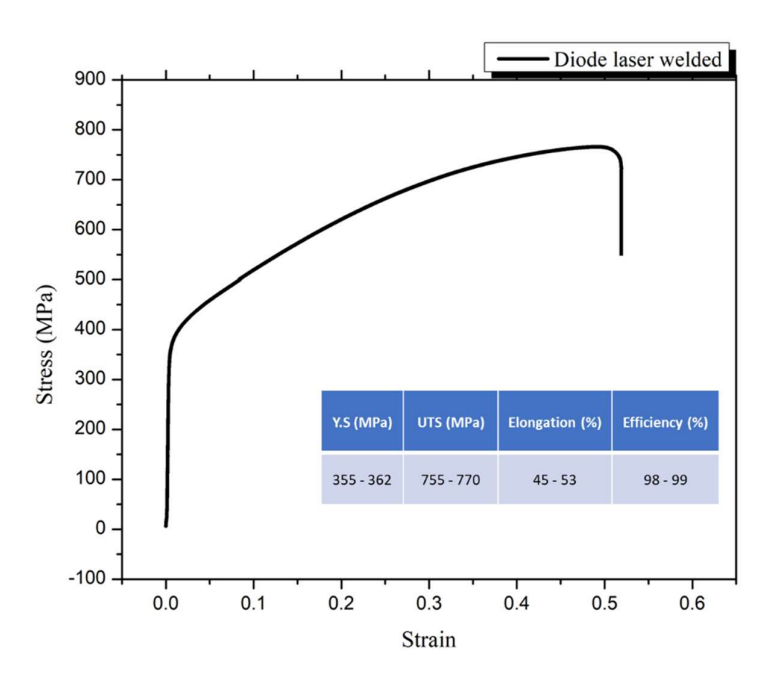


Figure 7.11. Stress-strain graphs of welded Inconel 617 alloy produced by RSM optimized parameters

Further to the validation of the RSM model, tensile testing of the optimized butt welded joint (processed with optimum conditions of 6 kW laser power (LP), 6 mm/s WS and -1.489 mm DF) conducted at room temperature to assess its joint efficiency and compared with previously obtained with DLW process. The engineering stress-strain curves of welded Inconel 617 alloy is presented in Figure 7.11 along with tensile properties evaluated. The YS and UTS of the optimized butt-welded joint are 355-362 and 755-770 MPa respectively with an elongation of 45-53 %. In contrast, BM showed YS and UTS of 325-335 and 765-769 MPa respectively with an elongation of 60-67%. A 98-99% joint efficiency along with improvement in YS, although with a reduction in elongation as compared to BM was achieved during autogenous diode laser welding at optimum conditions obtained from the RSM model. Moreover, the weld joint strength obtained in the present study is found to be slightly superior to that of previously observed by DLW methods as discussed in chapter 6. On the whole, welds

obtained by statistical modeling approach found to be superior as compared to the previous study. RSM model efficiently helped in reducing the critical welding defects such as underfills and root sag humps and thereby enhancing weld joint strength with improved weld quality. Indeed, fine-tuning of DF parameter played a decisive role in optimizing the process effectively with development of the mathematical model.

7.10 Conclusions

In the present study, RSM-BBD method with three-factor and three-level methodology was utilized to optimize the deep penetration diode laser welding critical process parameters to obtain full penetration welds with reduced welding defects such as underfill, undercuts, root sag humps. Influence of three Laser welding critical process parameters such as Laser power (LP), Welding speed (WS) and Defocusing distance (DF) on quality of welds such as Upper bead width (UBW), Fusion zone area (FZA), Weld penetration (WP) and Radius of curvature (ROC) were assessed. Following conclusions can be made:

- ➤ There exists an optimized process parametric range during deep penetration diode laser welding of 10-mm thick Inconel 617 superalloy, where a reduced underfill and root hump defects could be obtained.
- ➤ Process optimization was obtained by maximizing weld penetration and radius of curvature (ROC), whereas fusion zone area (FZA) and upper bead width (UBW) were kept in the obtained range.
- ➤ Based on regression equations obtained from the model indicated that the linear terms of all three input parameters such as LP, WS and DF exert significant effect on UBW, WP and FZA. Also, interactive terms between WS and DF has significant influence on formation of UBW. Quadratic terms of WS were found to have significant effect on both WP and FZA. However, for ROC response, only linear terms between LP and WS was found to have significant effect.
- ➤ Optimized process parameters were obtained from the model to achieve maximum depth of penetration in 10-mm thick Inconel 617 alloy with maximum ROC were, laser power of 6 kW, welding speed of 6 mm/s and a defocusing distance of -1.48 mm.
- ➤ Validation of the model was done using desirability approach and the experimental results were found to be in good agreement with the predicted one with <5% error.
- ➤ Tensile test results indicated that the weld joint efficiency of the optimized butt-welded joints obtained from RSM model are found to be in the range of 98 99% and superior to that of previously obtained by DLW

➤ Indeed, RSM methodology used for developing the model facilitated in fine-tuning defocusing distance effectively welding process with application of other parameters (LP and WS) in the applicable range and also optimize joint strength.

7.11 References

- 1. Šibalija, Tatjana V., and V. D. Majstorovic. Advanced Multiresponse Process. Optimisation. Berlin, Germany: Springer, 2016.
- 2. Moradi, Mahmood, and Majid Ghoreishi. "Influences of laser welding parameters on the geometric profile of NI-base superalloy Rene 80 weld-bead." The International Journal of Advanced Manufacturing Technology 55, no. 1 (2011): 205-215
- 3. Alcock, J. A., and B. Baufeld. "Diode laser welding of stainless steel 304L." Journal of Materials Processing Technology 240 (2017): 138-144
- 4. Kabir, A. S. H., X. Cao, M. Medraj, P. Wanjara, J. Cuddy, and A. Birur. "Effect of welding speed and defocusing distance on the quality of laser welded Ti-6Al-4V." Mater. Sci. Technol 4 (2010): 2787-2797
- Anusha, E., Adepu Kumar, and S.M. Shariff. "Numerical and statistical modelling of high speed rotating diode laser surface hardening process on a steel rod." Optics & Laser Technology 143 (2021): 107309.
- Benyounis, K. Y., Abdul-Ghani Olabi, and M. S. J. Hashmi. "Optimizing the laser-welded butt joints of medium carbon steel using RSM." Journal of Materials Processing Technology 164 (2005): 986-989.
- Zhang, Mingjun, Zheng Zhang, Kun Tang, Cong Mao, Yongle Hu, and Genyu Chen. "Analysis
 of mechanisms of underfill in full penetration laser welding of thick stainless steel with a 10
 kW fiber laser." Optics & Laser Technology 98 (2018): 97-105.
- 8. Zhang, Mingjun, Genyu Chen, Yu Zhou, and Shenghui Liao. "Optimization of deep penetration laser welding of thick stainless steel with a 10 kW fiber laser." Materials & Design 53 (2014): 568-576.
- Zhang, Mingjun, Shun Chen, Yingzhe Zhang, Genyu Chen, and Zhuming Bi. "Mechanisms for improvement of weld appearance in autogenous fiber laser welding of thick stainless steels." Metals 8, no. 8 (2018): 625.
- 10. Vijayan, K., and P. Ranjith Kumar. "Investigation of Process Parameters for Laser Welding of Low Carbon Steel using RSM." Asian Journal of Research in Social Sciences and Humanities 6, no. 8 (2016): 2005-2018.
- 11. Khan, M. M. A., Luca Romoli, Marco Fiaschi, Gino Dini, and F. Sarri. "Multiresponse optimization of laser welding of stainless steels in a constrained fillet joint configuration using RSM." The International Journal of Advanced Manufacturing Technology 62, no. 5 (2012): 587-603.
- 12. Ragavendran, M., N. Chandrasekhar, R. Ravikumar, Rajesh Saxena, M. Vasudevan, and A. K. Bhaduri. "Optimization of hybrid laser–TIG welding of 316LN steel using response surface methodology (RSM)." Optics and Lasers in Engineering 94 (2017): 27-36.
- 13. Shi, Hao, Ke Zhang, Zhengyi Xu, Tianyu Huang, Liwen Fan, and Weining Bao. "Applying statistical models optimize the process of multi-pass narrow-gap laser welding with filler wire." The International Journal of Advanced Manufacturing Technology 75, no. 1 (2014): 279-291.
- 14. Nishimoto, K., I. Woo, T. Ogita, and M. Shirai. "Factors affecting HAZ cracking susceptibility of laser welds. Study of weldability of Inconel 718 cast alloy (4th report)." (2001): 965-972.

- 15. Ren W, Lu F, Yang R, et al. Liquation cracking in fiber laser welded joints of inconel 617. J Materials Processing Technology. 2015;226:214-220.
- Changrong Chen, Xianbin Zeng, Qianting Wang, Guofo Lian, Xu huang, Yan Wang, Statistical modeling and optimization of microhardness transition through depth of laser hardened AISI 1045 carbon steel, Opt. Laser Technol. 124 (2020), 105976
- 17. Mahmoud Moradi, Hossein Arabi, Mahmoud Shamsborhan, Multi-Objective Optimization of High-Power Diode Laser Surface Hardening Process of AISI 410 by means of RSM and Desirability Approach, Optik 202 (2020), 163619.
- 18. Ali Khorram, Akbar Davoodi Jamaloei, Abed Jafari, Mahmoud Moradi, "Nd:YAG laser surface hardening of AISI 431 stainless steel; mechanical and metallurgical investigation", Opt. Laser Technol. 119 (2019), 105617.

Development of novel two-step diode laser welding technique without fillerwire feeding and designing of specific joint configuration for thick-section welding of superalloy

8.1 Introduction

Further to the difficulty in resolving defects of underfill, root sag and such similar defects in single-pass laser welding of 10-mm thick superalloy 617 material, it was felt necessary to develop a new modified process with manual placement of wire by tack welding and subsequent seam welding. Although various advanced methods of laser-hybrid-welding and multi-pass laser welding processes are available for thick-section welding (greater than 10 mm), the aim was to eliminate costly and cumbersome wire-feeder apparatus and additional heat sources like TIG, MIG etc. Apparently, other techniques like multi-pass welding with process variants such as both side autogenous welding, multi-layer/multi-groove welding with filler addition, single-pass welding with additional setups of magnetic stirring, welding with pre-heating of filler-wire and/or work piece were observed to resolve the issues of undercut/underfill and root sagging defects in thick section welding to certain extent [1-7], cost-effective welding in single-pass is the need of the hour and as a result development of new method using latest high-quality diode laser.

Moreover, multi-layer narrow-gap laser welding of Inconel 617 alloy effectively produced joints in thick plates, although with multiple-passes [1,6]. In their method, joint was made by continuous feeding of filler wire during laser seam welding with laser being focused on filler wire to fill the gap. However, defects such as lack of sidewall fusion and/or root nonfusion due to large gap width persisted. Although, welding of thick-sectioned large component could be made by above method with multi-pass and multi-layer deposition, the high heat-input welding strategy reduced the joint efficiency in terms of impact strength, elongation and creep resistance on account of large heat affected zone and residual stresses with heavy distortion. Additionally, the economy of the process will be higher due to the additional wire-feeding apparatus required for the purpose. Many a times, post-weld treatments and post-process machining requirements become mandatory to overcome these issues in thick-section welding for use in actual application [1-7]. Therefore, a novel laser welding technique involving two-

step welding method with addition of filler wire help facilitate to weld thick sections has been taken up and comprehensive elaborated the study undertaken in this chapter. The novel method (patented) provides a cost-effective single-pass laser welding method without wire feeder to obtain satisfactory full penetration welds in thick-sections with complete removal of underfill/undercuts, root humps defects etc. along with improvement in weld joint efficiency and significant reduction in distortion with good-bead appearance.

8.2 Experimental Methodology

The present novel welding method utilizes the same high-quality high-power fibrecoupled diode laser integrated to 6 + 2 axis robotic workstation (similar to that previously explained, shown in Figure 3.11) with additional fixturing and shielding setup as shown in Figure. 3.13, for joining thick-section metal plates using a newly designed butt joint configuration for preplacement of solid filler wire followed by two steps of laser welding. Base material utilized for the present study is a solid-solution strengthened nickel-based superalloy Inconel 617 in a form of plate of thickness 10 mm whose nominal composition is tabulated in Table 3.1. Details of optimum parameters and conditions including filler material type, size and groove geometry utilized in the present study is presented in Table 8.1. Appropriate fixturing setup designed and fabricated with shielding setup for the purpose as shown in inset image of Figure 3.13. Inert shielding gas (helium) was provided by a shielding nozzle to protect from atmospheric oxidation during welding. Furthermore, a back-purging shielding setup was also provided by supplying the same shielding gas at the root side of the weld during laser welding. Further, the included angle between the shielding nozzle and its vertical was in the range of $45 - 50^{\circ}$. The developed method involved two-step welding method (tack welding and seam welding). In the first step, filler wire was tack-welded with suitable laser processing parameters and conditions (based on plate thickness, groove-design, filler-wire type and size) so that wire should completely stick in between the grooves. After successful tack welding of filler wire into the narrow groove, seam welding (second step) was performed with optimized processing parameters and conditions. Details of optimized process parameters for laser tack and seam welding experiments are provided in Table 8.2 and 8.3 respectively. Subsequent to welding experiments, visual and radiography examination of welds were carried followed by macro and microstructural analysis by preparing the cross-sectional samples as per the standard metallography procedure. Further, hardness distribution and tensile properties were also evaluated to qualify the method developed.

8.3 Joint design configuration with setup conditions

As previusly observed, underfill and root hump defects in single-pass thick-section laser welded joint are common whenever full penetration is achieved. It is due to the violent ejection of molten metal with excessive downward melt flow on account of high heat input parameter involved with high viscous superalloy. High-speed downward flow of molten metal caused by the recoil pressure induced by the localized vaporization of metal in deep penetration keyhole welding played critical role for inducing surface underfill and root hump defects in weld bead [8-10]. Therefore, additional filler material at the top of the surface is required in such case to refill the underfill region during deep penetration laser welding in single pass. And at the same time, huge root hump defect occurs at the bottom surface, thus, a special groove design at the bottom surface was implemented to overcome this issue. Based on these observations, a new joint geometry was designed as shown in Figure 8.1a in the present study.

Geometry of butt-joint configuration needed appropriate included angles of top and bottom groove with sufficient depths to fix additional amount of melt depending on the size and type of filler material utilized. For the purpose, various filler wires of similar composition (as base material Inconel 617) but with different diameters ranging from 1.2 to 3.2 mm were utilized in this study. Figure 8.1b shows the positioning of filler rod onto the top groove of the butt joint. Initial welding experiments were carried out employing smaller diameter filler wire of size 1.2 mm in diameter for welding 10-mm thick Inconel 617 alloy. However, welds obtained using a 1.2 mm diameter wire consisted of underfill / undercut defects due to insufficient quantity of molten weld metal provided by the smaller filler wire during welding. Further, welding trials were carried out employing larger diameter filler wire of size 3.2 mm in diameter. Satisfactory welds in terms of filling were produced by employing a 3.2 mm diameter filler rod to weld 10-mm thick Inconel 617 superalloy. Details of optimized variables for joint configuration and filler material size are presented in Table 8.1. However, it is still a daunting task to obtain desired quality welds due to various factors such as exact location of filler material to be placed (completely inside the plates or outside or half-way through or halfinside) and appropriate tack welding between filler and base plate followed by final laser seam welding under optimum processing parameters and conditions. The included angle of 60 degree at top is found to be sufficient and effective to fix the filler wire with minimal gap between wire and groove edge (critical for suppressing porosity arising due to lack of melt pool sufficiency of filler metal mix with base plate). The included angle of 90 degrees at the bottom with 0.5 depth was found to be sufficient for avoiding excessive melt flow resulting in root hump based on the analysis and calculation observed on previous experimentation. Indeed, the amount of gap arising due to grooves designed at top and bottom were observed to be dependent on the filler material melt volume required to fill grooves adequately. Furthermore, the amount of heat input determined by critical processing parameters of laser power, welding speed and defocusing distance entail optimum filling of the underfill area with melting of filler at top and bottom grooves. Influence of all these factors will be discussed in detail in the following sections.

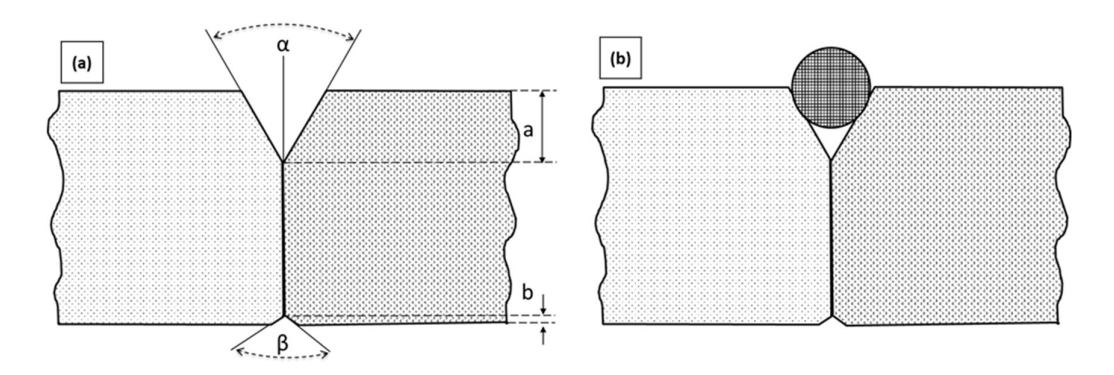


Figure 8.1. Schematic illustrations of (a) Design of joint configuration and fit-up and (b)

Filler wire pre-placed in the groove

Table 8.1. Optimized variables for joint configuration and filler wire

Parameters	Values
Base metal plates	Inconel 617 alloy
Thickness	10 mm
Filler material	ER NiCrMo-4
Filler material size	Ø 3.2 mm
Included top groove angle (α)	60°
Included bottom groove angle (β)	90 °
Depth of top groove (a)	3.6 mm
Depth of bottom groove (b)	0.5 mm

8.4 Process optimization of laser tack welding

The first task in developing the welding process after optimizing conditions of grove design and filler material requirement is to fix the filler wire laser tack welding appropriately onto the top groove with firm bonding that will not disturb during final seam welding. For laser tack welding experiments, pulsed-mode of spot welding adopted with specific pitch between the tacks by optimizing parameters of laser power, pulsing parameters and defocusing distance. Other common parameters of shielding gas conditions, positioning setup laser beam and shielding gas nozzle remained same (as previously adopted in welding experimentation). The critical parameters were varied in appropriate range to optimize tack-welding leading to firm fixing with strong interface bonding between base metal and filler wire with minimal melting of base plate (not crossing 0.1 mm penetration). Laser power was varied from 0.5 - 3 kW, whereas defocusing distances were varied from -3.2 to +3.2 mm (to match with filler wire diameter) for tack welding of 10-mm thick Inconel 617 superalloy with 3.2 mm diameter filler rod.

Figure 8.2 shows typically three different tack welds obtained with varying laser power in pulsed mode of spot welding. It can be observed that low laser power results in improper sticking of the filler wire to the base plate, while excessive laser power (determined by pulse width and laser power) caused improper melting of the filler material. Additionally, the focusing distance also determine the efficiency of melting the filler to entail appropriate bonding at its interface with sufficient nugget formation required for firm joint. Thus, experiments were conducted by varying laser power (both laser power and pulse width) and defocusing distance and studied bonding of the wire with base metal at top grove. It was found that defocusing distance is most critical parameter determining nugget formation with sufficient interface bonding without disturbing wire for effective tack welding. A negative defocusing distance obtained when laser focal point is below the filler rod, zero defocus obtained when focal point is on the surface, whereas positive defocus obtained when the focal point is above the filler rod surface. A negative defocus is preferable as compared to zero or positive defocus during tack welding experiments. Optimized defocusing distance and laser power for laser tack welding experiments are presented in Table 8.2.



Figure 8.2. Laser tack welds with variation in laser power

The criteria for optimization of these parameters were to obtain satisfactory tacks between filler and base plate, so that the filler material filler wire fuses with minimal melting of base plate to the extent sufficiently to entail metallurgical bonding between the wire and the plates without absence of any undulations throughout the groove of the plates and smooth edge fit up. Figure 8.3a depicts the cross-sectional macrograph of laser tack welds and Figure 8.3b shows the laser tack welded joint overview of sample plate obtained with an optimized parametric condition.

Table 8.2. Optimized process parameters for laser tack welding experiments

OPTIMIZED LASER TACK WELDING PARAMETERS						
Laser	Fiber-coupled diode laser					
Laser spot diameter	0.9 mm					
Laser power for Tack welds	2.5 kW					
Pulse width	150 ms					
Defocusing distance for tack welding	1 mm (inside filler rod)					
Shielding gas	100% Helium					
Gas pressure	3 bar					

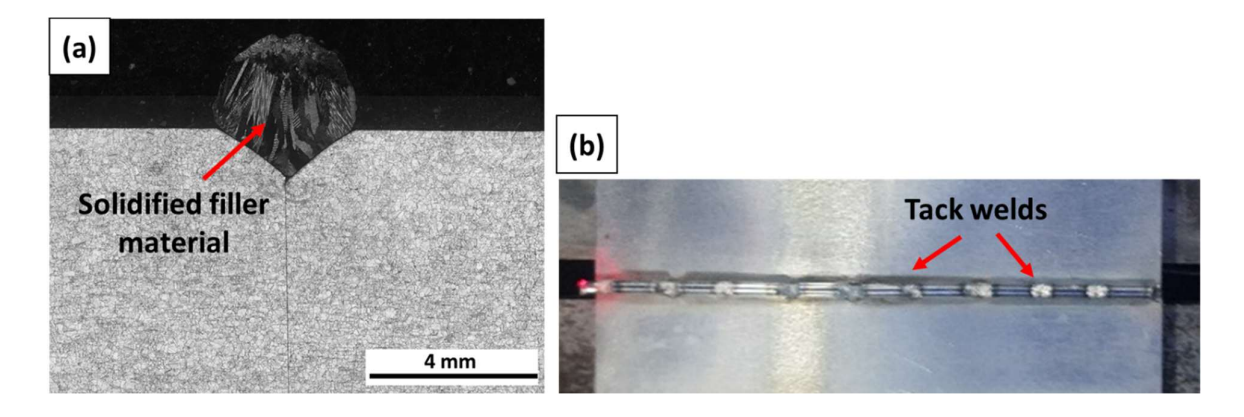


Figure 8.3. (a) Cross-sectional macrograph of tack-welded spot (b) Pre-placed filler wire on the top groove of base plate after tack welding

8.5 Process optimization of laser seam welding

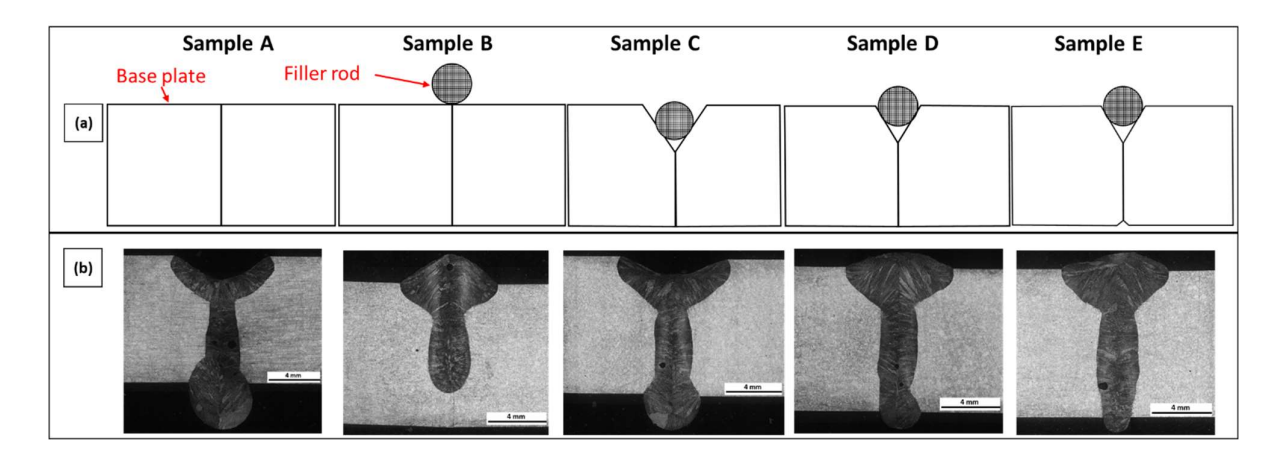


Figure 8.4. (a) Schematic representation of different methodologies adopted for laser welding and (b) Macrographs of the representative methodologies

As mentioned previously, the daunting task is to obtain desired quality welds with perfect location of filler material to be placed (completely inside the plates, completely outside or half-inside and half-outside), therefore, laser seam welding experiments to be carried out (after successful laser tack welding) with different methodologies as shown schematically in Figure 8.4a. Subsequent to laser tack welding, the plates were cleaned with acetone and wirebrush to remove any defects or un-melted or oxidized particles formed if any during tack welding operation. Furthermore, appropriate shielding and fixturing setup as described in chapter 3 was utilized for experimentation. All experiments for seam welding were conducted with similar optimum parameters obtained from study conducted for diode laser welding previously explained in chapter 7.

Table 8.3. Optimized process parameters for laser seam welding experiments

OPTIMIZED LASER SEAM WELDING PARAMETERS						
Laser	Fiber-coupled diode laser					
Laser spot dia	0.9 mm					
Laser power for seam welding	6 kW					
Defocusing distance for seam welding	1.5 mm inside filler rod					
Welding speed	6 mm/s					
Shielding gas	100% Helium					
Gas pressure	3 bar					

Figure 8.4b shows the cross-sectional macrographs obtained with different methodologies. It is clear from Figure 8.4b that without addition of filler rod and joint design,

as in case of sample A, resulted in huge underfill and root hump defects similar to that observed in previous chapters. Further, placing the filler rod completely on the surface without any joint design as in case of sample B resulted in lack of penetration and huge reinforcement. However, placing the filler material completely inside the base plates as in case of sample C resulted in again small amount of underfill and root hump defects as similar to that of sample A. Therefore, the filler wire was placed half inside the plate as in case of sample D. Underfill defects was found to be completely eliminated in sample D, however, slight root hump defects could still be observed. Thus, altered narrow groove was designed at the bottom of the plates as in case of sample E. It is clear from Figure 8.4 that the placing filler rod half-inside the base plates along with appropriate bottom groove design found to be the optimized joint configuration to obtain welds with complete elimination of underfill and root hump defects. Optimized process parameters for laser seam welding experiments in case of sample E are presented in Table 8.3. Furthermore, bead geometry measurements shown in Table 8.4 confirm that the root sag width of sample E was found to be smallest with no underfill as compared to that of other cases. It is also clear by comparing sample E with A, C and D that fusion zone area, weld bead width and penetration are found to be significantly adequate in case of sample E as compared to other cases.

Table 8.4. Bead geometry measurements of welds obtained by various methodologies

Bead geometry measurement	Sample A	Sample B	Sample C	Sample D	Sample E
Penetration (mm)	13.59	7.41	12.35	10.96	10.83
Bead width (mm)	8.20	6.74	8.10	7.31	7.17
Aspect ratio (depth-to-width)	1.65	1.09	1.52	1.49	1.51
Reinforcement (mm)	-	1.99	-	1.05	1.12
Fusion zone area (mm²)	48.47	32.66	43.05	40.56	38.25
Underfill depth (mm)	1.87	-	1.23	-	-
Root sag width (mm)	4.82	-	4.15	2.67	1.66

8.6 Weld joint characterization

Prior to weld bead characterization, the welded joints were subjected to visual, dye penetration and radiographic examination. Results indicated that the welds obtained by the novel method was free from porosities, incomplete fusion, underfills and root hump defects, cracks and undulations. Indeed, the novel method with two-step welding strategy with optimization of grove design and processing parameters facilitated in obtaining defect-free joint with complete elimination of underfill and minimization of root hump defects (Figure 8.5 (a)). Metallography analysis of cross-sectional weld seam was carried out to examine the weld bead profile across fusion, heat affected zone and substrate regions. Figure 8.5a shows the welded plate and Figure 8.5b shows the cross-sectional macrograph obtained produced by the two-step novel welding method. A typical Y-type bead shape were obtained with high aspect (depth to width) ratio and complete elimination of underfill/undercuts and root hump defects as shown in Figure 8.5b. Furthermore, the welds produced by this method constituted of uniform weld bead seam throughout the weld length with minimal distortion as well as small HAZ as compared to previously produced DLW and LHW techniques.

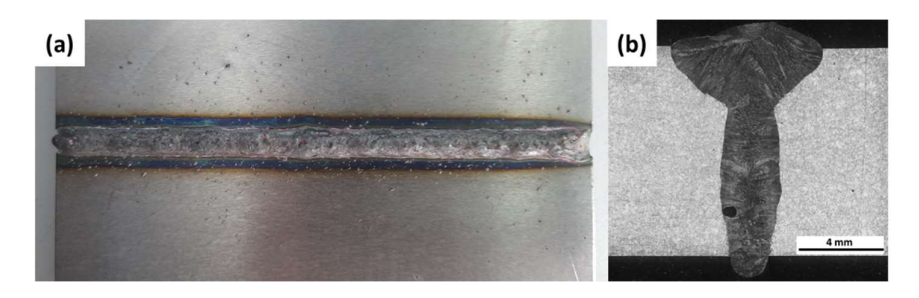


Figure 8.5. Weld obtained by novel method (a) Seam welded plate and (b) Macrograph

Further, detailed microstructural analysis was carried out using FESEM in order to examine any plausible microstructure variations arising within the fusion zone due to addition of filler rod. Figure 8.6 shows the high magnification FESEM images of the locations marked in the macrographs. It is clear from this microstructural analysis that the there are no significant boundary separations within the fusion zone microstructure (especially between filler rod and base metal at top grove region). It indicates complete mixing of filler material with the base metal during welding without any gaps as well as turbulent melt flows entailing voids/gaps/porosity. However, at the top region (as marked 1 in Figure 8.6), slight coarsening with enhanced secondary dendritic arm spacing (SDAS) was realized. It is due to the presence of filler rod at the top region causing significant coarsening of dendrites convergent with the prevailing cooling rates. This phenomenon can be correlated to the Laser-MIG hybrid welding

process, wherein wider top region with enhanced SDAS formed due to addition of filler wire by MIG arc heat source.

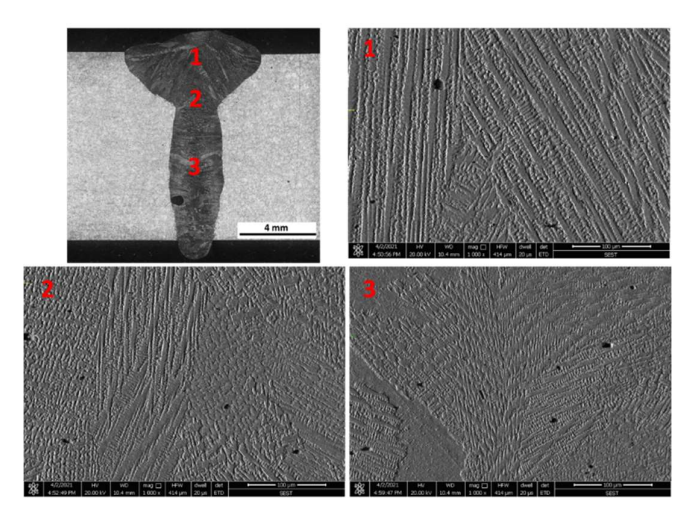


Figure 8.6. Novel ADLW macrograph with high magnification FESEM images at top, neck and bottom regions

Further to the microstructural analysis, tensile testing of the welded joint processed with the novel method conducted at room temperature to assess its joint efficiency and compared to that of BM. The YS and UTS of the welds produced by developed method are 355-365 and 760-775 MPa respectively with an elongation of 45-56 %. In contrast, BM showed YS and UTS of 325-335 and 765-769 MPa respectively with an elongation of 60-67%. Results indicated that the developed process produced welds with joint efficiency of 99 – 100 % with improvement in YS, although with a reduction in elongation as compared to BM. Moreover, the weld joint strength/efficiency of the developed novel method was found to be higher as compared to that of previously produced by autogenous diode laser welding and also reported studies of other researches adopting various multi-pass and modified advanced techniques of TIG, MIG or CMT. Fink et al. [11] obtained a joint strength of 761 MPa, 759 MPa and 764 MPa in CMT, Pulsed-MIG and Pulsed-Arc weldments of Inconel 617 alloy respectively. Moreover, Young et al. [12], obtained a joint strength of 675 MPa during multi-pass TIG welding of Inconel 617 alloy. Similarly, Shanlin et al. [13], obtained joint strength of 745 MPa in multi-layer NG-TIG welding of Inconel 617 alloy. Thus, it is evident that joint strength of high-power novel diode laser welded Inconel 617 alloy is stronger than that of joints produced with other arc welding methods.

Further, detailed analysis of weldments, microstructural analysis in fusion, PMZ, HAZ along with segregation behaviour and with assessment of mechanical properties and fracture

analysis were carried out in comparative study between novel diode laser welding method, laser hybrid welding and conventional TIG welding processes in the next chapter.

8.7 Conclusions

The present study demonstrated novel two-step laser welding methodology with preplacement of filler wire and appropriate butt joint design for joining thick sections of metallic material with complete elimination of underfills in single-pass for viscous materials such as superalloys. The developed method provided a cost-effective single-pass laser welding solution without wire feeder to obtain satisfactory full penetration welds in thick-sections with complete removal of underfill/undercuts, root humps etc. along with excellent joint efficiency.

The developed laser welding method involved two step welding procedure; Tack and Seam welding. A new joint configuration was developed and designed for pre-placement of filler wire/rod for the purpose. In first step, filler wire was tack welded in pulsed mode to the base plate with an optimized process parameter. Subsequent to tack welding, laser seam welding experiments were performed with optimum joint configuration and process parameters.

Welds produced by this method were found to be with uniform weld bead seam throughout the weld length with minimal distortion as well as small HAZ as compared to previously produced previously by DLW. Tensile test results indicated that the weld joint efficiency of the butt-welded joints obtained by novel ADLW method are found to be in the range of 99 – 100% and superior to that of previously obtained by DLW and RSM methodologies.

On the whole, it can infer that new single-pass diode laser welding method with addition of filler wire and without wire feeder proved to be a suitable welding method great promise to join Inconel 617 alloy in various engineering components of thermal power plant.

8.8 References

- Keßler, Benjamin, Berndt Brenner, Dirk Dittrich, Jens Standfuß, Eckhard Beyer, and Christoph Leyens. "Laser-multi-pass-narrow-gap-welding of nickel superalloy—Alloy 617OCC." Journal of Laser Applications 31, no. 2 (2019): 022412.
- 2. J. O. Milewski and E. Sklar, "Narrow gap laser welding," Google patent US5760365 A (June 1998)
- 3. "Laser wire-filled welding method for thick plate with narrow gap" Google patent CN103801833A, (May 2014)
- 4. "Butt laser welding method of welded plate material", Google patent JP6255314B2, (Dec 2017)

- 5. "Large-size structural member laser welding tool, system and method", Google patent CN112570888A, (Mar 2021)
- Sun, Junhao, Wenjie Ren, Pulin Nie, Jian Huang, Ke Zhang, and Zhuguo Li. "Study on the weldability, microstructure and mechanical properties of thick Inconel 617 plate using narrow gap laser welding method." Materials & Design 175 (2019): 107823.
- Ramakrishna R, V. S. M., P. H. S. L. R. Amrutha, R. A. Rahman Rashid, and S. Palanisamy. "Narrow gap laser welding (NGLW) of structural steels—a technological review and future research recommendations." The International Journal of Advanced Manufacturing Technology 111, no. 7 (2020): 2277-2300.
- 8. Zhang, Mingjun, Zheng Zhang, Kun Tang, Cong Mao, Yongle Hu, and Genyu Chen. "Analysis of mechanisms of underfill in full penetration laser welding of thick stainless steel with a 10 kW fiber laser." Optics & Laser Technology 98 (2018): 97-105.
- 9. Zhang, Mingjun, Genyu Chen, Yu Zhou, and Shenghui Liao. "Optimization of deep penetration laser welding of thick stainless steel with a 10 kW fiber laser." Materials & Design 53 (2014): 568-576.
- Zhang, Mingjun, Shun Chen, Yingzhe Zhang, Genyu Chen, and Zhuming Bi. "Mechanisms for improvement of weld appearance in autogenous fiber laser welding of thick stainless steels." Metals 8, no. 8 (2018): 625.
- 11. Fink C, Zinke M. Welding of nickel-based alloy 617 using modified dip arc processes. J Welding in the World. 2013;57(3):323-333
- 12. Park, Young Su, Hyo Sik Ham, Sang Myung Cho, and Dong Ho Bae. "An assessment of the mechanical characteristics and optimum welding condition of Ni-based super alloy." Procedia Engineering 10 (2011): 2645-2650.
- 13. Li, Shanlin, Kejian Li, Zhipeng Cai, and Jiluan Pan. "Behavior of M₂₃C₆ phase in Inconel 617B superalloy during welding." Journal of Materials Processing Technology 258 (2018): 38-46.

Comprehensive Comparative Study on Metallurgical, Mechanical and Hot Corrosion behavior of Weldments Produced by employing LHW, ADLW and TIG Welding Processes

9.1 Introduction

As discussed previously, multi-pass arc welding processes are currently being utilized for joining boiler components. However, conventional arc welding techniques often induce deleterious effects due to high heat input and the need for multiple weld passes also entail excessive filler material consumption. In addition, welding speed being low with multi-pass requirements envisage in large HAZ, poor process repeatability with cumbersome edgepreparation, high component distortion and high residual stresses and therby many a times require heavy post-weld machining corrections for distortion. Further, due to high viscous nature and poor weldability of Ni-based superalloy Inconel 617, several weld imperfections and defects are also encountered during thick-sections welding such as lack of fusion, high propensity to liquation cracking in HAZ and weld metal and porosity formation [1-5]. Thus, due to these circumstances, successful development a high efficiency welding process for welding moderately thick-sectioned Inconel 617 alloy materials for AUSC boiler components is the primary need. Therefore, it was felt pertinent to compare single-pass laser hybrid welding (LHW) and novel adaptive diode laser welding (ADLW) processes with conventional multipass TIG welding process with assessment of their metallurgical, mechanical and high temperature corrosion behavior.

9.2 Experimental Methodology

Conventional multi-pass TIG welding was carried out manually on 10-mm thick Inconel 617 alloy in a butt-joint configuration with a sum of 6 overlay deposition tracks with appropriate fixturing and shielding setup as shown in Figure 3.8. Welding current and voltage maintained were kept in the range of 130 - 140 amp and 11.5 - 13.5 volts and the welding speed was maintained between 50 - 60 mm/min. Details of conventional multi-pass TIG welding process parameters are described in chapter 3, section 3.4.4. Base material utilized for the present study is a solid-solution strengthened Nickel based superalloy Inconel 617 in a form

of plate of thickness 10 mm in solution-annealed condition with a nominal composition as tabulated in Table 3.1.

Further, Laser hybrid welding (LHW) of 10-mm thick alloy was carried out in a butt-joint configuration using CO₂ laser source integrated to MIG arc heat source as shown in Figure 3.7. Welding experiments were carried out with a CO₂ laser power of 3.5 kW and MIG arc current and voltage maintained was 167 amp and 28.2 volts respectively with a wire feed rate of 7 m/min. Details of LHW process parameters are described in Table 3.4. Furthermore, diode laser welding experiments were carried out based on the novel method developed as explained previously.

9.3 Weld bead profile and macrostructure analysis

As weld bead profile analysis in any weld joint determine joint efficiency and performance, detailed cross-sectional bead profile analysis of all three weldments were analysed and assessed macrographically with borderline etching of metallographic samples. Visual and radiography examination of all weldments showed no obvious external or internal welding defects and thereby envisaging effective optimization of welding process and confirming excellent reproducibility and optimum quality. Furthermore, distortion analysis of weldments measured by distortion angle at the end of welding (presented in Figure 9.1) envisaged possibly low residual stresses in ADLW as compared to that of LHW and TIG weldments. ADLW weldment showed a remarkable decrease in the distortion level represented by 0.43⁰ distorted angle as compared to that of single-pass LHW (1.29⁰) and multi-pass TIG (2.52°) weldments (as marked in Figure 9.1). The comparatively low level of distortion (2.52°) in six-pass TIG weldment, despite with high heat input (7760 J/mm) could be due to heavy clamping by tack-welding of the plates to a thick-sectioned heavy duty "C" clamp prior to TIG welding. Indeed, increase in heat input increased distortion as a direct influence of heat input involved in the process of welding (low heat input in laser-based welding processes such as LHW and ADLW and high heat input in TIG). Although, the heat input utilized in ADLW was twice to that of LHW, it showed reduction in distortion by half and this can be attributed to high depth-to-width aspect ratio obtained in ADLW weld bead accompanied with large thickness in lower bead and high energy coupling of metal with short-wavelength diode laser. In a similar study assessing distortion levels in weldments, heat input directly influenced distortion levels [6,7].

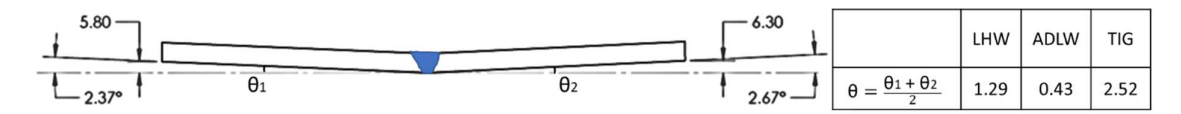


Figure 9.1. Schematic illustration of distortion measured in but joint after welding

Figure 9.2 illustrate cross-sectional macrographs of weld bead profiles obtained in all three different welding processes of ADLW, LHW and TIG. As such, fusion zones are defect-free with no cracks and porosity indicating effective optimization of the processes with full penetration obtained in single-pass ADLW and LHW weldments as against multi-pass TIG weldment. Corresponding bead geometry measurements for all three welded joints are depicted in Table 9.1. Weld bead profile characteristics such as upper bead width (UBW), lower bead width (LBW), depth-to-width aspect ratio (AR) and fusion zone area (FZA) were distinguishably different for different welding techniques owing to their significant variation in heat input, intensity profile distribution, number of heat sources and welding passes involved. It is clear that LHW produced 'wine-cup' shape bead, ADLW produced "Y" shaped bead and TIG resulted in "bath-tub" shaped bead profile as a consequence of distinguishably different heat inputs and energy distribution profiles of heat sources (dotted lines marked in the Figure 9.2 illustrate hypothetical energy distributions due to heat sources in single-pass LHW and ADLW and multi-pass TIG).

Wine-cup shaped bead in LHW characterized by wide UBW and narrow LBW could be the result of combined effect of laser beam and MIG arc heat sources with distinguishably different power density and energy-intensity distribution profiles. Indeed, the wide UBW (8.1 mm) with low LBW (1.1 mm) formed in LHW (Figure 9.2(a)) be attributed to low power density and wide radius spot of MIG arc (the distance at which the heat flux decays to 0.05 of the maximum value) [8] and intense focused CO₂ laser beam spot (180 µm diameter) with prevailing keyhole dynamics. Nearly spherical wide MIG are spot with low power density entails lateral expansion of melt volume in conduction mode causing weld bead to bulge with expansion of molten pool drop of supplied filler wire. Apparently, the narrow LBW with deep penetration in lower part of the weld bead be due to deep keyhole mode heat penetration associated with focused high-power density CO₂ laser beam. Thus, the "wine-cup" shaped narrow fusion bead in LHW determined the combined effect of both heat sources of MIG torch as well as CO₂ laser beam and the amount of heat input involved, as reported by several studies involving laser hybrid welding [9-11]. Indeed, presence of MIG source could only facilitate in improving gap bridgeability only, whereas, laser being principally responsible for weld penetration.

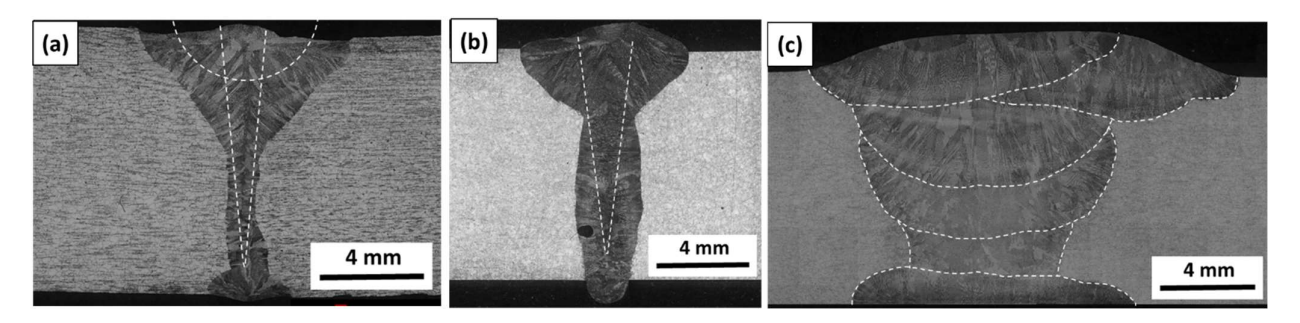


Figure 9.2. Cross-sectional weld-bead macrographs of (a) LHW, (b) ADLW and (c) TIG welded joints

As compared to "wine cup" shaped weld bead in LHW, single-pass ADLW involving multi-mode (Top-hat and Gaussian intensity distribution profiles) diode laser beam of 0.9 mm diameter with 820 J/mm power density produced "Y" shaped profile (Figure 9.2(b)) with wider UBW (6.8 mm) and narrow LBW (2.7 mm). Indeed, moderate top width of ADLW with relatively wider LBW as compared to that of LHW bead profile with high depth-to-width ratio entails high energy coupling efficiency of diode laser (shorter wave length of diode laser than CO₂ laser) coupled with input power density and multi-mode intensity profile distribution. Furthermore, the high focusability of the advanced diode laser used in the study enabled effective keyhole mode welding with deeper penetration in ADLW. Further, welding defects such as underfill and root sag hump were found to be completely eliminated by using the ADLW method as compared to such defects observed in DLW methods as explained in the previous chapters. Although with moderately enhanced aspect ratio in weld bead with wider LBW and similar UBW produced in ADLW as compared to that of LHW facilitated in improving gap bridgeability akin to that of laser-hybrid welding process.

Figure 9.2(c) depicting weld bead profile of conventional TIG-welded Inconel 617 alloy illustrate altogether a different profile, typically termed as "bath-tub", as compared to that of weld beads obtained in laser based LHW and ADLW techniques. Indeed, formation of such bead profile be attributed to multiple-pass welding procedure adopted with conduction-mode lateral expansion of melt of large sized TIG arcs. It manifests complete fusion of filler wire with adequate fusion of side walls of the metal in conjunction with the heat input involved coupled with design of multiple passes adopted. Sum total of six welding passes employed in TIG welding are clearly distinguishable in cross-sectional macrograph of Figure 9.2(c) as indicated by dotted lines. Indeed, wide UBW width to the tune of 18.2 mm and thick lower bead width of 12 mm corroborate huge melt volume with low aspect ratio in conventional multi-pass TIG process. Similar bead profile was also reported in several studies involving

conventional multi-pass TIG, MIG and similar techniques and attributed to high heat inputs involved with conduction mode of heat transfer and wide arc spots [1,12,13].

Table 9.1. Bead geometry measurements

Bead Geometry	LHW	ADLW	TIG
Fusion zone area (mm ²)	31.48	40.14	124.6
Upper bead width (mm)	8.15	6.82	18.13
Lower bead width (mm)	1.13	2.74	11.95
Aspect ratio (Depth to width)	1.22	1.46	0.55

Another point of concern to be noted is the influence of heat input on resulting weld bead profiles employing contrasting welding techniques with varied melt efficiency. In the present work, melt efficiency determined by FZA evaluation were observed to be 31.5 mm², 40.1 mm² and 124.6 mm² in ADLW, LHW and TIG respectively. It is obvious that highest bead width with huge FZA was obtained in TIG as a direct consequence of huge heat input (7760 J/mm in TIG as compared to that of 415 J/mm in LHW and 820 J/mm in ADLW) with multiple passes. Among the three welds, the highest depth-to-width aspect ratio of 1.5 was obtained in ADLW as against lowest of 0.55 in TIG counterpart. LHW exhibited an aspect ratio of 1.2, quite larger than that of TIG weld bead. The high aspect ratios in both laser-based welding processes of ADLW and LHW are due to laser assisted keyhole mode heat transfer involved due to narrow high energy intensity laser beam sources. Moreover, the melting efficiency (η) of all these different welding processes evaluated were consistent with energy consumed for melting of the metal as reported by several studies involving conventional as well as high energy beam welding processes [14,15]. The melting efficiency in laser-based welding processes such as LHW (0.43) and ADLW (0.37) are always found to be higher than that of TIG (0.09), convergent with energy distribution profiles of welding processes involved. Thus, it can be inferred that synergistic process combining laser with MIG, as in case of LHW, lead to significant enhancement in welding process efficiency [16]. When using laser alone process such as ADLW, the melting efficiency is still comparable to LHW on account of high quality (high focusability) low spot size and high coupling efficiency of diode laser as compared to that of CO₂ laser-MIG hybrid. Low melting efficiency in TIG welding process is obvious due to the lateral expansion of melt volume with a wider arc spot radius of TIG torch. On the whole, it is clear that the type of welding technique employed played significant role in weld bead profile formation and melt efficiency on account of their associated effects of power density, spot size, intensity distribution profile and energy coupling behaviour of laser/arcmaterial interaction.

9.4 X-ray diffraction phase analysis

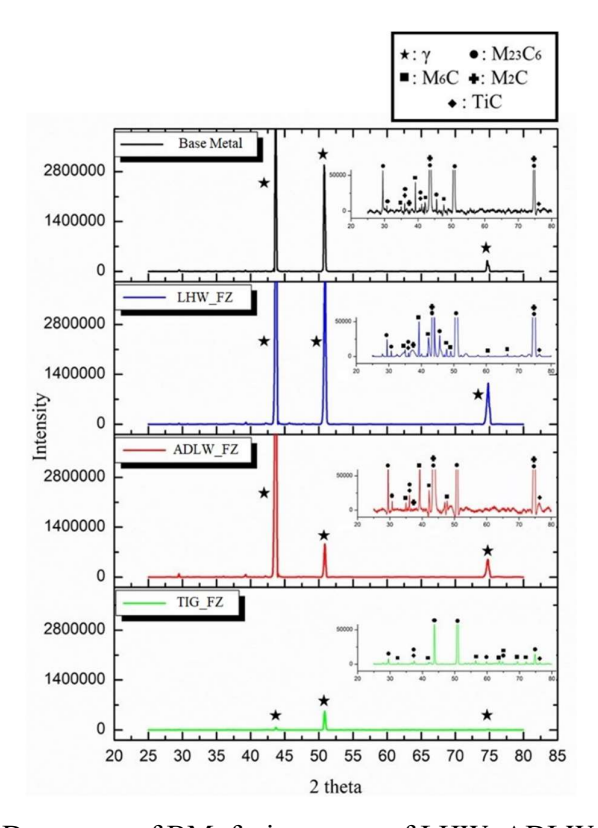


Figure 9.3. XRD patterns of BM, fusion zones of LHW, ADLW and TIG welds

Subsequent to bead profile analysis of weldments, it was felt pertinent to analyse phases formed in weld fusion zones of all three welds before undertaking comprehensive detailed microstructural analysis employing characterization tools of SEM, EDS and EBSD. Figure 9.3 illustrate XRD patterns obtained in fusion zones of LHW, ADLW and TIG welds as well as BM. For effective comparison, the central fusion regions in all weld beads were specifically sectioned and polished to scan X-ray to obtain diffraction patterns with slow scanning. The predominant X-ray diffraction peaks at 2θ values of 43.5°, 51° and 74.5° obtained in fusion zones of LHW, ADLW and TIG welds as well as BM correspond to γ (Ni-Cr-Co-Mo) dendrites / matrix. However, a zoomed-in inset image presented in the same figure indicated eruption of additional secondary carbide peaks of Mo-rich M₆C and Cr-rich M₂₃C₆ type in weld fusion zones of LHW, ADLW and TIG as compared to that of BM. It is possible that prevailing welding thermal cycle entail significant dissociation and transformation of M₂₃C₆ carbides into

 M_6C carbides with increased Mo diffusion as reported in several welding studies employing Inconel 617 [17,18].

Comparing XRD patterns within weld fusion zones of LHW, ADLW and TIG welds, it is clear that relatively more high-intensity carbide peaks of $M_{23}C_6$ and M_6C carbides (diffraction peaks located between 55° to 75° (as marked in Figure 9.3)) discernible in TIG as compared to that of LHW and ADLW counterparts. It is possible that repeated thermal cycling history associated with multi-passes and slow cooling rates experienced in TIG favour diffusion and precipitation of $M_{23}C_6$ and M_6C carbides in the fusion zone microstructure. Additionally, few pockets of low intensity M_2C (M=Cr, M_0) carbide peaks were also observed in BM and as well as in weld fusion zones of ADLW and LHW. It is noteworthy to mention that intensity of diffraction peaks of austenitic γ (Ni-Cr-Co-Mo) in dendritic microstructure of TIG weld is significantly low as compared to that of LHW and ADLW. Indeed, involvement of huge heat input (ten times to that of laser-based welding processes) with significant reduction in cooling rate in TIG welds facilitate higher carbide segregation in interdendritic matrix microstructure of weld fusion zone.

9.5 Microstructural analysis

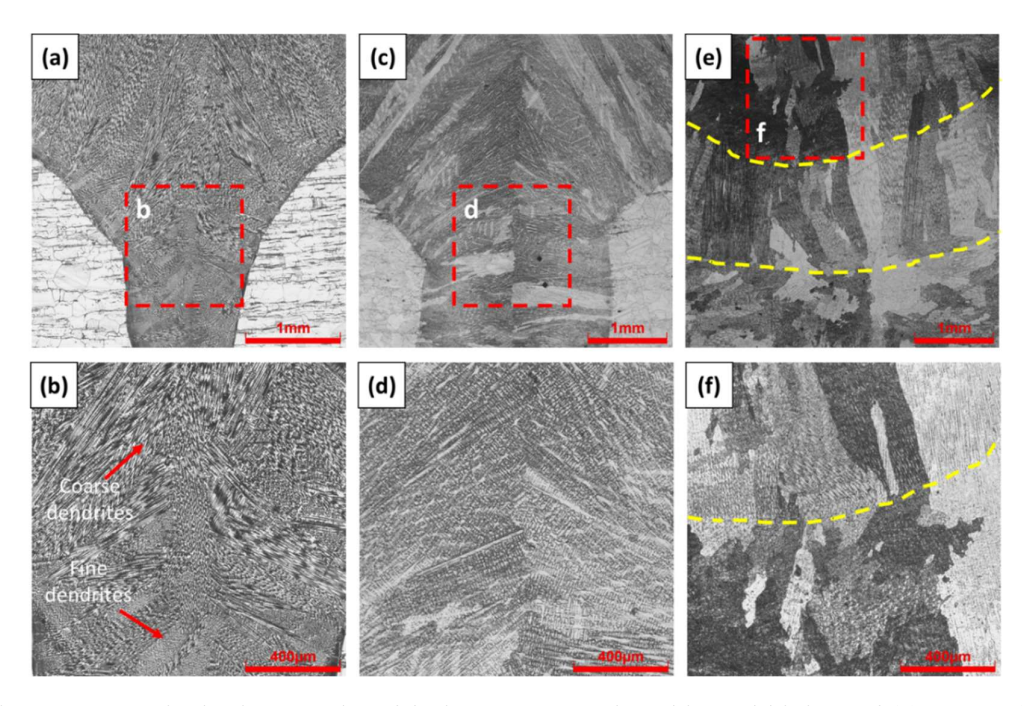


Figure 9.4. Optical micrographs of fusion zones produced in weld joints of (a) LHW, (c) ADLW, and (e) TIG with zoomed sections of respective NFZs in (b), (d) and (f).

Prior to assessing joint efficiencies of weldments, it is necessary to assess solidification behaviour with microstructure analysis of welds on account of distinguishably different welding methods involved in the study. Figure 9.4 depicts cross-sectional optical micrographs of fusion zones in Inconel 617 butt joints produced by LHW, ADLW and TIG processes. Although dendrites of γ (Ni-Cr-Co-Mo) in fusion zone microstructures are same in all welds, their size and morphology varied on account of variation in heat input, cooling rate and solidification behaviour of the prevailing weld cycles. Fusion zone microstructures of LHW and ADLW (depicted in Figures 9.4(a-d)) predominantly comprised of columnar dendrites aligned to central weld line opposite to the heat transfer direction. Indeed, the directional nature of these microstructures be attributable to the symmetrical distribution of laser beam energy as against non-symmetric dendrites alignment discernible in weld fusion zone of TIG (depicted in Figure 9.4(e-f)) [14,19]. In fusion of LHW, the microstructure transformed from coarse dendrites at top to fine dendrites in neck and lower regions of fusion zone on account of cooling rate variation within weld bead with transition from MIG zone to Laser zone entailed by change in mode of transfer in conduction-dominated upper zone to keyhole mode in laser-alone affected lower zone.

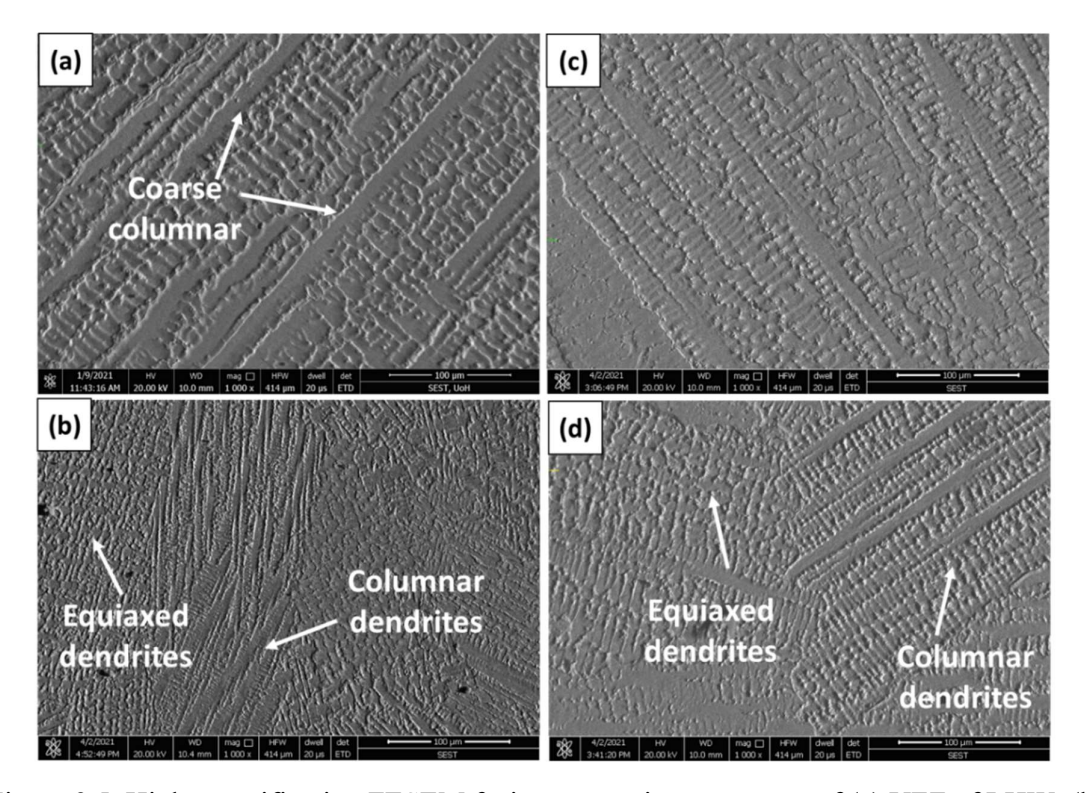


Figure 9.5. High magnification FESEM fusion zone microstrucrures of (a) UFZ of LHW, (b) NFZ of LHW, (c) UFZ of ADLW and (d) NFZ of ADLW

High magnification SEM micrographs depicted in Figures 9.5 and 9.6 along with EDS analyses (depicted in Table 9.2) provide deeper insight into the microstructural variations observed in fusion zones of welds processed with different methods. Indeed high-magnification microstructures of UFZ and NFZ of LHW, depicted in Figures 9.5(a) and (b) reconfirm this aspect with average secondary dendritic arm spacing (SDAS) changing from 6.5 μm in upper region to 3.6 μm in neck region and 2.7 μm in lower region. High cooling rate that prevails in lower fusion zone of LHW is a consequence of laser alone effect as compared to that of combined effect of laser and MIG arc in UFZ [20]. Furthermore, the microstructure at the central fusion zone of LHW appears inhomogeneous with mix of coarse and fine columnar dendrites, along with equiaxed dendrites, as a result of mixing of heat sources of MIG and Laser. In contrast to LHW, ADLW involving higher heat input (twice that of LHW) with low thermal gradient exhibited comparable columnar dendrites in microstructure of UFZ (5.7 μm) as evident from micrograph of Figure 9.5(c) [21]. Unlike LHW, relatively no much significant variations be observed in fusion microstructures of UFZ and LFZ in ADLW weld bead as the welding process involved only one heat source of laser.

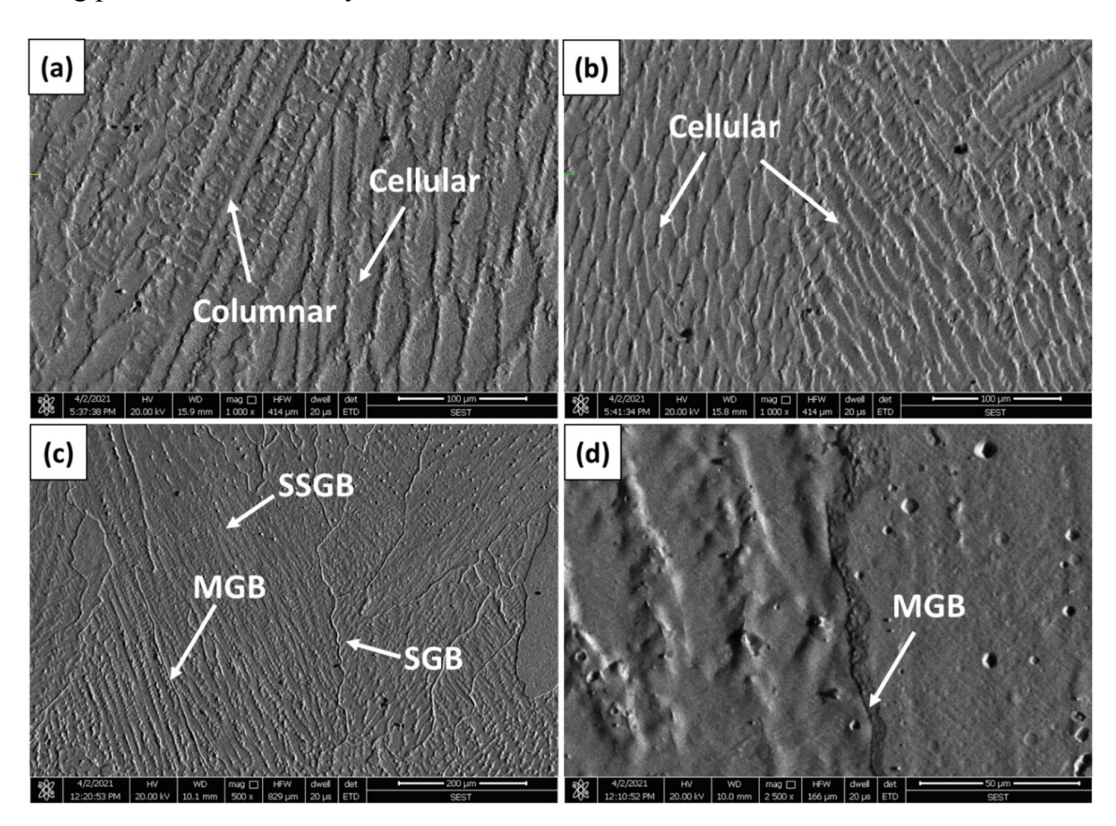


Figure 9.6. High-magnification FESEM fusion zone microstrucures with various regions of TIG welded joint

Cross-sectional optical micrographs of multi-pass TIG weld presented in Figures 9.4(e) and 7(f) show altogether a different microstructure with no directional solidification behaviour on account of multi-pass welding involvement. High magnification FESEM images of TIG fusion region, shown in Figures 9.6(a) and 9(b) disclosed a mix of coarse columnar and cellular dendrites as a result of the prevailing re-heating thermal cycle effect associated with multiple welding passes. The average SDAS of multi-pass TIG weld bead was found to be 12.6 μm (twice that of LHW and ADLW weld beads). Indeed, coarse fusion zone microstructure in TIG weld be attributed to the prevailing low cooling rate and high heat input [22,23]. Moreover, along with solidification grain boundaries (SGB) and solidification sub-grain boundaries (SSGB), migrated grain boundaries (MGB) were also observed in weld fusion zone (discernible from micrographs of Figures 9.6(c) and 9(d)) as a consequence of reheating associated with multi-pass TIG welding. Generally, in multi-pass welding process, the first bead experiences repeated thermal cycle by virtue of subsequent pass and thereby emancipating parent SGB to migrate during solidification. Thus, anisotropic characteristics of dendrites within grain prevail in solidification microstructure. Furthermore, SSGBs evolve in boundaries between sub-grains of cells/dendrites wherein SGBs intersect with sub-grains as a consequence of competitive growth during solidification. Thus, tortuous SSGBs are evidently different from quite straight MGBs (marked in Figure 9.6(c)), as discernible from fusion zone microstructures of TIG [23].

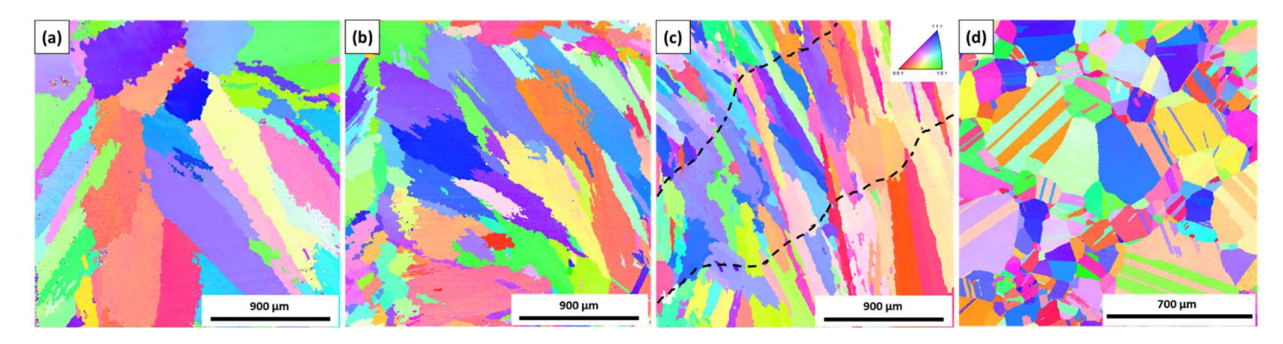


Figure 9.7. EBSD analysis of fusion zone microstructure of (a) LHW, (b) ADLW, (c) TIG welds and (d) BM

In multi-pass welding such as TIG, it is possible that SGBs migrate to few micrometres at the end of the solidification, in which case, new boundary emerges (marked in Figure 9.6(d) with different morphological structure) formally termed as MGB. The driving force for such MGBs could be the lowering of boundary energy, akin to that of simple grain growth. These fusion metal MGBs are high-angle crystallographic boundaries that usually originate from parent SGBs with pinning of precipitates [16,23]. Moreover, few reports on tensile testing of such multi-pass TIG joints attributed failure due to crack nucleation at such MGBs or ductility

dip cracking surrounding MGBs [23-25]. Thus, in accordance with the reported studies, similar microstructural observations with presence of significant SSGBs and MGBs were observed in our present six-pass TIG joint as against no-such grain boundary segregation in ADLW and LHW. Furthermore, Inverse pole figure (IPF) map of weld fusion zone microstructure (more specifically at NFZ) elucidating grain size and grain boundary misorientation angle distribution presented in Figure 9.7 of all these three weld joints reconfirm directional nature of dendrites in both LHW and ADLW as against non-directional nature in TIG. Dendrite/cellular austenitic grain size evaluated as per EBSD analysis reconfirmed their increase from 540 µm in ADLW to 620 µm in LHW and 850 µm in TIG welds in accordance with prevailing thermal gradient associated with heat input and thereafter cooling rate of weld thermal cycle. BM microstructure revealed refined grains with size varying between 20 and 250 µm (depicted in Figure 9.7(d)), always lower than that observed in fusion microstructure of any weldment. Apparently, evaluation of grain boundary misorientation in BM and welds represented by fraction of high angle boundaries (ranging from $10-65^{\circ}$) and low angle boundaries (ranging from $5-25^{\circ}$) indicated 0.10, 0.12 and 0.2 of HABs ADLW, LHW and TIG respectively as against 0.15 in BM. Thus, highest fraction of HABs was observed in TIG as against lowest in ADLW on account of the prevailing cooling rate of the welding cycle. Thus, increase in cooling rate promoted generation of low angle boundaries while reducing high angle boundaries and thereby enhancing boundaries with substructures. Furthermore, strength of γ (Ni-Cr-Co-Mo) dendrite in fusion microstructure varied based on grain size distribution and misorientation of grain boundaries, explained later with nano-indentation analysis. Similar observations in terms of variation in authentic grains and grain boundaries misorientation on account of cooling rate were reported in studies involving laser welding of superalloys [26].

Table 9.2. EDS analysis of fusion zones in LHW, ADLW and TIG welds (D – Dendritic core, IR – Interdendritic region, SR – Segregation ratio)

Sample	Region	Cr	Мо	Ni	Co	Al	Ti
LHW	Dendrite (γ)	21.3	8.7	53.9	11.8	0.65	0.45
	IR (Carbides)	25.8	12.4	43.1	9.4	0.72	0.59
ADLW	SR	0.82	0.70	1.25	1.25	0.90	0.76
	Dendrite (γ)	22.9	8.9	51.7	11.3	0.41	0.42
	IR (Carbides)	24.6	11.7	42.7	9.5	0.55	0.54
	SR	0.93	0.76	1.21	1.18	0.80	0.77
TIG	Dendrite (γ)	20.6	7.4	50.2	10.8	0.71	0.43
	IR (Carbides)	27.3	13.9	39.7	8.24	0.85	0.61

	SR	0.75	0.53	1.26	1.31	0.83	0.70
D84	Matrix (γ)	24.87	8.68	50.78	12.41	0.45	0.63
ВМ	Carbides	60.24	14.13	12.56	6.12	0.22	0.37

Microstructure analysis assessing micro-segregation at interdendritic regions provide further insight into understanding strengthening mechanisms of weld fusion zone that significantly affect joint strength. Thus, EDS analysis with spot elemental distribution within dendrite (D) as well as at inter-dendritic region (IR) of critical NFZ presented in Table 9.2 help facilitate in understanding solidification behaviour with segregation due to welding technique involved. Since there is no specific bead profile of NFZ in multi-pass TIG welds, EDS analysis was assessed at fusion region falling between the two weld passes. Results indicated significant variation in concentrations of Cr, Mo, Ti and Al in austenitic dendritic core and interdendritic grain boundaries (carbides), depending on the welding method involved. Segregation of Mo and Ti is dramatically high in interdendritic boundaries (carbides) than that of Cr and Mo as they are powerful carbide formers with low diffusivity in γ -Ni. As such, concentration of these elements (in the form of carbides) in the interdendritic region increased with increase in heat input of welding cycle (low heat input in laser-based ADLW and LHW to high-heat input in TIG). The elemental concentrations of Ni and Co were obviously lower in the interdendritic region as compared to dendritic core. Thus, segregation ratio (SR) evaluated based on the equation provided in [14,27] showed less than unity for Cr, Mo, Ti and Al in all welds. Moreover, as diffusivity of the Mo and Ti are significantly low in γ -Ni, it gets easily expelled from dendritic matrix [17].

The segregation of Cr and Mo in interdendritic region results in formation of secondary carbides at the end of the solidification [14]. Higher concentrations of Cr and Mo in the interdendritic region (carbides) of TIG fusion zones (shown in Table 9.2) could be due to high heat input coupled with repetitive heating due to multiple-weld passes as against low heat input with high cooling rate in ADLW and LHW. Repetitive heating enhances diffusion of alloying elements and provides enough time for precipitation and growth to occur, thus, large number of Cr, Mo-rich carbide phases (9.1% of volume fraction) with enlarged sizes appear in multipass TIG welded fusion zone microstructure as compared to LHW (7.5% in UFZ and 2.9% in LFZ) and ADLW (6.1% in UFZ and 5.0% in LFZ) counterparts. Segregation of these elements into the interdendritic region results by virtue of Cr, Mo-rich M₂₃C₆ carbides through SSGB and MGBS in multi-pass TIG weld fusion microstructure that weaken strength of matrix and as a result joint efficiency [28]. Indeed, EDS results indicating enrichment of Cr and Mo in

interdendritic region accompanied with depletion in Ni and Mo in TIG corroborate their aspects. The degree of enrichment (segregation) with SR ratio (>1 in Ni and Co and <1 in Cr, Mo, Al and Ti) increased with reduction in cooling rate of the welding process. Highest in TIG followed by LHW and ADLW. Similar observations to the effect of heat input on the segregation behaviour were reported in several studies involving laser welding [14,29].

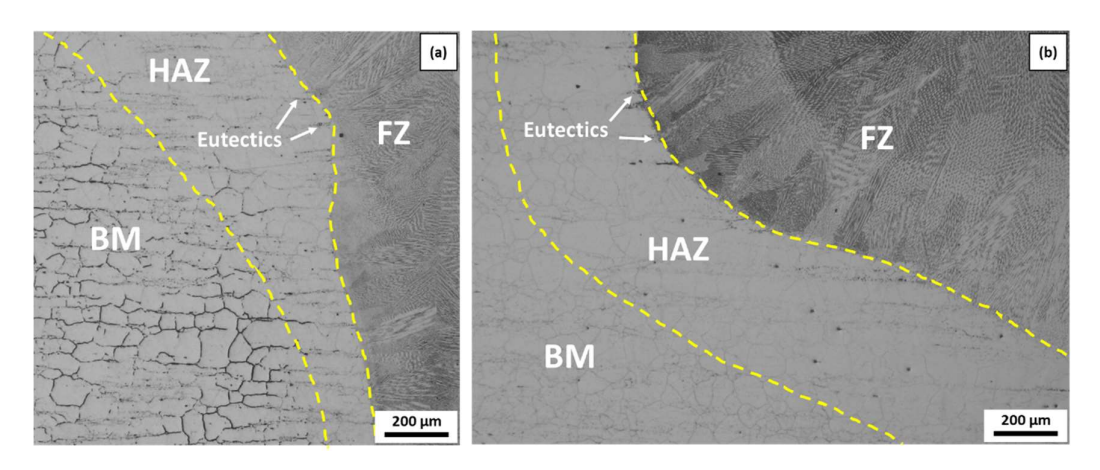


Figure 9.8. Weld interface micrographs of (a) LHW/ADLW and (b) TIG

Further to understand joint strength, apart from analysing microstructure at weld fusion, determining strength of interface at heat affected zone (preferably at weak neck zone) is necessary in terms of interface microstructure analysis (interface microstructures of laser welded as well as conventional TIG presented at Figure 9.8). As heat affected regions in both LHW and ADLW are more or less similar, representative interface microstructure of only one laser-based process considered, i.e., ADLW. The maximum width of HAZ region was observed to be $150 - 400 \mu m$ in LHW and $120 - 300 \mu m$ in ADLW as against $350 - 550 \mu m$ in TIG. The widest HAZ width with large grain growth accompanied with dissolved secondary carbides is clearly discernible in multi-pass TIG weld as compared to narrow HAZ with enhanced low melting eutectics in both LHW and ADLW. Indeed, the cooling rate of the weld thermal cycle determined formation of LMEs and grain growth with/without dissolution of Cr and Mo rich carbides. The presence of continuous eutectic network along the GBs may plausibly weakens the connection between the grains and thus micro-racking could easily be facilitated and propagate along these GBs during tensile testing of laser weldments [30]. In contrast, significant reduction in LMEs accompanied with increased dissolution of carbides may help facilitate in strengthening of HAZ microstructure of TIG, despite grain coarsening. Overall, strength of HAZ microstructures in weld joints are found to enhance in high heat input TIG process as compared to LHW and ADLW counterparts on account of dissolution of carbides in matrix.

9.6 Mechanical properties of the weldments

9.6.1 Hardness distribution analysis

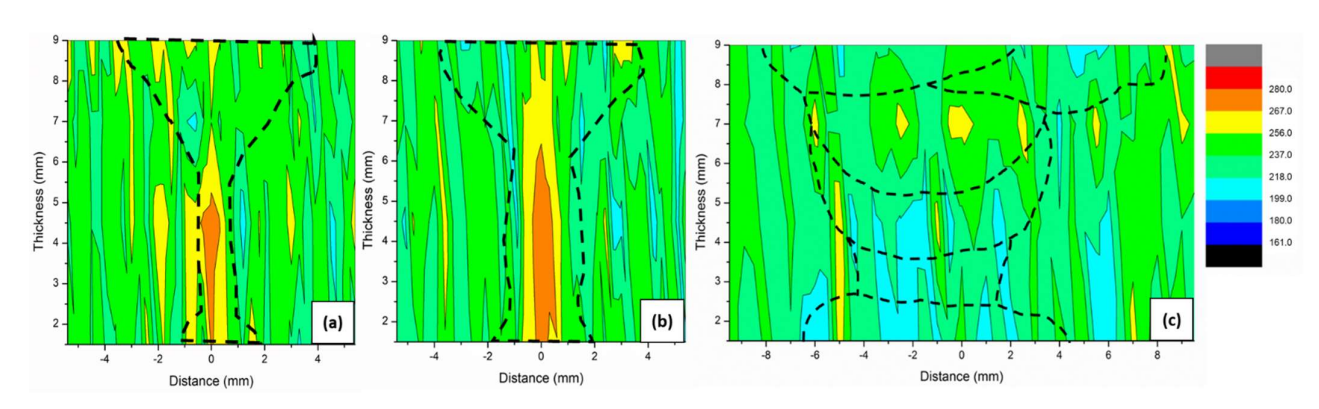


Figure 9.9. Micro-hardness contour plots of welded joints of (a) LHW, (b) ADLW and (c) TIG

Further to microstructure analysis with phase identification and compositional changes of weld joint, micro-hardness as well as nano-hardness distribution within the weld regions was carried out by employing conventional Vickers micro-hardness and high-speed nanoindentation techniques. Figure 9.9 illustrate micro-hardness contour graphs of LHW, ADLW and TIG weld cross-sections that envisage varied strengthening effects within weld microstructure with welding method involved. The hardness of the BM varied between 232 – 266 HV with significant scatter due to mixture of fine and coarse austenitic grains as previously explained. Apparently, significant variation in hardness within fusion zone of especially LHW and ADLW be associated with the cooling rate of the prevailing weld thermal cycle with single and multiple heat sources. Microhardness was found to be in range of 218 – 278 HV in FZ of LHW, 235 – 272 HV in ADLW, and 210 – 260 HV in TIG. The slight scatter in hardness of LHW and ADLW could be attributed to the significant variations in interdendritic carbides and SDAS as visualized in microstructure and phase analysis previously discussed. Indeed, relatively high micro-hardness concentrated in LFZ of both LHW and ADLW indicates refined dendritic microstructure (including dendritic arm spacing) with hard carbide segregation as previously confirmed by microstructure analysis.

However, high heat input with slow cooling rate in multiple-pass cycle of TIG envisaged no such significant variation in hardness of upper and lower zones as observed in LHW and ADLW. Comparing micro-hardness distribution within fusion regions of LHW, ADLW and TIG, one can see marginally high hardness in LHW and ADLW as compared to TIG counterpart. This evidently indicates the influence of heat input and the prevailing cooling

rate associated with input energy intensity profile involved in the laser-based welding process. Indeed, hardness distribution in weld microstructures reconfirm microstructural changes previously observed and explained. Similar variation in microhardness distribution of weld fusion regions was reported in studies involving laser and conventional fusion welding processes of Inconel 617 and attributed to the prevailing thermal cycles [13,14,31].

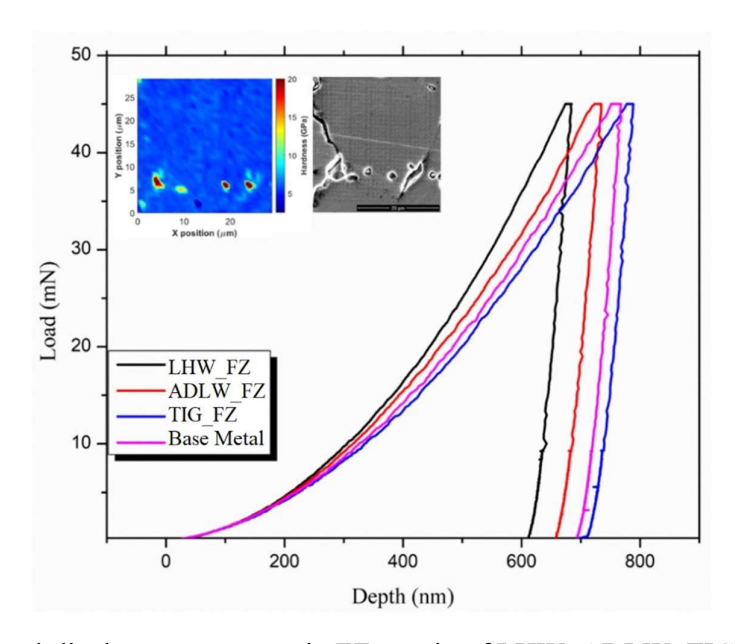


Figure 9.10. Load-displacement curves in FZ matrix of LHW, ADLW, TIG and BM (inset image illustrating typical representative hardness mapping and FESEM image for BM)

Further to understand hardness variation within various regions of weld microstructure, nano-hardness analysis with cluster mapping carried out using a high-speed nano-indentation system. Figure 9.10 illustrate typical load-displacement curve obtained on austenitic dendrite of central region of fusion zone of all welds and austenitic grain of substrate with nano-hardness values of dendrites in weld (D) / grains in substrate and inter-dendritic (IR) / grain-boundary regions being presented in Table 9.3. The inset micrograph presented in Figure 9.10 shows a typical representative cluster hardness map of BM along with FESEM image. It is clear that the nano-hardness of austenitic dendrites as well as inter-dendritic region constituting different carbides varied with type of welding employed. This could be plausibly due to compositional variation in dendritic and inter-dendritic segregation regions of the microstructure associated with temperature-gradient and cooling rate of welding cycle. Indeed, nano-hardness in inter-dendritic region (carbides) of LHW and ADLW welds are predominantly higher when compared to TIG weld as a consequence of diffusion rates during solidification of welding cycle. Moreover, dendritic matrix hardness for LHW and ADLW was found to be in the range of 5.2 – 6.7 GPa and 5.4 – 6.3 GPa respectively, whereas in TIG counterpart, relatively low

nano-hardness in the range of 2.9 – 4.3 GPa observed. As previously discussed in microstructural analysis, severe segregation of alloying elements with Cr and Mo-rich carbides accompanied with grain coarsening envisaged depletion of matrix strength in fusion zone of TIG weld. Furthermore, load-displacement curve presented in Figure 9.10 fortify these effects as nano-hardness of austenitic dendrite decreased from ADLW to LHW to TIG, necessarily in the order of heat input. Thus, it may be presumed that FZ of TIG is comparatively weaker to that of laser-based welding processes of LHW and ADLW and BM.

Table 9.3. Nano hardness range (GPa) of dendrites/interdendritic region carbides in welds and grains/grain boundary carbides in substrate, LHW. ADLW, and TIG specimens

	Matrix (Grains/dendrites)	GB/Interdendritic carbide
LHW_FZ	5.2 – 6.7	19.4 - 23.3
ADLW_FZ	5.4 – 6.3	17.2 – 20.6
TIG_FZ	3.9 – 4.3	12.4 – 15.8
ВМ	4.2 – 5.5	24.6 – 29.3

Furthermore, nano-hardness of low melting eutectics (LME) observed in PMZ close to NFZ of all welds provide further insight to co-relate with weld joint strength. Nano-hardness of LME region of LHW was in the range of 11.2-13.5 GPa, whereas LME region for ADLW exhibited hardness in the range of 8.2-10.8 GPa. Indeed, high cooling rate with wide temperature gradient associated with ADLW caused significant reduction of LME hardness than that of LHW. Indeed, high level of diffusion of Cr and Mo possible in LME region of LHW as compared to that ADLW (as previously analyzed by EDS) corroborated its effect. However, comparing nano hardness values of inter-dendritic carbides of LMEs in welds to that of intergranular carbides (nano-hardness in the range of 24.6-29.3 GPa) of BM, it can be concluded significant diffusion of Cr with enrichment of Mo at interface of $M_{23}C_6/\gamma$ -Ni boundary during welding caused specific ternary eutectic phase (γ -Ni + $M_{23}C_6$ + M_6C) that entailed depletion of strength in LME of weld-PMZ as compared to hard intermetallic Cr, Morich $M_{23}C_6$ carbides in as-received BM.

Indeed, local enrichment with subsequent formation of LME in PMZ of both LHW and ADLW welds caused significant depletion of strengthening elements in the surrounding matrix with lowering of hardness i.e., local softening at PMZ. In similar studies involving laser as well as electron-beam welding process of superalloys, such reduction of nano-hardness in

PMZ/EQZ matrix with dissolution of strengthening precipitates and local softening were reported [32,33]. Apparently, no such depletion in strength of PMZ observed in TIG on account of significant low cooling rate that prevail in multi-pass welding cycle.

9.6.2 Tensile and Impact properties

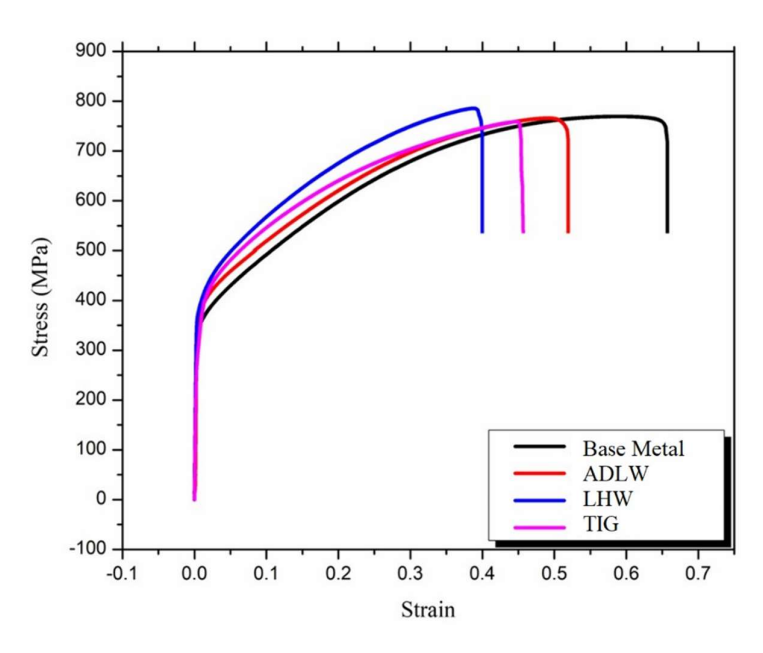


Figure 9.11. Tensile stress-strain curves of LHW, ADLW, TIG and BM

Mechanical properties of the welded joints produced employing ADLW, LHW and TIG as well as BM were assessed by subjecting to room temperature uniaxial transverse tensile testing as well as impact testing as per ASTM standards. Figures 9.11 and 9.12 illustrate engineering stress-strain curves and impact energy absorbed employing *Charpy*-type notch specimens by welded joints as well as BM. Maximum ultimate tensile stress of LHW, ADLW and TIG welded joints were found to be 780-785, 760-775 and 748-757 MPa respectively as against 765-769 MPa in BM. The yield strength of the weld joints is always higher than that of BM in all cases, although, with reduction in elongation. Yield strength of the welded joints and BM were found to reduce in the order of BM< TIG <ADLW <LHW. It is clear that weld joints produced by laser-based welding processes of LHW and ADLW are superior in tensile strength to BM with joint efficiency being obtained in the range of 99 – 100%.

The TIG welded joint whose ultimate tensile strength was 748-757 MPa was found to be lower than that of BM with 97 - 98% joint efficiency. The enhanced tensile strengths in laser welded joints could be attributed to refined weld fusion microstructures with finer SDAS and low segregation in interdendritic regions. Indeed, high cooling rates that prevail in laser

welding processes entail refinement in microstructure with limited inter-dendritic segregation as previously explained in microstructure analysis. In contrast, despite with marginally coarse dendritic fusion microstructure in TIG, evolution of large boundaries with micro-segregation that reduce ductility entailed reduction of tensile strength, lower than that of BM. In contrast, ductility of the weld joints represented by elongation are lower than that of BM. This could be assessed by analysing fracture surface morphologies discussed later.

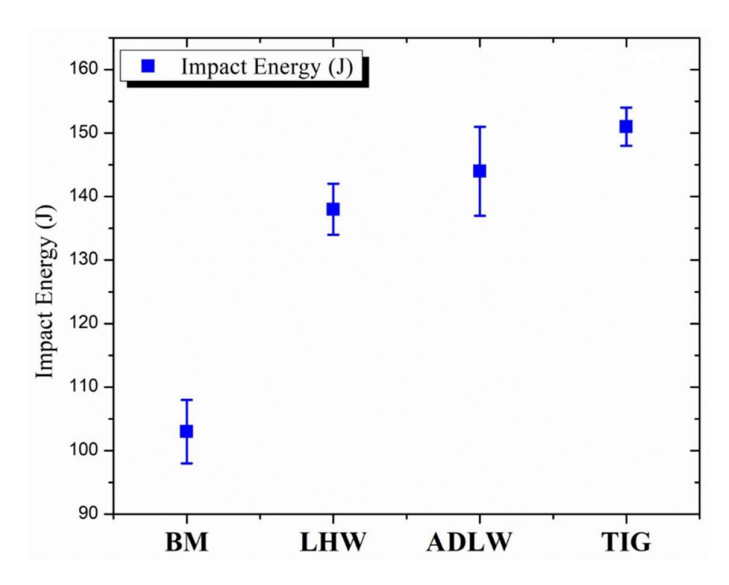


Figure 9.12. Impact energy (J) of LHW, ADLW, TIG and BM

The micro-segregation into the interdendritic region in any superalloy weld during solidification play pivotal role in producing tensile strength, although it depends on amount of heat input involved in the welding process [13,31]. When using localised low-heat input processes such as LHW and ADLW, because of rapid cooling, the microstructure becomes finer and hence limits micro-segregation. However, when using high-heat input process with repetitive thermal cycle employing multi-pass such as TIG entail low cooling rates (observed nearly two-to-three times lower to laser welding processes) and associated high micro-segregation with SSGB and MGB. Indeed, EDS results of the interdendritic boundaries and dendritic core previously reported reconfirmed their effects in weakening the joint strength. Apparently, fusion zone area being maximum in TIG further exacerbates the strength of the joint [34].

On the whole, once sound fusion/substrate interface is produced in the welded joint, it is the proportion of fusion area and strength of fusion microstructure determined by dendritic refinement and micro-segregation that determine the tensile strength of the fusion welded joint. Moreover, the weld joint strength obtained in the present study by LHW and ADLW processes

are comparable and in fact slightly superior to that of reported studies of other researchers adopting multi-pass conventional fusion welding techniques [1,31,35]. Indeed, the strength of the fusion welded joints was found to depend greatly on the strength of the microstructure with amount of micro-segregation and dendritic refinement coupled with fusion/substrate interface strength.

As compared to tensile strength of the welded joints, room-temperature impact-fracture absorbed energies presented in Figure 9.12 of welded joints as well BM show altogether different behaviour on account of loading mechanism involved in testing. It can be evidently seen that all impact absorbed energy values of welded joints are significantly higher by 35 – 50% as compared to that of BM. Apparently, the impact energy value of TIG welded specimen is higher by 150 J as against 138 J for LHW and 144 J for ADLW specimens. As these values of both tensile strength and impact energies satisfies application requirements, they can be adopted in industry. As Inconel 617 is a solid solution strengthened superalloy with no ability to form significant precipitation strengthening phases, it is the misorientation distribution of dendrites/grains coupled with grain boundary / inter-dendritic segregation strengthening elements that govern the impact absorbed energies of fusion microstructures as reported by various studies reported [26,36]. Thus, presence of many misorientation grain boundaries (of approximately 60^{0}) coupled with high-angle grain-boundaries analysed as per EBSD analysis in TIG entail highest impact energy followed by ADLW, LHW, and BM. Indeed, it is reported that once micro crack initiates and propagates into the surrounding region, amount of misorientation grain boundaries and their degree of misorientation can effectively arrest micro cracks as well as their propagation [26,36]. Thus impact-fracture absorbed energies increased in the order of BM<LHW<ADLW<TIG convergent with fusion zone microstructural changes associated with welding thermal histories.

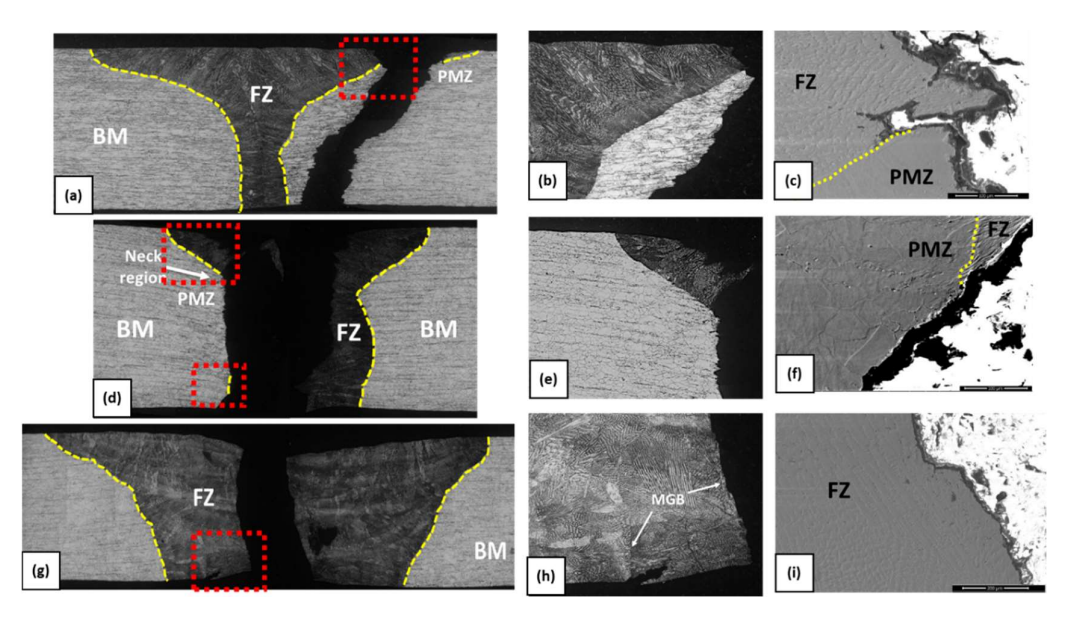


Figure 9.13. Cross-sectional tensile-test fractured micrographs of LHW, ADLW, and TIG welds

Further to understand the mechanism underlying tensile behaviour, fractured tensile test specimens of all welds were assessed for location of failure and presented in Figure 9.13. It is clear that location of failure in case of LHW and ADLW was at PMZ/FZ boundary regions (Figures 9.13a-f)), whereas, location of failure in case of TIG specimen is in FZ (shown in Figures 9.13g). This suggests that weld fusion zone is weaker in TIG than that of ADLW and LHW counterparts and as a result joint strength of TIG weld is relatively lower than that of LHW, ADLW and BM. High magnification images of TIG FZ shown in Figures 9.13(h) and (i) reconfirmed occurrence of fracture along the SGBs. Additionally, evidence of MGBs in the vicinity along the fractured path was also observed from high-magnification SEM analysis. Indeed, similar influence of fracture occurrence in weld zone along the grain boundaries envisaging weak tensile strength observed in multi-pass welds and associated with grain boundary segregation and their migration in superalloy welds [24,25].

In contrast to TIG specimen, LHW and ADLW tensile specimens failed slightly away from the weld fusion zone indicating strong weld joint compared to TIG counterpart. A close look at the crack propagation morphology of LHW and ADLW indicates that plausibly, crack initiated form soft PMZ (more precisely at localized highest ductility-dipped neck region) and propagated through fusion boundary into the weld fusion zone in ADLW and towards HAZ/BM interface in LHW. As previously reported in microstructure analysis, PMZ in the vicinity of neck zone in both ADLW and LHW welds entail high heat stagnation and thereby microfissuring and/or continuous film formation of low melting eutectics along GBs. Thus,

possible crack initiation regions at PMZ during tensile loading observed in laser welds. Similarly, mechanisms of failure in tensile loading were reported in several superalloy weldments and attributed to micro fissures and/or liquid films along GBs in PMZ [32,38].

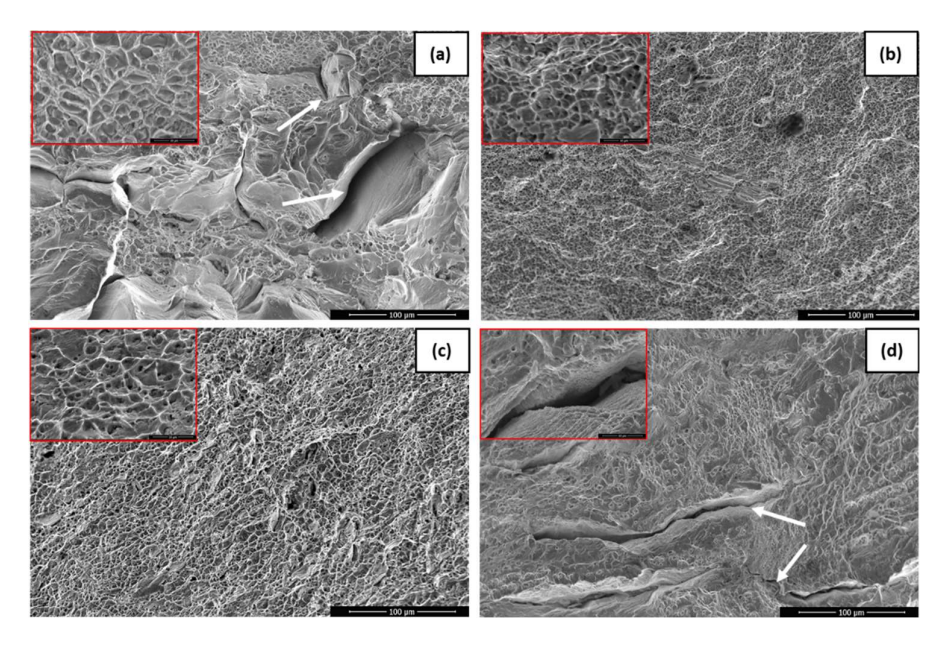


Figure 9.14. Fractographs of fractured tensile-tested coupons of (a) BM, (b) LHW, (C) ADLW, and (d) TIG

A close look at high magnification SEM fractographs of tensile test specimens depicted in Figure 9.14 demonstrate possible reasons for variation in tensile strengths and ductility of various weld joints and base metal. The general texture of fractured surfaces of all specimens indicate that mode of fracture was observed to be ductile rupture in both BM and welded specimens with major difference between fracture surfaces was the morphology and size of dimples. The dimple size exhibits direct proportional relation with the ductility of the joint or base metal, finer the dimple size, higher will be the ductility of the joint or material [39]. As per fractured surface morphologies of all welded specimens, it is the ADLW specimen (Figure 9.14(b)) that is exhibiting finest dimples with deeper depths which explicitly imply better plasticity and highest elongation of 45-55% as compared to LHW and TIG. However, dimples were further finer with higher amounts with multiple cracks observed in BM as a result lower strength (compared to ADLW and LHW) with maximum elongation. Moreover, intergranular cracking in fusion region was more prevalent in TIG specimen (Figure 9.14(e)) that entailed lower strength coupled with reduced ductility as compared to BM and laser welded joints.

Comparing laser welded LHW and ADLW fractured surfaces with that of TIG, predominantly large quantities of dimples were observed in laser welded specimens with fracture surface of TIG joint exhibiting a layered-crack morphology (marked in Figure 9.14(e)). Indeed, shallow dimples with layered crack morphology in TIG joint could be attributed to the larger columnar dendritic microstructure of fusion zone [19], as TIG joint failed completely in weld region. Result further corroborated occurrence of cracking along GBs in TIG associated with segregation of ductility-dipped SSGBs and MGBs emancipated from the multi-pass TIG welding technique. Overall, analysis of tensile specimen fractographs helped to understand the underlying mechanism of failures in weld joints in conjunction with microstructural analysis entailed by thermal histories of the welding processes. Single-pass laser-based welding processes clearly demonstrated the feasibility of obtaining better joint strengths and efficiencies than that of conventional multi-pass TIG, more particularly ADLW welding for easy adoption for applications owing its engineering advantage of reduced distortion and ease of process maneuverability.

9.7 High temperature corrosion behaviour of superalloy joints and base metal

As previously explained in literature review, higher operating temperatures of AUSC boilers can cause premature failure of the boiler components due to combined effect of coal ash and flue gas environment encountered in thermal power plant boilers which significantly accelerates the corrosion reactions. Further to the optimization and qualification of the welding process in terms of joint strength, it was felt necessary to assess high temperature corrosion behaviour of welded surface and compare with base metal to adopt in fabrication of parts of thermal power plant. Thus, detailed comparative analysis of hot corrosion resistance both in coal-ash coated and salt-coated environment are tested and analysed. In the present study, high temperature corrosion test of weldments and untreated base metal was performed at 600°C for a time period of 1000 hours in 5 cycles (200, 400, 600, 800 and 1000h) using a horizontal tubular furnace as shown in Figure 3.23. In this type of hot corrosion test setup, actual power plant environment be simulated in laboratory by combining synthetic coal-ash mixture with flowing synthetic flue gas. The synthetic coal-ash comprised of Fe₂O₃ (6 %) + 1.6 % K₂SO₄ + Al_2O_3 (30 %) + SiO_2 (60 %) + 0.4 % Na_2SO_4 + TiO_2 (2 %) (in wt. %). The salt composition used was in the ratio of Na₂SO₄: K₂SO₄: Nacl – 75:24:1. The synthetic flue gas mixture composed in the ratio of CO_2 cylinder $-N_2$: CO_2 : O_2 – 75.99 : 3.44 : 20.57 and SO_2 cylinder - SO₂ : N2 - 0.134 : 99.866. The synthetic flue gas mixture was passed through the furnace tube at a flow rate of 100 ml/min.

The corrosion rate was determined in terms of thickness of corroded layer formed at the end of the duration of test. The characteristics of the corroded layer was analysed for elemental composition as well as phases by employing XRD, FESEM and EDS tools with elemental mapping and spot elemental analysis at appropriate regions of microstructure covering weld zones and base metal.

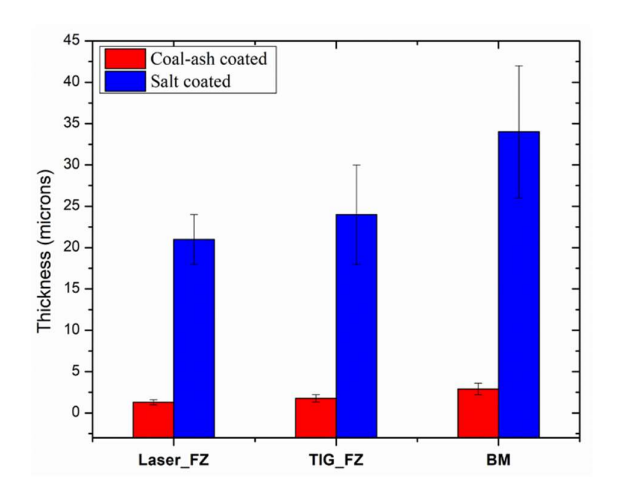


Figure 9.15. Variation of thickness of the corroded layer in fusion zones of ADLW (laser), TIG welded and BM in coal-ash and salt-coated conditions

Figure 9.15 illustrates thickness of corroded layer obtained in weld fusion zone region as well as base metal in ADLW (represented here as laser), TIG and BM after exposing in coalash as well as salt-coated environments at 600°C for 1000 hours. Corroded layer at the centre of the exposed sample was considered for examination to obtain comprehensive analysis. It is clear that thickness of the corroded layers in weld fusion zones of ADLW, TIG and BM specimens in salt-coated environmental condition were always higher (3 – 5 fold) when compared to that in case of coal-ash coated environment. In both the environment (coal-ash and salt-coated), ADLW specimens provided best corrosion resistance as compared to TIG and BM counterparts. Further the weight gain per unit surface area was found to increase monotonically with increase in the exposure time for a period of 1000 hours at 600°C. Weight gain was observed to be very less in ADLW specimens as compared to that of TIG welded and BM specimens. The cumulative weight change in ADLW specimen was observed to be 1.5 – 3 times less than that of TIG welded and BM specimens. However, in salt coated conditions, a rapid increase in weight was observed in both ADLW/TIG weldments and BM due to the

presence of corrosive salt mixtures of Na₂SO₄, K₂SO₄, and NaCl in salt-coated environment that entail acceleration of corrosion rate rapidly [40,41].

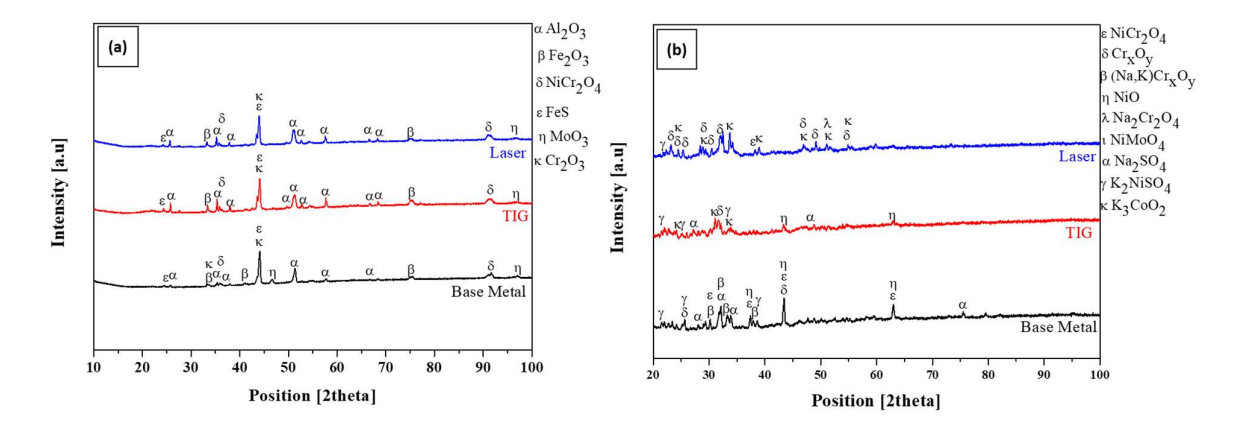


Figure 9.16. XRD patterns of hot corroded specimens after exposed to 1000 hours at 600°C (a) Coal-ash coated and (b) Salt-coated conditions

Further, X-ray diffraction analysis of specimen surfaces after corrosion test was carried out to identify the corrosion products that formed on the surface of the corroded specimens after exposing to coal-ash and salt-coated environment for 1000 hours at 600°C. Figure 9.16 shows the XRD patterns of ADLW, TIG welded and BM specimens after exposed to coal-ash and salt-coated environments. Major phases found in the corrosion product after exposed to 1000 hours in coal-ash environments were Cr₂O₃, Al₂O₃ and FeS in all specimens. However, NiCr₂O₄ spinel phase was found to be predominant in case of welded specimens as compared to that of BM counterparts. Generally, oxides of Cr₂O₃, Al₂O₃, NiO and spinel oxides of NiCr₂O₄ are intended to form as corrosion products due to high-temperature corrosion exposure of superalloy material [40]. However, these oxide phases formed at the surface provide different levels of protection against corrosion based on their types. Among them, Cr₂O₃ and Al₂O₃ were envisaged to offer high resistance against high temperature oxidation and corrosion. In Ni-based superalloys, spinel oxide phase is usually designated as combination of NiO and Cr₂O₃ (alternatively termed as NiCr₂O₄). Presence of oxides of Cr and Mo on any Nibased superalloy surface react with NiO to nucleate and form spinel oxide phases of Ni(Cr, Mo)₂O₄ which eventually further act as a highly dense protective oxide layers at elevated temperature.

These phases inevitably prevent further diffusion of oxygen and thereby decelerate rate of corrosion. Indeed, corrosion rate in BM specimen tested under synthetic coal-ash environment could be relatively high on account of presence of meagre spinel phases as

compared to that of welded specimens. Figure 9.16b corroborate these aspects represented by XRD patterns of ADLW, TIG welded and BM specimens exposed to salt-coated environments. Major phases found in the form of corrosion products after exposure for 1000 hours in salt-coated environments were Cr₂O₃, NiO, Ni(Cr, Mo)₂O₄, Na₂SO₄, K₂NiSO₄, K₃CoO₂ and (Ni, Cr)S. In ADLW specimens, Cr₂O₃, Ni (Cr, Mo)₂O₄ and K₃CoO₂ were predominant oxides observed, whereas, NiO, Na₂SO₄, K₂NiSO₄ and K₃CoO₂ were found to be more dominant in TIG-welded specimens. However, in addition to oxides of Cr₂O₃, NiO, Na₂SO₄, Ni(Cr, Mo)₂O₄ and K₂NiSO₄, few other complex oxides of Na and K were also observed in BM. Thus, it infers from the qualitative and quantitative analysis of various corrosion products as per XRD, BM experienced highest corrosion rate followed by TIG and ADLW specimens, as a consequence of varied reaction products with complex compounds of Na and K salts.

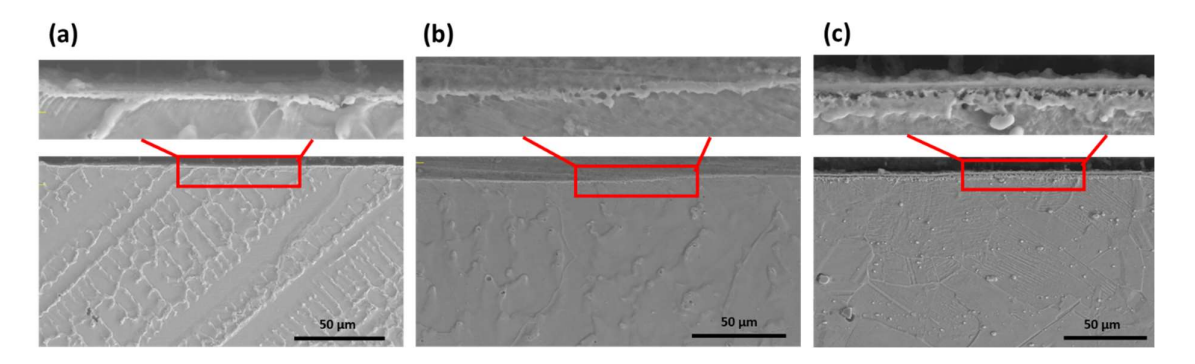


Figure 9.17. FESEM micrographs of hot corroded specimens in Coal-ash condition (a) ADLW, (b) TIG and (c) BM

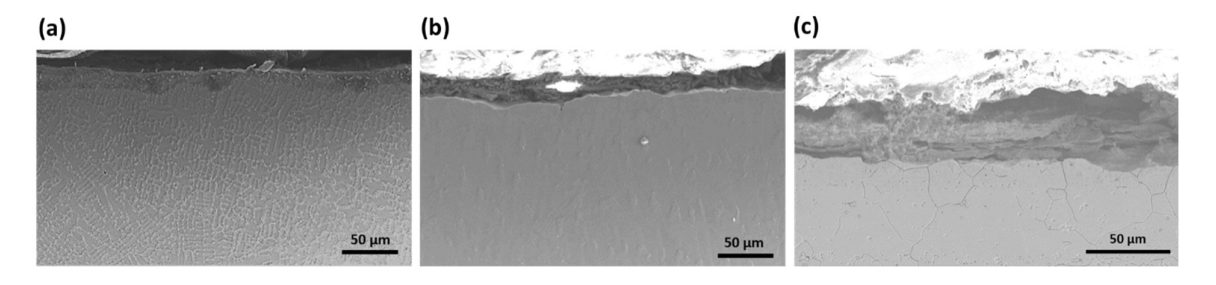


Figure 9.18. FESEM micrographs of hot corroded specimens in Salt-coated condition (a) ADLW, (b) TIG and (c) BM

Figure 9.17 illustrate cross-sectional FESEM images of ADLW and TIG weld fusion zone specimens along with BM at the end of the exposure duration. Indeed, distinguishably different thicknesses of the corroded layers are discernible on account of variation in corrosion rates determined by the microstructural features. The thickness of the corroded layer in coal-

ash tested condition of weld fusion zones of ADLW and TIG were observed to be 1.3 ± 0.3 µm and 1.77 ± 0.45 µm, whereas, BM exhibited corroded layer thickness of 2.9 ± 0.7 µm. In case of salt-coated environment (shown in Figure 9.18), corroded layer thicknesses were observed to be 21 ± 3 µm, 24 ± 6 µm, and 34 ± 8 µm, respectively in ADLW, TIG and BM. It is clear that ADLW specimen exhibited highest hot corrosion resistance than TIG-welded and BM counterparts. The scale formed on TIG welded and BM specimens (Figure 9.18 (b and c)) are with quiet irregular, whereas, relatively uniform thin-scale observed in ADLW specimen (Figure 9.18(a)). Indeed, as determined by XRD analysis previously, formation of complex oxides of Na₂SO₄, K₂NiSO₄ coupled with presence of other compounds of Na and K in TIG welded as well as BM plausibly accelerated the corrosion rate resulting in porous, non-uniform and thick corroded layers.

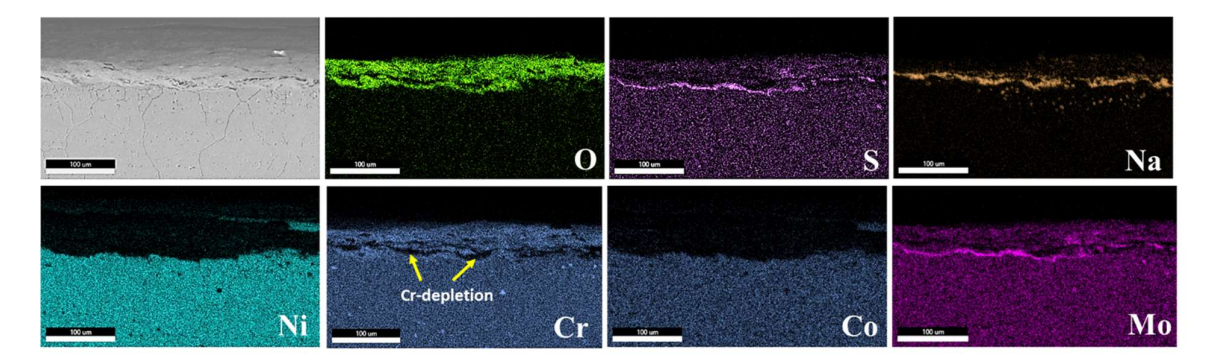


Figure 9.19. Elemental mapping of the BM cross-sectional after exposed to 1000 hours in salt-coated condition

Further to understand type of oxide products formed due to high-temperature corrosion, subsurface EDS analysis has been carried out for all welded ADLW/TIG and BM cross-sectioned specimens. The surface oxide layer formed on the specimens were found to be enriched with Cr, Mo, O, S and Na, although their quantity varied with type of corroded layer. However, no elements of Ni and Co were detected on the surface owing to their depletion by corrosion. Agglomerates constituting Cr, Ni, Mo and Co were predominantly found in higher amounts in ADLW when compared to TIG and BM counterparts. Thus, results elemental composition analysis indicated formation of corrosion resistant oxide scale, (Cr-O) rich Cr₂O₃, in both coal-ash and salt-coated environment, consistent with phase analysis observed previously. Another aspect observed is the presence of higher amounts of Na and K in TIG and BM specimens tested with salt-coated environment as previously observed in XRD analysis.

Thus, it reaffirms relatively enrichment of Na and K in TIG and BM samples leading to formation of complex compounds of various Na and K-rich salt species.

Further, to understand the elemental distribution in oxide layer formed on the specimen surface and subsurface, elemental mapping was carried out and depicted in Figure 9.19, which revealed, presence of oxide layer on the surface to a depth of $21 \pm 3 \mu m$, $24 \pm 6 \mu m$, and $34 \pm$ 8 μm, respectively in ADLW, TIG and BM after 1000 hours of exposure at 600°C in salt-coated environment. It is clear from Figure 9.19 that the oxide layer formed on the surface of the BM specimen are enriched with O, Cr, Mo and S with elimination of Ni and Co. Among these elements, Cr and O were observed in large quantity envisaging formation of oxides of Cr₂O₃, NiO predominantly coupled with few spinel oxide phases of Ni(Cr, Mo)₂O₄ as observed from XRD analysis. Indeed, many reports on hot corrosion analysis of superalloy materials evidenced reaction of Cr and Mo oxides with NiO at elevated temperatures to form such complex spinel oxide [40,42-44]. Furthermore, non-uniform porous oxide layer formation indicates formation of sulphides of Mo [42,45]. In addition, evidence of Cr-depleted region as marked in X-ray map of Figure 9.19 evidently reaffirm severe depletion of Cr due to high temperature corrosion. Essentially of sulphides of molybdenum particles could be observed as reported in hot corrosion studies of Inconel 617 alloy [42,43,45]. Moreover, Inconel 617 alloy containing Mo may suffer rapid hot corrosion rate due to the reaction between Mo oxide and Na₂SO₄ present in the salt and thereby form complex compounds of Na₂MoO₄ [46]. Moreover, TIG welds showed higher number of Mo-rich carbides (at SSGBs and MGBs) as compared to that of laser welds that may plausibly accelerated corrosion rate.

Another aspect that can distinguishably observed is the difference in thickness of corroded layers of welded and BM specimens. Indeed, ADLW specimen exhibiting significant amounts of Ni(Cr,Mo)₂O₄ inevitably prevent further diffusion of oxygen and thereby reduce rate of corrosion to a great extent. However, in TIG welded and BM specimens, extensive weight gain and thick corroded layer entailed absence of protective surface layer to hinder the diffusion of oxygen and corrosive salts into the specimen. Similar observations were found in the study analysing hot corrosion behaviour of superalloy coatings deposited by laser and TIG techniques, wherein presence of continuous protective Cr₂O₃ scale layers on laser deposited specimens provided better hot corrosion resistance as compared to TIG counterpart and BM counterparts [40,47]. Overall, laser welding by ADLW was found to impart noticeably better hot corrosion resistance as compared to that of TIG welded and BM counterparts on account of refined microstructure with reduced micro-segregation and less dispersoids-agglomeration.

9.8 Conclusions

The present study compared the single-pass laser and laser hybrid welding of 10-mm thick nickel-based Inconel 617 superalloy with multi-pass conventional TIG in terms of metallurgical and mechanical properties evaluation and assessment. Following conclusions can be made:

The welds produced by LHW and ADLW constitute 'wine-cup' and 'Y-shape' bead profiles with high aspect (depth-to-width) ratios, reduced weld fusion zones and low distortion levels as against large weld fusion zone with 'bath-tub shape' bead profile of multi-pass TIG weld on account of highly localized low heat input high-power density laser beams involved in laser-based welding processes with high energy coupling. Microstructural analysis indicated that the fusion zone microstructures of LHW and TIG welds were found to be inhomogeneous owing to the involvement of double heat sources of laser and arc in LHW and multiple weld passes in TIG. Indeed, uniform and refined microstructure with finer SDAS and reduced microsegregation of Cr and Mo in interdendritic regions observed in LHW and ADLW owing to fast cooling rates of laser welding cycle.

X-ray diffraction phase analysis of weld fusion zones revealed presence of more number of M₂₃C₆ and M₆C Carbide peaks in TIG as compared to that of LHW and ADLW counterparts and attributed to high heat input with low cooling rate with possible microsegregation at GBs experienced by repeated thermal cycles of multiple weld passes involved. Micro and Nano-hardness profiling indicated that the hardness of fusion region of TIG welds are comparatively lower to that of ADLW and LHW on account of enhanced segregation of inter-dendritic Cr-rich and Mo-rich carbides and grain coarsening effect.

Tensile test results indicated that the joint strength of TIG weldment is lower than that of base metal as against superior strengths observed in both laser welded joints of LHW and ADLW to that of base metal. Indeed, formation of ductility-dipped SSGBs and MGBs in weld fusion zone of TIG entailed weakening of the joint strength and failing in fusion zone. High temperature corrosion studies conducted in both salt coated and coal-ash mixed flue gas environment indicated that laser welded specimens provided higher resistance than that of TIG and BM counterparts owing to refined microstructure with less micro-segregation.

On the whole, the joint efficiency of single-pass laser based ADLW and LHW weldments along with impact resistance are superior to that of TIG and BM and thereby suggest

ease adoption in fabrication of high-temperature corrosion resistant superalloy components for thermal power plant and other application sectors.

9.8 References

- 1. Fink, Carolin, and Manuela Zinke. "Welding of nickel-based alloy 617 using modified dip arc processes." Welding in the World 57, no. 3 (2013): 323-333.
- Kessler, Benjamin, Dirk Dittrich, Berndt Brenner, Jens Standfuss, and Christoph Leyens.
 "Extension of the process limits in laser beam welding of thick-walled components using the Laser Multi-Pass Narrow-Gap welding (Laser-MPNG) on the example of the nickel-based material Alloy 617 occ." Welding in the World 65, no. 7 (2021): 1359-1371.
- 3. Viswanathan, R., K. Coleman, and U. Rao. "Materials for ultra-supercritical coal-fired power plant boilers." International journal of pressure vessels and piping 83, no. 11-12 (2006): 778-783.
- 4. Di Gianfrancesco, Augusto, ed. Materials for ultra-supercritical and advanced ultra-supercritical power plants. Woodhead Publishing, 2016.
- 5. Ribic, B., T. A. Palmer, and T. DebRoy. "Problems and issues in laser-arc hybrid welding." International materials reviews 54, no. 4 (2009): 223-244.
- 6. Xu, Guoxiang, Haichao Pan, Peng Liu, Pengfei Li, Qingxian Hu, and Baoshuai Du. "Finite element analysis of residual stress in hybrid laser-arc welding for butt joint of 12 mm-thick steel plate." Welding in the World 62, no. 2 (2018): 289-300.
- 7. Kim, You-Chul, Mikihito Hirohata, Masaki Murakami, and Koutarou Inose. "Effects of heat input ratio of laser–arc hybrid welding on welding distortion and residual stress." Welding International 29, no. 4 (2015): 245-253.
- 8. Wu, Chuan Song. "Computer Simulation of Three-Dimensional Convection in Travelling MIG Weld Pools." Engineering computations (1992).
- 9. Li, G., M. Gao, C. Chen, C. Zhang, and X. Y. Zeng. "Characterisation comparison of laser and laser—arc hybrid welding of Invar 36 alloy." Science and Technology of Welding and Joining 19, no. 1 (2014): 30-37.
- 10. Piekarska, W., and M. Kubiak. "Three-dimensional model for numerical analysis of thermal phenomena in laser—arc hybrid welding process." International Journal of Heat and Mass Transfer 54, no. 23-24 (2011): 4966-4974.
- 11. Piekarska, W., and M. Kubiak. "Modeling of thermal phenomena in single laser beam and laser-arc hybrid welding processes using projection method." Applied Mathematical Modelling 37, no. 4 (2013): 2051-2062.
- Mageshkumar, K., P. Kuppan, and N. Arivazhagan. "Characterization of microstructure and mechanical properties of nickel based superalloy 617 by pulsed current gas tungsten arc welding technique." Materials Research Express 5, no. 6 (2018): 066541.
- 13. Liu, Wen, Fenggui Lu, Xinhua Tang, Renjie Yang, and Haichao Cui. "The microstructure evolution and element segregation of Inconel 617 alloy tungsten inert gas welded joint." Journal of Materials Research 31, no. 4 (2016): 435-442.
- Ren, Wenjie, Fenggui Lu, Renjie Yang, Xia Liu, Zhuguo Li, and Seyed Reza Elmi Hosseini. "A comparative study on fiber laser and CO2 laser welding of Inconel 617." Materials & Design 76 (2015): 207-214.
- 15. Zhao, Yaobang, Zhenglong Lei, and Yanbin Chen. "Analysis of melting characteristics of laser-arc double-sided welding for stainless steel." Chinese Journal of Lasers 38, no. 2 (2013): 0203001.

- 16. Liming, Liu, Wang Jifeng, and Song Gang. "Hybrid laser–TIG welding, laser beam welding and gas tungsten arc welding of AZ31B magnesium alloy." Materials science and engineering: A 381, no. 1-2 (2004): 129-133.
- 17. Sun, Junhao, Wenjie Ren, Pulin Nie, Jian Huang, Ke Zhang, and Zhuguo Li. "Study on the weldability, microstructure and mechanical properties of thick Inconel 617 plate using narrow gap laser welding method." Materials & Design 175 (2019): 107823.
- 18. Ren, Wenjie, Fenggui Lu, Pulin Nie, Renjie Yang, Xia Liu, Kai Feng, and Zhuguo Li. "Effects of the long-time thermal exposure on the microstructure and mechanical properties of laser weldings of Inconel 617." Journal of Materials Processing Technology 247 (2017): 296-305.
- Zhang, Lin-Jie, Qing-Lin Bai, Jie Ning, An Wang, Jian-Nan Yang, Xian-Qing Yin, and Jian-Xun Zhang. "A comparative study on the microstructure and properties of copper joint between MIG welding and laser-MIG hybrid welding." Materials & Design 110 (2016): 35-50.
- 20. Gao, Zhiguo, and O. A. Ojo. "Modeling analysis of hybrid laser-arc welding of single-crystal nickel-base superalloys." Acta materialia 60, no. 6-7 (2012): 3153-3167.
- Zhang, Mingjun, Genyu Chen, Yu Zhou, and Shenghui Liao. "Optimization of deep penetration laser welding of thick stainless steel with a 10 kW fiber laser." Materials & Design 53 (2014): 568-576.
- 22. Wang, Q., D. L. Sun, Y. Na, Y. Zhou, X. L. Han, and J. Wang. "Effects of TIG welding parameters on morphology and mechanical properties of welded joint of Ni-base superalloy." Procedia Engineering 10 (2011): 37-41.
- 23. Lippold, John C., and Damian J. Kotecki. Welding metallurgy and weldability of stainless steels. 2005.
- 24. Lee, Dong Jin, Youn Soo Kim, Yong Taek Shin, Eon Chan Jeon, Sang Hwa Lee, Hyo-Jong Lee, Sung Keun Lee, Jun Hee Lee, and Hae Woo Lee. "Contribution of precipitate on migrated grain boundaries to ductility-dip cracking in Alloy 625 weld joints." Metals and Materials International 16, no. 5 (2010): 813-817.
- Mo, Wenlin, Shanping Lu, Dianzhong Li, and Yiyi Li. "Effects of filler metal composition on the microstructure and mechanical properties for ER NiCrFe-7 multi-pass weldments." Materials Science and Engineering: A 582 (2013): 326-337.
- Palanivel, R., I. Dinaharan, R. F. Laubscher, and Ibrahim M. Alarifi. "Effect of Nd: YAG laser welding on microstructure and mechanical properties of Incoloy alloy 800." Optics & Laser Technology 140 (2021): 107039.
- 27. Osoba, L. O., R. G. Ding, and O. A. Ojo. "Microstructural analysis of laser weld fusion zone in Haynes 282 superalloy." Materials Characterization 65 (2012): 93-99.
- Jeshvaghani, R. Arabi, M. Jaberzadeh, H. Zohdi, and M. Shamanian. "Microstructural study and wear behavior of ductile iron surface alloyed by Inconel 617." Materials & Design (1980-2015) 54 (2014): 491-497.
- Wang, Ling, Yijun Yao, Jianxin Dong, and Maicang Zhang. "Effect of cooling rates on segregation and density variation in the mushy zone during solidification of superalloy Inconel 718." Chemical Engineering Communications 197, no. 12 (2010): 1571-1585.
- 30. Liu, Wen, Fenggui Lu, Renjie Yang, Xinhua Tang, and Haichao Cui. "Gleeble simulation of the HAZ in Inconel 617 welding." Journal of Materials Processing Technology 225 (2015): 221-228.
- Li, Shanlin, Kejian Li, Zhipeng Cai, and Jiluan Pan. "Behavior of M23C6 phase in Inconel 617B superalloy during welding." Journal of Materials Processing Technology 258 (2018): 38-46.

- 32. Chen, Xi, Zhenglong Lei, Yanbin Chen, Bing Han, Meng Jiang, Ze Tian, Jiang Bi, and Sanbao Lin. "Nano-indentation and in-situ investigations of double-sided laser beam welded 2060-T8/2099-T83 Al-Li alloys T-joints." Materials Science and Engineering: A 756 (2019): 291-301.
- 33. Sahul, Miroslav, Martin Sahul, Marián Haršáni, and Mária Dománková. "On the microstructure and mechanical properties of AW2099 aluminium lithium alloy joints produced with electron beam welding." Materials Letters 276 (2020): 128276.
- 34. El-Batahgy, Abdel-Monem, and Tarasankar DebRoy. "Nd-YAG laser beam and GTA welding of Ti-6Al-4V alloy." Int J Eng Tech Res 2, no. 12 (2014): 43-50.
- 35. Ahmed, Nasir, ed. New developments in advanced welding. Taylor & Francis US, 2005.
- 36. Chen, Yanbin, Jiecai Feng, Liqun Li, Shuai Chang, and Guolong Ma. "Microstructure and mechanical properties of a thick-section high-strength steel welded joint by novel double-sided hybrid fibre laser-arc welding." Materials Science and Engineering: A 582 (2013): 284-293.
- Cao, X., P. Wanjara, J. Huang, C. Munro, and A. Nolting. "Hybrid fiber laser–Arc welding of thick section high strength low alloy steel." Materials & Design 32, no. 6 (2011): 3399-3413.
- 38. Hong, J. K., J. H. Park, N. K. Park, I. S. Eom, M. B. Kim, and C. Y. Kang. "Microstructures and mechanical properties of Inconel 718 welds by CO2 laser welding." Journal of materials processing technology 201, no. 1-3 (2008): 515-520.
- Sathiya, P., Mahendra Kumar Mishra, and B. Shanmugarajan. "Effect of shielding gases on microstructure and mechanical properties of super austenitic stainless steel by hybrid welding." Materials & Design 33 (2012): 203-212.
- Fesharaki, Mohammad Naghiyan, Reza Shoja-Razavi, Hojjat Allah Mansouri, and Hossein Jamali. "Evaluation of the hot corrosion behavior of Inconel 625 coatings on the Inconel 738 substrate by laser and TIG cladding techniques." Optics & Laser Technology 111 (2019): 744-753.
- 41. Wang, Qin-Ying, Yang-Fei Zhang, Shu-Lin Bai, and Zong-De Liu. "Microstructures, mechanical properties and corrosion resistance of Hastelloy C22 coating produced by laser cladding." Journal of alloys and compounds 553 (2013): 253-258.
- 42. Hari, P. R., N. Arivazhagan, M. Nageswara Rao, and A. H. V. Pavan. "Comparative studies on corrosion of alloy 617 OCC at 700 C in air and simulated coal ash environments." Materials Today: Proceedings 5, no. 5 (2018): 11452-11459.
- 43. El-Awadi, G. A., S. Abdel-Samad, and Ezzat S. Elshazly. "Hot corrosion behavior of Ni based Inconel 617 and Inconel 738 superalloys." Applied surface science 378 (2016): 224-230.
- 44. Khan, M. Adam, S. Sundarrajan, S. Natarajan, P. Parameswaran, and E. Mohandas. "Oxidation and hot corrosion behavior of nickel-based superalloy for gas turbine applications." Materials and manufacturing processes 29, no. 7 (2014): 832-839.
- 45. Hari, P. R., N. Arivazhagan, M. Nageswara Rao, and A. H. V. Pavan. "High temperature corrosion of alloy 617 OCC at 700° C in simulated USC power plant environment." Materials Research Express 6, no. 7 (2019): 076557.
- Muktinutalapati, Nageswara Rao, Arivazhagan Natarajan, and Moganraj Arivarasu. "Hot Corrosion of Superalloys in Boilers for Ultra-Supercritical Power Plants." Superalloys for Industry Applications 29 (2018).
- 47. Molian, P. A., Y. M. Yang, and P. C. Patnaik. "Laser welding of oxide dispersion-strengthened alloy MA754." Journal of materials science 27, no. 10 (1992): 2687-2694

10.1 Conclusions

In the present research work, three different laser-based welding processes constituting CO₂ laser, CO₂+MIG and Diode laser were utilized to weld moderately thick sections of Inconel 617 superalloy material for AUSC boiler applications with assessment of their metallurgical, mechanical and corrosion properties. Initially, autogenous CO₂ laser welding (ALW) and CO₂+MIG laser-hybrid welding (LHW) techniques were utilized and their joint properties were evaluated. Later, an advanced high-power diode-laser based welding (DLW) technique was used to weld 10-mm thick Inconel 617 alloy in butt joint configuration. However, to overcome welding persisting defects of underfill and root sag hump, a novel welding method (patented) termed as Adaptive diode laser welding – ADLW developed using same diode laser with specially designed joint configuration and a two-step joining strategy for welding thick metal in a single pass. In order to compare engineering advantages and economics of the process, this single-pass ADLW technique was compared with LHW and conventional multi-pass TIG welding process. Furthermore, comprehensive metallurgical, mechanical and corrosion properties was carried out utilizing advanced characterization techniques of EBSD, Nano-Indentation and Micro-focus XRD tools.

Various work elements constitute: (a) Comprehensive study on process optimization of laser and laser hybrid welding of Inconel 617 alloy (b) Detailed study with understanding and analysis of liquation cracking susceptibility in both ALW and LHW processes in Inconel 617 alloy (c) Process optimization of thick-sectioned autogenous laser welding using high-power fiber-coupled diode laser with assessment of weld joint mechanical properties. (d) Statistical modelling with multi objective optimization employing RSM-BBD method with desirability approach for deep penetration laser welding of thick sections using DLW (e) Setting up of an apparatus and a method for laser welding of thick metallic material such as Inconel 617 using two-step welding procedure using same DLW and finally, (f) Comprehensive comparative study on single-pass ADLW / LHW processes with conventional multi-pass TIG welding process with assessment of their metallurgical, mechanical and hot-corrosion behavior.

From the preliminary study on influence of heat input in both ALW and LHW of 10-mm thick Inconel 617 alloy and its liquation cracking susceptibility assessment; following conclusions are drawn:

- ➤ LHW weld bead profile showed a typical wine-cup shape, whereas ALW produced a Y-shape bead profile on account of differences in the number of heat sources and their intensities profiles
- ➤ Weld bead width, penetration depth, and FZ area were found to increase with an increase in heat input of both LHW and ALW processes. The FZ area of LHW was three times larger than that of ALW, although, heat input in LHW involved was 2.5 times higher in ALW
- ➤ Wider width of HAZ observed at neck zone due to heat stagnation in both ALW and LHW. Radius of curvature at neck zone increased with increase in heat input and significantly larger in LHW with low cooling rates due to extended wide weld bead obtained by employing an additional MIG arc.
- Ternary eutectic network phase constituting γ-Ni + M₂₃C₆ + M₆C has formed on account of eutectic reaction associated with constitutional liquation with cracking in PMZ region of both welds, with amount of network being high in LHW than ALW
- > Susceptibility to PMZ liquation cracking was found to be higher in ALW than LHW and attributed to high cooling rate that prevails in laser cycle and susceptibility reduces with increase in heat input in both welds
- ➤ LHW provided enhancement in nano-hardness of eutectic network than that of ALW and attributed to dissolution of Mo content in PMZ
- > LHW was more beneficial in terms of resistance to liquation cracking susceptibility as compared to ALW process

From the comprehensive study on process optimization of autogenous single-pass diode laser welding (DLW) of Inconel 617 and their assessment of tensile properties, the following conclusions are drawn:

- ➤ Depth of penetration, depth-to-width aspect ratio and weld bead profile in DLW is mainly controlled by defocusing distance, laser power and welding speed.
- > Full penetration could only be achieved at a negative defocusing distance and lower welding speed due to effective energy coupling with keyhole formation associated with laser heat input but with underfill/undercuts and root hump defects.

- \triangleright DLW produced a Y-shape weld bead profile with wider at top and narrower at bottom with fusion zone microstructure constituting dendrites of γ -matrix with directional solidification and segregation of Mo and Cr carbides along interdendritic regions
- ➤ Weld joint efficiency of diode laser welded Inconel 617 alloy was found to be in the range of 97 99 % with improved yield strength as compared to base metal

From the study on optimization of high-power diode laser welding (DLW) process by adopting Response Surface Methodology (RSM) and validation with desirability approach, influence of three critical processing parameters, namely, Laser Power (LP), Welding Speed (WS) and Defocusing distance (DF) on the quality of weld joint in terms of upper bead width (UBW), weld penetration (WP), fusion zone area (FZA) and radius of curvature (ROC) were investigated and assessed, the following conclusions are drawn:

- ➤ There exists an optimized process parametric range during deep penetration diode laser welding of 10-mm thick Inconel 617 superalloy, where a reduced underfill and root hump defects could be obtained.
- ➤ Based on regression equations obtained from the model indicated that the linear terms of all three input parameters such as LP, WS and DF exert significant effect on UBW, WP and FZA. Also, interactive terms between WS and DF has significant influence on formation of UBW.
- ➤ Optimized process parameters were obtained from the model to achieve maximum WP in 10-mm thick Inconel 617 alloy with maximum ROC were, laser power of 6 kW, welding speed of 6 mm/s and a defocusing distance of -1.48 mm.
- ➤ Validation of the model was done using desirability approach and the experimental results were found to be in good agreement with the predicted one with <5% error.
- ➤ Tensile test results indicated that the weld joint efficiency of the optimized butt-welded joints obtained from RSM model are found to be in the range of 98 99% and superior to that of previously obtained by DLW
- ➤ Indeed, RSM methodology used for developing the model facilitated in fine-tuning defocusing distance effectively welding process with application of other parameters (LP and WS) in the applicable range and also optimize joint strength.

From the comprehensive study carried out to develop novel two-step diode laser welding (Adaptive diode laser welding ADLW) methodology with pre-placement of filler wire and

appropriate butt joint design for joining thick sections of superalloy material with complete elimination of underfills in single-pass, the following conclusions are drawn:

- ➤ The ADLW method involved two step welding procedure; Tack and Seam welding. A new joint configuration was developed and designed for pre-placement of filler wire/rod for the purpose.
- ➤ In first step, filler wire was tack welded in pulsed mode to the base plate with an optimized process parameter. Subsequent to tack welding, laser seam welding experiments were performed with optimum joint configuration and process parameters
- ➤ Welds produced by this method were found to be with uniform weld bead seam throughout the weld length with minimal distortion as well as small HAZ as compared to previously produced previously by DLW
- ➤ Tensile test results indicated that the weld joint efficiency of the butt-welded joints obtained by novel ADLW method are found to be in the range of 99 100% and superior to that of previously obtained by DLW and RSM methodologies
- Microstructure and mechanical behaviour of Inconel 617 weldments produced by ADLW technique are found to be similar to that obtained in DLW joints except for excess reinforcement due to addition of additional filler rod in ADLW process.
- ➤ On the whole, it can infer that new single-pass diode laser welding method with addition of filler wire and without wire feeder proved to be a suitable welding method great promise to join Inconel 617 alloy in various engineering components of thermal power plant.

Finally, from the comparative study conducted between single pass welding processes employing ADLW, LHW with multi-pass TIG with comprehensive metallurgical, mechanical and hot corrosion properties evaluation, following conclusions can be drawn:

- The welds produced by LHW and DLW constitute 'wine-cup' and 'Y-shape' bead profiles with high aspect (depth-to-width) ratios, reduced weld fusion zones and low distortion levels as against large weld fusion zone with 'bath-tub shape' bead profile of multi-pass TIG weld on account of highly localized low heat input high-power density laser beams involved in laser-based welding processes with high energy coupling.
- Microstructural analysis indicated that the fusion zone microstructures of LHW and TIG welds were found to be inhomogeneous owing to the involvement of double heat sources of laser and arc in LHW and multiple weld passes in TIG. Indeed, uniform and

refined microstructure with finer SDAS and reduced micro-segregation of Cr and Mo in interdendritic regions observed in LHW and DLW owing to fast cooling rates of laser welding cycle.

- ➤ X-ray diffraction phase analysis of weld fusion zones revealed presence of strong M₂₃C₆ and M₆C Carbide peaks in TIG as compared to that of LHW and DLW counterparts and attributed to high heat input with low cooling rate with possible microsegregation at GBs experienced by repeated thermal cycles of multiple weld passes involved.
- ➤ Micro and Nano-hardness profiling indicated that the hardness of fusion region of TIG welds are comparatively lower to that of DLW and LHW on account of enhanced segregation of inter-dendritic Cr-rich and Mo-rich carbides and grain coarsening effect.
- ➤ Tensile test results indicated that the joint strength of TIG weldment is lower than that of base metal as against superior strengths observed in both laser welded joints of LHW and DLW to that of base metal. Indeed, formation of ductility-dipped SSGBs and MGBs in weld fusion zone of TIG entailed weakening of the joint strength and failing in fusion zone.
- ➤ High temperature corrosion studies conducted in both salt coated and coal-ash mixed flue gas environment indicated that laser welded specimens provided higher resistance than that of TIG and BM counterparts owing to refined microstructure with reduced micro-segregation in fusion microstructures.

On the whole, the welded joints produced employing single-pass laser based DLW and LHW systems were comparable to tensile strength requirements with superior impact resistance as compared to TIG and BM and thereby suggest easily adoptable in fabrication of high-temperature corrosion resistant superalloy components for thermal power plant and other application sectors. Indeed, the novel single-pass ADLW process developed proved to be more advantageous in terms of eliminating underfill/root sag defects with joint efficiencies on par with other laser-based welding methods and conventional TIG. Additionally, ADLW process developed is found to provide tremendous economic advantage with enhanced process manoverability with elimination of wire-filler feeding apparatus and additional heat source.

10.2 Future Scope of work:

Although extensive research work has been conducted in developing and assessing feasibility of CO₂ laser, Diode laser and laser hybrid welding of thick Inconel 617 alloy and assessing

their microstructural, mechanical and corrosion properties of joints, it is apparent that there are ample scopes for further work in this area.

- ➤ High temperature tensile testing of the novel-ADLW and LHW weldments and comparison with conventional TIG weldments
- ➤ Applications of ADLW processing on actual Tube-to-Tube and Tube-to-Fin joints of Superheater and Reheater tubings
- ➤ Application with actual in plant testing of LHW, DLW and ADLW joints used in boilers parts of thermal power power plants
- > Further studies on high temperature corrosion and oxidation behaviour of weldments for longer period of time (>1000 hours) at various exposure temperatures
- > Creep rupture strenght analysis of weldments
- ➤ Modeling with experiments of ALW, LHW, DLW, ADLW and TIG welding techniques with process validations

Publications

- 1. **Mohd Aqeel, S.M Shariff, J.P Gautam & G. Padmanabham**, "Liquation cracking in Inconel 617 alloy by Laser and Laser-Arc Hybrid welding", *2020*, Materials and Manufacturing Processes, doi.org/10.1080/10426914, 2020 1866200
- Mohd Aqeel, J.P Gautam & S.M Shariff, "Influence of heat input on bead profile and microstructure characteristics in laser and laser-hybrid welding of Inconel 617 alloy", 2022, Welding International Journal, doi.org/10.1080/09507116.2022.2063093
- 3. **Mohd Aqeel, J.P Gautam & S.M Shariff**, "Process optimization and analysis of deep penetration welding of Inconel 617 alloy using high power diode laser", *2022*, Journal of Optics and Laser Technology (Under Review)
- Mohd Aqeel, J.P Gautam & S.M Shariff, "Comparative study on autogenous Diode Laser, CO₂ Laser-MIG hybrid and multi-pass TIG welding of 10-mm thick Inconel 617 superalloy, 2022, Journal of Materials Processing Technology (Under Review)

Presentations in International Conference

 Oral Presentation in Second International Structural Integrity Conference & Exhibition (SICE-2018) entitled "Laser Hybrid welding of Inconel 617 for Advanced ultra-super critical Boiler (AUSC) Applications" (25 – 27 July 2018)

Manuscripts under submission

- 1. **Mohd Aqeel, J.P Gautam & S.M Shariff**, "Statistical modeling of Autogenous single-pass diode laser welding process of Inconel 617 alloy".
- 2. **Mohd Aqeel, J.P Gautam & S.M Shariff**, "A Novel method for single-pass diode laser welding process for thick-sections of Inconel 617 alloy".

Patent (Filed)

1. **Mohd Aqeel, J.P Gautam, S M Shariff, E Anusha, & P S Ganesh**, "Autogenous Laser Welding System and Method for Joining Thick Metallic Parts without Filler Wire Feeder, *2022*, Indian Patent No. 202211005404, dated 01-02-20222

CURRICULAM VITAE

Name : Mohd Aqeel

Date of Birth : 08th September 1991

Educational Qualifications :

B.Tech (2014) : MGIT, Hyderabad

Specialization : Metallurgical and Materials Engineering

M.Tech (2016) : JNTUH, Hyderabad

Specialization : Metallurgical Engineering

Pursuing PhD : University of Hyderabad, Hyderabad

Research Interests : Materials Characterization,

Laser-based welding, Arc welding,

Corrosion

Address : H. No: 20-6-3, Gazi banda street,

Hyderabad, India

Email : mohdaqeel180@gmail.com

Contact Number : +91 7702932193

Investigation on metallurgical and mechanical behavior of thick-sectioned Inconel 617 alloy weldments by Laser-based welding processes

by Mohd Ageel

Submission date: 04-May-2022 11:40AM (UTC+0530)

Submission ID: 1827887824

File name: Ageel Thesis 2 May 2022 final copy.pdf (11.67M)

Word count: 64344 Character count: 339769 Investigation on metallurgical and mechanical behavior of thick-sectioned Inconel 617 alloy weldments by Laser-based welding processes

ORIGINALITY REPORT

16%

2%

INTERNET SOURCES

15%

PUBLICATIONS

0%

STUDENT PAPERS

PRIMARY SOURCES

Mohd Aqeel, J.P Gautam, S.M Shariff.
"Influence of Heat Input on Bead Profile and
Microstructure characteristics in Laser and
Laser-Hybrid Welding of Inconel 617 alloy",
Welding International, 2022

Publication

Mohd Aqeel, J. P. Gautam, S. M. Shariff.

"Influence of heat input on bead profile and microstructure characteristics in laser and laser-hybrid welding of Inconel 617 alloy",

Welding International, 2022

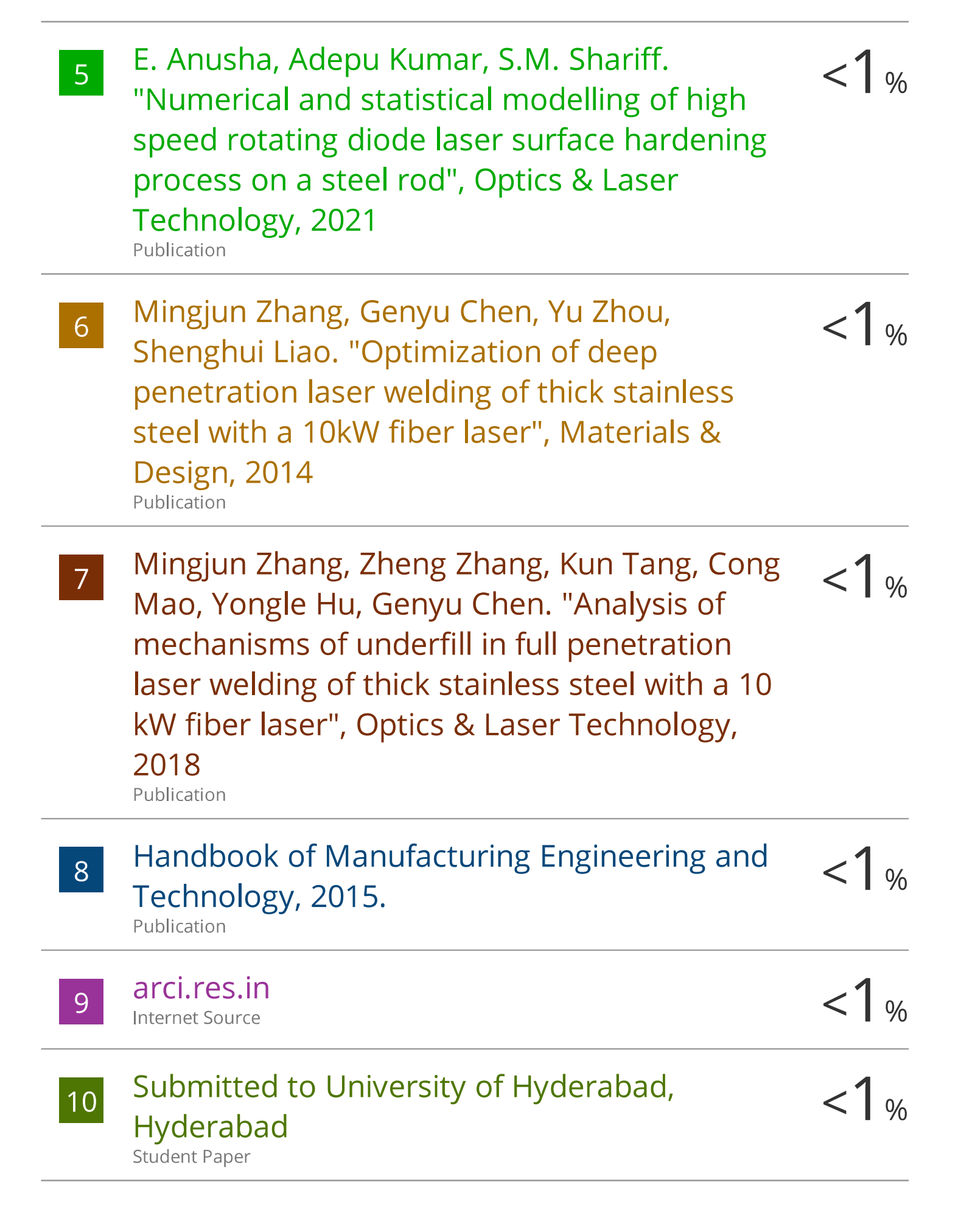
Publication

3 www.science.gov

<1%

P R Hari, N Arivazhagan, M Nageswara Rao, A H V Pavan. "High temperature corrosion of alloy 617 OCC at 700 °C in simulated USC power plant environment", Materials Research Express, 2019

Publication



11	Carton, Marc, Ennis, Philip James, Lecomte-Beckers, Jacqueline and Schubert, Florian. "Materials for Advanced Power Engineering 2002 (CD)", Forschungszentrum Jülich, Zentralbibliothek, Verlag, 2006. Publication	<1%
12	Bappa Acherjee. "Hybrid laser arc welding: State-of-art review", Optics & Laser Technology, 2018 Publication	<1%
13	B. Acherjee. "Laser Arc Hybrid Welding", Elsevier BV, 2018 Publication	<1%
14	Li, Li, Hu, Wu, Cai, Pan. "The Mechanism for HAZ Liquation of Nickel-Based Alloy 617B During Gas Tungsten Arc Welding", Metals, 2020 Publication	<1%
15	spectrum.library.concordia.ca Internet Source	<1%
16	"Superalloys 2016", Wiley, 2016 Publication	<1%
17	Wheeldon, J. M., and J.P. Shingledecker. "Materials for boilers operating under supercritical steam conditions", Ultrasupercritical coal power plants, 2013. Publication	<1%

18	Padmanabham. "Liquation cracking in Inconel 617 alloy by Laser and Laser-Arc Hybrid welding", Materials and Manufacturing Processes, 2021 Publication	<1%
19	A. Alaswad, K.Y. Benyounis, A.G. Olabi. "Optimization Techniques in Material Processing", Elsevier BV, 2016 Publication	<1%
20	Seiji Katayama. "Fundamentals and Details of Laser Welding", Springer Science and Business Media LLC, 2020 Publication	<1%
21	www.tandfonline.com Internet Source	<1%
22	eprints.nottingham.ac.uk Internet Source	<1%
23	Mohammad Naghiyan Fesharaki, Reza Shoja- Razavi, Hojjat Allah Mansouri, Hossein Jamali. "Evaluation of the hot corrosion behavior of Inconel 625 coatings on the Inconel 738 substrate by laser and TIG cladding	<1%
	techniques", Optics & Laser Technology, 2019 Publication	

and innovations in laser beam welding of

wrought aluminum alloys", Welding in the World, 2016

Publication

- Liu, Wen, Fenggui Lu, Renjie Yang, Xinhua <1% 25 Tang, and Haichao Cui. "Gleeble simulation of the HAZ in Inconel 617 welding", Journal of Materials Processing Technology, 2015. Publication dx.doi.org <1% 26 Internet Source Haidou Wang, Lina Zhu, Binshi Xu. "Residual Stresses and Nanoindentation Testing of Films and Coatings", Springer Science and Business Media LLC, 2018 Publication V. S. M. Ramakrishna R, P. H. S. L. R. Amrutha, <1% 28 R. A. Rahman Rashid, S. Palanisamy. "Narrow gap laser welding (NGLW) of structural steels —a technological review and future research recommendations", The International Journal of Advanced Manufacturing Technology, 2020 Publication <1%
 - L. Subashini, K. V. Phani Prabhakar, Swati Ghosh, G. Padmanabham. "Comparison of laser-MIG hybrid and autogenous laser welding of M250 maraging steel thick sections —understanding the role of filler wire

addition", The International Journal of Advanced Manufacturing Technology, 2020

Publication

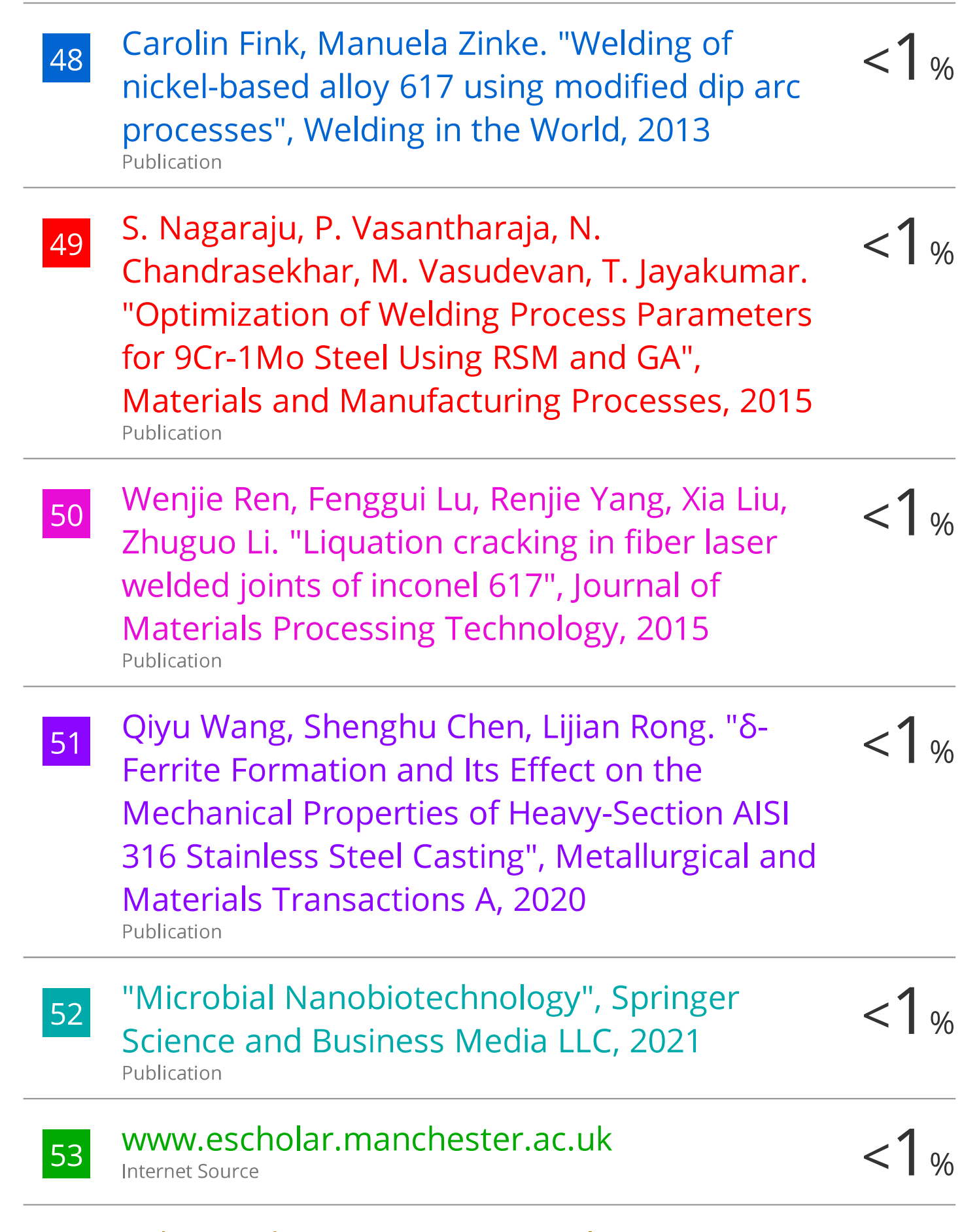
30	"Energy Materials 2014", Springer Science and Business Media LLC, 2016 Publication	<1%
31	Xiaopeng Li, Jing Feng, Jikang Fan, Yong Peng, Kehong Wang. "Parametric investigation of femtosecond laser welding on alumina using Taguchi technique", Optik, 2021 Publication	<1%
32	P.R. Hari, N. Arivazhagan, M. Nageswara Rao, A.H.V. Pavan. "Comparative Studies On Corrosion Of Alloy 617 OCC At 700°C In Air And Simulated Coal Ash Environments", Materials Today: Proceedings, 2018	<1%
33	Maajid Ali, S. K. Vadali. "Development of Electron Beam Welding Procedure for Nb-1Zr- 0.1C Alloy", Materials Today: Proceedings, 2016 Publication	<1%
34	www.insa.nic.in Internet Source	<1%
35	www.mdpi.com Internet Source	<1%

36	Huali Xu, Wen Liu, Fenggui Lu, Peng Wang, Yuming Ding. "Evolution of carbides and its characterization in HAZ during NG-TIG welding of Alloy 617B", Materials Characterization, 2017 Publication	<1%
37	Sanphawat Phromphithak, Puttinan Meepowpan, Sirivatch Shimpalee, Nakorn Tippayawong. "Transesterification of palm oil into biodiesel using ChOH ionic liquid in a microwave heated continuous flow reactor", Renewable Energy, 2020 Publication	<1%
38	Harooni, Masoud, Junjie Ma, Blair Carlson, and Radovan Kovacevic. "Two-pass laser welding of AZ31B magnesium alloy", Journal of Materials Processing Technology, 2015. Publication	<1%
39	Robert W. Messler. "Principles of Welding", Wiley, 1999	<1%
40	Swapan Basu, Ajay Kumar Debnath. "Advanced Ultrasupercritical Thermal Power Plant and Associated Auxiliaries", Elsevier BV, 2019 Publication	<1%
41	wrap.warwick.ac.uk Internet Source	<1%

Huali Xu, Wen Liu, Fenggui Lu, Peng Wang,

42	Choon-Man Lee, Wan-Sik Woo, Jong-Tae Baek, Eun-Jung Kim. "Laser and arc manufacturing processes: A review", International Journal of Precision Engineering and Manufacturing, 2016 Publication	<1%
43	Hao Shi, Ke Zhang, Zhengyi Xu, Tianyu Huang, Liwen Fan, Weining Bao. "Applying statistical models optimize the process of multi-pass narrow-gap laser welding with filler wire", The International Journal of Advanced Manufacturing Technology, 2014 Publication	<1%
44	P PINHERO. "Welding", Smithells Metals Reference Book, 2004	<1%
45	etheses.whiterose.ac.uk Internet Source	<1%
46	Colin Tong. "Introduction to Materials for Advanced Energy Systems", Springer Science and Business Media LLC, 2019 Publication	<1%
47	Xiaohong Zhan, Dan Zhang, Yanhong Wei, Yuhua Wang. "Research on the microstructure and properties of laser-MIG hybrid welded joint of Invar alloy", Optics & Laser Technology, 2017	<1%

Publication



Manufacturing Science and Engineering, 2013.

Publication

60	novel method of laser surface hardening treatment inducing different thermal processing condition for Thin-sectioned 100Cr6 steel", Optics & Laser Technology, 2020 Publication	<1%
61	Ezeonu Stella. "Chapter 15 Laser Soldering", IntechOpen, 2013 Publication	<1%
62	F. Dalle, M. Blat-Yrieix, S. Dubiez-Le Goff, C. Cabet, Ph. Dubuisson. "Conventional austenitic steels as out-of-core materials for Generation IV nuclear reactors", Elsevier BV, 2017 Publication	<1%
63	G. Padmanabham, B. Shanmugarajan, K. V. Phani Prabhakar. "LASER-MIG Hybrid Welding of Thick Plates of Mild Steel in Single Pass", Indian Welding Journal, 2012 Publication	<1%
64	Andrea Tonti. "Cyclic capability of steam generators, EN12952-4, other codes and experimental results", International Journal of Pressure Vessels and Piping, 2010 Publication	<1%
65	Prasanta Sahoo, Tapan Barman, João Paulo Davim. "Fractal Analysis in Machining",	<1%

Springer Science and Business Media LLC, 2011

Publication

Rajakumar, S.. "Predicting tensile strength, hardness and corrosion rate of friction stir welded AA6061-T"6 aluminium alloy joints", Materials and Design, 201105

<1%

Publication

Zhang, X.. "Developments in multi-pass laser welding technology with filler wire", Handbook of laser welding technologies, 2013.

<1%

Publication

Frank Vollertsen, Stefan Grünenwald, Michael Rethmeier, Andrey Gumenyuk, Uwe Reisgen, Simon Olschok. "Welding Thick Steel Plates with Fibre Lasers and GMAW", Welding in the World, 2013

<1%

Publication

M. M. A. Khan, L. Romoli, Marco Fiaschi, G. Dini, F. Sarri. "Multiresponse optimization of laser welding of stainless steels in a constrained fillet joint configuration using RSM", The International Journal of Advanced Manufacturing Technology, 2012

<1%

Padmanaban, G.. "Fatigue crack growth behaviour of pulsed current gas tungsten arc, friction stir and laser beam welded AZ31B

<1%

magnesium alloy joints", Journal of Materials Processing Tech., 201107

Publication

Internet Source

71	K Nishimoto, I Woo, T Ogita, M Shirai. "Factors affecting HAZ cracking susceptibility of laser welds. Study of weldability of Inconel 718 cast alloy (4th report)", Welding International, 2001	<1%
72	Rao, A.C. Umamaheshwer, V. Vasu, S.M. Shariff, and K.V. Sai Srinadh. "Influence of diode laser surface melting on microstructure and corrosion resistance of 7075 aluminium alloy", International Journal of Microstructure and Materials Properties, 2016. Publication	<1%
73	T. S. Balasubramanian, V. Balasubramanian, M. A. Muthumanikkam. "Fatigue Performance of Gas Tungsten Arc, Electron Beam, and Laser Beam Welded Ti-6Al-4V Alloy Joints", Journal of Materials Engineering and Performance, 2011 Publication	<1%
74	edallcoin.fatcow.com Internet Source	<1%
75	idr.l3.nitk.ac.in	< 1 04

76	"Hot Cracking Phenomena in Welds III", Springer Science and Business Media LLC, 2011 Publication	<1%
77	Submitted to Indian Institute of Technology, Kanpur Student Paper	<1%
78	J. Yang. "Typical Joint Defects in Laser Welding of Aluminium-Lithium Alloy", Proceedings of the 36th International MATADOR Conference, 2010 Publication	<1%
79	Poon, M "Efficient interactive 3D Livewire segmentation of complex objects with arbitrary topology", Computerized Medical Imaging and Graphics, 200812	<1%
80	hdl.handle.net Internet Source	<1%
81	uomustansiriyah.edu.iq Internet Source	<1%
82	G. Padmanaban. "An experimental investigation on friction stir welding of AZ31B magnesium alloy", International Journal of Advanced Manufacturing Technology, 10/28/2009 Publication	<1%

Meng Jiang, Wang Tao, Yanbin Chen, Fukang Li. "Comparison of processing window in full penetration laser welding of thick high-strength steel under atmosphere and subatmosphere", Optics & Laser Technology, 2019

<1%

Publication

R. Viswanathan. "U.S. Program on Materials Technology for Ultra-Supercritical Coal Power Plants", Journal of Materials Engineering and Performance, 06/01/2005

<1%

Publication

Sukhomay Pal, Surjya K. Pal, A. K. Samantaray. "Prediction of the quality of pulsed metal inert gas welding using statistical parameters of arc signals in artificial neural network", International Journal of Computer Integrated Manufacturing, 2010

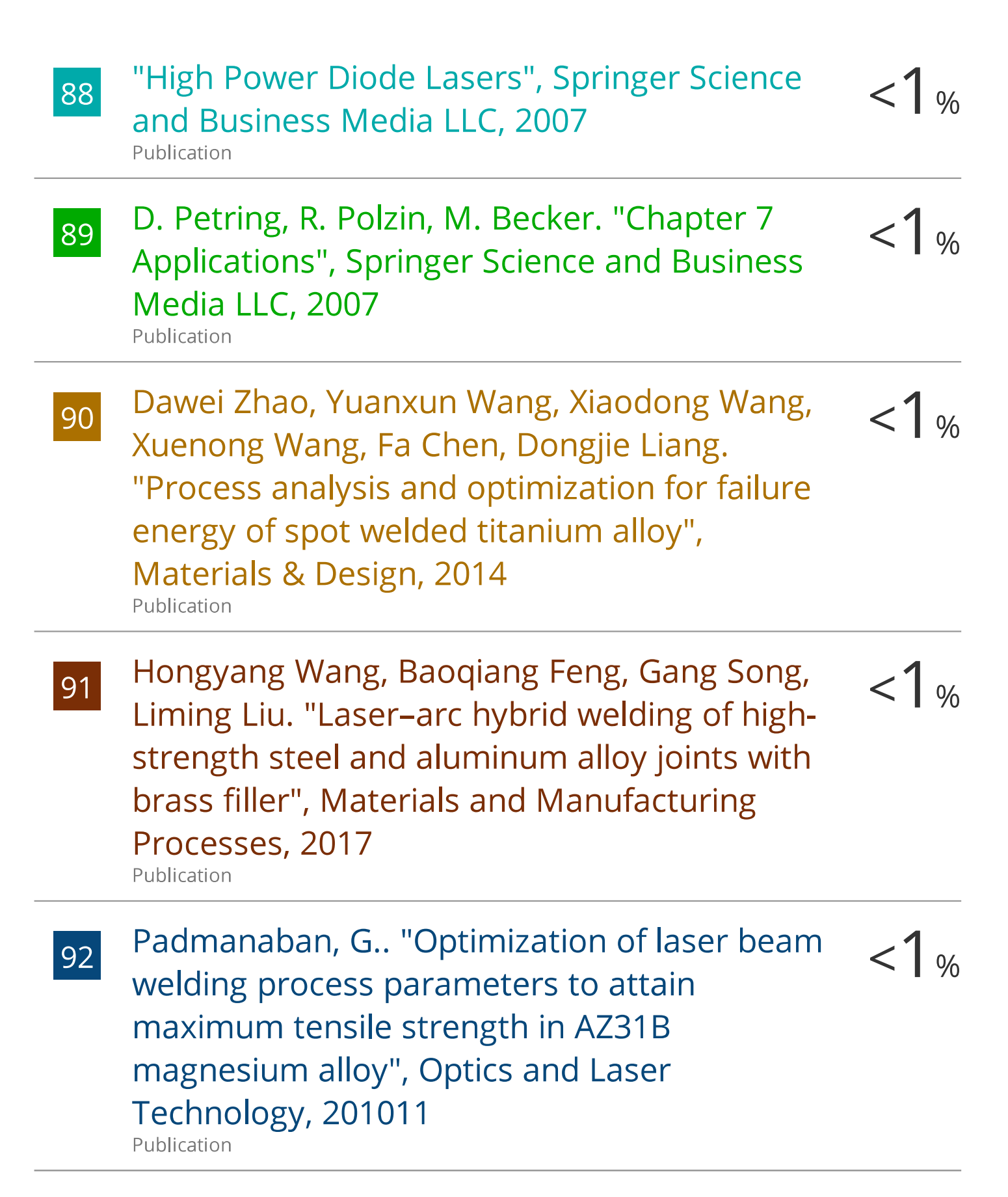
<1%

Wei Liu, Junjie Ma, Fanrong Kong, Shuang Liu, Radovan Kovacevic. "Numerical Modeling and Experimental Verification of Residual Stress in Autogenous Laser Welding of High-Strength Steel", Lasers in Manufacturing and Materials Processing, 2015

<1%

Publication

docshare01.docshare.tips
Internet Source



V. Maduraimuthu, P. Vasantharaja, M. Vasudevan, B.S. Panigrahi. "Microstructure and Mechanical properties of 9Cr-0.5Mo-

<1%

1.8W-VNb (P92) Steel Weld Joints Processed by Fusion Welding", Materials Science and Engineering: A, 2021
Publication

94	Z. Sun: "Fusion Zone Microstructures of Laser and Plasma Welded Dissimilar Steel Joints", Materials and Manufacturing Processes, 2007 Publication	<1%
95	ebin.pub Internet Source	<1%
96	epdf.pub Internet Source	<1%
97	livrepository.liverpool.ac.uk Internet Source	<1%
98	waseda.repo.nii.ac.jp Internet Source	<1%
99	www.atshph.com Internet Source	<1%
100	1library.net Internet Source	<1%
101	H Tong, T Ueyama, T Kihara, K Nakata, M Ushio. "High speed welding of aluminium alloy sheets with using the laser/AC pulsed MIG hybrid process", Welding International, 2005	<1%

102	tracking in laser hybrid welding", Machine Vision and Applications, 02/2009 Publication	\ %
103	Idowu, O.A "Effect of heat input on heat affected zone cracking in laser welded ATI Allvac 718Plus superalloy", Materials Science & Engineering A, 20070425 Publication	<1%
104	Submitted to Loughborough University Student Paper	<1%
105	Pallavi Pant, Jagesvar Verma, Ravindra Taiwade, K. V. Phani Prabhakar. "Influence of advanced laser-arc hybrid welding and conventional MIG process on microstructure, mechanical properties and corrosion resistance of dissimilar joints", Materials Research Express, 2018 Publication	<1%
106	W. Guo, J. A. Francis, L. Li, A. N. Vasileiou, D. Crowther, A. Thompson. "Residual stress distributions in laser and gas-metal-arc welded high-strength steel plates", Materials Science and Technology, 2016 Publication	<1%
107	Wei Guo, Dave Crowther, John A. Francis, Alan	<1%

Thompson, Zhu Liu, Lin Li. "Microstructure

Henri Fennander. "Visual measurement and

and mechanical properties of laser welded S960 high strength steel", Materials & Design, 2015

Publication

108	academic.oup.com Internet Source	<1%
109	"High-Power Diode Lasers", Springer Nature, 2000 Publication	<1%
110	Ai, Yuewei, Ping Jiang, Xinyu Shao, Peigen Li, and Chunming Wang. "A three-dimensional numerical simulation model for weld characteristics analysis in fiber laser keyhole welding", International Journal of Heat and Mass Transfer, 2017. Publication	<1%
111	Anup Kulkarni, Dheerendra K. Dwivedi, M. Vasudevan. "Effect of oxide fluxes on activated TIG welding of AISI 316L austenitic stainless steel", Materials Today: Proceedings, 2019 Publication	<1%
112	Hao Cheng, Li Kang, Jincheng Pang, Boce Xue, Dong Du, Baohua Chang. "Effect of the welding position on weld quality when laser	<1%

welding Inconel 617 Ni-based superalloy",

Optics & Laser Technology, 2021

Publication

Jeffrey W. Sowards, Dong Liang, Boian T.
Alexandrov, Gerald S. Frankel, John C. Lippold.
"Solidification Behavior and Weldability of
Dissimilar Welds Between a Cr-Free, Ni-Cu
Welding Consumable and Type 304L
Austenitic Stainless Steel", Metallurgical and
Materials Transactions A, 2011

<1%

Publication

Sachin Balbande, Ravindra V Taiwade, A P Patil, Ujjawal Pathak. "Cold metal transfer welding of duplex with ferritic and super austenitic stainless steel", Materials Research Express, 2019

<1%

Publication

Wei Guo, Shiyun Dong, Wei Guo, John A. Francis, Lin Li. "Microstructure and mechanical characteristics of a laser welded joint in SA508 nuclear pressure vessel steel", Materials Science and Engineering: A, 2015

<1%

116

Xuyang Chen, Gang Yu, Xiuli He, Shaoxia Li. "Investigation of thermal dynamics for different leading configuration in hybrid laser-MIG welding", Optics & Laser Technology, 2021

<1%

Publication

Exclude quotes On Exclude matches < 14 words

Exclude bibliography On